

Release Kinetics of Volatiles from Smectite Clay Minerals

THÈSE N° 4379 (2009)

PRÉSENTÉE LE 11 JUIN 2009

À LA FACULTÉ SCIENCES ET TECHNIQUES DE L'INGÉNIEUR
LABORATOIRE DE TECHNOLOGIE DES COMPOSITES ET POLYMÈRES
PROGRAMME DOCTORAL EN SCIENCE ET GÉNIE DES MATÉRIAUX

ÉCOLE POLYTECHNIQUE FÉDÉRALE DE LAUSANNE

POUR L'OBTENTION DU GRADE DE DOCTEUR ÈS SCIENCES

PAR

Pascal CLAUSEN

acceptée sur proposition du jury:

Prof. W. Andreoni, présidente du jury
Prof. J.-A. Manson, Dr J. C. Plummer, directeurs de thèse
Dr E. Hughes, rapporteur
Dr L. Meier, rapporteur
Dr F. Rotzinger, rapporteur



ÉCOLE POLYTECHNIQUE
FÉDÉRALE DE LAUSANNE

Suisse
2009

Acknowledgements

This PhD thesis was carried out at the Nestlé Research Center (NRC), Vers-Chez-Les-Blanc, in collaboration with the Laboratoire de Technologie des Composites et Polymères (LTC) of the Ecole Polytechnique Fédérale de Lausanne (EPFL).

Firstly, I would like to express my thanks to my supervisors at EPFL, Dr. C. J. G. Plummer and Prof. J.-A. E. Månson, for their supervision involving discussions and suggestions given during these 4 years.

Many thanks to the members of the jury for having accepted to be the examiners.

I wish to thank all the people from Nestlé Research Center, who contributed to this thesis: especially Dr. E. Hughes who involved himself in the supervision of my work at NRC during the course of the thesis, Dr. B. Watzke for her supervision of the finite element calculations, M. Rouvet for the SEM micrographs, M.-L. Dillmann for the TEM micrographs, Dr. P. Pollien for his supervision of the mass spectrometry measurements, the pilot plant team and the workshop team, and all the people who supported this project.

I wish to acknowledge hospitality at the IBM Zurich Research Laboratory where the *ab initio* calculations have been performed and to thank Prof. W. Andreoni and Prof. A. Curioni for their supervision.

I wish to thank Dr. M. Signorelli, Prof. D. Fessas and Prof. A. Schiraldi from the University of Milano for their collaboration on the Knudsen thermogravimetry measurements.

I wish also to thank Dr. Lorenz Meier, Dr. Johan Ubbink, Dr. Hans-Jörg Limbach for valuable discussions on my thesis work, to thank everyone at the EPFL who helped me and all the teachers I had the opportunity to meet during the doctoral courses.

Abstract

The focus of this thesis was on the mechanisms of release of volatile molecules from smectite clay minerals. The weight loss was monitored by thermogravimetry, differential calorimetry, and mass spectrometry under isothermal conditions and under ramp temperature conditions. Modeling of the clay-volatile release systems was performed with the help of finite element method calculations at the macroscopic level and *ab initio* calculations at the molecular level.

A first comparison between finite element method simulations and experimental data for the evaporation of bulk volatile liquids under a convective gas flow showed the calculations to be in good agreement with experiments. Results of the simulations were used to develop a semi-analytical model explaining the dependence of the evaporation on the total pressure, the carrier gas flow, the temperature, and material constants. In particular, its temperature dependence could be approximated to good accuracy by an Arrhenius-type equation derived from the semi-analytical model. Differential calorimetry measurements of the heats of vaporization showed equilibrium conditions at the surface of the liquids to be satisfied.

The same approach was extended to the release of model volatiles (water, ethanol, ethyl acetate and toluene) from smectite clays. At high coverage, the release was found to be close to that for the bulk liquids. Its decrease with time followed the behaviour observed in the respective curves of the gas/condensed phase partition coefficients, the equilibrium desorption isotherms. Equilibrium condition at the surface of the sample was evidenced by a comparison between the measured heats of vaporization and the equilibrium desorption isotherms.

The differences observed in the measured equilibrium desorption isotherms of the volatile on the smectite clays could be rationalized by the use of *ab initio* calculations of the binding of the volatiles on the surface of a sodium smectite clay. At low coverage, the differences could be attributed to their differences in binding energies with the clay counter ions, which could be explained in terms of the chemical nature of the interacting species. At high coverage, the differences could be related to the properties of the bulk liquids, because high coverage corresponds to high activities of the volatiles on the clay samples.

The differences observed in the measured rates of release of the volatiles from the smectite clays could be rationalized by the use of finite element calculations and the semi-analytical model developed for the bulk liquids, taking as input parameters the measured equilibrium desorption isotherms, that determines the volatile gas phase concentration at the surface of the sample. The slower rates of release of ethanol and ethyl acetate from the smectite clay,

compared to water, could be explained from their differences in their equilibrium desorption isotherms from the clay, though diffusion effects also played a minor role. However, the slower rate of release of toluene, compared to water, could only be explained by its slow diffusion in the smectite clay. Diffusion effects were found to be enhanced with an increase in the size of the aggregate, such that, in addition to the binding strength of the counter ions, the swelling capacity of the clay, allowing the clay to clump, was also found to be an important factor for the controlled release of volatiles from the clay.

Ion-exchange of the clay with lithium cations was found to be optimal in terms of ionic strength of the cation and swelling capacity, as compared to other metallic cations and small organic cations. This clay modification was tested on the release of malodorous compounds determined in cat urine by mass spectrometry and sniffing experiments. The smectite clay modified by ion-exchange with lithium cations showed improved controlled release of volatile organic compounds found in cat urine, compared to the sodium smectite, and improved clumping capacity compared to the calcium smectite. The calcium smectite clay used by Nestlé Purina could be modified by column exchange with lithium cations in high quantities. However the potential toxicity of the lithium is unknown.

Additional information was obtained by *ab initio* calculations on the interaction of water with the smectite. The calculations of the binding of one to six water molecules on the surface of a sodium clay showed the water molecules bind to the cation and form hydrogen bonds between each other and with the clay oxygens, leading to the formation of different configurations for the same number of water molecules on the clay surface. With an increase in the number of water molecules on the surface of the clay, intermolecular interaction between the water molecules became gradually more important than sodium-water interactions. The binding energy was also found to be dependent on the location of the charge substitution in the clay (tetrahedral or octahedral) and to the formation of hydrogen bonds between the water molecule and a basal oxygen linked to a tetrahedral replacement. With an increase in the number of water molecules bound to one counter ion, the sodium counter ion was found to move away from the clay surface. The dynamic calculations of water molecules in the clay interlayer showed both the water molecules and the cations to be mobile, The average diffusion coefficient of the water molecules was reduced compared to that of bulk water, due to restrictions imposed by both the clay platelets and the counter ions. The structure of the water molecules showed to be similar to that of bulk water with a preferential orientation of their hydroxyl group almost perpendicular to the clay surface. The difference in the state of order of the water molecules around the sodium cation was interpreted as a symptom of hysteresis as observed in the measured equilibrium sorption isotherm.

Keywords

ab initio / adsorption / binding / cat litter / cat urine / clay / density functional theory / DFT / desorption / differential scanning calorimetry / DSC / ethanol / ethyl acetate / evaporation / finite element method / FEM / ion exchange / Kunipia-F / light scattering / modeling / malodour / mass spectrometry / MS / molecular dynamics / octane / pyridine / rate of release / release kinetics / smectite / sorption / transmission electron microscopy / TEM / TG / thermogravimetry / toluene / volatile / water

Résumé

La présente thèse porte sur les mécanismes de relargage de molécules volatiles évaporées d'argiles de type smectite. La perte en molécules volatiles fût mesurée par thermogravimétrie, calorimétrie différentielle, et spectroscopie de masse à température constante et sous rampe de température. Les méthodes de simulations par éléments finis et les méthodes de calculs *ab initio* ont été utilisés pour la modélisation macroscopique et moléculaire du système.

Une première comparaison entre les simulations par la méthode des éléments finis et les données expérimentale pour l'évaporation sous flux convectif de liquides volatiles a montré une bonne concordance entre les calculs numériques et les mesures expérimentale. Les résultats obtenus à partir des simulations furent utilisés pour la construction d'un modèle semi-analytique afin d'expliquer la dépendance de la vitesse d'évaporation en fonction de la pression totale, le flux du gas porteur, la température, et les constantes physico-chimiques des molécules volatiles. En particulier, sa dépendance en fonction de la température fût modélisée en très bonne approximation par une équation de type Arrhenius dérivée du modèle semi-analytique.

La même approche fût ensuite appliquée au relargage de molécules volatiles évaporées d'argiles de type smectite. Il a été montré qu'en haute adsorption, les vitesses de relargage sont proches de celles des liquides volatiles. En outre, leur diminution au cours du temps suit les tendances observées sur les courbes isothermes de désorption à l'équilibre. Les conditions d'équilibre à la surface des échantillons d'argile ont été confirmées par une comparaison entre les mesures d'énergies d'évaporation et les isothermes de désorption à l'équilibre.

Les différences observées entre les courbes d'isothermes de désorption des molécules volatiles sur les argiles ont pu être rationalisées par le calcul de l'adsorption des molécules volatiles sur la surface de l'argile. A faible adsorption, les différences entre les isothermes de désorption ont pu être attribuées aux différences entre les énergies de liaison des molécules volatiles avec les contre-ions de l'argile, qui ont pu être à leur tour expliquées par la nature chimique des molécules. A haute adsorption, les différences entre les isothermes de désorption ont été attribuées aux différences entre les propriétés des liquides volatiles, du fait qu'une haute adsorption correspond à une haute activité des volatiles dans l'argile.

Les différences observées dans les vitesses de relargage des molécules volatiles des argiles ont pu être rationalisées à l'aide des simulations par la méthode des éléments finis et du modèle semi-analytique, prenant comme paramètre d'entrée les courbes d'isothermes de

désorption. La plus faible vitesse de relargage de l'éthanol et de l'acétate d'éthyle de l'argile, par rapport de l'eau, a pu être expliquée par les différences observées entre les isothermes de désorption, les effets de diffusion jouant un rôle mineur. En revanche, dans le cas du toluène, les effets de diffusion expliquèrent sa faible vitesse de relargage par rapport à l'eau. Il a été montré que les effets de diffusions augmentent avec une augmentation de la taille de l'échantillon d'argile. En plus de l'énergie d'adsorption des molécules volatiles sur l'argile, la capacité de gonflement de l'argile est donc importante dans la mesure où cela permet de former un gros agrégat à partir des granules après adsorption de liquide.

Il a été montré que l'échange d'ions de l'argile par des ions de lithium produit un résultat optimale en terme d'énergie d'adsorption avec le contre-ion et de capacité de gonflement. Cette modification fût testée à l'aide de spectrométrie de masse et de testes d'odeurs sur le relargage de composants malodorants se trouvant dans l'urine de chat s'évaporant de l'argile. Il a été montré que l'argile modifié avec les cations de lithium comporte des propriétés de contrôle de relargage supérieures à un argile avec des contre-ions de sodium et des propriétés de gonflement supérieures à celles d'un argile avec des contre-ions de calcium. L'argile avec contre-ions de calcium utilisé par Nestlé a pu en outre être modifiée avec succès. Cependant, l'éventuelle toxicité du lithium n'a pas encore été déterminée.

D'autres informations ont aussi été obtenues par calculs *ab initio* sur l'interaction de l'eau avec l'argile de type smectite. Les calculs de l'adsorption de une à six molécules d'eau sur la surface de l'argile ont montrés que les molécules d'eau s'attachent principalement au contre-ions de sodium et forment des ponts hydrogen entre elles et avec les oxygènes basales, resultant en différentes configurations pour le même nombre de molécules sur la surface. Avec une augmentation du nombre de molécules, les ponts hydrogène entre molécules deviennent plus important que l'interaction avec le contre-ion. Il a été montré que l'énergie de liaison est dépendante de l'emplacement de la charge dans l'argile (tétraédrale ou octahédrale) et de la formation de ponts hydrogènes avec les oxygènes basales. Avec une augmentation du nombre de molécules attachées au contre-ion, celui-ci s'éloigne de la surface. Les simulations dynamiques ont montré qu'aussi bien les molécules d'eau que les contre-ions sont mobiles, le coefficient de diffusion des molécules d'eau étant réduit par rapport à celui de l'eau liquide due aux barrières imposées par la surface de l'argile et les contre-ions. La structure de l'eau dans l'argile obtenue est très similaire à celle de l'eau liquide avec toutefois une préférence d'orientation des hydroxyl des molécules d'eau perpendiculaires à la surface de l'argile. La différence entre les arrangements des molécules d'eau autour du contre-ion a été interprétée comme symptôme de l'hystérèse observée dans l'isotherme de sorption à l'équilibre.

Mots clés

ab initio / absorption / attachement / argile / calorimétrie différentielle / cinétique d'évaporation / désorption / dynamique moléculaire / eau / échange d'ions / éthanol / éthyl acétate / évaporation / Kunipia-F / litière / diffraction lumineuse / méthode des éléments finis / microscopie électronique à transmission / modélisation / odeur / octane / pyridine / smectite / sorption / spectroscopie de masse / théorie de la fonctionnelle de densité / thermogravimétrie /

List of acronyms

3QMAS	Triple quantum magic angle spinning
AIMD	Ab initio molecular dynamic
BO	Born-Oppenheimer
CEC	Cation exchange capacity
DFT	Density functional theory
DLVO	Derjaguin, Landau, Verwey, Overbeek
DSC	Differential scanning calorimetry
DTA	Differential thermal analysis
DVS	Dynamic vapour sorption
FEM	Finite element methods
FTIR	Fourier transform infrared
GC/MC	Grand canonical monte carlo
GC-MS	Gas chromatography - mass spectrometry
GGA	Generalized gradient approximation
IR	Infrared
KTGA	Knudsen thermogravimetry
LAMMP	Large-scale atomic/molecular massively parallel
LDA	Local density approximation
LJ	Lennard-Jones
LSER	Linear solvation energy relationship
MAS	Magic angle spinning
MC	Monte carlo
MD	Molecular dynamic
MS	Mass spectrometry
MT	Martins-Trouiller
NMR	Nuclear magnetic resonance
PB	Poisson-Boltzmann
PBE	Perdew-Burke-Ernzerhof
PDE	Partial differential equation
PGSE	Pulsed-gradient-spin-echo
QENS	Quasi elastic neutron scattering
RDF	Radial distribution function
RH	Relative humidity
TG	Thermogravimetry
XRD	X-Ray diffraction

Table of content

CHAPTER 1	Introduction	15
1.1.	Motivation and aim of the thesis	15
1.2.	Approach/Thesis plan.....	16
CHAPTER 2	Literature Review	20
2.1.	Introduction	20
2.2.	Clay definition and structure	20
2.2.1.	Definition of clays	20
2.2.2.	Classification of clay minerals.....	21
2.2.3.	Smectite clays	25
2.3.	Smectite applications and modifications.....	26
2.4.	Interactions of clay with water	29
2.4.1.	Overview.....	29
2.4.2.	Types of water in the clay interlayer.....	30
2.4.3.	Arrangement of water in the clay interlayer	33
2.4.4.	Structural changes of the clay	35
2.5.	Swelling of smectite-water systems: experimental observations.....	36
2.5.1.	Overview	36
2.5.2.	Coexistence of two states of expansion	37
2.5.3.	Crystalline swelling	38
2.5.4.	Osmotic swelling	45
2.6.	Swelling mechanisms.....	47
2.6.1.	Overview.....	47
2.6.2.	Enthalpy as driving force for the layer expansion	49
2.6.3.	Free energy as driving force for the expansion of the clay.....	54
2.6.4.	Hysteresis in the crystalline swelling viewed from experimental observations.....	55
2.6.5.	Mechanisms of osmotic swelling.....	57
2.7.	Dynamics of water in smectite clays.....	59
2.7.1.	Overview.....	59
2.7.2.	Mobility and diffusion of water in the clay interlayer	60
2.7.3.	Quasi elastic neutron scattering measurements	61
2.7.4.	Effective diffusion coefficients of water in the clay-water systems	64
2.8.	Interaction between smectites and small organic molecules.....	74
2.8.1.	Overview	74
2.8.2.	Interactions between volatile molecules and smectites	75
2.8.3.	Influence of the organic cation	81
2.9.	Release kinetics of volatiles from smectite clays.....	83
2.9.1.	Overview	83
2.9.2.	Modeling the evaporation of bulk liquids.....	84
2.9.3.	Release of volatiles from smectite clays.....	86
2.9.4.	Adsorption kinetics of water on smectite clays	89
2.10.	Molecular simulations	92
2.10.1.	Overview	92
2.10.2.	Classical MD simulations with rigid clay structures.....	98
2.10.3.	Classical MD simulations with flexible clay structures.....	113
2.10.4.	Quantum calculations.....	115

2.11.	Malodours in cat urine.....	120
CHAPTER 3 Theory		123
3.1.	Different types of physical modeling.....	123
3.2.	Finite element method.....	125
3.2.1.	Overview.....	125
3.2.2.	Choice of the PDE's	126
3.2.3.	Discretization of the continuum.....	126
3.2.4.	The weak form	127
3.2.5.	The boundary conditions	129
3.2.6.	Solving the nonlinear system of equations	129
3.3.	Ab initio calculations	130
3.3.1.	Overview.....	130
3.3.2.	Born-Oppenheimer Approximation.....	131
3.3.3.	Density functional theory.....	131
3.3.4.	The Kohn-Sham method.....	133
3.3.5.	Choice of the exchange-correlation functional : PBE functional	134
3.3.6.	Choice of the basis set : Plane waves	135
3.3.7.	Use of pseudopotentials	136
3.3.8.	Born-Oppenheimer and Car-Parrinello dynamics	137
3.3.9.	Analysis of the data.....	139
CHAPTER 4 Choice of the Materials and Experimental Procedures		140
4.1.	Choice of the materials.....	140
4.2.	Clay characterizations	142
4.3.	Clay modifications	143
4.4.	Synthesis of the organic salts	145
4.5.	Determination of the equilibrium sorption isotherms	145
4.5.1.	Sorption isotherms with DVS instrumentation.....	145
4.5.2.	Desorption isotherms with Knudsen thermogravimetry.....	146
4.6.	Determination of water content at 43 %RH by saturated salt solutions.....	148
4.7.	Measurement of the release kinetics	148
4.1.	Urine extraction.....	150
CHAPTER 5 Numerical Methods		151
5.1.	Finite element methods	151
5.1.1.	Physical equations and boundary conditions	151
5.1.2.	Physical input parameters	153
5.2.	Ab initio calculations	155
5.2.1.	Computational approach	155
5.2.2.	Validation of the DFT approach	157
CHAPTER 6 Evaporation of Pure Liquids		173
6.1.	Introduction.....	173
6.2.	Semi-analytical model.....	173
6.3.	Effect of the temperature.....	176
6.4.	Effect of the carrier gas flow rate.....	177
6.5.	Effect of the type of chemical	178
6.6.	Conclusion.....	179
CHAPTER 7 Characterization of the Clay.....		181
7.1.	Introduction.....	181
7.2.	Elemental analysis and purity of the clay	181
7.3.	Morphology and size distribution of the clay	183
7.3.1.	Dimensions of the smectite platelets: Light scattering measurements	183
7.3.2.	Dimensions of the smectite platelets: TEM measurements	186
7.3.3.	Morphology of the powder aggregates	187
7.1.	Conclusion.....	187

CHAPTER 8	Interactions between Volatiles and the Sodium Smectite	189
8.1.	Introduction	189
8.2.	Building of the sodium smectite models	189
8.3.	Equilibrium interlayer distance of the dry smectite	190
8.4.	The 221 surface model of the sodium smectite	191
8.4.1.	Positions of the counter ions	191
8.4.2.	Structural features and sodium counter ion adsorption energies	194
8.5.	Binding of volatiles on the 221 surface model	198
8.5.1.	Binding of one water molecule	198
8.5.2.	Binding of other single volatiles	202
8.5.3.	Binding of two to six water molecules	207
8.6.	Dynamics of water in the smectite interlayer	222
8.6.1.	Introduction	222
8.6.2.	Configuration of the sodium cations	223
8.6.3.	Configuration of the water molecules	224
8.6.4.	Diffusion of the water molecules	227
8.7.	Possible explanation for the swelling hysteresis	228
8.7.1.	Introduction	228
8.7.2.	Results	230
8.8.	Conclusion	233
CHAPTER 9	Equilibrium Sorption Isotherms of Volatiles on Smectite Clays	236
9.1.	Introduction	236
9.2.	Equilibrium desorption isotherms of volatiles on the sodium smectites	236
9.2.1.	Reproducibility of the equilibrium desorption isotherms measurements	236
9.2.2.	Comparison between the KTGA and DVS measurements for water	239
9.2.3.	Effect of temperature on water desorption isotherm	240
9.2.4.	Comparison between volatiles	242
9.3.	Equilibrium sorption isotherm of water on the modified smectites	246
9.4.	Conclusion	247
CHAPTER 10	Release Kinetics of Volatiles from Smectite Clays	249
10.1.	Introduction	249
10.2.	Release kinetics of water from a sodium smectite clay	249
10.2.1.	Link with the equilibrium desorption isotherm	249
10.2.2.	Effect of the internal diffusion coefficient	250
10.2.3.	Heat of vaporization and temperature effect	253
10.3.	Release kinetics of water from the modified smectites	256
10.3.1.	Rate of release	256
10.3.2.	Heat of vaporization	257
10.4.	Retention of volatiles from the smectite ion exchange with lithium cations	259
10.5.	Release of volatiles from the sodium smectite	261
10.6.	Conclusion	265
CHAPTER 11	Application	267
11.1.	Introduction	267
11.2.	Characterization of odorous compounds in cat urine	267
11.3.	Ion-exchange with lithium counter ions for improved controlled release of cat urine	278
11.4.	Conclusion	283
CHAPTER 12	Conclusion	284

CHAPTER 1 INTRODUCTION

1.1. MOTIVATION AND AIM OF THE THESIS

In 2002 Nestlé SA purchased the company Ralston Purina for just over ten billion dollars. The acquisition included the pet litter products and pet food division. This takeover was of particular significance for the pet litter industry in that Purina is a world leader in the pet food market with their own clay mining operations in California, Illinois, and Missouri [1]. The mines provide a material rich in smectite clays, which are used for animal litters because of their exceptional sorption properties. Smectite clays are an abundant component of the earth's crust [2] and are available in large quantities at a relatively low price. In addition, no important transformations are necessary to convert the raw material into the cat litter product currently sold to consumers. In order to maintain its market position, it is therefore of great interest to Nestlé Purina to optimize and improve their existing products. Although efforts have been made by Purina to reduce malodor in bedding by adding alpha, beta-unsaturated methyl-branched ethylesters, the bedding may still smell strongly and slightly unpleasant after contact with cat urine [3,4]. This provides the driving force for formulating new cat litter clays with improved odor control properties.

At the industrial level, attempts to develop new products are often based on trial and error. This approach has the advantage of providing relatively rapid tests on the product itself, without the need for simplified model systems, giving direct access to the market. It may be based on a sound understanding of the underlying physical and chemical processes, but the evaporation of urine from cat litter clays is a complex process and knowledge of the mechanisms of evaporation of urine from clay and on the interactions of malodorous compounds with clay is insufficient to provide a basis for the formulation of new litters. The aim of this thesis has therefore been to provide an account of the mechanisms of desorption of volatile molecules from smectite clay, together with a better understanding of the relationship between the interactions of volatile molecules with the clay and their rates of release.

1.2. APPROACH/THESIS PLAN

This section describes the overall approach taken here to the study and modelling of the rate of release of volatiles from smectite clays. This approach is based on the results from the literature review given in CHAPTER 2. The release of model volatiles from model smectites into the gas phase is modelled using finite element methods and monitored by thermogravimetry, differential calorimetry and mass spectrometry. Investigations of the interactions between the volatiles and the smectites are studied by *ab initio* molecular calculations. The theoretic background to the finite element methods and *ab initio* calculations is given in CHAPTER 3, the experimental procedures and the choice of the chemicals are detailed in CHAPTER 4, and a description of the numerical methodologies is given in CHAPTER 5.

Only a few studies have been devoted to the release kinetics of volatiles from smectite clays to the gas phase (section 2.9.3), or to the kinetics of adsorption of volatiles from the gas phase into smectite clays (section 2.9.4). In these studies the experimental data were fitted with different analytical or numerical models. However, model fitting does not allow one to draw conclusions regarding the mechanisms of desorption. The present approach is based on the comparison of experimental measurements and finite element method calculations of the rate of release of volatiles from smectite clays. In the finite element calculations, the release is separated into three processes: (i) internal diffusion of the volatile in the sample; (ii) gas/condensed phase adsorption and desorption of the volatile onto the surface of the sample; (iii) diffusion and convection of the volatile in the gas phase. A reasonable assumption is that of local instantaneous equilibrium conditions between the rate of gas/condensed phase desorption and the rate of gas/condensed phase adsorption (section 2.9.2), so that process (ii) may be replaced by a boundary condition at the surface of the sample, i.e. equilibrium partition between the concentration inside the sample and the gas phase concentration.

The modelling approach is first tested on the rate of evaporation of pure model volatile liquids by comparing experimental measurements and the finite element calculations (CHAPTER 6). In this case, the boundary condition (ii) is given by the saturated vapour pressure of the liquid. These experiments also allow investigation of the effect of the type of volatile, the carrier gas flow rate, the temperature, and the external total pressure on the rate of evaporation and development of a

semi-analytical model applicable to the further study of the rate of release of the volatiles from the smectite samples.

In the case of the release of the volatiles from smectites (characterization of the model smectite is given in CHAPTER 7), the boundary condition (ii) is given by the amount of volatile adsorbed in the smectite as a function of the concentration of volatiles in the gas phase, or equivalently the relative vapour pressure of the volatile, i.e. the equilibrium sorption isotherm. Two input material parameters are therefore required: the equilibrium sorption isotherm and the diffusion coefficient. Both the equilibrium sorption isotherms and the diffusion coefficients are expected to be influenced by the interactions of the volatiles with the smectite.

An extensive literature exists on the equilibrium sorption isotherms of water on smectite clays (sections 2.4, 2.5, 2.6, and 2.10). The increased adsorption of water in smectites with alkali or alkali-earth counter ions with relative humidity causes the smectite platelets to swell in a stepwise manner, showing steps in the equilibrium sorption isotherm. The ease of expansion is dependent on the hydration energy of the counter ion, so that the expansion is generally attributed to the hydration of the counter ions. The steps are reported to be accompanied by the formation of one, two and sometimes three layers of water, though the notion of water layers as a source of controversy. The equilibrium sorption isotherm and swelling show also hysteresis, adsorption and desorption proceeding differently. Results from classical molecular simulations showed the hysteresis to arise from the formation of metastable states separated by an energy barrier. However, explanations for the molecular origin of this energy barrier are not satisfactory. (arrangement and binding) Far less information is available on the equilibrium sorption isotherms of volatiles on smectites, and, in particular, on the desorption branch of the sorption isotherm, and the type of interaction with the smectite surface (section 2.8). π -cation interactions have been proposed for various aromatic compounds and dipole-cation interactions for various polar compounds. However, dipole-cation interactions are not satisfactory to explain the stronger retention of ethanol than water.

Literature data exist for the dynamics of water in smectite clays (section 2.7), but the data for the effective diffusion coefficients show considerable variations. The effective diffusion coefficients could be theoretically calculated from a knowledge of the tortuosity, the porosity and the molecular diffusion coefficient of water in the smectite. However, literature data for the

molecular diffusion coefficients of water in the interlayer of smectites are few and again show considerable variations, ranging from the self-diffusion coefficient of bulk water to values two orders of magnitude lower. Quasi-elastic-neutron-scattering (QENS) studies suggest the water molecules hydrating the cations do not exhibit translational mobility at the experimental timescale but a planar rotational motion, and water not directly coordinated to the cations to be confined to a cage formed by the silicate layers and the hydrated cations, and to jump intermittently between cages. However, interpretations from QENS are dependent on the model applied on the experimental data and further information at the molecular level is necessary to validate these interpretations.

Ab initio molecular calculations were performed here in order to improve the understanding of the interactions between model volatiles and a sodium smectite. These calculations are detailed in CHAPTER 8. The large majority of molecular calculations of the interactions between smectites and other chemicals are based on classical molecular dynamic simulations or classical Monte Carlo simulations (section 2.10). The present method is based on density functional theory in the plane wave – pseudopotential scheme, which provides the best compromise between computational cost and accuracy for such a study, and does not suffer from approximations of classical simulations where the smectite structure is considered as rigid, and where the atomic interactions are considered as pair-wise point charge potentials. The binding of volatiles on the surface of a sodium smectite is first discussed. The results are expected to contribute to the understanding of the different types of binding on the smectite surface and help explain the differences observed in the equilibrium sorption isotherms of the different volatiles. In a second step, the dynamics of water in the interlayer of a sodium smectite are studied. The results are expected to improve understanding of the mechanisms of diffusion and the structure of the water molecules between the smectite platelets. Finally, an attempt is made to provide an explanation for the molecular origin of the hysteresis in the equilibrium sorption isotherm of water on the sodium smectite based on the idea that the different swelling states for the same number of molecules adsorbed in the smectite interlayer correspond to different states of hydration of the sodium counter ion.

In CHAPTER 9, the equilibrium desorption isotherms of model volatiles on a sodium smectite are investigated using a standard dynamic vapour sorption method and a dynamic thermogravimetric method in which standard pans are replaced by Knudsen cells. The two

methods are compared and the results are discussed on the basis of conclusions obtained from *ab initio* calculations. Modification of smectites by ion exchange with metallic cations and organic cations is well known (section 2.3). Organically modified smectites are usually used to improve adsorption of pollutants from aqueous solutions, the adsorbant acting as a partition medium (section 2.8). However, the effect of modified smectites on the rate of release of volatiles into the gas phase is not understood. Therefore in this thesis the equilibrium desorption isotherms of water on smectites modified with both metallic cations and small organic cations are measured.

In CHAPTER 10 the rates of release of volatiles from smectites are measured and the results are compared with finite element calculations using the equilibrium desorption isotherms measured in CHAPTER 9 and numerical calculations using the semi-analytical model developed for the evaporation of the pure liquids in CHAPTER 6. The results are analyzed such, so as to propose a sound understanding of the mechanisms of release of the model volatiles from smectite clays.

The results obtained from CHAPTER 6 to CHAPTER 10 are applied in CHAPTER 11 to the improvement of the controlled release of urine from a smectite clay. Malodorous compounds in cat urine are first characterized by sniffing experiments and mass spectrometry. Then the smectite clay is modified by ion exchange and its performance tested by mass spectrometry.

CHAPTER 2 LITERATURE REVIEW

2.1. INTRODUCTION

This chapter is devoted to a literature survey of topics related to the release of volatiles from unmodified and modified smectite clays. Except for sections 2.2 and 2.3, each section starts with a simple summary followed by more detailed subsections. In section 2.2, clays and clay minerals are defined and the phyllosilicates, and smectite clays in particular, are described in detail. Section 2.3 presents the application of smectite clays in relation to their various modifications. Sections 2.4 to 2.7 treat smectite-water systems. In section 2.4, the focus is on the interactions of water molecules with the smectite, their arrangements in the smectite interlayer, and structural changes associated with hydration and dehydration of the clay. Section 2.5 summarizes the experimental observations on the swelling of smectites as a result of hydration and dehydration; swelling mechanisms are addressed in section 2.6. The dynamics of water in the smectite-water systems are considered in section 2.7. The interactions of low molecular weight compounds, in particular volatiles, with smectites, including smectites exchanged with organic cations are reviewed in section 2.8. Section 2.9 provides information on the evaporation of bulk liquids, and on the sorption kinetics of volatiles from smectite clays. Section 2.10 presents results from molecular simulations. Finally, section 2.11 lists the organic compounds found in cat urine.

2.2. CLAY DEFINITION AND STRUCTURE

2.2.1. Definition of clays

Clays and clay minerals are two terms that are easily confused. There exists no unique definition of the term “clay”. The term clay includes two concepts, one related to the size of grains and the other to the mineralogy. The definition depends on the domain of activity. Geologists denote clay by a particle size smaller than two or four microns. Engineers denote clay by certain physical properties such as plasticity, whatever the particle size. In general clays are crystalline (clay minerals), even though amorphous clays exist (e.g. allophanes). Clay minerals mainly form part

of a subclass of the silicate minerals known as the phyllosilicates. However, not all clay minerals are phyllosilicates (e.g. quartz, feldspath), or even silicates.

2.2.2. Classification of clay minerals

Tetrahedral, dioctahedral and trioctahedral sheets are the fundamental building blocks of phyllosilicates. Tetrahedral sheets (T) are composed of individual tetrahedra which share 3 out of every 4 oxygens. They are arranged in a hexagonal pattern with the basal oxygens linked and the apical oxygens pointing up/down (Fig. 2.1). The resultant sheet composition is M_2O_5 where M denotes the common tetrahedral cations (Si, Al and sometimes Fe and B). Octahedral sheets (O) are composed of individual octahedrons with shared edges, composed of oxygen and hydroxyl anion groups, with Al^{3+} , Mg^{2+} , Fe^{3+} and Fe^{2+} typically serving as the coordinating cation. Ca^{2+} , Na^+ and K^+ are too large to serve as coordinating cations in the octahedral sheet. These octahedra are also arranged in a hexagonal pattern (Fig. 2.2). In the phyllosilicate subclass, rings of tetrahedrons are linked by shared oxygens to other rings (e.g. octahedra) in a two dimensional plane that produces a sheet-like structure. Classification criteria are based on the following parameters:

- The type of tetrahedral-octahedral sheet combination. Possibilities include T:O (1:1), T:O:T (2:1) and T:O:T:O (2:1:1).
- The cation content of the octahedral sheet in the 1:1 or 2:1 layer type (*i.e.* trioctahedral or dioctahedral).
- Magnitude of the layer charge (most often for the 2:1 and 2:1:1 structures). Sheets may be electrically neutral or they may bear a net negative charge. Charge imbalances usually come about by isomorphous substitution or vacancies.
- The interlayer composition (cations, NH_4^+ , organic cations, hydroxyl sheets, water, polar organics).

Secondary criteria are:

- Polytype (a special case of polymorphism, stacking directions of the layer types).

- Chemical composition.
- Type of component layers and nature of stacking for mixed-layer clays.

Table 2.1 shows a classification of phyllosilicates related to clay minerals as recommended by the AIPEA (Association Internationale Pour l'Etude des Argiles)

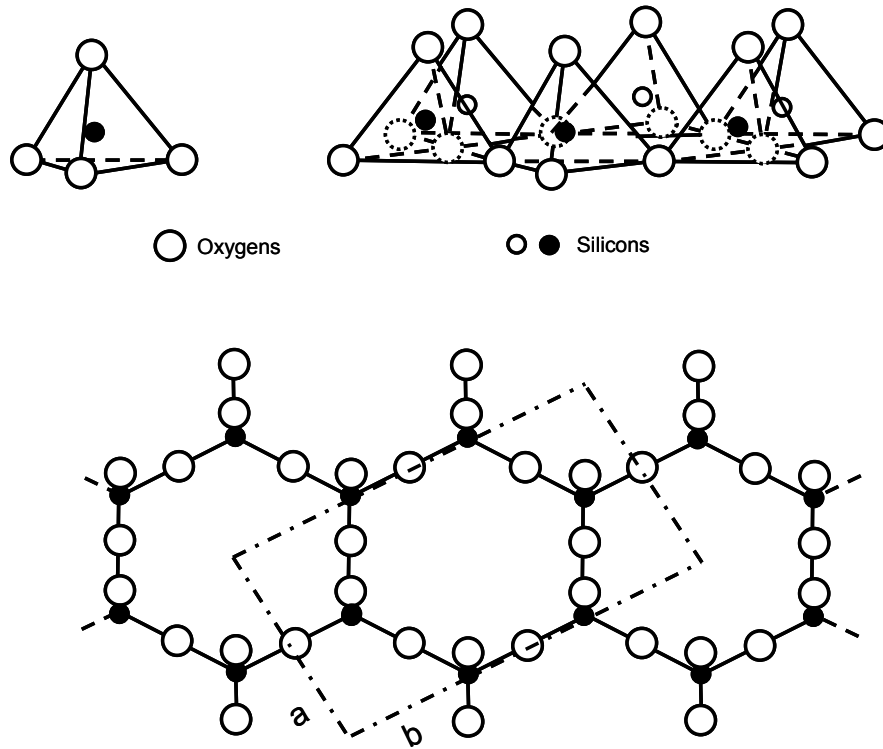


Fig. 2.1 : Tetrahedron and hexagonal arrangement of the tetrahedral sheet

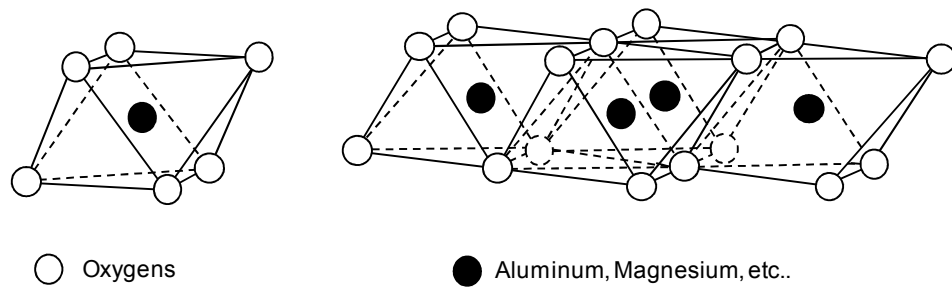


Fig. 2.2 : Octahedron and arrangement of the octahedral sheet.

Table 2.1. Classification of clay minerals

Layer type	Interlayer Material	Group	Charge per formula unit (O ₁₀ (OH) ₂)	Sub-group (cation content)	Spacing	Species examples (possible isomorphous substitution)
T:O (1:1)	None or H ₂ O only	Serpentine - kaolin	~ 0	Serpentines (tri)	stable	Chrysotile (Mg), Antigorite (Mg), Lizardite (Mg,Al)
				Kaolins (di)	variable stable variable	Cronstedite (Fe ²⁺ , Fe ³⁺), Berthierine (Al, Fe ²⁺), Amesite (Al, Mg) Kaolinite (Al), Dickite (Al), Nacrite (Al), Fireclay (Al) Halloysite (Al)
T:O:T (2:1)	None	Talc - pyrophyllite	~ 0	Talcs (tri)	stable	Talc (Mg), Willemseite
				Pyrophyllites (di)	stable	Pyrophyllite (Al)
	Hydrated exchangeable cations	Smectite	~ 0.2 - 0.6	Saponites (tri)	variable	Saponite (Mg), Hectorite (Mg, Li), Sauconite (Mg, Zn), Stevensite (Mg), Bowlingite (Mg, Fe ²⁺), etc.
				Montmorillonites (di)	variable	Montmorillonite (Al), Beidellite (Al, Fe), Nontronite (Fe ³⁺)
		Vermiculite	~ 0.6 - 0.9	Vermiculite (tri)	variable	trioctahedral vermiculite, Batavite (Mg)
				Vermiculite (di)	variable	dioctahedral Vermiculite (Al)
Non-hydrated cations	True Mica	~ 0.5-1.0	True Micas (tri)	stable	Phlogopite, Biotite, Lepidolite (Mg, Fe, K), Annite, Illite (Mg, Fe, K), Phlogite (Mg)	
			True Micas (di)	stable	Muscovite (Al, K), Illite (Al, K), Glauconite (Al, Fe), Paragonite (Al, Na), Celadonite (Al, Fe), Sericite (Al, K), Damourzite (Al, K), Pengite?	
T:O:T:O (2:1:1)	Hydroxide	Chlorite	variable	Brittle Micas (tri)		Clintonite, Anandite
				Brittle Micas (di)		Margarite
Modulated 2:1 Layer	Hydrated exchangeable cations	Sepiolite - Palygorskite	variable	Chlorites (tri)	stable	Clinochlore, Chamosite, Nimite, Penmanite
				Chlorites (di)	stable	Donbassite
				Chlorites (di or tri)	stable	Cookeite, Sudoite
	Variable	No group name	variable	No subgroup name	stable	Sepiolite, Loughlinit
				Palygorskites	stable	Palygorskite (= Attapulgit)
				No subgroup name		Minnesotait (Mg, Fe ²⁺), Stipnomelane, Zussmanite

CHAPTER 2 Literature Review

Modulated Layer	1:1	None	No group name	0	No subgroup name	Antigorite, Greenalite (Fe ²⁺ ,Mg,Zn)
2:1 mixed-layer (regular)		Variable	none		none	Hydrobiotite, rectorite, corrensite, aliettite, tosudite, kulkeite

2.2.3. Smectite clays

In the present work, the focus is on the use of smectites as release systems. These clay minerals belong to the phyllosilicates with T:O:T (2:1) type of tetrahedral-octahedral sheet combination; the central octahedral sheet of alumina or magnesia is fused to two external silica tetrahedra by the apex so that the oxygen ions of the octahedral sheet also belong to the tetrahedral sheets (Fig. 2.3). Their layer thickness is around 1 nm and the lateral dimensions of these layers may vary from 300 Å to several microns.

Talc and pyrophyllite are both neutral smectites, and have therefore no counter ion. For 3 octahedra units of talc, all three coordinating cation sites are occupied by Mg^{2+} . This arrangement is referred as a trioctahedral structure. In this special case, the octahedral sheet with composition $Mg_3(OH)_2$ is called brucite and the resultant composition of the talc is $Mg_3Si_4O_{10}(OH)_2$. For 3 octahedra units of pyrophyllite, 2 out of 3 sites are occupied by Al^{3+} and the third one is vacant. This arrangement is referred to as a dioctahedral structure. In this special case, the octahedral sheet with composition $Al_3(OH)_2$ is called gibbsite and the resultant composition of the pyrophyllite is $Al_2Si_4O_{10}(OH)_2$.

In charged smectites, isomorphic substitutions within the octahedral sheet (for example, Al^{3+} replaced by Mg^{2+} or by Fe^{2+} , or Mg^{2+} replaced by Li^+), and isomorphic substitutions of Si by Al^{3+} in the tetrahedral sheets, generate negative charges that are counterbalanced by alkali or alkaline earth cations situated in the interlayer (exchangeable cations or counter ions), such as sodium, or calcium. The smectite clay itself derives from the aggregation of those layers. Saponite is generally defined as a class of trioctahedral smectites with predominantly tetrahedral substitutions, whereas montmorillonite is generally defined as a class of dioctahedral smectite with predominantly octahedral substitutions.

The rock in which these smectites are dominant is usually called bentonite. However, in economical geology, the term bentonite denotes a deposit of montmorillonite that can be commercially exploited, whereas in sedimentary geology, it denotes distinctive beds formed by the deposition and alteration of volcanic ash, typically composed of montmorillonite, but containing also glass, mixed-layer clays, illite, kaolinite, quartz, zeolites, carbonates, and other minerals.

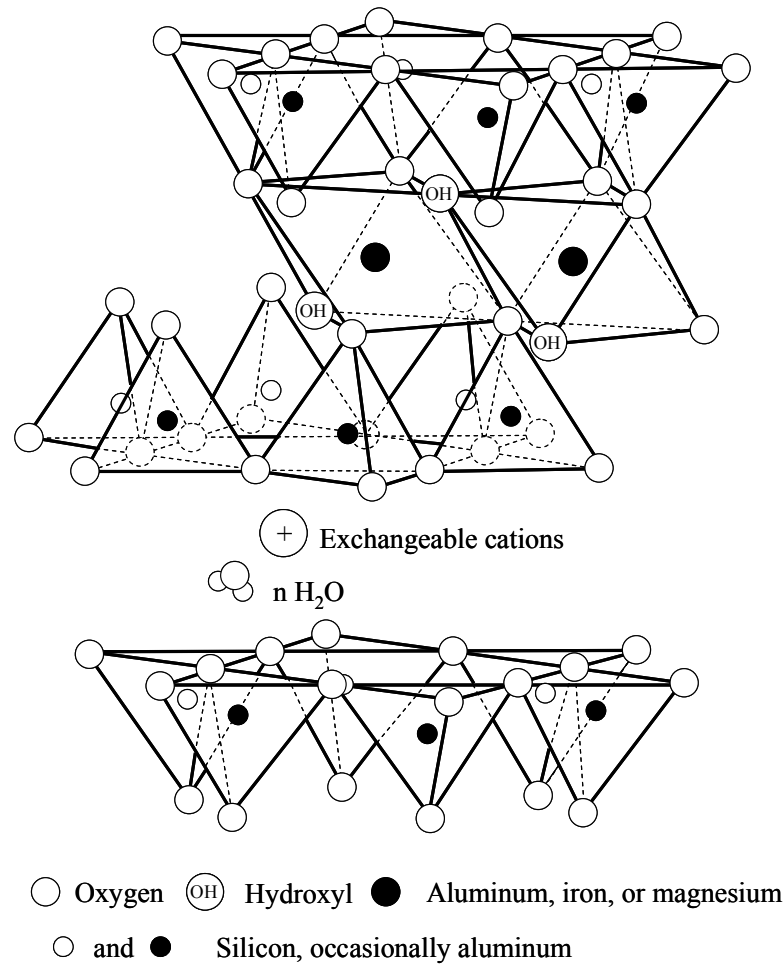


Fig. 2.3 : Smectite structure.

2.3. SMECTITE APPLICATIONS AND MODIFICATIONS

Together with water, clay minerals are the most common substance in the earth crust [2]. They have been used from ancient times to fabricate jars, bowls or amphora. The propensity of clays to adsorb huge quantities of water and then to exfoliate, that is to lose their layered structure, makes them very malleable. On heating, the loss of the water then strengthens the structure of the clay. Their wide availability and their unusual properties make them of interest for commercial applications. Smectites in particular, which can be found all over the world (Fig. 2.4), have a large number of applications, and the range of uses is still increasing [5] (Table 2.2). Swelling behavior, adsorption properties, high surface area, very fine particle size, colloidal and rheological phenomena contribute to the physical and chemical properties that are determinant

for many industrial applications of smectites. The primary uses of Na-smectites are in drilling muds thanks to their swelling properties. Na-smectites are also used extensively to pelletize iron ores because of their superior dry strength. Blends of Na- and Ca-smectites are commonly used to provide optimum properties for moulding sand in foundries. Ca-smectites are suitable materials for bleaching oils and as absorbents. They are used as animal feed and binders acting as adsorbents for bacteria and certain enzymes. Another large and growing use for the Ca-smectites and Na-smectites is as pet waste adsorbent.

Clay properties can be changed by modification of the clay. There are different ways to modify 2:1 clay minerals [5]: (1) adsorption, (2) ion exchange with inorganic cations and cation complexes, (3) ion exchange with organic cations, (4) binding of inorganic and organic cations at the edges, (5) grafting of organic compounds, (6) reaction with acids, (7) pillaring by different types of poly (hydroxo metal) cations, (8) interlamellar and interparticle polymerization, (9) dehydroxylation and calcination, (10) delamination and reaggregation of smectite clay minerals, and (11) physical treatments such as lyophilisation, ultrasound, and plasma.

Ion exchange with organic ions is a well-known method of making clay minerals and clays dispersible in organic solvents and rendering them compatible with hydrophobic materials in compounding processes. These organic-clays are used as thickeners in paints, oil-based drilling fluids, to gel various organic liquids, to stabilize the gel properties of lubricating greases, and to thicken and gel certain cosmetics. Another recent development is the separation of the unit layers into almost unit cell thickness for use in plastics compositions called nanocomposites. With only a few percent of fillers, these nanocomposites show enhanced moduli, strength, thermal stability, flame retardancy, and decreased gas permeability compared with conventional composites at comparable loadings depending on the extent of dispersion of the filler in the plastic. In this case, organoclays are used to improve the extent of dispersion in the plastic. Additional interest in organoclays originates from the need to remove toxic compounds from the environment and to reduce the dispersion of pollutants in water. For these applications, the organic fraction of the organoclay acts as a partition medium for hydrophobic compounds [6]. Because of their size, the organic cations also increase the distance between the layers, as compared to the non-modified clays, facilitating the penetration of molecules between the layers. Depending on the type of organic ion, the clay can also show catalytic effects, increasing detoxification [7]. Complexations of smectites with food-grade organic compounds have also been reported [8,9,10,11].

Pillared clays are another recent development in which the ions on the smectite are exchanged with bulky polyoxo and polyhydroxy metal cations [12]. On calcination they are converted into metal oxide clusters creating an interlayer space of molecular dimensions and a well-defined pore system, that can be tailored for specific catalyst and adsorbent uses.

Some smectites are acid activated, making them effective in decolourizing mineral, vegetable, and animal oils, and in adsorbing mycotoxins [13,14], and some gases [15]. The Ca-montmorillonite is generally activated by using either hydrochloric or sulphuric acid. The acid attack starts with the acid adsorption on the solid surface which leads to the substitution of the exchange cations by protons. Then the adsorbed protons diffuse into the layers and attack the structural OH groups. Central atoms from the octahedral and tetrahedral sheets are liberated, causing an increase in the number of acidic sites, creating the clay to interact more favourably with basic compounds, and increasing the specific surface area of the clay [16,17,18,19,20].

Table 2.2 : Industrial uses of smectite clays (from Murray [21,22])

Drilling mud	Medical formulations	Crayons
Foundry bond clay	Polishing and cleaning agents	Cement
Pelletizing iron ores	Detergents	Dessicants
Sealants	Aerosols	Cosmetics
Animal feel bonds	Adhesives	Paint
Bleaching clay	Pharmaceuticals	Paper
Industrial oil adsorbents	Food additives	Fillers
Agricultural carriers	De-inking of paper	Ceramics
Cat box adsorbents	Tape-joining compounds	Catalysts
Beer and wine clarification	Emulsion stabilizer	Pencil leads



Fig. 2.4: Localities of montmorillonites around the world (reproduced from www.mindat.org).

2.4. INTERACTIONS OF CLAY WITH WATER

2.4.1. Overview

This section describes the interactions of the water molecules with the clay, their arrangements in the clay interlayer galleries, and structural changes associated with hydration and dehydration of the clay. The section 2.4.2 summarizes experimental evidence for the different types of interactions of water with the clay: (1) water molecules bound to the counter ions attached to the clay surface (inner hydration sphere); (2) water molecules bound to fully hydrated counter ions detached from the surface (outer hydration sphere); (3) water molecules forming hydrogen bonds with each other and with the smectite surface. Some authors also propose the water to be sorbed in the ditrigonal cavity of the smectite. Experiments show that the interaction of the water molecules with the smectite results in a preferential average orientation of the water molecules relative to the clay surface (section 2.4.3). In particular, some of the water molecules are found to have their hydroxyl group oriented almost perpendicular to the smectite surface. Nuclear magnetic resonance measurements suggest that the cations are located in the hexagonal cavities in the dry sample, forming a planar structure with the surrounding basal oxygen atoms of the clay structure, and with the increase in water content that the cations are hydrated and their structures change from planar to octahedral. The hydration of the clay is also associated with changes in the orientation of the structural hydroxyl groups, the length of the b lattice constant, and the distortion or rotation of the tetragonal bases (section 2.4.4). Changes in the orientation of the clay

hydroxyl groups are suggested to be caused by the movement of the cations out of the ditrigonal cavity as they are solvated.

2.4.2. Types of water in the clay interlayer

Dielectric relaxation measurements of water in clay-water systems give an indication of the ability of the water molecules to change their orientation in the clay environment. The broader distribution of relaxation times observed for water adsorbed by homoionic montmorillonite, in contrast to the situation in bulk liquid and ice, indicate therefore that a broad variety of molecular environments exists for water in the smectite clay [23,24]. In addition to dielectric relaxation measurements, the occurrence of at least two type of water in the clay interlayer is attested by differential thermal analysis (DTA), infrared spectrometry (IR), and nuclear magnetic resonance (NMR) spectroscopy [25].

2.4.2.1. DTA MEASUREMENTS

Temperature ramp measurements of the weight loss of water from smectites measured by differential thermal analysis [26,27,28] give raise to multiple peaks, suggesting at least two kinds of interlayer water in smectites: water that is readily removable through drying or heating to about 105 °C, and water that is more strongly bound. The highest peak temperatures for magnesium, calcium, strontium, barium, and lithium clays are found to correlate with the hydration energies of the cations. Therefore, these are assigned to the interaction of the clay with the cation, and the total area under the curves indicate a number of about six water molecules per cation, at the first step of hydration for divalent cations, and about three water molecules for lithium and sodium cations. Water lost below 150 °C is assigned to bulk water and weakly bound water [26]. The water lost above 600 °C is assigned to dehydroxylation of the clay and accounts for about 4.8 wt% [26].

2.4.2.2. NMR MEASUREMENTS

NMR measurements of water in Li-hectorite reveal two populations of the longitudinal T_1 spin-lattice relaxation time, attributed to two different types of water [23]. Both populations have T_1 values about two orders of magnitude smaller than the value in bulk liquid water, and therefore reflect a considerably stronger proton-proton interaction, attributed to the interaction of the water molecules with the cations.

2.4.2.3. IR MEASUREMENTS

Ions affect the modes of vibrations of water molecules by polarization of the water molecules and distortion of the H₂O structure [28]. Spectral absorptions due to molecular water in montmorillonite are influenced by both the interlayer cation and the moisture content [28].

Spectral features attributed to interlayer water molecules in smectites have been analyzed [28,29,30] as a function of water content, interlayer cation, and cation exchange capacity. Fig. 2.5 shows the spectral features assigned by Bishop et al [28]. H-O-H asymmetric stretching vibrations are assigned to bound H₂O at about 3620 cm⁻¹ and adsorbed H₂O at about 3450 cm⁻¹. The symmetric vibrations depend more strongly on the cation and are assigned to the range 3520-3550 cm⁻¹ for bound (inner sphere and surface-bonded) H₂O and 3400-3350 cm⁻¹ for adsorbed H₂O. H-O-H bending vibrations are observed in the range 1617-1630 cm⁻¹ for bound H₂O and at shorter wavelengths for adsorbed H₂O. The bending overtone is observed at 3230 cm⁻¹. A rough estimate of the polarizing power of the cations was calculated by dividing the charge on the cation by the radius of the hexa-coordinated metals. This approximate polarizing power increases from Na⁺ (0.86 charge/Å) to Ca²⁺ (1.75 charge/Å) to Mg²⁺ (2.33 charge/Å) to Fe³⁺ (3.82 charge/Å). Increasing polarizing power of the interlayer cations produce, in general, higher energy bending vibrations and lower energy symmetric stretching vibrations (H behaved in a different manner). The infrared absorptions due to structural OH in montmorillonite include the O-H stretching vibration at 3632 cm⁻¹ and in-plane librations at 915-950 cm⁻¹, about 890 cm⁻¹, and about 840 cm⁻¹ due to Al₂OH, Fe³⁺AlOH, and MgAlOH. In the near infrared, the combination bands involving bound H₂O vibrations have higher energies (shorter wavelengths) and occur near 7090 cm⁻¹ (1.41 μm) and 5240 cm⁻¹ (1.91 μm). Also observed at 1.41 μm in spectra of montmorillonite is an overtone of the structural OH stretching mode. Shoulders on each of these features due to adsorbed H₂O combinations arise at 6820-6860 cm⁻¹ (about 1.46 μm) and 5040-5120 cm⁻¹ (about 1.97 μm) as the amount of interlayer water increases. The infrared absorption of molecular water in montmorillonite and hectorite are found to be remarkably similar. This is attributed to the fact that both have octahedral cation replacements, rather than tetrahedral cation replacements as in saponite and vermiculite. These smectites have slightly different infrared absorptions from those of motmorillonite and hectorite as a result of a difference in the distribution of negative charge on the interlayer siloxane surface.

Further results from infrared spectroscopy show that, at high water contents in Na/Li-montmorillonites (water activities higher than 0.7), the positions of the water vibrational bands were similar to those of bulk water [29]. Upon lowering the water content, the water OH stretching band (about 3400-3460 cm^{-1}) shifts to higher frequency and the water H-O-H bending bands (about 1626-1638 cm^{-1}) shift to lower frequency, suggesting that water sorbed to the clay is less hydrogen bonded than that of bulk water. The results indicate also that water is less hydrogen bonded with a decrease in water content [29].

The structural OH peak at 3625 cm^{-1} and the D₂O absorption at 2685, 2510, 2400, and 1205 cm^{-1} do not show any shift as the cation exchange capacity (CEC) of the Na-montmorillonite is decreased [30]. However, the intensity of the D₂O absorption changes significantly. This is an indication that adsorbed water on Na-montmorillonite is primarily solvation water of the exchangeable cations [30].

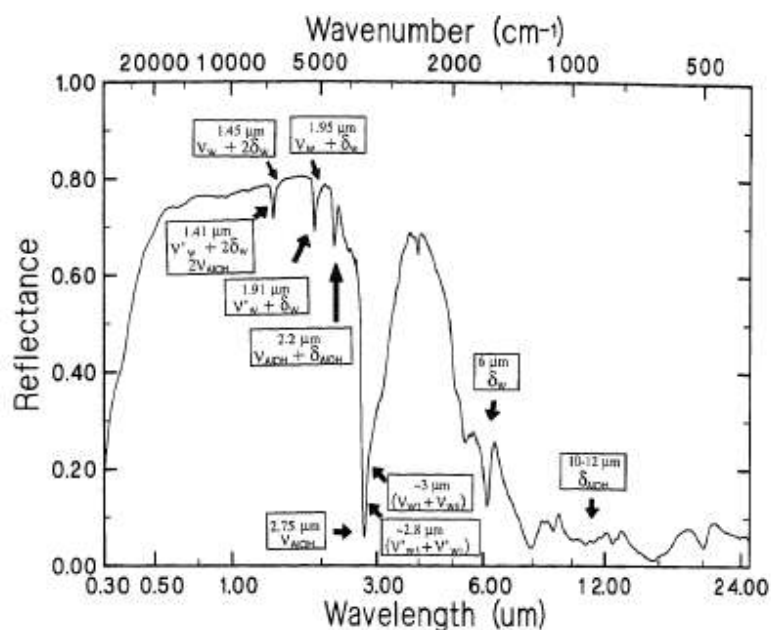


Fig. 2.5 : Reflectance spectrum of SWy montmorillonite (0.3-0.25 μm) (from [28]). Stretching vibrations are labeled with ν , bending vibrations with δ . The subscripts W and OH refer to molecular water in the interlayer region and structural OH, respectively. Stretching vibrations due to inner sphere (bound) H_2O are indicated by ν' and those due to adsorbed H_2O are indicated by ν .

2.4.3. Arrangement of water in the clay interlayer

IR spectrum of progressively deuterated adsorbed water in Li-hectorite indicated that the water molecules were located on sites with C_{2v} symmetry. A band at 3610 cm^{-1} was observed for the OH groups in HOD, showing the water to form weak hydrogen bonds, and the dichroism of the high-wavenumber member of the doublet at $3580\text{-}3640\text{ cm}^{-1}$ (symmetric and antisymmetric vibrations of the water molecule) showed the transition dipole moment of the antisymmetric mode pointed nearly along a normal to the hectorite surface, suggesting the proton of the water molecule to lie along an axis normal to the clay surface [23].

NMR measurements provide further evidence of oriented water in the clay interlayer gallery. The characteristic features of proton NMR spectra of hydrated montmorillonite, beidellite, saponite, and hectorites saturated with Na^+ , Ca^{2+} exchangeable cations, are a doublet, arising from the nonzero average magnetic dipole-dipole interactions, and a central line whose appearance depends on the temperature, the water content, and the orientation of the clay sample [23,24]. This behaviour is interpreted to be evidence for a doublet separation proportional to $|\beta\cos(\delta)^2-1|$

were δ is the angle between the applied magnetic field and a normal to the plane of the clay sample. The adsorbed water molecules on smectite surfaces are found to be oriented preferentially in space at low water contents and at temperatures near 298 K, and that the fact that this average preferred orientation is diminished by increasing water content or temperature suggests the forces causing it are not very strong. The proton doublet splitting for the one-layer hydrate of Li-hectorite is interpreted by Fripiat et al with the model expression:

$$h = (2.7 \cdot 10^{-4})(3 \cos^2 \gamma - 1)(3 \cos^2 \Psi - 1)(3 \cos^2 \delta - 1) \quad (2.1)$$

Where h is the doublet separation in tesla, γ is the angle between the axis of rotation of a water molecule and the vector between its protons, and Ψ is the angle between the axis and a normal to the hectorite surface. Assuming that the axis of rotation is the symmetry axis of the water molecule, then $\gamma = 90^\circ$, and $\Psi = 70^\circ$ is required in order to fit the experimental values of $h(\delta)$. Thus the results suggest the water molecules to be oriented with one of their OH group forming an angle of about 15° with the normal to the clay surface.

The hydration structures of Na^+ ions in the interlayer spaces of dry and hydrated Kunipia-F Na-montmorillonites have been studied by Ohkubo et al [31] using high resolution MAS (Magic Angle Spinning) NMR and triple quantum (3Q) MAS NMR methods. The line shape is observed to become sharper and the chemical shifts to move to lower magnetic field with increasing water content (Fig. 2.6). In spite of the solid state nature of the samples, ^{23}Na MAS NMR spectra of the hydrated samples showed narrow lines as observed in the ^{23}Na NMR spectra for liquid samples containing Na^+ . These results suggest that the Na^+ ions in the interlayer spaces of the hydrated samples are in the form of the hydrated ions with the symmetric structure as the Na^+ ions in aqueous solutions. The quadrupole coupling constants values are expected to become small with an increase in the symmetry of the nearest neighbour coordination sphere of hydrated ions. The isotropic chemical shifts and quadrupole coupling constants calculated from the ^{23}Na 3QMAS NMR measurements vs. the water content are plotted in Fig. 2.7. The isotropic chemical shifts values are approximately identical in all samples except the dry one. But the quadrupole coupling constants values increased in the hydrated sample with increasing water content up to about 5 water molecules per cation, then decrease and approached zero in the hydrated sample at the highest water content, suggesting that the structures of hydrated ions corresponding to 5 to 7 water molecules per cation are less symmetric than those of the dry and other hydrated samples.

They suggest that the cations are located in the hexagonal cavities in the dry sample, forming a planar structure with the surrounding basal oxygen atoms of the clay structure, and with the increase in water content that the cations are hydrated and their structures change from planar to octahedral.

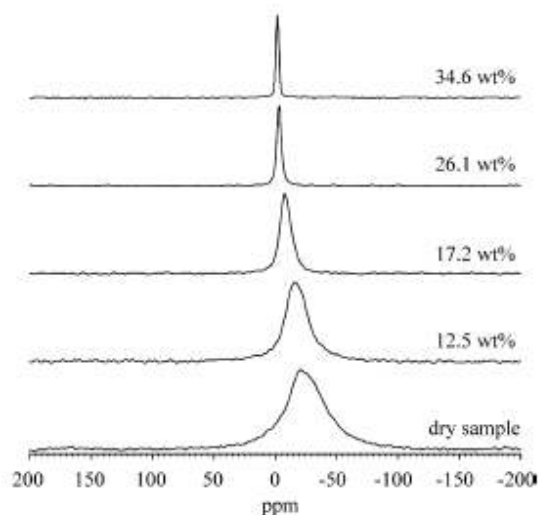


Fig. 2.6 : ^{23}Na 3Q MAS NMR spectra of dry and hydrated Na-montmorillonite samples (from [31]).

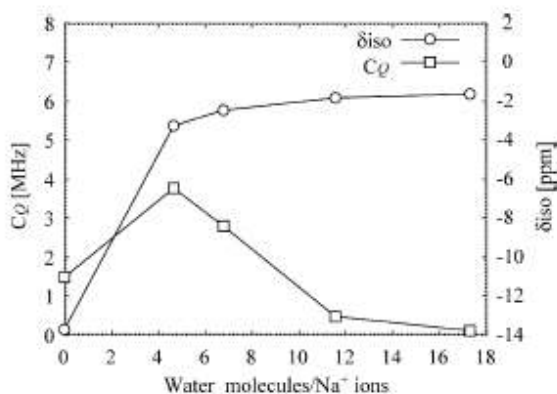


Fig. 2.7 : ^{23}Na isotropic chemical shifts and ^{23}Na quadrupole coupling constants calculated from the ^{23}Na 3Q MAS NMR measurements vs water content (from [31]).

2.4.4. Structural changes of the clay

The IR spectra of water sorbed in different smectites showed that hydration of the clay tended to increase the intensities of the peaks near 918 , 885 , and 851 cm^{-1} , assigned to the clay hydroxyl

groups [23,30,29]. The shift in intensity is most pronounced for OH-bending mode of MgAlOH or AlAlOH which suggests that a change occurs in the orientation of the OH groups owing to the penetration of water molecules [29,32] or cations [30] into the siloxane ditrigonal cavities. In the second case, the cause of this intensity change is suggested to be the movement of exchangeable Na^+ out of the ditrigonal cavities in the silicate surface as these cations become solvated by the D_2O molecules [30].

It is also found that the b lattice constant of the host silicate layers changes (Fig. 2.8) during hydration and dehydration [33]. The transitions in Na-vermiculite involve a substantial host-lattice distortion or rotation of the tetragonal bases in the host silicate layers. The torsional Raman peak at 105 cm^{-1} for a monolayer of water sorbed between the clay platelets (first water layer hydrate (see section 2.5.3.2)) has a narrower peak width than for the dry clay and for a double-layer of water sorbed on the clay. This indicates that the intercalates may be disordered.

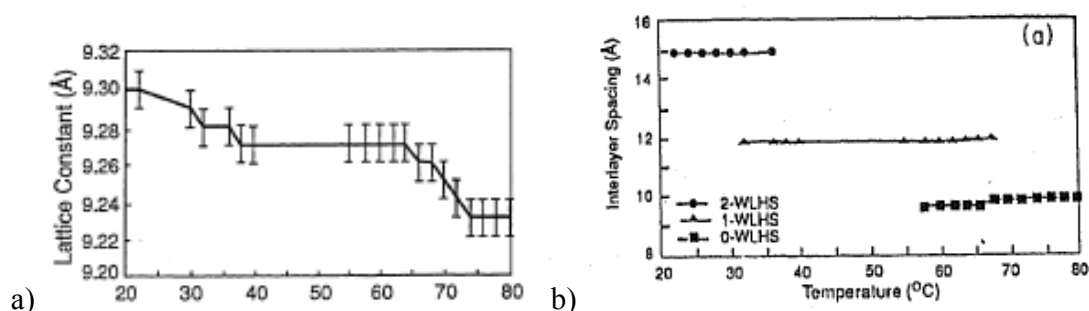


Fig. 2.8 : a) basal spacing versus temperature, and b) lattice constant b versus temperature. WLHS stands for water layer hydrates. (from [33]).

2.5. SWELLING OF SMECTITE-WATER SYSTEMS: EXPERIMENTAL OBSERVATIONS

2.5.1. Overview

This section surveys experimental data for the swelling of clay platelets as a result of hydration or dehydration. In general the distance between the clay platelets increases as a result of the hydration; i.e. the adsorption of water can cause swelling. The swelling can be differentiated in

two states, a partially expanded state (up to about 19 Å) and a fully expanded state (about 40 Å) (section 2.5.2). The two states are energy minima separated by an energy barrier. They can therefore exist simultaneously, but are generally studied separately. The first state is referred as crystalline swelling (section 2.5.3). In this case the expansion is usually studied as a function of relative humidity. The layers expand in steps corresponding to discrete interlayer distances. The steps are generally accompanied with the formation of one, two and sometimes three layers of water, though the notion of water layers is a source of controversy. The crystalline swelling also shows hysteresis; adsorption and desorption proceeding differently. Both the ease of crystalline expansion and the ease of replacement of one counter ion by another correlates with the hydration energy of the counter ion. The crystalline expansion is therefore attributed to the hydration of the counter ions. The charge density and charge location of the clay affect the maximal basal spacing; smectites with tetrahedral substitutions and higher charge tend to have lower maximal basal spacing. The second state is referred as osmotic swelling (section 2.5.4). Depending on the electrolyte concentration and the clay concentration in the clay-water systems, these mixtures can form isotropic liquids, thixotropic gels (isotropic or nematic), and for too high salt concentration, may also flocculate. As opposed to crystalline swelling, the extent of osmotic swelling does not correlate with the hydration energy of the cations. In particular, smectites with monovalent cations, like sodium and lithium, show osmotic swelling, whereas divalent cations, with higher hydration energies, like calcium, do not show osmotic swelling. The tendency for osmotic swelling is also reduced for the more highly charged smectites, especially those with significant tetrahedrally derived components. Possible explanations on the swelling mechanisms is given in section 2.6.

2.5.2. Coexistence of two states of expansion

Zhang and Low studied the effects of monovalent, exchangeable cations and electrolytes on the relation between the swelling pressure and the interlayer distance of Li-, Na-, and K-montmorillonite-water systems [34]. In their method, a gel of oriented clay is formed on a flat, rigid filter enclosed in a chamber. Nitrogen gas is admitted to the environmental chamber at successively higher pressures and the solution expelled from the gel is captured in a reservoir. After equilibrium is achieved, an X-ray diffraction pattern of the clay gel is obtained. At equilibrium, the swelling pressure of the clay is equal to the applied pressure, allowing one to

express the interlayer distance as a function of the swelling pressure. The results of these measurements are represented by the diagram in Fig. 2.9. Clay layers can exist simultaneously in two states, namely, a partially expanded state and a fully expanded state. Layers in the partially expanded state occupy a primary energy minimum and are separated by relatively short distances, whereas layers in the fully expanded state are separated by longer distances, the two energy minimum being separated by an energy barrier. The distribution of layers between the two states at equilibrium is governed by the Maxwell-Boltzmann Law. Indeed, other authors showed that smectite gel at ambient temperature can contain quasi-crystals with 4-5 platelets in face-to-face association as well as isolated single platelets [23]. We note also that the distance between layers in the partially expanded state is insensitive to the applied pressure, whereas the distance between the layers in the fully expanded states varies with the applied pressure.

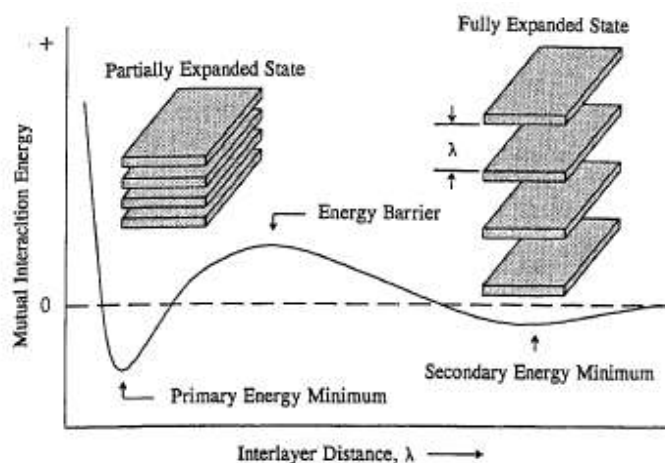


Fig. 2.9 : Mutual interaction energy vs interlayer distance for two interacting clay layers (from [34]).

2.5.3. Crystalline swelling

2.5.3.1. GENERAL OBSERVATIONS

A typical way of quantifying the “crystalline” swelling is to measure the water content and the basal spacing of the clay mineral as a function of the relative humidity. The shapes of the equilibrium sorption isotherms (i.e water content measured as a function of relative humidity), measured by gravimetric method, are complex and cannot be assigned to BET and Langmuir isotherms, or other types of standard isotherm shapes [35,36,37,38,39]. They show steps and hysteresis; i.e. the amount of water adsorbed on the desorption branch is always higher than that corresponding to the adsorption branch [40,41,42,43] (Fig. 2.10 and Fig. 2.11). The stepwise and

hysteretic behaviours are found also in the interlayer distance measured by the X-ray diffraction as a function of clay hydration (Fig. 2.15). Plateaus are observed at about 10 Å, between 12 and 13 Å, between 15 and 16 Å, and sometimes between 18 and 19 Å. At the same relative humidity different basal spacings can coexist [44] (Fig. 2.13). When the interlayer distance is plotted as a function of relative humidity (Fig. 2.15), the basal spacing is higher for the adsorption branch than for the desorption branch [45]. However, when the interlayer distance is plotted as a function of water content (Fig. 2.12 and Fig. 2.16), the basal spacing is lower for the adsorption branch than for the desorption branch [45]. Other properties show hysteresis like the water hydroxyl stretching frequency and the degree of order in the stacking of the clay layers [45].

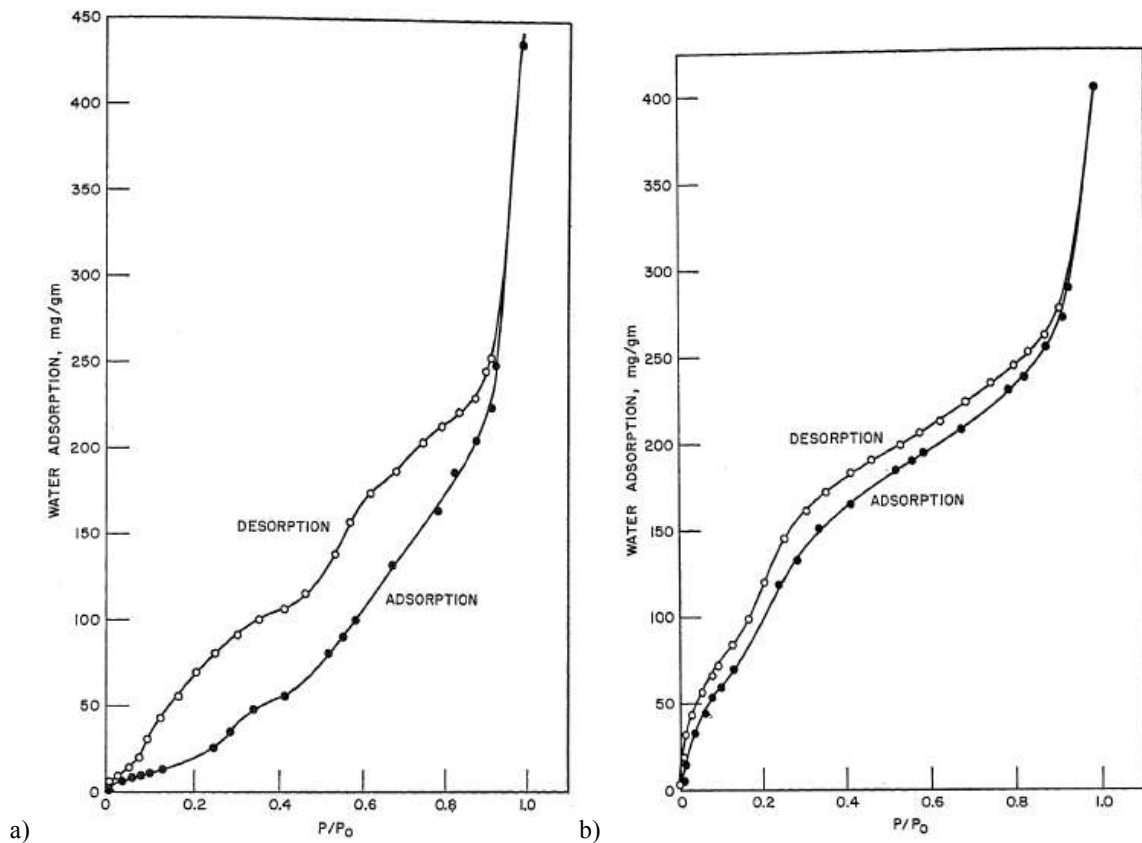


Fig. 2.10 : Measured adsorption-desorption isotherm obtained at 25 °C on a) sodium Wyoming bentonite, and b) calcium Wyoming bentonite (from [43]).

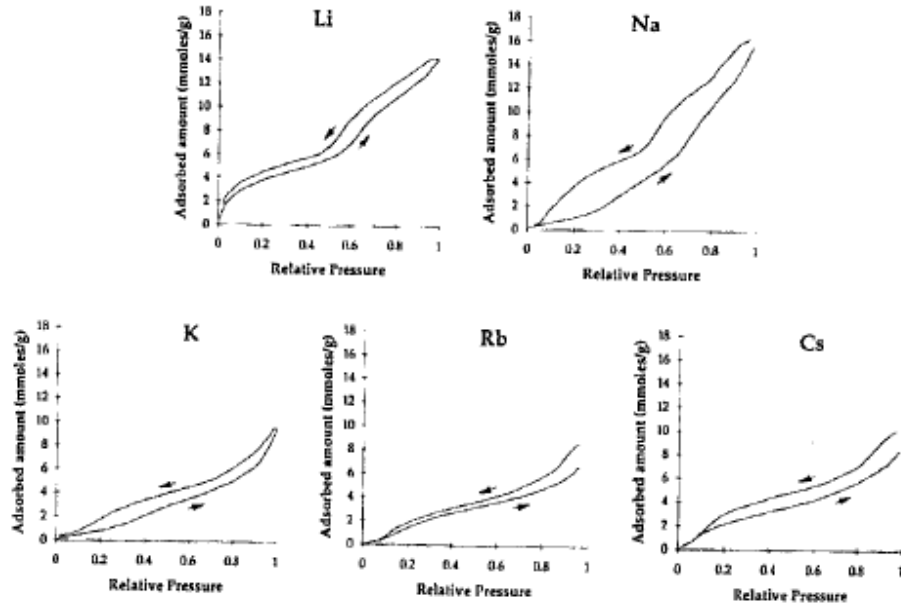


Fig. 2.11 : Water adsorption and desorption isotherms onto Li-, Na-, K-, Rb-, Cs-montmorillonite (from [46]).

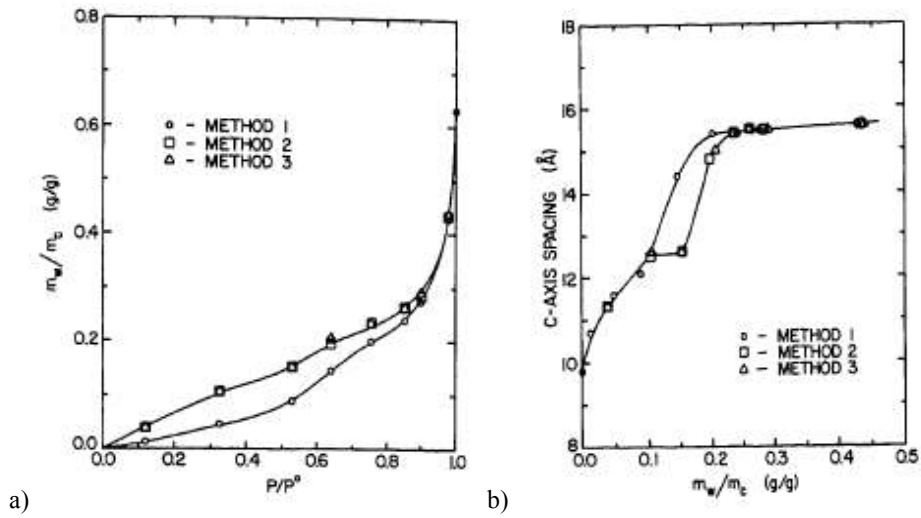


Fig. 2.12 : a) equilibrium sorption isotherm of water on upton Na-montmorillonite, and b) basal spacing as a function of water content. Method 1 (adsorption): dry samples were first enclosed in desiccators over saturated solutions. Method 2 (desorption): dry samples were first enclosed in a desiccator over pure water and then enclosed in desiccators over saturated salt solutions when equilibrium was reached. Method 3 (desorption): dry samples were sprayed with sufficient liquid water to a water content of 2 g of water per gram of clay, and then enclosed in desiccators over saturated salt solutions. (from [45]).

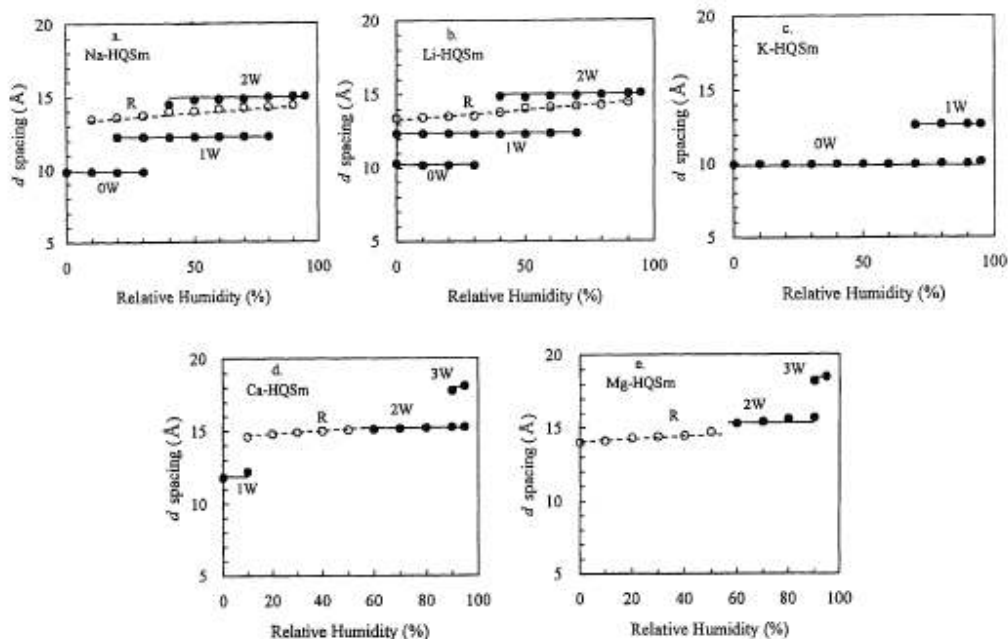


Fig. 2.13 : Basal spacing of synthetic Na-, Li-, K-, Ca-, and Mg-montmorillonite as a function of relative pressure (from [44]).

2.5.3.2. LAYER HYDRATES

Addition of a layer of water molecules at the surface of smectite clay would result in a change of about 3.0 \AA in the separation of the silicate layers [26]. The first layer hydrate would thus have a spacing of about $12.0\text{-}13.0 \text{ \AA}$, a second layer hydrate with two water layers about $15.0\text{-}16.0 \text{ \AA}$, and a third layer at about $18.0\text{-}19.0 \text{ \AA}$ [27]. Therefore the sorption of the water molecules was assigned to the formation of layer hydrates [27]. In general, a change in the numbers of layers between platelets occurs at the same relative pressure or water content as that at which a change in the slope of the isotherm is taking place [40,42]. Therefore the general interpretation is that these represent spacings in the direction of the c-axis for dry montmorillonite and lattices expand by the presence of one, two, or sometimes three layers of water molecule [42,26]. However neutron diffraction patterns of water in the interlayer of synthetic saponite clay samples showed a complete extinction of the d_{001} line of D_2O , suggesting that the classically used notion of a one-layer state for clay minerals is inappropriate for describing these clay minerals [47]. In addition intermediate basal spacing are reported between 10 \AA and 12 \AA [47] (Fig. 2.14). Also the layer hydrates appear to be modified according to both layer charge and relative pressure, such that the notion of layer hydrates cannot be considered as defined states.

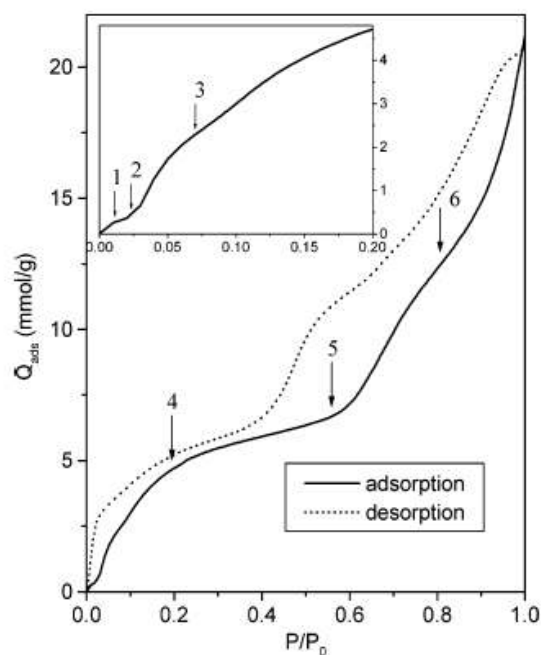


Fig. 2.14 : Measured adsorption-desorption isotherm obtained at 303 K on a synthetic saponite sample (from [47]).

2.5.3.3. INFLUENCE OF THE TYPE OF COUNTER ION

Trends in the sorbed amount of water, the ease of expansion, and the enthalpy of hydration as a function of the type of counter ion have led to the suggestion that the principal mechanism underlying the observed variations is the solvation of the exchangeable cations followed by the adsorption of water molecules in the interlamellar space between cation solvation shells [23].

For the amount of water sorbed at low water contents, the more strongly hydrated cations retain more interlayer water molecules [29,27,48,44,49] (Fig. 2.10 and Fig. 2.11). The sorption isotherms show also little hysteresis for the strongly hydrated cations like calcium and lithium [29], whereas significantly greater hysteresis is observed for the sodium montmorillonite [29] (Fig. 2.10 and Fig. 2.11). Oriented X-ray spacings for vermiculite and montmorillonite were obtained by Kittrick [50] as the sample temperature was changed at a constant rate. The temperature at which an abrupt change in spacing takes place indicates the relative ease of expansion or contraction for a series of interlayer cations. It is found that lower temperatures are necessary to decrease the basal spacing for lower hydration energy, and higher temperatures are required to reexpand the layer silicate prior to sorption of a corresponding water layer, the hysteresis being less pronounced as the hydration energy of the interlayer ion decreases. In general, for crystalline swelling, a higher expansion and a lower amount of coexistent basal

spacings correlate with an increase in the hydration energy of the cations [44,46,48,27,40,42,49]. Data for the enthalpy of hydration of smectites, obtained from the immersion of the smectites in pure water, indicates that the cation hydration makes an important contribution [23,48,44].

2.5.3.4. INFLUENCE OF THE CHARGE DENSITY AND CHARGE LOCATION

Michot et al [51] studied the influence of layer charge on the hydration and swelling behavior of four synthetic sodium saponite samples, by combining gravimetric water adsorption measurements and X-ray diffraction experiments under controlled water pressure. The main consequence of tetrahedral charge localization, as compared to octahedral substitutions, is that the hydration states observed by X-ray diffraction appear more homogeneous, with marked swelling steps. All the samples exhibit a significant hysteresis in the region of relative pressure corresponding to the transition from the “one-layer” hydrate to the “two-layer” hydrate, the amplitude of which decreasing with increasing layer charge (Fig. 2.15). When the layer charge increases, swelling occurs for lower values of the chemical potential, i.e. at lower relative pressure (Fig. 2.15). In parallel, a greater amount of water is needed to initiate swelling for higher-charged samples (Fig. 2.17).

Sato et al [52] studied the effect of charge layer and charge location on the basal spacing of smectite clays hydrated between 0 %RH and 100 %RH. From 0 %RH to 90 %RH, three stable interlayer distances were found at 10.0 Å, 12.4 Å, and 15.6 Å. At 100 %RH, most of the samples expanded further to a basal spacing of about 18.5 Å to 19.0 Å, while some samples did not expand further. The spacings of the samples with negative charge dominantly in the octahedral sites gave larger basal spacings, suggesting that the differences in expansion of these samples could be attributed to charge location.

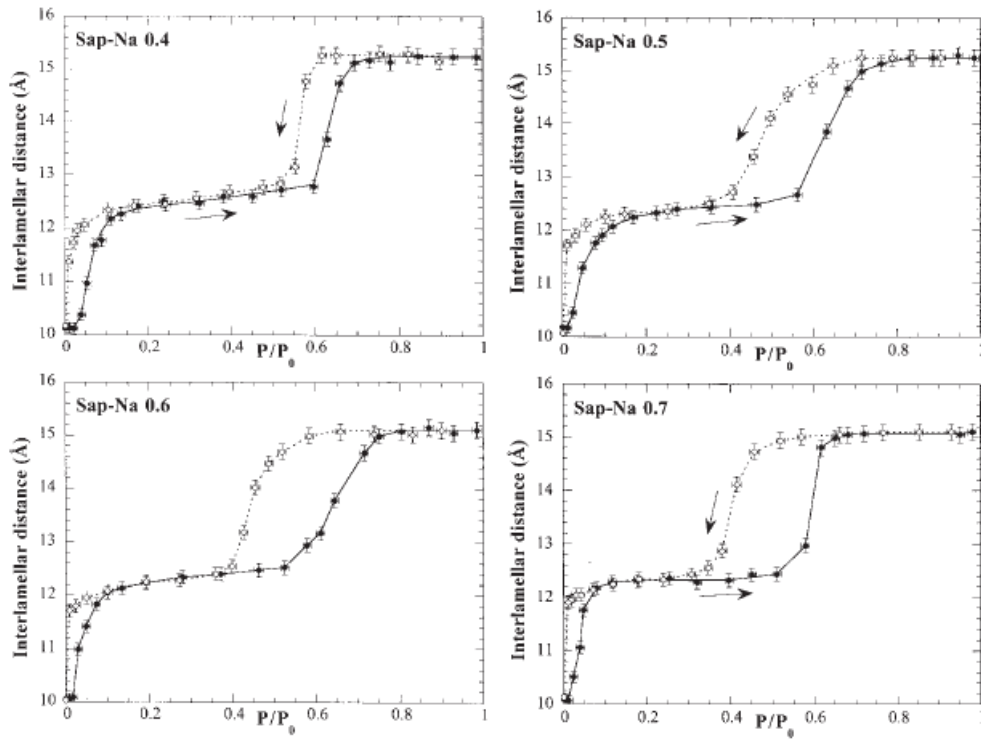


Fig. 2.15 : Evolution of the interlayer distance as a function of relative water pressure for the Na-saponite samples at 303 K (from [51]).

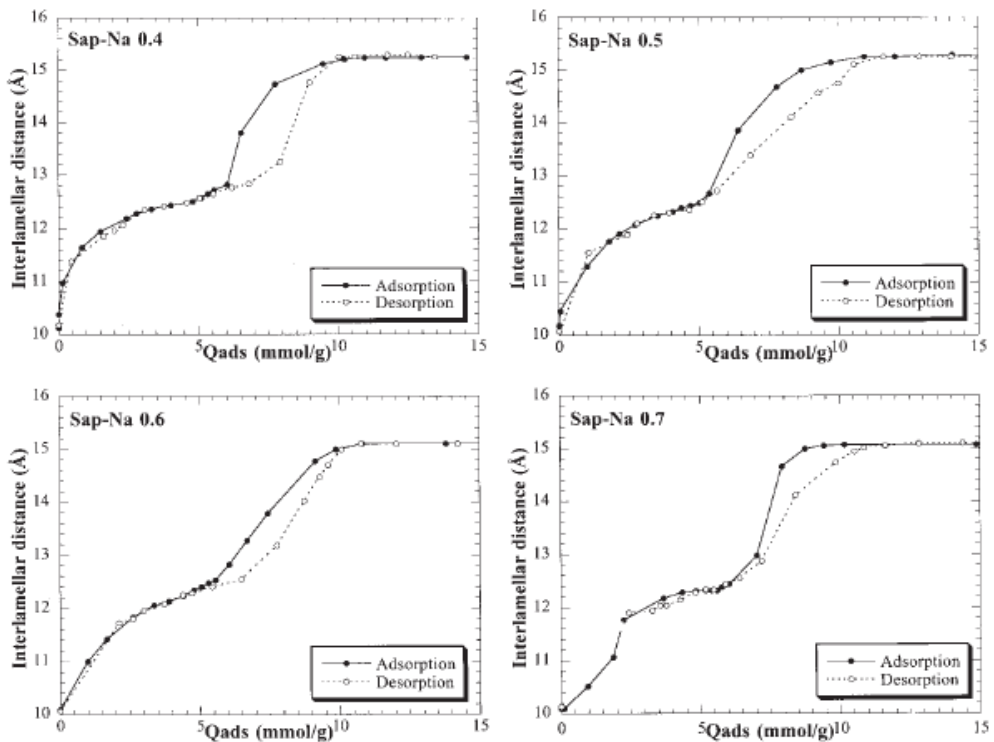


Fig. 2.16 : Evolution of the interlayer distance as a function of amount of water for the Na-saponite samples at 303 K (from [51]).

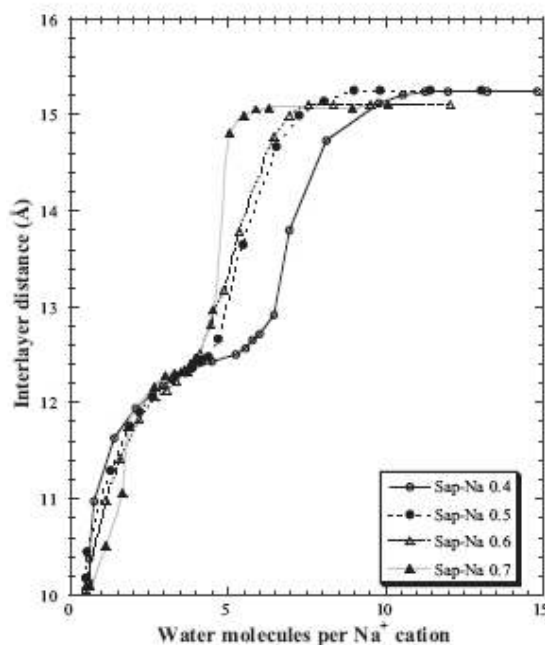


Fig. 2.17 : Evolution of the interlayer distance as a function of number of water molecules per sodium cation of the Na-saponite samples at 303 K (from [51]).

2.5.4. Osmotic swelling

2.5.4.1. PHASE DIAGRAM

The suspensions of smectites in water can form thixotropic gels on standing and the gelation of smectite clay minerals have been extensively studied [53,54,55,56,57,58]. The gels have been characterized by small angle X-ray scattering measurements, rheological measurement, transmission electron microscopy (TEM) observations of cryofracture gels, osmotic pressure determination and observation of nematic liquid-crystal textures, focussing mainly on a synthetic Laponite clay [59], because of its well-defined disc-shape morphology with a diameter of 25 to 30 nm [60]. As the clay suspension is allowed to settle, it separates into two phases: a dilute isotropic (disordered phase) and a concentrated (ordered) nematic one. A phase diagram can be constructed, as shown in Fig. 2.18. Four phases have been identified experimentally in this clay-electrolyte-concentration diagram: isotropic liquid, isotropic gel, nematic gel, and flocculated suspension. This diagram illustrates the fact that the clay particle concentration as well as the electrolyte concentration determine particle ordering.

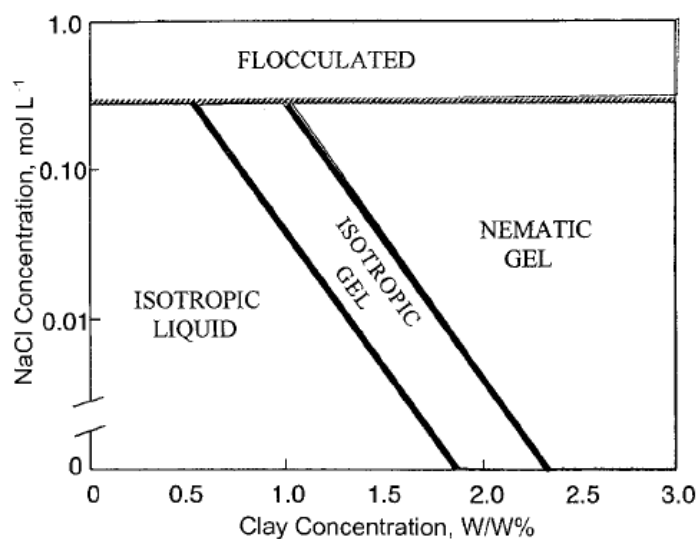


Fig. 2.18: Phase diagram for a Na-smectite suspension (from McBride *et al* [61])

2.5.4.2. INFLUENCE OF THE TYPE OF COUNTER ION

The extent of osmotic swelling is dependent upon the type of counter ion and the charge of the clay. The expansion of montmorillonites with charges balanced by polyvalent ions, such as Ca^{2+} , is found to be limited to a basal spacing of 19 Å or less, whereas montmorillonites with monovalent cations, such as Na^+ or Li^+ , exhibit extensive osmotic swelling in solution [62,23]. For montmorillonites with monovalent cations, more extensive swelling is found for counter ions with higher hydration energy. In particular, The Li-montmorillonite is found to form single platelets in suspension, whereas K- and Cs-montmorillonites, that have counter ions with lower hydration energies, show a tendency to remain at 15 Å [63] and form aggregates with two and three platelets, respectively [23]. For the charge, the highly charged smectites, especially those with significant tetrahedrally derived components do not swell beyond 15 to 16 Å [64,62] (Fig. 2.19). Measurements of the basal spacing of a set of smectites, with variable layer charge and charge location, in equilibrium with NaCl solutions, show that the osmotic pressure for the transition from 18.5 Å to 15 Å, that reflects the ease of expansion, decreases with increasing total layer charge and tends to increase with tetrahedral charge (Table 2.3) [34,49,62].

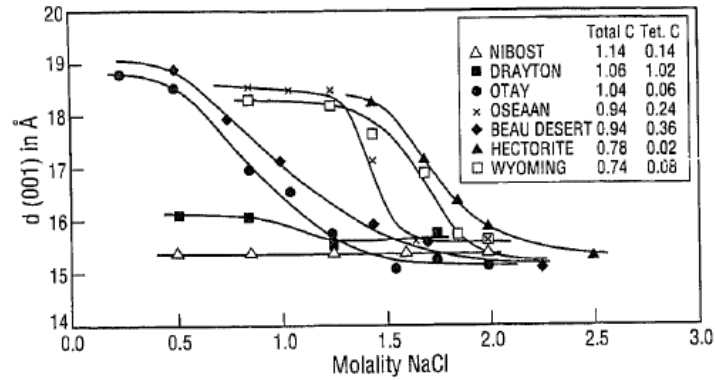


Fig. 2.19 : Relation of basal spacings of Na-saturated smectite samples and the concentration of NaCl solutions. Total C = total charge. Tet C = tetrahedral charge(from [62]).

Table 2.3 : Osmotic pressure and relative water vapor pressure for the 18.5 Å to 15 Å transition in relation to charge characteristics (reproduced from [62]).

Material	solution characteristics at half-transition (d(001)=17 Å)		charge (electrons) per unit cell	
	Osmotic pressure (MPa)	relative vapour pressure (p/p ₀)	total	tetrahedral
Wyoming	8.2	0.943	0.74	0.08
Oseaan	6.7	0.953	0.94	0.24
Beaudesert	4.7	0.967	0.94	0.36
Otay	3.7	0.974	1.04	0.06

2.6. SWELLING MECHANISMS

2.6.1. Overview

This section presents possible explanations on the mechanisms for the crystalline and the osmotic clay swelling. Explanations based on the results from classical molecular simulations will be given in the section on molecular simulations (section 2.10). The sections 2.6.2 and 2.6.3 detail the driving forces that have been advanced to account for the expansion of the clay platelets. The ease of expansion correlates with the energy of hydration of the exchangeable ions and clay

minerals without interlayer counter ions, such as pyrophyllite and illite, do not swell. Therefore, it is of general acceptance that the energy of hydration of the ion is a key parameter in the expansion of the clay layers. The charge of the clay and its location influence the expansion as well, such that ion-clay interactions are also taken into account. Energies arising from van der Waals forces between the platelets, from the hydration of the counter ions, and from the interactions of the counter ions with the clay surface, have been considered. Entropical effects have also been considered for the calculation of the free energy. However, the form chosen for the interaction forces (for example point charge interactions between the clay and the counter ion), the assumptions made on the parameters chosen for the calculations (counter ion placed in the middle of the interlayer; negative clay charge sites considered in terms of their equivalent anion), together with the form chosen for the net energy, whether enthalpic or entropic, can easily be a source of controversy and lead to different conclusions. The balance between interlayer forces, in addition to entropical contributions, is not clear, and though widely studied, the hydration states and structural configuration of water molecules in the interlayer spaces of smectite clay samples remain an open question [51].

There is also little consensus on the molecular origin of the hysteresis in clay crystalline swelling [65]. In section 2.6.4 a possible explanation for the hysteresis is given based on experimental observations. It is shown that enthalpy is gained reversibly during adsorption and desorption, whereas the degree of order achieved during adsorption is not entirely lost until desorption is essentially finished, such that the entropy on the adsorption isotherm is different than the one on the desorption isotherm. Any property that depends on entropy, or degree of order, is hysteretic. The difference in entropy was attributed to changes that occur in the alignment of the clay sheets and the arrangement of the water in the clay interlayer. For the dry clay, rotation of the silicate tetrahedral, due to the electrostrictive influence on the cations on the clay structure, does not allow the clay layers to fit together in any periodic or regular way. With an increase in the interlayer water, the exchangeable cation is thought to move out of the ditrigonal cavity, reducing its influence on the clay sheet that can relax. The increased orderliness of the clay layers and interlayer water sharpens the XRD peak and reduces then entropy and the O-D deuterated water vibration frequency.

In section 2.6.5 possible explanations for the mechanisms of osmotic swelling are given. The Sogami-Ise theory, first developed by Langmuir and then by Sogami, Ise, and Smalley, explains

satisfactorily the experimental observations on clay gels. The pair potential is written as the sum of a purely repulsive osmotic force arising from the small counter ions trapped between the plates, a purely attractive force exerted by the small ions against the plates surface from the outside, and a term resulting from the electrical interaction at equilibrium between the counter ions and the charged plates. The latter term leads to a long-range attraction between the plates. Under certain circumstances, this electrical term is sufficiently large to completely balance the repulsive term, causing particles to attain a stable separation distance at the potential minimum. It is thereby shown that there is an interparticle repulsion at small separation distances, and an attraction at larger distances. A secondary free energy minimum results at intermediate interparticle separations, where the attractive electrostatic potential balances the purely repulsive contribution because of entropic contributions of the counter ions. The potential minimum being deeper than the thermal energy, it allows particles to order into stable but fragile (thixotropic gel) lattice arrays.

2.6.2. Enthalpy as driving force for the layer expansion

Different models have been proposed to explain the expansion of the clay layers upon hydration. Pyrophyllite and talc do not expand, and do not have interlayer ions. To account for the ion-water force Van Olphen proposed clay surface hydration and van der Waals forces for the weak expanding and contracting forces respectively [50]. London dispersion forces, which are due to the polarisation of one molecule by fluctuations in the charge distribution in the second molecule, account for nearly all the Van der Waals attraction in colloidal systems. The attractive energy between two semi-infinite flat plates may be expressed by the following equation [66]:

$$V_A = -\frac{A}{12\pi} \left(\frac{1}{h^2} + \frac{1}{(h+2t)^2} - \frac{1}{(h+t)^2} \right) \quad (2.2)$$

where A is the Hamaker constant, h is the distance between the surfaces of the plates, and t is the thickness of the clay platelet. However, the fact that expansion and contraction are dependent upon ion-water forces is an indication of possible strong balancing ion-clay forces. Zhang and Low [67] proposed that the repulsive force between montmorillonite layers arises because the surfaces of these layers and the interlayer cations tend to hydrate and that the effect of the interlayer cations predominates at relatively small interlayer distances. As a result, the repulsive

force increases as the hydration energy of the exchangeable cations increases, and vice versa. Opposing the repulsive force are the van der Waals attractive force between the layers and the Coulomb attractive force between the layers and the interlayer cations. When the repulsive force exceeds the attractive force, the layers jump apart, so that the hydration energy of the interlayer cations determines the interlayer distance at which jumping begins. In the strong-force model [68], expansion forces considered are due to hydration of the interlayer cation, the negative charge site and the silicate surface. The contraction force is considered to be due primarily to electrostatic attraction between the interlayer cation and the negative charge site. Norrish [69] considered an interlayer cation midway between the layers of montmorillonite. The relationship between the ion and the silicate surface was regarded as a point charge, $\nu e/2$, at a distance D from a thick plane conductor for which the potential of the ion is $\nu e^2/4D\epsilon$, where ϵ is the permittivity in the interlayer, and D (in Å) is given by

$$D = \frac{d - 10}{2} \quad (2.3)$$

where d is the increase in basal spacing relative to the dry clay. If the silicate sheet has a surface density of charge σ , the number of interlayer cations is $2\sigma/\nu e \text{ cm}^{-2}$ so that the attractive potential between the ions and the silicate sheet was given by

$$E = \frac{\sigma^2 \nu e}{2D\epsilon} \quad (2.4)$$

Alternatively the interlayer cations and the charge silicate sheet was regarded as the plates of a condenser where

$$E = \frac{2\pi\sigma^2 D}{\epsilon} \quad (2.5)$$

The actual force being a compromise between the two forces. Given the total hydration energy U , the ratio between between the total hydration energy and the attractive potential between the ions and the silicate sheet, $U\epsilon/\nu^2$, would give an index of the swelling ability with respect to U and ν . A good agreement between this index and the maximum crystalline swelling of montmorillonites with various exchangeable cations was found ($\text{Li}^+ > \text{H}_3\text{O}^+ > \text{Al}^{3+} > \text{Mg}^{2+} > \text{Na}^+ > \text{Ca}^{2+} > \text{Ba}^{2+} > \text{K}^+ > \text{NH}_4^+ > \text{Cs}^+$).

Keren et al [70] extended the strong-force model to include hydrogen bonds between water molecules. They based their theoretical calculation of the heat of adsorption on the hydration energy, the energy of hydrogen bonds, and the attraction energy between the adsorbed ion and the charged platelet. In their model the water molecules in the hydration shell lose the energy, E_a , resulting from ion dipole forces which bind the water molecules to the ion, but gain the energy, E_w , resulting from the reduced possibilities of hydrogen bonding with other water molecules, as occurs in bulk water. The net change in energy, E_A , was computed as:

$$E_A = E_a + E_w \quad (2.6)$$

in which

$$E_a = -\frac{N_A n Z_i e \mu_w}{\epsilon_w (r_i + r_w)^2} \quad (2.7)$$

where N_a is Avogadro's number, n is the number of water molecules in the first layer, Z_i is the ion valency, e is the electronic charge, μ_w is the dipole moment of the water molecules (1.84 D [71]) in the liquid phase, r_i and r_w are the ion and water molecule radii ($r_{Na^+} = 0.95 \text{ \AA}$, $r_{Ca^{2+}} = 0.99 \text{ \AA}$) and ϵ_w is the dielectric constant of the medium. For the first layer of molecules surrounding an ion, the dielectric constant is about 5 [72]. The H₂O molecule can participate in four hydrogen bonds in bulk water. The water molecule coordinated to an ion can coordinate with only two other molecules instead of four. As a result of losing the possible association of these two neighbours, the water molecules gains an average energy E_w of about 2.3 kcal/mol (9.6 kJ/mol) [73]. In their model the main attractive force in the system was the electrostatic interaction between the adsorbed ions and the charge plates. The relationship of the ion to the silicate surface was treated similarly to that of a point charge. The attraction energy, E_r , between an adsorbed ion and the electrostatic charge of the platelet was given by:

$$E_r = -\frac{q_1 q_2}{\epsilon r} \quad (2.8)$$

where q_1 and q_2 are the charges of the adsorbed ion and the clay, respectively, r is the distance between the adsorbed ion and the negative charge of the plate, required to push the platelets apart was then:

$$\Delta E_r = E_{r_1} - E_{r_2} = \frac{q_1 q_2}{\epsilon} \left(\frac{1}{r_1} - \frac{1}{r_2} \right) \quad (2.9)$$

where r_1 is the distance between the adsorbed ion and the plane of negative charge in the dry clay (4.8 Å), and r_2 is the distance between the adsorbed ion and the plane of negative charge in the hydrated clay (6.3 Å at a spacing of 12.6 Å, and 7.5 Å at a spacing of 15 Å). The cations were assumed to be centred between the clay layers. The net energy change in the hydration process of adsorbed ions on clays would then be given by

$$\Delta E = E_a + E_w + \Delta E_r \quad (2.10)$$

Experimental values for Na- and Ca-montmorillonites were calculated from

$$E_1 = \frac{U_{N_2} - U_{N_1}}{N_2 - N_1} \quad (2.11)$$

where U_{N_1} and U_{N_2} are the heats of immersion of clays adsorbed with N_1 and N_2 moles of water, respectively (Fig. 2.20). The heat of adsorption of the first layer of water molecules around the exchangeable cations were found to be 1.8 and 3.3 kcal/mol (7.5 and 13.8 kJ/mol) of H₂O for Na- and Ca-montmorillonite, respectively. Comparison between calculated values and experimental values are given in Table 2.4.

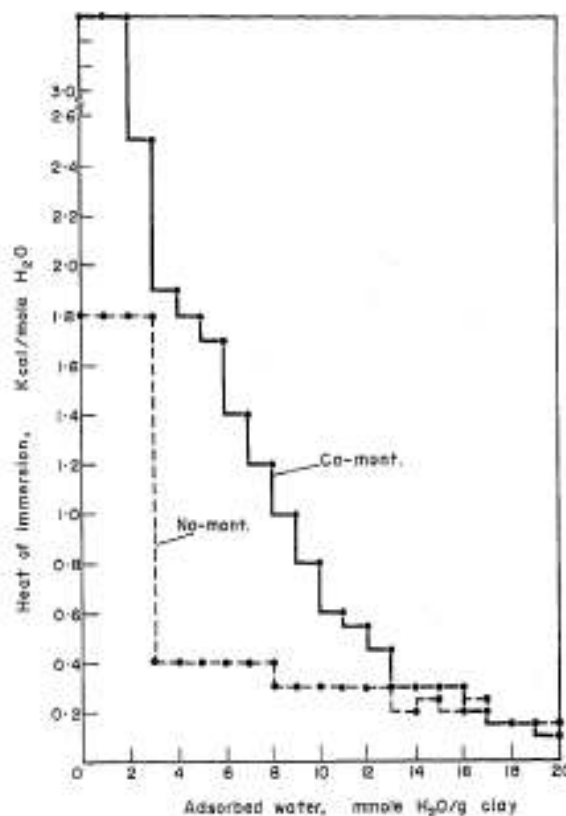


Fig. 2.20 : Amount of heat released per mmol of water adsorbed on Na-and Ca-montmorillonit (from [70]).

Table 2.4 : Energy released for the three mmole of water adsorbed on Na- and Ca-montmorillonite (experimental and calculated values at 25 °C) (reproduced from [70])

adsorbed ion	hydration number	calculated values (kcal/mol)				experimental values (kcal/mol)		
		E_a	E_w	ΔE_r	ΔE_{calc}	1 st	2 nd	3 rd
Na	3	-4.4	+2.3	+1.1	-1.2	-1.8	-1.8	-1.8
Ca	6	-8.8	+2.3	+3.3	-3.2	-3.3	-3.3	-2.5

Of particular interest is the behaviour of vermiculite relative to montmorillonite. Vermiculite expands more readily than montmorillonite with interlayer ions of hydration energy equal to that of Na^+ and above. With interlayer ions of hydration energy equal to that of K^+ and below, montmorillonite expands less readily than previously but vermiculite switches to spontaneous contraction. Therefore, Sato et al [52] proposed the following expansion energy, taking into account the location of the clay charge [52]:

$$\Delta E_r = E_{r_1} - E_{r_2} = \frac{q_t q_t}{\epsilon} \left(\frac{1}{r_{1t}} - \frac{1}{r_{2t}} \right) + \frac{q_t q_o}{\epsilon} \left(\frac{1}{r_{1o}} - \frac{1}{r_{2o}} \right) \quad (2.12)$$

where r_{1t} , r_{2t} , r_{1o} , and r_{2o} are the distances between the interlayer cations and the tetrahedral (t) and octahedral (o) charges in the expanded state 1, and expanded state 2.

2.6.3. Free energy as driving force for the expansion of the clay

Kittrick [68] proposed that the differences observed between the expansion and contraction of montmorillonite and vermiculite can be explained in terms of their dependence upon the change in randomness (entropy), in addition to their dependence upon the force balance, which is essentially an enthalpy consideration. For the thermodynamic approach, the free energy of reaction ΔG is considered:

$$\Delta G = \Delta H - T\Delta S \quad (2.13)$$

Where T is the temperature, ΔH and ΔS is the change in enthalpy and entropy of the system for water sorption. The negative charge sites of vermiculite were considered in terms of their equivalent anion. With Na^+ as exchangeable cation, Eisman computed effective anion radius of the tetrahedrally substituted charge site to be 1.92 Å from basic electrostatic theory. Thus for bonding purposes, the tetrahedrally substituted charge could be represented by the Br^- ion (radius of 1.95 Å) for the Na-vermiculite. A negative charge site with the effective anion radius of Cl^- (1.81 Å) would have a $-T\Delta S$ corresponding to the entropy energy measured by Van Olphen for a Na-vermiculite. Thus, from an entropy point of view, the negative charge sites and the water molecules in Na-vermiculite could effectively act as if a Cl^- ion were being hydrate in bulk solution. The net entropy term is given by the contribution from the hydration of interlayer cation and the hydration of negative charge sites:

$$-T\Delta S = (-T\Delta S)_{\text{cation}} + (-T\Delta S)_{\text{site}} \quad (2.14)$$

The net enthalpy term is given by the contribution from the hydration of interlayer cation and the hydration of negative charge sites, the hydration of the vermiculite surface, the clay expansion, and the clay contraction:

$$\Delta H = (\Delta H)_{\text{cation}} + (\Delta H)_{\text{site}} + (\Delta H)_{\text{surface}} - (\Delta H)_{\text{contraction}} = (\Delta H)_{\text{expansion}} - (\Delta H)_{\text{contraction}} \quad (2.15)$$

Negative values of the free energy favour sorption, whereas positive values favour desorption of water on the vermiculite. The values, estimated by Kittrick (Table 2.5), predict spontaneous sorption of water for Li and Na vermiculites and spontaneous desorption of water for K, Rb, and Cs vermiculites. However, the reason for the choice of the equivalent anion is obscure, and if the Cl^- anion is chosen in place of the Br^- anion for the Na-montmorillonite ($\Delta H_{\text{lat}} = 187.9$ kcal/mol), or if the Br^- anion is chosen in place of the Cl^- anion for the K-montmorillonite ($\Delta H_{\text{lat}} = 163$ kcal/mol), the value of ΔG becomes positive (+ 4), respectively negative (- 2), and the predictions fail for the Na-, and K-montmorillonites. In addition, the free energy results from the subtraction of large numbers but is relatively small as compared to those numbers such that small errors in those numbers can lead to completely different conclusions for the free energy

Table 2.5 : Thermodynamic estimates based upon the strong-force model for sorption of water by Li, Na, K, Rb, and Cs vermiculites at 25 °C. Values are in kcal/mole of exchangeable ions and favor water sorption when negative, desorption when positive (reproduced from [68])

	$-\text{T}\Delta\text{S}_{\text{cation}}$	$-\text{T}\Delta\text{S}_{\text{site}}$	$-\text{T}\Delta\text{S}$	$\Delta\text{H}_{\text{cation}}$	$\Delta\text{H}_{\text{site}}$	$\Delta\text{H}_{\text{surface}}$	$\Delta\text{H}_{\text{expansion}}$	$\Delta\text{H}_{\text{contraction}}$	ΔH	ΔG
Li	8	7	15	-121	-90	-11	-222	180 (LiI)	-42	-27
Na	6	7	13	-95	-90	-11	-196	76 (NaBr)	-20	-7
K	4	7	11	-75	-90	-11	-176	168 (KCl)	-8	+3
Rb	3	7	10	-69	-90	-11	-170	164 (RbCl)	-6	+4
Cs	3	7	10	-61	-90	-11	-162	158 (CsCl)	-4	+6

2.6.4. Hysteresis in the crystalline swelling viewed from experimental observations

Fu *et al* [45] gave the following interpretation of the sorption hysteresis in terms of changes that occur in the structure of the material while the adsorbate is being adsorbed. In a dry montmorillonite, the silicate tetrahedra in the tetrahedral sheet are rotated alternately clockwise and counterclockwise in order to articulate with the alumina octahedral in the octahedral sheet and are coordinated with the exchangeable cations occupying the ditrigonal cavities formed by the surface oxygens [74]. These cations electrostrict the surrounding structure, and its b lattice constant therefore decreases as the crystallographic radius of the exchangeable cation decreases [75]. Rotation of the silicate tetrahedra causes the surface network of oxygens to assume ditrigonal symmetry. This kind of symmetry does not allow the clay layers to fit together in any

periodic or regular way. Under such conditions, the degree of disorder is relatively high, and the X-Ray diffraction (XRD) peaks are correspondingly broad. If the dry clay layers are exposed to water vapour, water molecules penetrate in the interlayer space [42] and hydrate most of the clay layer surfaces and exchangeable cations [44]. In the following process, the exchangeable cations move out of the ditrigonal cavities [30], their electrostrictive influence on the surrounding structure is reduced, and the structure relaxes [75]. Some of the energy released in the hydration of the surfaces and cations and in the relaxation of the mineral structure is utilized to remove the cations from the ditrigonal cavities and to separate the layers against the prevailing attractive forces, but most of it is lost as heat. During the initial stages of hydration, the water molecules must depart from their normal tetrahedral arrangement so that they can coordinate simultaneously with the surface oxygens of the clays and the exchangeable cations. More strain exists in the resulting arrangement than in the arrangement characteristic of bulk water, and, accordingly, then entropy and O-D vibration frequency are relatively high. With an increase in the interlayer water, the orderliness of the layers and interlayer water sharpens the XRD peak and reduces the entropy and the O-D vibration frequency. At a water content of about 45 % the system reaches its most ordered state and the entropy is at a minimum (Fig. 2.21b). Moreover, the value of the D-O vibration frequency is close to that of bulk water. When desorption follows adsorption, all of the process are reverse and energy is gained reversibly (Fig. 2.21a). The degree of order achieved during adsorption, however, is not entirely lost until desorption is essentially finished (Fig. 2.21b). Thus, hysteresis occurs because the orderliness of the system is not reversible, and any property that depends on orderliness is hysteretic.

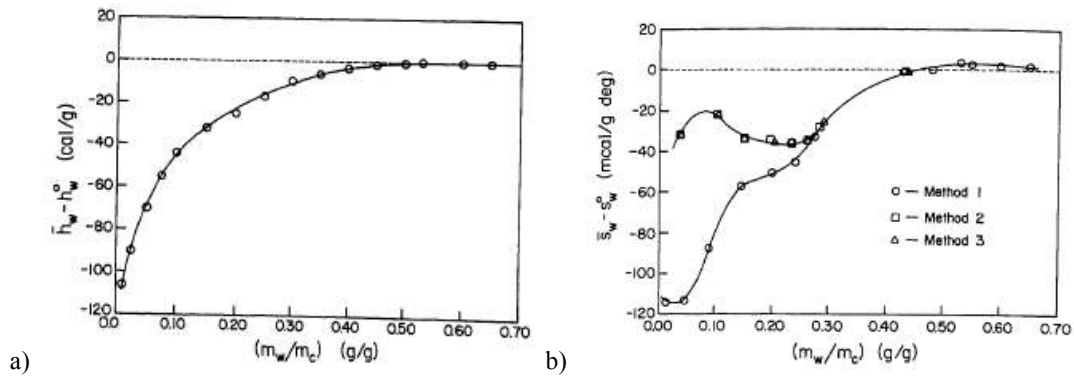


Fig. 2.21 : a) Relation between relative partial specific enthalpy of water adsorbed on Na-montmorillonite at 25 °C and the water content, and b) Relation between relative partial specific entropy of water adsorbed on Na-montmorillonite at 25 °C and the water content. Method 1 (adsorption): dry samples were first enclosed in desiccators over saturated solutions. Method 2: dry samples were first enclosed in a desiccator over pure water and then enclosed in desiccators over saturated solutions when equilibrium was reached. Method 3: dry samples were sprayed with sufficient liquid water to a water content of 2 g of water per gram of clay, and then enclosed in desiccators over saturated salt solutions. (from [45]).

2.6.5. Mechanisms of osmotic swelling

The coexistence of a condensed ordered phase with a disordered phase in smectites is generally viewed as evidence for a long-range attractive force [61]. It is shown that the covolume theory of Onsager in some cases could explain the existence of apparent long-range forces and the transition between ordered and disordered states in colloidal dispersions [61]. The isotropic/nematic phase transition of anisotropic particles like smectite clays has been reported to be driven by the entropy self-assembly of the anisodimensional particles: the anisotropic solid particles organize themselves, reducing their rotational entropy in order to optimize their translational entropy [76,61]. The role of clay concentration is easily understood in light of the covolume effect leading to ordering and phase transition. However, the effect of electrolyte concentration on phase transition (Fig. 2.18), favoring the isotropic phase at low concentration, implies that the electrostatic interaction between the negatively charged clay particles must also influence particle-particle interaction forces. It is this phenomenon that provided much of the evidence for the existence of diffuse double layers and long-range attractive or repulsive forces among colloidal particles in suspension. The DLVO (Derjaguin, Landau, Verwey and Overbeek) model assumes that the coulombic interaction between like-charged particles in water or

electrolyte solutions is pure repulsion, as a result of the imagined overlap of diffuse double layers associated with neighbouring particles. Under these assumptions of the DLVO theory, attraction is caused by van der Waals forces. However, the van der Waals forces can only exceed thermal energies for colloidal particles in solution that are almost in contact, separated by less than a few nanometers. Van Olphen proposed a mechanism by which the microfloculation is promoted by attraction between the oppositely charged edges and faces of the clay platelike particles and reinforced by van der Waals interactions, yielding to the “house of cards” structure [54]. However van der Waals attractive forces are negligible when the separation distance between colloidal particles is more than a few nanometers, as observed for the clay suspensions, and experimental studies were not able to demonstrate the existence of direct and sticky contact between particles [54]. On the contrary, the studies have provided evidence for a more extended nematic order where face to face mutual orientation is favoured [54].

The Sogami-Ise theory, first outlined by Langmuir (“the Coulomb attraction between the micelles (clay particles) and the oppositely charges ions gives an excess of attractive force which must be balanced by the dispersive action of thermal agitation and another repulsive force. Thus there is no reason to assume long-range van der Waals forces”), and further developed by Sogami, Ise, and Smalley, begins with the assumption of a Boltzmann distribution of counterions at the particle surface, as in the DLVO model. Via the Poisson-Boltzmann (PB) equation, the total electrostatic energy of the electrolyte solution is obtained, and the Gibbs free energy is calculated. The essential features of departure of the Sogami-Ise theory from the DLVO theory is given by the difference in the Helmholtz pair potential, $V(x)$. For the Sogami-Ise theory, the pair potential is given by:

$$V(x) = V^{el}(x) + V_i^o(x) + V_o^o(x) \quad (2.16)$$

Where x is the plate separation. $V_i^o(x)$ is purely repulsive, and represents the osmotic contribution of the small counterions trapped between plates. $V_o^o(x)$ is purely attractive, arising from the osmotic pressure of the small ions, exerted against the plate surfaces from the outside. $V^{el}(x)$ results from the electrical interaction at equilibrium between the counterions and the charged plates. In particular, Trizac *et al* constructed a pair potential for discs valid at large distances within linearized PB theory, incorporating approximately both the non-linear effects of

counter ion condensation and the anisotropy of the charged platelets [77]. The electrical term in the equation leads to a long-range attraction between the plates. Under certain circumstances, the electrical term is sufficiently large to completely balance the repulsive term, causing particles to attain a stable separation distance at the potential minimum. It is thereby shown that there is an interparticle repulsion at small separation distances, and an attraction at larger distances. A secondary free energy minimum results at intermediate interparticle separations, where the attractive electrostatic potential balances the purely repulsive contribution because of entropic contributions of the counterions. Because the Gibbs free energy shows a minimum with a potential well that is deeper than that of the thermal energy, it allows particles to order into stable but fragile (thixotropic gel), lattice arrays at room temperature at separation distances comparable in magnitude to several particle radii, which for some colloids is in the range of 1000 nm or more. The DLVO potential corresponds essentially to the osmotic component, the last two terms in Eq. (2.16), and therefore predicts only pure (osmotic) repulsion. The repulsive force in the DLVO model originates in the electrostatic repulsion inherent to the Debye-Huckel theory of small ions, which requires that ionic interaction energies be less than thermal energy, an assumption that does not hold for colloidal particles with high charge or for nondilute solutions of ions. The fundamental reason for the difference of the Sogami-Ise theory from the DLVO theory is that the former theory allows for the clouds of counterions in colloidal suspensions to compress around and between highly charged particles, generating interparticle attraction via the counterions, and lower the free energy.

2.7. DYNAMICS OF WATER IN SMECTITE CLAYS

2.7.1. Overview

This section describes the dynamics of water in the clay-water systems. Section 2.7.2 to 2.7.3 details experimental measurements of the dynamics of water in the clay interlayer. The structure of water in smectites is predominantly liquidlike, subject to the constraints imposed by the nearby presence of the silicate surfaces and the counter ions. Quasi-elastic-neutron-scattering (QENS) studies suggest the water molecules hydrating the cations do not exhibit translational mobility at the experimental timescale but a planar rotational motion, and water not directly coordinated to the cations to be confined to a cage formed by the silicate layers and the hydrated cations, and

intermittently jumping between cages. The reported values of the molecular diffusion coefficients of water in smectites measured by QENS are scarce and show large variability. These are dependent on the type of smectite, the water content, the measurement's method, the duration of the experiment and the density of counter ions. They range from $2 \times 10^{-11} \text{ m}^2/\text{s}$ for a calcium clay at 15 %RH to $1.2 \times 10^{-9} \text{ m}^2/\text{s}$ for another calcium clay at a water content corresponding to a two-layer hydrate. The apparent (macroscopic) diffusion coefficients of water in smectites, show a dependence on the water content and on the diffusional direction relative to the platelet orientation due to the anisotropy of the clay particles (Section 2.7.4). The apparent diffusion are also found to depend on the dry density of the clay sample, due to the presence of micropores. However, the values of the apparent diffusion coefficients again show considerable variability. Attempts have also been made to model the diffusion coefficients in smectite clays (Section 2.7.4). Models for the tortuosity coefficient in the generally accepted theoretical framework for effective diffusion coefficients of small molecules in porous materials have been developed to account for the improved property barriers of clay nanocomposites. However, a macroscopic model of diffusion in smectite clays requires an accurate description of the behaviour of water in the clay interlayer and of tortuosity effects due to the platelets and to the aggregation of platelets, resulting in micropores. As pointed out by Michot et al [78] and by Murad and Cushman [79] the general problem of taking into account the specific behaviour of vicinal water in transport phenomena in clay barriers remains largely unsolved.

2.7.2. Mobility and diffusion of water in the clay interlayer

2.7.2.1. NUCLEAR MAGNETIC RESONANCE AND DIELECTRIC RELAXATION MEASUREMENTS

The reorientational motions of water molecules adsorbed on Na-, and K-montmorillonite, obtained by dielectric relaxation measurements, were found to be on the same time scale as those in liquid water, even at low water content, whereas the reorientational motions for water molecules on Li-, Mg-, Ca-, Sr-, and Ba-montmorillonite was comparable to that of ice [23]. However, in another study, the orientational correlation time of water in Li-hectorite obtained from the temperature dependence of the inverse of the longitudinal relaxation time, $1/T_1$, measured by NMR, showed the water to rotate less freely than in liquid water, but more freely than in ice [23].

2.7.3. Quasi elastic neutron scattering measurements

From a model incorporating either two-dimensional translational diffusion or isotropic translational diffusion simultaneously with isotropic rotational diffusion, Cebula *et al* [23] calculated the diffusion coefficients of water adsorbed on Li-montmorillonite, the rotational diffusion time constant, and the correlation time. By comparing those values with those of bulk water, they concluded that water molecules adsorbed by Li-montmorillonite diffuse much more slowly than those in bulk water. The authors also concluded from the absence of a distinct elastic peak that none of the water molecules was stationary on the time scale of the neutron scattering measurements. This result indicated that none of the adsorbed water molecules are rigidly bound to the exchangeable Li^+ cations.

However, Estrade-Szwarckopf *et al* [23] studied Li-hectorite at much lower water contents and found that the experimental quasielastic peak broadenings they observed could be fitted by a model that assumed all of the water molecules to be strongly bound to the (stationary) exchangeable Li^+ cations, each solvating water molecule being allowed to rotate about its own symmetry (C_2) axis and about an axis perpendicular to the clay platelet through the exchangeable cation. These motions alone were considered to produce the observed broadening.

Tuck *et al* [80] used a similar approach for the molecular diffusion coefficients of water in Ca^{2+} -montmorillonite, at different relative humidities, and in Ca^{2+} -, Mg^{2+} -, and Na^+ -vermiculite samples at a fixed relative humidity. Table 2.6 shows the results. The authors noted the following features: (1) the quasi-elastic intensity decreased with increasing scattering vector at fixed relative humidity, (2) the quasi-elastic intensity increased with increasing relative humidity and hence with increasing water content and (3) the broadening curve for the narrow quasi-elastic fraction was essentially independent of the relative humidity within experimental error. This led to the conclusion that the broadening was caused mainly by two separate phases of motion. The authors proposed a model in which the water molecules hydrating the cations do not exhibit translational mobility at the experimental timescale. The more mobile water component, which was attributed to water not directly coordinated to the cations, was initially confined to a cage formed by the silicate layers and the hydrated cations (phase 1) but could intermittently jump between cages (phase 2). Thus phase 1 gave rise to the observed spatially restricted diffusion, while phase 2 gave rise to the observed unbounded diffusion. As a consequence, the inter-cage

diffusion is inferred to be regulated by the number of hydrated cations present between the layers. Indeed, the results for Ca^{2+} -, Mg^{2+} -, and Na^+ -vermiculite samples at a water activity of 0.76 were significantly different from those for Ca^{2+} -montmorillonite, which was attributed to the high charge of the vermiculite, leading to a more densely packed network of hydrated cations. In addition, the relative intensities in the quasi-elastic scattering at high and low wavevectors suggested the measurements also detect rotations of the complete six-fold coordinated hydration shells of the cations about one of the axes of the octahedral hydration shell.

Table 2.6 : Water content and effective diffusion coefficients of samples used in QENS studies of Ca^{2+} -montmorillonite and Ca^{2+} -, Mg^{2+} -, and Na^+ -vermiculite (reproduced from [80])

clay	exchangeable cation	p/p ₀	water content (g _{H₂O} /g)	D _{eff} / 10 ⁻¹⁰ m ² s
montmorillonite	Ca^{2+}	0.15	0.09 ± 0.1	0.2 ± 0.1
		0.2	0.12 ± 0.1	2.3 ± 0.6
		0.33	0.17 ± 0.1	4.5 ± 0.9
		0.43	0.19 ± 0.1	5.1 ± 0.2
		0.58	0.23 ± 0.1	4.5 ± 0.4
		0.76	0.22 ± 0.1	4.5 ± 0.7
		0.98	0.26 ± 0.1	4 ± 1
vermiculite	Ca^{2+}	0.76	0.19 ± 0.1	2.6 ± 1.2
	Mg^{2+}	0.76	0.21 ± 0.1	0.5 ± 0.1
	Na^+	0.76	0.20 ± 0.1	0.3 ± 0.05

The same model was used by Swenson *et al* [81] and by Anderson *et al* [82]. The results of Swenson *et al* [81] on a Na-vermiculite for zero, one, or two molecular layers of water showed that the two-layer hydrate exhibit a planar rotational motion of water molecules, forming hydration shells around the Na ions, and an essentially two-dimensional translational jump-diffusion motion. The results showed also that almost no hydrogen motion occurred in the direction perpendicular to the clay platelets at a time scale of 2 to 40 ps. An effective diffusion coefficient of $8.8 \times 10^{-10} \text{ m}^2/\text{s}$ was obtained from the mean jump length of 1.1 Å and the average residence time of 2.3 ps. The correlation time of the rotational motion was estimated to be approximately 27 ps. In the case of the one-layer hydrate only planar rotational motion could be observed with a rotational correlation time of 16 ps, suggesting that the translational motion, if

present, was too slow to be observed on the experimental time scale. The results of Anderson et al [82] on Ca-, and hexadecyltrimethylammonium (HDTMA) exchanged bentonites showed the translational diffusion of water in two clays to be lower than bulk water and dependent on relative humidity (Fig. 2.22). They found similar mean jump lengths for the two cations at equivalent water content, and a decrease of the jump length with increasing water content. The jump lengths ranged from 0.27 to 0.5 nm and were 2 to 4 times greater than that for bulk water (0.13 nm). Mean residence times were 3 to 30 times longer than that for bulk water (1.2 ps) and also decreased with increasing water content. Also, torsional motion was less strongly influenced by the presence of the clay surface than translational motion.

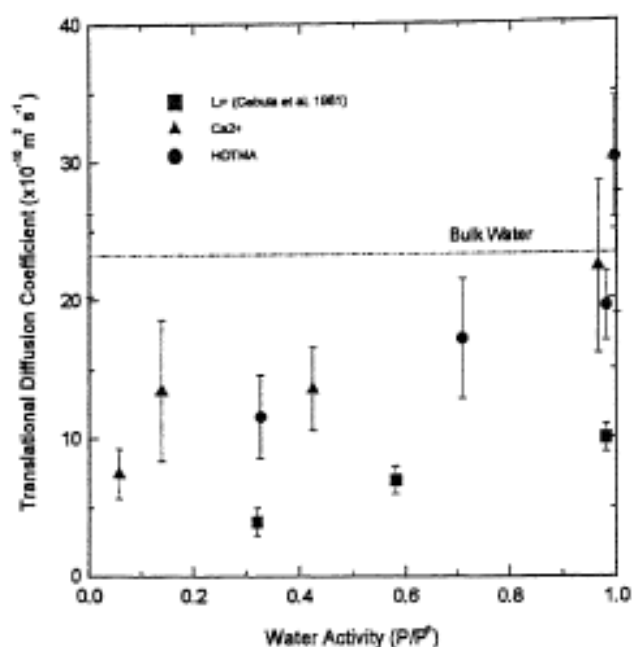


Fig. 2.22 : Translational diffusion coefficient versus water activity for Ca- and HDTMA-exchanged bentonite. Results from Cebula et al [83] for Li-montmorillonite are included. (from [82])

Literature values of molecular diffusion coefficients of water in different smectite clays obtained from neutron scattering experiments are given in Table 2.7. The values show significant variability. This variability can be attributed to the type of counter ion, the number of counter ions per volume, the water content, the model used to interpret the data and the type of neutron scattering experiment, and the duration of the experiment. In particular, diffusion coefficients of water on Cs-, and Na-montmorillonite in the hydrated and bihydrated states corresponding to 6

and 12 water molecules per cation, have been measured by Malikova et al [84] by time-of-flight (TOF) techniques and neutron spin-echo (NSE) technique. The neutron spin-echo (NSE) technique, which can probe correlation times up to approximately 300 to 500 ps, provided diffusion coefficients of the order of $(1-3) \times 10^{-10} \text{ m}^2/\text{s}$ for Na-, and Cs-monohydrated montmorillonite. For the bihydrated samples, the NSE data gave a diffusion coefficient of approximately $5 \times 10^{-10} \text{ m}^2/\text{s}$, whereas the TOF data yield a diffusion coefficient of approximately $10 \times 10^{-10} \text{ m}^2/\text{s}$, both showing however faster dynamics for the bihydrated samples than for the monohydrated samples.

Table 2.7 : Literature values of molecular diffusion coefficients D_m of water in smectites interlayer.

reference	smectite	number of water layers	p/p ₀	D _m (m ² /s)
Malikova et al, 2006 [84]	Na-montmorillonite	1		$(1-3) \times 10^{-10}$
Malikova et al, 2006 [84]	Na-montmorillonite	2		$(5-10) \times 10^{-10}$
Chang et al, 1995 [85]	Na-montmorillonite	2		1×10^{-9}
Skipper et al, 2006 [86]	Na-vermiculite	2		1.7×10^{-9}
Skipper et al, 2006 [86]	Na-vermiculite	2		2.6×10^{-9}
Tuck et al, 1985 [87]	Na-vermiculite	2	0.76	3×10^{-11}
Swenson et al, 2000 [81]	Na-vermiculite	2		8.8×10^{-10}
Cebula et al, 1981 [83]	Li-montmorillonite	1		4×10^{-10}
Cebula et al, 1981 [83]	Li-montmorillonite	2		7×10^{-10}
Cebula et al, 1981 [83]	Li-montmorillonite	3		1×10^{-9}
Poinsignon et al, 1989 [88]	Li-vermiculite	2		3.4×10^{-10}
Tuck et al, 1985 [87]	Ca-montmorillonite		0.15	0.2×10^{-10}
Tuck et al, 1985 [87]	Ca-montmorillonite	1	0.2	2.3×10^{-10}
Tuck et al, 1985 [87]	Ca-montmorillonite		0.33	4.5×10^{-10}
Tuck et al, 1985 [87]	Ca-montmorillonite		0.43	5.1×10^{-10}
Tuck et al, 1985 [87]	Ca-montmorillonite		0.58	4.5×10^{-10}
Tuck et al, 1985 [87]	Ca-montmorillonite	2	0.76	4.2×10^{-10}
Tuck et al, 1985 [87]	Ca-montmorillonite	3	0.98	4×10^{-10}
Tuck et al, 1984 [89]	Ca-montmorillonite	2		1.2×10^{-9}
Tuck et al, 1985 [87]	Ca-vermiculite	2	0.76	2.6×10^{-10}
Tuck et al, 1985 [87]	Mg-vermiculite	2	0.76	0.5×10^{-10}

2.7.4. Effective diffusion coefficients of water in the clay-water systems

2.7.4.1. DEFINITIONS OF APPARENT AND EFFECTIVE DIFFUSION COEFFICIENTS

Given the diffusion equation:

$$\partial_t c = \nabla D_e \nabla c \quad (2.17)$$

where t is the time, c is the concentration of the water in the clay, the effective diffusion coefficient D_e is related to the apparent diffusion coefficient D_a by:

$$D_e = \varepsilon D_a \quad (2.18)$$

where ε is the clay porosity, that represents the fraction of molecules that effectively diffuse. The apparent (macroscopic) diffusion coefficients can be modelled using the following equation [90,91]:

$$\frac{D_a}{D_m} = \frac{1}{\tau} \quad (2.19)$$

where D_m is the molecular diffusion coefficient, τ is the tortuosity factor that describes the influence of pore-network geometry. The effective diffusion coefficient is given by:

$$\frac{D_e}{D_m} = \frac{\varepsilon}{\tau} \quad (2.20)$$

An analog equation can be obtained for the permeability of a gas in a polymer containing fillers, such as clay particles [92]:

$$\frac{P_a}{P_0} = \frac{\phi}{\tau} \quad (2.21)$$

where ϕ is the volume fraction of the polymer, equivalent to the porosity in the case of a porous material, P_a is the permeability of the gas in the polymer with fillers and P_0 is the permeability of the gas in the pure polymer. The molecular diffusion is sometimes modelled as [90]:

$$D_m = \delta D_0 \quad (2.22)$$

δ is the constrictivity factor that reflects in some way the properties of diffusing molecules that are vicinal to the basal surfaces bounding interlayers, and D_0 is the diffusion of the bulk liquid without adsorbent.

Physically, tortuosity can be defined as the ratio of the actual distance Δl travelled by the species per unit length Δx of the medium [93,92].

$$\tau = \frac{\Delta l}{\Delta x} \quad (2.23)$$

Different models have been proposed to calculate the tortuosity of the smectites.

2.7.4.2. EFFECTIVE DIFFUSION MODEL OF FRICKE'S

Duval *et al* [94] measured the diffusion of water in Laponite gels as a function of water content. The diffusion measured along the compression axis was found always to be smaller than that measured perpendicular to this axis (Fig. 2.23). The authors used the extension of the Maxwell's theory by Fricke to the case of oblate and prolate ellipsoids to model the apparent diffusion coefficient. The model leads to Eq. (2.24):

$$\frac{D}{D_0} = \frac{1}{1 - (\beta + 1)(1 - \phi)} \quad (2.24)$$

Where

$$\beta = -\frac{1}{3} \frac{1 + 3/2M}{M(1 - 1/2M)} \quad (2.25)$$

$$M = \frac{\theta - 1/2 \sin 2\theta}{\sin^3 \theta} \cos \theta \quad (2.26)$$

$$\frac{h}{d} = \cos \theta \quad (2.27)$$

Where h is the thickness of the clay platelets, d is the diameter of the clay platelets, ϕ is the water volume fraction, and D_0 is the bulk water diffusion coefficient. The h/d value for Laponite is about 1/30 [60]. Fig. 2.23 shows the good agreement between the model and the measured values.

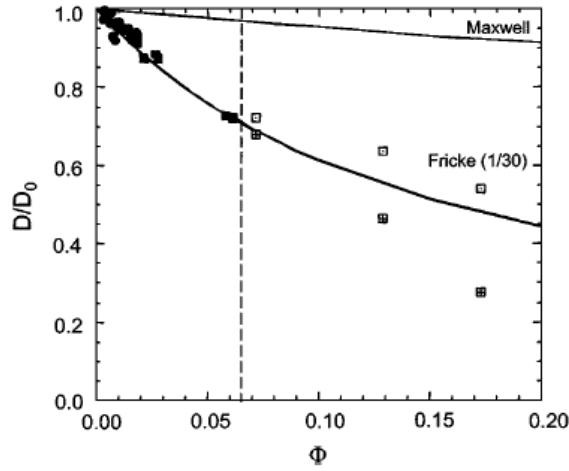


Fig. 2.23 : PSGE NMR self-diffusion coefficient of water (D , normalized with respect to diffusion in pure water (D_0), vs Laponite volume fraction ϕ . Open squares with cross: anisotropic samples, with diffusion parallel to the compression axis. Open squared without cross : anisotropic samples with diffusion perpendicular to the compression axis. The lines are the predictions from the Maxwell's model for spheres and the Fricke's model for ellipsoids with an aspect ratio of 1/30, respectively. (from [94])

2.7.4.3. EFFECTIVE DIFFUSION MODEL OF NAKASHIMA

Nakashima measured the diffusion of water in montmorillonites and hectorites, and stevensites gels at different water contents and temperatures [95,96,97,98,99]. The values of the apparent diffusion coefficients were found to obey simple empirical temperature-independent equations:

$$\ln\left(\frac{D}{D_0}\right) = \alpha[\exp(-\beta w) - 1] \quad (2.28)$$

For the montmorillonites and

$$\ln\left(\frac{D}{D_0}\right) = \exp(-\alpha' w) \quad (2.29)$$

for the stevensites and the hectorites, where α , β , and α' are dimensionless constants, and w is the clay weight fraction of the gel. The activation energies obtained from the temperature dependence of the measured diffusion coefficients were found to be nearly equal to that for bulk water, suggesting that water molecules in the gel were in the same chemical environment as in bulk water, so the effects of structurally ordered water molecules near the surface of the clay were probably negligible. Therefore the authors proposed bound water layers on the clay platelets

to be obstacles to the diffusion of unbound water molecules and therefore reduce the water self-diffusion coefficient of water as compared to bulk liquid water.

2.7.4.4. TORTUOSITY MODEL OF BHARADWAJ

The extension of the tortuosity model of Nielsen [92] by Bharadwaj [100] to include orientational order in the tortuosity factor of polymer nanocomposites is given by Eq. (30):

$$\tau = 1 + \frac{d}{2h}(1 - \phi) \frac{2}{3} \left(S + \frac{1}{2} \right) \quad (2.30)$$

where

$$S = \langle 3 \cos^2 \theta - 1 \rangle \quad (2.31)$$

where d is the diameter of the platelets, h is the thickness of the platelets, ϕ is the volume fraction of the polymer, S is the orientational order parameter and θ is the angle between the direction of the preferred orientation and the sheet normal. This function ranges from $-1/2$, for orthogonal orientation, and 1 , for perpendicular orientation. $S=0$ corresponds to a random orientation of the platelets.

2.7.4.5. TORTUOSITY MODEL OF LUSTI AND GUSEV

Finite element calculations of the barrier properties of the clay platelets were carried out by Lusti *et al* [101] to obtain a mathematical model of the restricted permeability in polymer-based nanocomposites.

$$\tau_{random} = \frac{\phi}{1 - \chi(1 - \phi / \tau_{aligned})} \quad (2.32)$$

where τ_{random} is the tortuosity factor of randomly aligned platelets, and χ and $\tau_{aligned}$ are the polynomial function for random orientation, and the tortuosity factor of fully aligned platelets given by:

$$\chi = -0.0082x^2 + 0.0879x + 0.4157 \quad (2.33)$$

$$\tau_{aligned} = \phi \exp \left\{ \left(\frac{x}{x_0} \right) \beta \right\} \quad (2.34)$$

$$x = \alpha(1 - \phi) \quad (2.35)$$

$$\alpha = \frac{d}{h} \quad (2.36)$$

The constants are given by $x_0=3.47$ and $\beta=0.71$.

However, we note that the mathematical model was obtained from a fit on a range of relatively low volume fraction of the clay platelets in the polymer, as can be found in nanocomposite. If the model is used at high volume fraction of the clay, or equivalently low water content, as would be the case for water diffusion in the clay interlayer, the values of the tortuosity factor are smaller than one. Therefore the model cannot be used at high clay volume fraction.

2.7.4.6. NUMERICAL CALCULATION OF EFFECTIVE DIFFUSION COEFFICIENTS

An attempt was made by Fujii et al [102] to develop a multiscale calculation of the effective diffusion coefficients of water in bentonites by taking into consideration the molecular diffusion of water in the clay interlayer, the number of clay lamellae forming separate stacks of microaggregates, and the microporous structure of the clay (Fig. 2.24). The molecular diffusion coefficients were calculated from classical molecular dynamic simulations. The models contained one clay minerals layer and 3000 water molecules, and the size of the cell was about 3.1 nm x 2.7 nm x 15.9 nm. No more detail was given about the numerical procedure. The results of the calculated diffusion coefficients and basal spacing as a function of water content are given in Fig. 2.25. We note the semi-quantitative agreement between the calculated and experimental values of the basal spacing (Fig. 2.25b). The calculated effective diffusion coefficient is found to increase with the number of lamellae (Fig. 2.26a) and to decrease with the dry clay density (Fig. 2.26c). We point out that the decrease in the diffusion coefficient with an increase in water content is unexpected, because of the increase in tortuosity from the models of Bharadwaj and Duval, and from the decrease in the molecular diffusion coefficient (Fig. 2.26b). The tortuosity values obtained from these calculations ranged between 1 and 1.62.

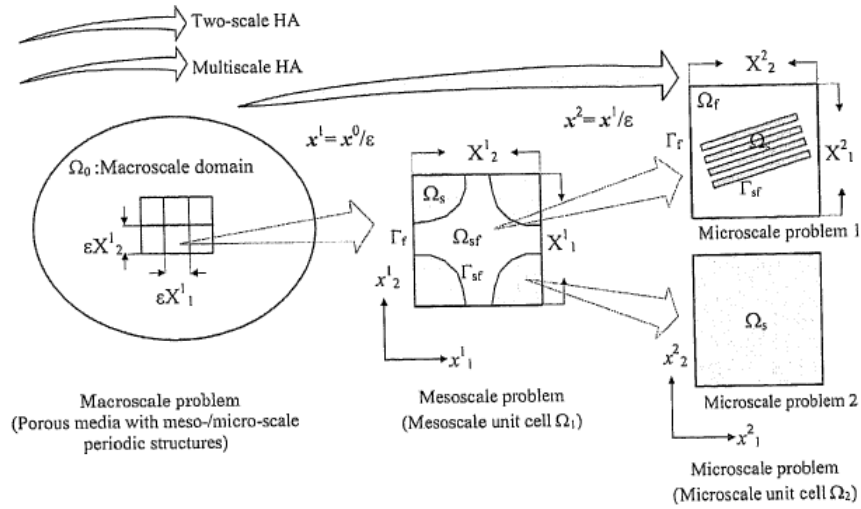


Fig. 2.24 : Macro-, meso- and microscale problems (from [102])

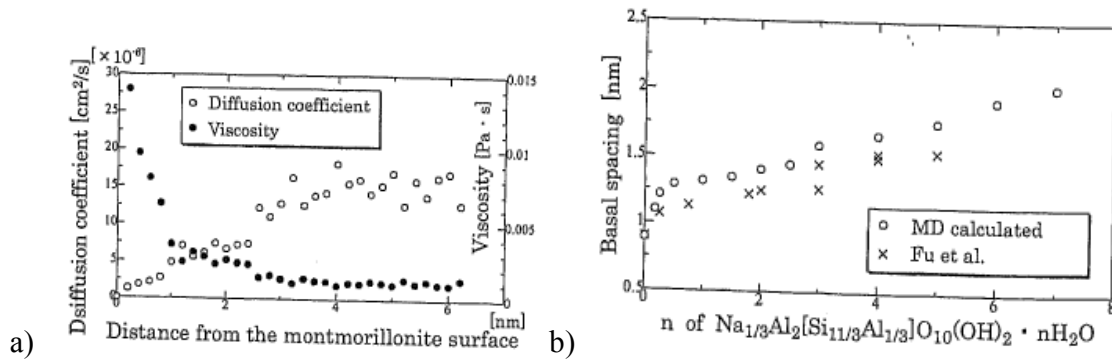


Fig. 2.25 : a) Diffusivity distribution of water in Na-montmorillonite calculated from classical molecular dynamic simulations. b) Calculated and experimental data of the swelling property for Na-montmorillonite (from [102])

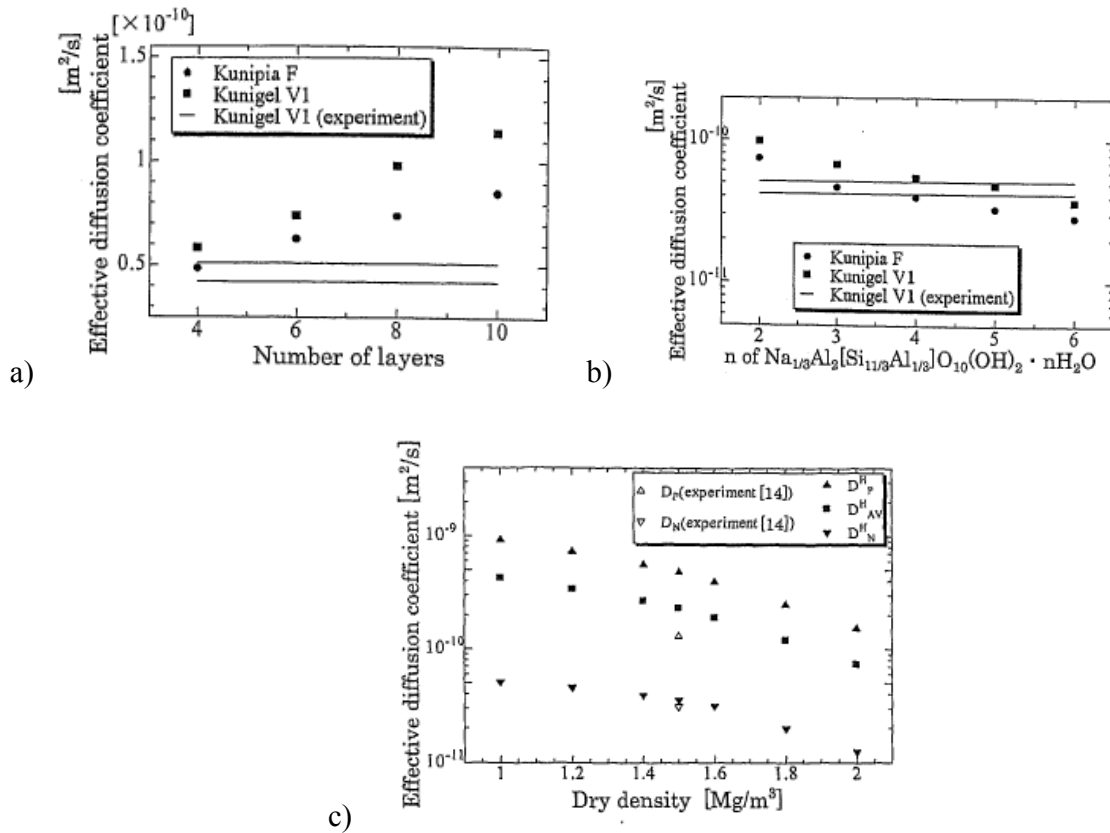


Fig. 2.26 :a) Effective diffusion coefficient and the number of lamellae. b) Effective diffusion coefficient and the number of H_2O of interlamellar water. c) Anisotropic diffusion coefficient in relation to dry density (from [102])

2.7.4.7. MEASURED EFFECTIVE AND APPARENT DIFFUSION COEFFICIENTS

The apparent diffusion coefficient of non-sorptive tritiated water (HTO) in Na-bentonites was measured by Sato *et al* [103]. The sample was sandwiched between two liquid solutions. One containing the HTO tracer and one without tracer. At the end of the diffusion experiment, the bentonite block was cut into slices to obtain the thickness of the slice and the amount of HTO. Prior to experiments the bentonite was compacted, allowing the platelets to orient perpendicular to the direction of compaction. The diffusion experiment was performed with the sample aligned with the compacted direction in the direction parallel and perpendicular to the flow. The accumulative quantity that permeated through the bentonite specimen was fitted with the following equation from which the apparent diffusion coefficient D was obtained.

$$\frac{Q(t)}{ALC_0} = \frac{D}{L^2}t - \frac{\alpha}{6} - \frac{2\alpha}{\pi^2} \sum_{n=1}^{\infty} \left\{ \frac{(-1)^n}{n^2} \exp\left(-\frac{Dn^2\pi^2 t}{L^2\alpha}\right) \right\} \quad (2.37)$$

where $Q(t)$ is the accumulative quantity of the tracer permeated through the bentonite specimen at time t , A is the cross-sectional area of the bentonite, L is the thickness of the bentonite, C_0 is the concentration of the tracer in the tracer cell, and α is the rock capacity factor given by

$$\alpha = \phi + \rho_d K_d \quad (2.38)$$

where ϕ is the porosity, ρ_d is the dry density of the bentonite, and K_d is called the distribution coefficient. The values of the apparent diffusion obtained with this method (Table 2.8) show the diffusion to be affected by the orientation properties of the clay particles. The same kind of experiments were reconducted to measure the apparent diffusion of HDO in Na-bentonites subjected to saturated vapour pressure [104]. Here again, as already reported [105,106], the apparent diffusion coefficients show a dependence on the orientation of the clay platelets relative to the flux direction (Table 2.9).

Table 2.8 : Summary of the apparent diffusion values of HTO in compacted bentonite (reproduced from [103]). D_{ef} : effective diffusivity in the filter. D_e effective diffusivity in bentonite.

Bentonite	Dry density (Mg/m ³)	Diffusion direction	Effective diffusion coefficients (m ² /s)	
			D_{ef}	D_e
Kuniel-VI	1.0	Axial	2.7e-10	3.9e-10
		Perpendicular	2.8e-10	4.1e-10
	1.5	Axial	2.1e-10	2.1e-10
		Perpendicular	2.1e-10	2.0e-10
Kunipia-F	1.0	Axial	2.7e-10	2.6e-10
		Perpendicular	3.0e-10	1.2e-10
	1.5	Axial	3.1e-10	2.7e-10
		Perpendicular	3.0e-10	3.3e-10
		Perpendicular	2.5e-10	1.3e-10

Table 2.9 : Effective diffusion coefficient for HDO with respect to experimental temperature, dry density and diffusion direction (from [104])

ρ_{dry} [Mg/m ³]	Diffusional direction	D_e [$\times 10^{-10}$ m ² /s]				Activation energy [kJ/mol]
		298 K	313 K	323 K	333 K	
0.9	P	2.8 ± 0.1	3.3 ± 0.0	4.8 ± 0.0	6.1 ± 0.1	10 ± 4
	N	1.6 ± 0.0	1.8 ± 0.0	2.6 ± 0.0	3.7 ± 0.1	21 ± 5
1.35	P	1.7 ± 0.0	2.2 ± 0.0	2.9 ± 0.0	4.6 ± 0.1	23 ± 5
	N	0.84 ± 0.03	0.95 ± 0.01	2.0 ± 0.0	2.2 ± 0.1	25 ± 7

Different studies showed that compacted, water-saturated Na-bentonite contains both nanoscale interlayer pores (nanopores), and larger intra- or inter-aggregate pores (macropores) [90,103]. It was emphasized by Sposito *et al* [23] that the motions of water molecules in both the interlamellar spaces and in the micropores contribute to the effective diffusion coefficient of water. Taking into account macropores, and interlayer nanopores, Bourg *et al* [90] proposed the following model for the apparent diffusion D_a of water at concentrations above the one layer hydrate.

$$\frac{D_a}{D_0} = \frac{\delta}{G} = \frac{1}{G} \left[(1 - f_{interlayer}) + \delta_{interlayer} f_{interlayer} \right] \quad (2.39)$$

where D_0 is the diffusion coefficient of bulk water, G is the geometric factor that describes the influence of pore-network geometry, $\delta_{interlayer}$ is the constrictivity factor in the clay interlayer and ϕ is the volume fraction of interlayer nanopores given by

$$f_{interlayer} = \frac{1}{d_{mont}} \frac{\rho_{b,mont}}{\rho_{mont} - \rho_{b,mont}} \frac{1}{\frac{\xi_{2-layer}}{d_{2-layer}} + \frac{1 - \xi_{2-layer}}{d_{3-layer}}} \quad (2.40)$$

where $d_{mont} = (d_{basal} - d_{interlayer})$, where d_{basal} is a basal spacing of a montmorillonite hydrate as measured by XRD and $d_{interlayer}$ is the statistical thickness of water in its interlayers (equal to $d_{2-layer}$ and $d_{3-layer}$, respectively, in the 2- and 3-layer hydrates). $\rho_{b,mont}$ is the mass density of the hydrated clay and ρ_{mont} is the mass density of the dry clay. $\xi_{2-layer}$ and $\xi_{3-layer}$ are the volume fraction of the 2-layer and 3-layer hydrates in the nanopores. They compiled experimental values of the relative apparent diffusion coefficient (D_a/D_0) of water tracers in saturated Kunipia-F and Na-montmorillonites at 298 K and fitted the data with their model to obtain an average geometric factor of 4.0 ± 1.6 for the diffusion of water in Na-bentonites. The experimental values and the

corresponding fit (Fig. 2.27) are in good agreement but the plots show significant variability in the data.

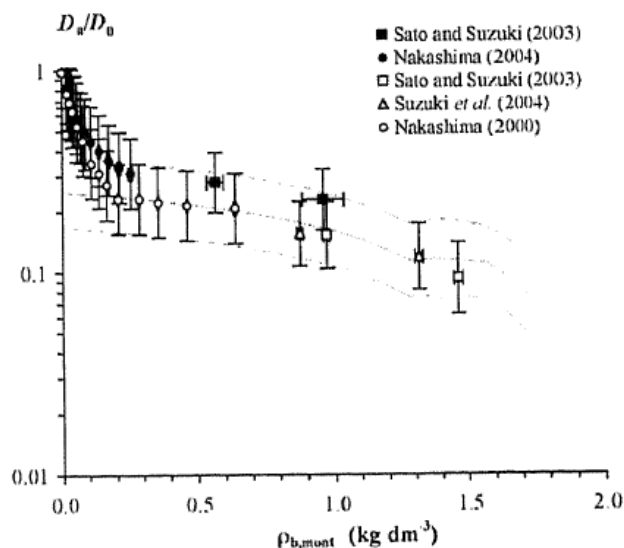


Fig. 2.27 : Logarithm of the relative mean principal apparent diffusion coefficient of water tracers at 298 K in compacted bentonite (filled symbols: Kunipia-VI; Open symbols: Kunipia-F and Na-montmorillonite) plotted against the partial montmorillonite dry density. (from [90])

2.8. INTERACTION BETWEEN SMECTITES AND SMALL ORGANIC MOLECULES

2.8.1. Overview

This section gives information on the interactions between smectite clays and low molecular weight compounds. The interactions between volatile molecules and the clay are reviewed in section 2.8.2. Different types of interactions have been evoked to account for the adsorption of organic compounds on smectite clays, including van der Waals forces, coordination complexes with the counter ion, cation-dipole interactions, hydrogen bonding with the clay surface, and bridging complexes in the presence of water. More specifically, the interaction of aromatic molecules such as benzene and toluene with the clay have been interpreted in terms of cation- π interactions with the counter ion or the silicate surface, and the interactions of polar compounds with the clay have been interpreted in terms of ion-dipole interactions. For the latter, water is expected to be bound more strongly to the clay than ethanol. However, the contrary has been reported for temperature ramp measurements on water and ethanol on smectite clays, so that the

proposed mechanism of interactions for polar compounds remains somewhat controversial. The interaction of ethanol with the clay is sufficient for the ethanol molecule to be able to penetrate in the clay interlayer and expand the platelets up to a distance equivalent to a monolayer of water. The higher the charge of the clay, the more vapour pressure is required for the ethanol to penetrate inside the layers, and at low coverage, depending on the charge of the clay, the ethanol may only adsorb at the external surface. Liquid toluene was also found to be able to penetrate in the clay interlayer up to a distance equivalent to a monolayer of water, but a fraction of the clay platelets remain unexpanded. No data have been found for the interactions between ethyl acetate and smectite clays.

The effect of ion exchange with organic cations on the interactions with low molecular weight compounds is reviewed in the section 2.8.3. With increased hydrophobicity of the organoclay, the mechanism of sorption of molecules from aqueous solution shows a shift from a predominantly adsorptive process to a partition-dominated process, particularly in the case of hydrophobic compounds. Depending on the extent of ion exchange the clay can behave as a dual adsorbent in the sorption of organic compounds from aqueous solution, in which the mineral fraction functions as a solid adsorbent and the organic phase a partition medium. For the organoclays the silicate layers are held apart by the large organic cations, such that penetration in the interlamellar space is facilitated for some organic molecules and adsorption may be increased when compared with the non-modified clay.

2.8.2. Interactions between volatile molecules and smectites

Bailey *et al* [107] postulated different mechanisms of adsorption of organic compounds on smectites.

- Physical adsorption due to van der Waals's forces
- Hydrogen bonding
- Coordination complexes
- Association or bridging complexes
- Chemical adsorption: (i) protonation at the silicate surface by reaction of a base with the hydronium ion on the exchange site, (ii) protonation in the solution phase with

subsequent adsorption of the organic molecule via ion exchange; and (iii) in system having low water content, protonation by reaction with dissociated protons from the residual water present on the surface or that in coordination with exchangeable cation.

2.8.2.1. APOLAR AROMATIC MOLECULES

Apolar aromatic molecules, like toluene and benzene, were proposed to form coordination complexes with montmorillonites, their π electrons interacting with the clay counter ion (π -cation interactions) [108]. Benzene has been reported to form hydrogen bonds with water. However, the H-bonds strengths are relatively low (< 2 kcal/mol [109]) compared with that of the cation- π interactions (approximately 20 kcal/mol for pure cation-benzene complex [110]). In addition to cation- π interactions, possible existence of trapping mechanisms in restricted interlayer geometries was not excluded. Comparison of the measured H^2 NMR line shape of benzene adsorbed on Ca-montmorillonite between experiments and simulations based on a MXQET program reflected the molecule to show a small-wobble with rapid and discrete jumps around its C_6 axis at low temperatures between -120 °C and -75 °C and to show large-angle wobbling with some molecules starting to desorb from the counter ion at temperatures between -50 °C and 25 °C [111].

The evolution of the XRD spectra of liquid toluene onto Na-montmorillonite showed that the toluene could penetrate into the clay interlayer, but the broadening of the spectra indicated that part of the clay platelets did not expand (Fig. 2.28), suggesting the interaction between toluene and the clay counter ion to be relatively weak [112].

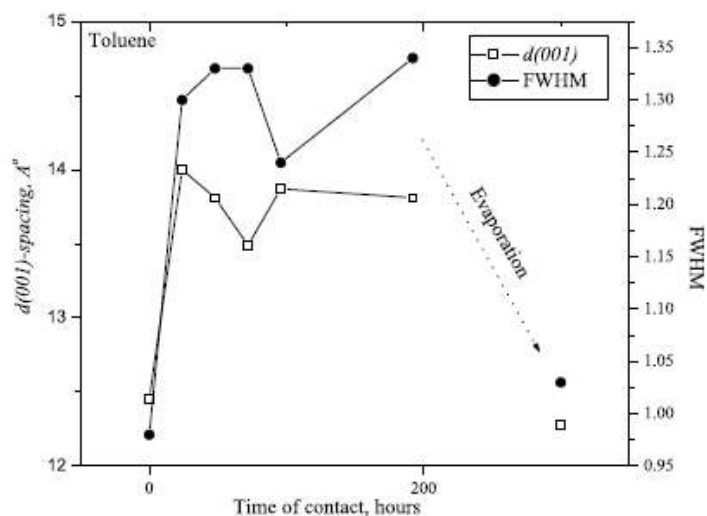


Fig. 2.28 : Evolution of d(001)-spacing and FWHM for toluene uptake on natural montmorillonite clay. (from [112])

2.8.2.2. POLAR AROMATIC MOLECULES

The adsorption of phenol by smectites was found to be accompanied by partial dehydration of the clay, indicating phenol to replace interlayer water during the mechanochemical process [113]. In the spectrum of phenol-beidellite the ring vibration at 1606 cm^{-1} was not observed. The disappearance of this band was a possible indication of π interactions of the aromatic ring with the oxygen plane of the alumino-silicate layer [113]. In the phenol-montmorillonite complex this band was observed but was weak relative to the other ring vibrations, indicating that the π interactions in montmorillonite are weaker than in beidellite, because of the higher number of tetrahedral substitutions in beidellite than in montmorillonite [113]. A shift of the ring vibration that appeared in the spectra of beidellite, natural vermiculite, exfoliated vermiculite, montmorillonite, and Laponite at 1487 , 1489 , 1490 , 1491 , and 1493 cm^{-1} , respectively, was attributed to π interactions, because a shift to lower wavenumbers indicates an increase in the strength of the π -bond [113]. In this case, however, the phenol was proposed to interact with the oxygen plane of the silicate layers. Because of the inductive effect of the cation, the water molecules were proposed to behave as Brønsted acids. The phenol may form a hydrogen bond with the water molecule by accepting a proton from this acidic species. Such bonding would imply a reduction in the delocalization energy of the benzene ring, giving rise to shifts of ring vibrations from 1595 and 1498 cm^{-1} in the spectrum of a benzene solution of phenol to higher and lower frequencies, respectively. The phenol may also form a hydrogen bond with water

molecules by proton donation. This would imply an increase in the double bond character of the C-O band, giving rise to a shift from 1186 cm^{-1} to higher frequencies [113].

Haderlein *et al* [6] measured the adsorption of a large number of nitroaromatic compound on Li-, Na-, Mg-, Ca-, Al-, NH₄, K-, Rb-, Cs-kaolinites from aqueous solutions. Substituents with strong electron-withdrawing and electron-delocalizing properties (e.g., NO₂, CHO, COCH₃, and CN) strongly enhanced sorption, and showed large enthalpies of adsorption ($-40 \pm 5\text{ kJ/mol}$). It was therefore proposed that electron donor-acceptor complexes between surface electron donor functions and the aromatic compound acting as electron acceptor are responsible for the strong adsorption.

2.8.2.3. POLAR NON-AROMATIC MOLECULES

The correlation between the association of ethanol and acetone on K-, Na-, Ca-, Ba-montmorillonites and the calculated values for ethanol-cation and acetone-cation dipole interactions (Table 2.10) suggested cation-dipole interactions play an important role in the adsorption process [114]. Moreover, the heat of interactions, obtained from the dependence of the chromatographic specific retention volume on the temperature, was in very good agreement with the theoretical values (Table 2.11) [115].

XRD spectra showed that the clays expanded up to about 13 \AA for the Na-, and K-montmorillonites, with two to three molecules of either ethanol or acetone per cation, and up to about 17 \AA for the Ca-, and Ba-montmorillonites, with four to five of either ethanol or acetone per cation. The expansion of the basal spacing was also found to depend on the charge of the clay (Fig. 2.29) [116]. At very low vapour pressures the molecules adsorbed to the external surface because no increase in basal spacing was observed. At higher vapour pressures, the high charge clays expanded less than the low charge clays. At the highest vapor pressures, adsorption appears to proceed by capillary condensation in micropores, because of the observed stable basal spacing. A comparison with the expansion of the clay with toluene adsorption suggests that the interaction of the ethanol and acetone molecules with the clay is stronger than for toluene.

Table 2.10 : Theoretical cation-dipole interaction energies (reproduced from [114])

Cation	Ethanol		Acetone	
	$(\mu = 1.73 \times 10^{-18} \text{ esu.cm})$		$(\mu = 2.86 \times 10^{-18} \text{ esu.cm})$	
	$r_0(\text{\AA})$	$\phi_p(\text{kcal/mol})$	$r_0(\text{\AA})$	$\phi_p(\text{kcal/mol})$
K	3.24	11.4	4.07	11.9
Na	2.91	14.1	3.71	14.4
Ba	3.26	22.5	4.09	23.6
Ca	2.94	27.7	3.75	28.1

Table 2.11 : Comparison between measured heats of adsorption and theoretical cation-dipole interaction energies (reproduced from [115])

		Charomatographically	Theoretical cation-
		determined heat of	dipole interaction
		adsorption	energy
		(kcal/mol)	(kcal/mol)
Ethanol	K	14.4	11.3
	Na	16.1	14.0
	Ba	21.8	22.1
	Ca	29.3	27.5
Acetone	K	14.3	11.9
	Na	16.0	14.4
	Ba	23.1	23.6
	Ca	30.1	28.1

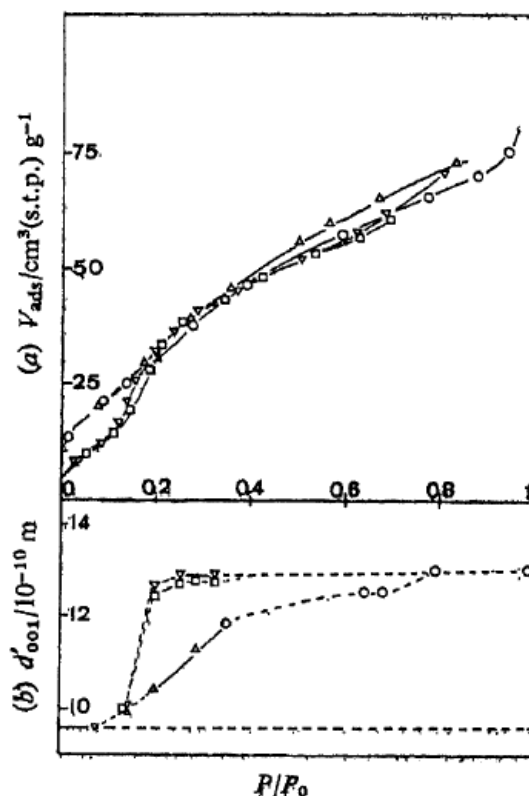


Fig. 2.29 (a) Adsorption isotherms of ethanol on montmorillonites with charges of (Δ) 1.039, (\circ) 1.050, (\square) 0.975, (∇) 0.911, in milli-equivalent per gram of dry clay. (from [116])

Temperature ramp measurements of the release of water, ethanol, ethylene glycol, and dimethyl formamide from Na, Ca, and Mg-montmorillonites showed the temperature peak positions to follow the order: water < ethanol < dimethyl formamide < ethylene glycol [117]. The strong binding of those molecules was here again attributed to a cation-dipole interaction between the molecules and the clay. We note however, that the water molecule has a larger dipole moment than ethanol [118] and the cation-dipole interaction, should therefore be more strongly bound than the ethanol molecule.

Bridging coordination of 1,2-dichloroethylene with water adsorbed on hydrated hectorites exchanged with Pb^{2+} , Hg^{2+} , Cd^{2+} , Ca^{2+} , Ag^+ , and Na^+ was also reported [119]. This interpretation was concluded from the observed linear correlation between the integrated absorbance of the hydration water OH stretching band and the monolayer content, together with a CCl stretching frequency that was unaffected by the cation type, suggesting no direct interaction with the cation.

However, the adsorption by divalent cations was found to be four times stronger than for monovalent cations, suggesting that even without direct interaction with the cation, the binding strength increased with the ionic strength of the cation.

2.8.3. Influence of the organic cation

Ion exchange of smectites with organic cations decreases the amount of water adsorbed on the clay, depending on the solvating power of the cations [120]. As a result, for the sorption from aqueous solution on smectites exchanged with organic cations, partitioning of a given compound into the organic phase is commonly assumed to be the major sorption mechanism, particularly with hydrophobic compounds [6]. Linear isotherms and lack of solute competition in binary-solute systems provided evidence for a partition-dominated process where the degree of uptake from water was determined mostly by the water insolubility of the solute. Also, straight-chain alkyl cations lead to greater adsorption of hydrophobic compounds such as benzene and toluene from aqueous solution on the organoclay than comparable cyclic alkyl cation, because the rearrangements in the alkyl groups facilitate sorption in a manner analogous to solvation [121]. For the polar molecules, ethanol, and butanol, the amount adsorbed on the organoclays, and the heat of immersion, were found to decrease with increasing chain length of the short-chain alkylammonium organic cations, showing a decreased polar interaction. For benzene, the amount adsorbed on dry Ca-smectite was found to be very low compared with the same clay modified with hexadecyltrimethylammonium (HDTMA). This was attributed to the inability of benzene to penetrate the interlamellar surface of the unmodified clay, whereas for the hexadecyltrimethylammonium (HDTMA)-smectite, the internal surfaces are available to benzene because the silicate layers are held apart by the large organic cations [122].

For metallic cations, the mechanism of adsorption is different, and seems to be driven by the ion strength of the counter ion. Indeed, Bailey *et al* [107] found that regardless of chemical character of the organic compounds (s-triazines, substituted ureas, phenylcarbamates, aniline, anilides, phenylalkanoic acids, benzoic acids, and picolinic acids) adsorption from aqueous solutions on montmorillonites was stronger on the H-montmorillonite than for the Na-montmorillonite. For the organic cations, the mechanism of adsorption may depend on the hydrophobicity of the counter ion. Roberts *et al* [123] showed a shift in the sorption mechanism of 1,3-dinitrobenzene,

2,4-dinitrotoluene, and naphthalene from water on organoclays, from a predominantly adsorptive process in the case of NH₄ and tetramethylammonium (TMA) smectites, to a partition-dominated process for hexadecyltrimethylammonium (HDTMA)-smectites. In addition, depending on the extent of modification of the clay, a HDTMA-smectite may behave as a dual adsorbent in the sorption of organic compounds from aqueous solution, in which the mineral fraction functions as a solid adsorbent and the organic phase a partition medium [122].

Tian *et al* [124] measured the partition coefficients of 22 volatile molecules on cetyltrimethylammonium bromide (CTMAB) bentonite by inverse gas chromatography. The basal spacing of the modified smectite was found to be larger than for the non-modified one, but the reverse was observed for the surface area, probably due to the large volume of the organic cation. The values of the partition coefficients were fitted using a linear solvation energy relationship (LSER) of the type:

$$\log(K_c) = c + rR_2 + s\pi_2^H + a\sum\alpha_2^H + b\sum\beta_2^H + l\log L^{16} \quad (2.41)$$

where K_c is the partition coefficient, R_2 represents the excess molar refractivity of the solute, i.e. the ability of the solute to interact with a sorbent through π/n -electron pair, π_2^H is a measure of the dipolarity/polarizability of the solute, $\sum\alpha_2^H$ is a measure of the hydrogen-bond donor acidity, $\sum\beta_2^H$ is a measure of the hydrogen-bond basicity, and $\log L^{16}$ is the gas-liquid partition coefficient of the solute in hexadecane (Ostwald partition coefficient) accounting for dispersion/cavity formation, and $c=0.434$, $r=0.968$, $s=-0.0886$, $a=2.170$, $b=1.611$, and $l=0.417$ are the fitting constants. The fitted LSER equation suggested that the CTMAB-bentonite was an adsorbent with insignificant dipolarity/polarizability, interacted with solutes partly through π/n -electron pairs, behaving both as hydrogen-bond donor and hydrogen-bond acceptor, and could interact with solutes by cavity/dispersion interaction. However, the difference between values predicted by the LSER equation and the measured values were quite large (Table 2.12), with consequences for the ranking of the partition coefficients (for example : pentan-1-ol and n-butyl acetate).

Table 2.12 : Observed and calculated partition coefficients of various VOCs on a CTMAB-bentonite from aqueous solution. (reproduced from [124])

VOC	K_c (mL/g)	$\log K_c^a$	$\log K_{c,cal}^a$	error (%)
benzene	241.24	2.38	2.37	-0.66
toluene	313.33	2.62	2.59	-1.1
ethylbenzene	749.58	2.87	2.79	-2.85
p-xylene	781.54	2.89	2.87	-0.94
o.xylene	1099.51	3.04	2.95	-3.1
m-xylene	1263.47	3.1	2.8	-7.21
chlorobenzene	1488.25	3.17	2.71	-14.57
n-hexane	31.76	1.5	1.56	3.57
n-heptane	60.35	1.78	1.76	-1.26
n-octane	126.8	2.1	1.97	-6.38
cyclohexane	70.53	1.85	1.94	5.19
methanol	524.77	2.72	2.51	-7.54
ethanol	472.57	2.67	2.68	0.22
butan-1-ol	1687.8	3.23	3.14	-2.65
pentan-1-ol	984.36	2.99	3.35	11.86
n-butyl acetate	846.81	2.93	2.59	-11.6
trichloromethane	118.64	2.07	2.3	10.71
tetrachloromethane	56.49	1.75	2.03	15.88
1, 1,2-trichloroethene	127.63	2.11	2.45	16.54
cyclohexanone	482.02	2.68	3.1	15.6
pyridine	2120.97	3.33	3.37	1.45
water	940.69	2.97	2.85	-4.21
propan-2-one	156.41	2.19	2.17	-1.14
dichloromethane	144.77	2.16	1.9	-12.14
ethyl acetate	246.33	2.39	2.2	-7.9
diethyl ether	54.32	1.73	2.03	1.15
propan-1-ol	1230	3.09	2.94	-4.76

2.9. RELEASE KINETICS OF VOLATILES FROM SMECTITE CLAYS

2.9.1. Overview

This section provides information on the evaporation of bulk liquids and the sorption kinetics of volatiles from smectite clays. The evaporation of small, water droplets under ambient conditions have been studied experimentally and calculated by numerical simulations assuming quasisteady state conditions at the surface of the droplet [125,126,127,128] (section 2.9.2), though without including gas convection effects. The evaporation of water droplets into vacuum was also treated by kinetic theory methods with good agreements with experimental data [129,130,131,132,133].

Only a few studies have been devoted to the release kinetics of volatiles from smectite clays to the gas phase [134,135,136,137] (section 2.9.3), or to the kinetics of adsorption of volatiles from the gas phase into smectite clays [138,139,140] (section 2.9.4). Studies of the release of toluene from various smectites suggested an initially rapid desorption, followed by slower desorption of the remaining fraction of toluene. The origin of the slow release fraction is not clear; Strong adsorption of toluene on the smectite, reaction of the toluene with the smectite, and slow diffusion of the toluene molecules in the smectite were proposed. In one of those studies, an analytical solution of the diffusion equation was used to fit the rate of release of toluene from the smectite clay, giving a diffusion coefficient of $7.4 \times 10^{-17} \text{ m}^2/\text{s}$ for the toluene molecules inside the clay. Analytical empirical models were also used to fit the rate of adsorption of water on various smectites. However, we point out that model fitting does not allow one to conclude about mechanisms of desorption [141,136,142]. In particular, the rates of release of water from Ca-montmorillonite could be fitted equally well with various analytical rate laws, so that it was not possible to conclude about a defined release mechanism. A SoilCover commercial software developed to model the transient liquid and vapour flow on the basis of Fick's Law and Darcy's Law was also used for predicting the rate of evaporation from soil surfaces. This package is limited to one-dimensional flows and does not include convection and gas diffusion effects through empirical models.

2.9.2. Modeling the evaporation of bulk liquids

Hu *et al* [126] calculated the rate of evaporation of 5 μl water droplets on a flat glass coverslip under ambient conditions by finite element methods (FEM) and compared the results with experimental measurements. Fluorescent particles were used as tracers to map the droplet profile by fluorescence microscopy and thereby calculate the droplet volume. The radius of the droplet at the contact line was about 1 mm. During the experiments the droplet remained in the shape of a spherical cap at all times during evaporation, with a contact angle decreasing roughly linearly with time. The decrease in contact angle during evaporation was also observed by Crafton *et al* [127] for 5 μl heated water droplets on an aluminium surface. The droplet shape is controlled by the Bond number $Bo = \rho g R h_0 / \sigma$, which accounts for the influence of surface tension and gravitational force on the droplet shape, and the capillary number $Ca = \mu u_r / \sigma$. Here $\rho = 1 \text{ g/cm}^3$ is

the density of liquid water, R is the radius of the droplet at the contact line, g is the gravitational constant, h_0 is the initial height of droplet, σ is the air-water surface tension, μ is the liquid viscosity, and u_r is the average radial velocity induced by droplet evaporation. For water the Bond number is in the range of 0.03-0.04, and the capillary number is around 10^{-8} , so that the droplet shape may be effectively regarded as a spherical cap. The time required for the vapour-phase water concentration to adjust to changes in the droplet shape is of the order of R^2/D , where a value of $D = 2.61 \times 10^{-5} \text{ m}^2/\text{s}$ was used for the diffusivity of water in air. The ratio of this time to the droplet evaporation time t_f is $R^2/Dt_f \cong c_v(1-H)\rho = 0.000014 \ll 1$, where $c_v = 2.32 \times 10^{-8} \text{ g/mm}^3$ is the saturated vapour concentration, and H is the relative humidity of the ambient air far from the droplet. Therefore the water vapour concentration adjusts rapidly compared to the time required for droplet evaporation, so that the water evaporation may be considered to be in a quasi-steady state, and the moving-free-surface problem may be converted into a series of steady-state solutions of the Laplace equation (steady-state diffusion equation). Calculations were found to be in close agreement with experimental measurements [126].

Girard *et al* [125] calculated the rate of evaporation of small heated water droplets by finite element methods (FEM). The radius of the droplet (about 1 mm) at the contact line was assumed to be constant during evaporation. The droplet was assumed to keep a spherical cap geometry during evaporation. In principle the rate determining step could be either the mass-transfer rate across the free interface or diffusion of the molecules in the vicinity of the droplet. The transfer rate across the interface is a molecular process is typically associated with times of about 10^{-10} s , whereas the diffusion of molecules in air is $R^2/D \cong 10^{-5} \text{ s}$, where a value of $D = 2.443 \times 10^{-5} \text{ m}^2/\text{s}$ was used for the diffusivity of water in air, and R is the radius of the droplet at the contact line. Here again, the time scales are different by five orders of magnitude, so that the droplet surrounding gaseous phase could be considered to be in quasi equilibrium, and diffusion in air may be assumed to be a quasisteady state process. As a result, the vapour concentration field was again governed by the Laplace equation. However, in this work, the substrate temperature ranged between 30 °C and 70 °C, while the far-field temperature, at a distance of $160R$ from the droplet, was fixed at 20 °C. Because of the temperature difference between the substrate and the far-field, temperature gradients determined the evaporation dynamics of the droplet. Heat diffusion was also assumed to be a quasi-steady process. The resolution of Laplace, heat, and Navier-Stokes equations determined the outgoing heat flow for each interface element.

2.9.3. Release of volatiles from smectite clays

2.9.3.1. RELEASE OF WATER

Bray *et al* [134] studied the isothermal release kinetics of water from a Ca-montmorillonite for temperatures ranging between 20 °C and 150 °C. The release curves were fitted by various rate equations, each linked to a defined rate mechanism:

$$g(\alpha) = kt \quad (2.42)$$

where α is the fraction of volatiles transferred from the adsorbed phase to the gas phase, the function $g(\alpha)$ depends on the mechanism of reaction (Table 2.13), k is the rate constant and t is the time. The release curves were also fitted using the empirical Avrami and Austin-Rickett rate laws :

$$\ln(-\ln(1-\alpha)) = m \ln k + m \ln t \quad (2.43)$$

$$\ln\left(\frac{\alpha}{1-\alpha}\right) = m_A \ln k + m_A \ln t \quad (2.44)$$

where m and m_A are the Avrami and Austin-Rickett rate exponents. From the temperature dependence of the rate constant, they obtained activation energies ranging from 28.6 to 40.5 kJ/mol.

Table 2.13 : Integrated rate equations. (from Bray *et al* [134])

Mechanism	Function $g(a)$	Slope (m)	Slope (m_A)
Zero order	α	1.17	1.36
R2 - phase boundary reaction, cylindrical	$1-(1-\alpha)^{1/2}$	1.10	1.31
R3 - phase boundary reaction, spherical	$1-(1-\alpha)^{1/3}$	1.06	1.27
F1 - random nucleation, one nucleus/particle	$-\ln(1-\alpha)$	1.00	1.19
A2 - random nucleation, Avrami equation I	$[-\ln(1-\alpha)]^{1/2}$	2.00	2.39
A3 - random nucleation, Avrami equation II	$[-\ln(1-\alpha)]^{1/3}$	3.00	3.58
D1 - one-dimensional diffusion	α^2	0.60	0.72
D2 - two-dimensional diffusion, cylindrical	$(1-\alpha)\ln(1-\alpha)+\alpha$	0.57	0.67
D3 - three-dimensional diffusion, spherical	$[1-(1-\alpha)^{1/3}]^2$	0.53	0.63
D4 - three-dimensional diffusion, spherical, Ginstling-Broughtein	$(1-(2\alpha/3)-(1-\alpha)^{2/3})$	0.55	0.66

2.9.3.2. RELEASE OF TOLUENE

Morrisey *et al* [135] studied the isothermal release of acetone, benzene and toluene from montmorillonite clay. The release curves were fitted with the following analytical solution of the diffusion equation for a finite slab of thickness l exposed to a constant gaseous sorbate concentration at the sample surface and with impermeable boundary at the bottom of the sample:

$$\frac{M_t}{M_\infty} = \lambda \left[1 - \frac{8}{\pi^2} \sum_{n=0 \rightarrow \infty} \frac{1}{(2n+1)^2} \exp\left(-\frac{D_1(2n+1)^2 \pi^2 t}{l_1^2}\right) \right] + (1-\lambda) \left[1 - \frac{8}{\pi^2} \sum_{n=0 \rightarrow \infty} \frac{1}{(2n+1)^2} \exp\left(-\frac{D_2(2n+1)^2 \pi^2 t}{l_2^2}\right) \right] \quad (2.45)$$

where λ is the mass fraction of volatiles sorbed onto the surface of the mineral particles and $(1-\lambda)$ the remaining fraction of volatiles sorbed at the intra-particle surfaces, D_1 and D_2 are the diffusion coefficients of the volatiles at the surface of the clay and at the intra-particle surface, respectively, l_1 and l_2 are the bulk profile thickness and the thickness of an individual particle, respectively, M_t is the mass of volatile released at time t , and M_∞ is the total mass of volatile. Assuming a particle size of 2 μm , a very low diffusion coefficient of $7.4 \times 10^{-17} \text{ m}^2/\text{s}$ is obtained for toluene in this case (intra-particle surface diffusion). Other studies suggested an initially rapid desorption, followed by slower desorption of the remaining fraction of toluene [137,143,144,145]. The results were interpreted in terms of strong interactions of the toluene molecules with the clay.

Steinberg *et al* [145] investigated the influence of the type of counter ion (K^+ , Na^+ , Ca^{2+} , Mg^{2+} and Fe^{3+}) on the desorption of toluene at 25 °C in a laboratory fume hood, from montmorillonites previously incubated in liquid toluene or treated with toluene vapor. When toluene was added in the vapour phase, the concentration of the “slowly diffusing fraction “ was found to correspond to the extent of exchangeable cation ($\text{K} > \text{Na} > \text{Mg} > \text{Ca}$). Experiments were also performed by inundating toluene-exposed montmorillonites with ion-exchange solutions and then vigorously agitating in an effort to cause shock desorption of recalcitrant toluene. In all cases, the amount of “slow diffusing“ toluene was found to increase with increasing agitation. A model was proposed in which the residual toluene was hold within water-stable aggregates.

In another study Chang *et al* [143] investigated the sorption of toluene on Ca-montmorillonite for relative vapour pressures ranging between 0.3 and 0.4 under both high and low relative humidity (RH) conditions at 25 °C. Fourier transform infrared (FTIR) spectroscopy suggested three phases:

labile (gaslike), slow sorption (liquidlike), and a resistant-to-desorption phase. The sorption phase showed both liquid toluene bands and some new bands. At low RH three new bands appeared as soon as the sorption started, in the region of aromatic carbon-hydrogen (C-H) bending and ring torsion, usually seen in compounds with methyl-substituted benzene rings. The large shifts of these bands suggested strong interactions between the sorbate and the clay, which restrict the CH-bending and the ring torsion. Four other new bands appeared only after longer time, and remained after purging of the clay sample with dry nitrogen gas. Moreover, no bands with wave numbers higher than 3000 cm^{-1} were observed after purging, suggesting the absence of aromatic C-H stretching. Additionally, at high RH, seven new bands, of which two were tentatively assigned to C-O stretching and C-O bending. This spectral information suggested the formation of new organic chemical structures, identified previously by Mortland *et al* [146] in a chloroethane/Cu-montmorillonite system. The possible reactions include benzene ring opening, oxidation, and alkylation. In similar experiments Shih *et al* [144] studied the sorption of toluene on Ca-, and Cu-montmorillonites under dry and humid (about 40 %RH) conditions. A residual fraction of toluene (about 10 %) was observed over 60 days of desorption from the Ca-montmorillonite under dry conditions, whereas no residues were seen in the experiments in humid conditions. The diffusivity of toluene in clay estimated by Morrissey *et al* [135] from kinetics of desorption studies and Arocha *et al* [147] from adsorption studies ranged from 3.7×10^{-16} to $3.5 \times 10^{-19}\text{ m}^2/\text{s}$. Thus, diffusion was considered to be a possible explanation for the slow sorption of toluene, otherwise, the slow sorption was attributed to the intrinsic reaction between the sorbent and the sorbate. For the sorption of toluene on Cu-montmorillonite, the authors also observed the appearance of new vibrational modes, and strong shifts in the vibrational modes of the CH_3 deformation, the C-C stretching modes, indicating that some toluene molecules could have been chemically bound to the Cu-montmorillonite.

Keyes *et al* [136] studied the influence of heating rate, clay type, particle size, and purge gas flow on the temperature ramp desorption of toluene from montmorillonite clay particles. The curves were fitted with a model taking into consideration the intraparticle gas phase and the adsorbed phase, three mass-transport mechanisms, molecular diffusion, Knudsen diffusion, and pressure-driven bulk flow. The purge gas flow rate was intentionally maintained high enough to remove dependencies on flow rate, meaning that the mechanism of external mass transfer was assumed to be not rate-controlling. The authors could not conclude about which mechanism was the most

influential, because all of the single-mechanism models correlated adequately the experimental data.

2.9.4. Adsorption kinetics of water on smectite clays

2.9.4.1. EMPIRICAL MODELS

Grismer [139,140] studied the adsorption of water vapour on bentonite. The adsorption curves were fitted with the following model:

$$\frac{d\theta}{dt} = c_m \left(\frac{\theta_m - \theta}{\theta_m} \right) \theta \quad (2.46)$$

where t is the time, θ is the coverage of volatile on the clay at time t , θ_m is the saturated coverage, and c_m is a fitting constant.

Montes-H *et al* [138] studied the influence of the type of interlayer cation, the mechanical compaction, the drying temperature of the sample prior to experiments, the relative humidity, and the amount of sample, on the adsorption of water on bentonite. The adsorption curves were fitted using a kinetic model of the second order:

$$\frac{dW}{dt} = k_a (W_m - W)^2 \quad (2.47)$$

where W is the amount of water adsorbed at time t , k_a is the kinetic coefficient, and W_m is the maximum of water adsorbed. The half sorption time is defined by:

$$b = \frac{1}{k_a W_m} \quad (2.48)$$

The half-sorption time increased proportionally to the increase in relative humidity. The speed of adsorption decreased when the amount of sample was increased. The drying temperature of the sample prior to experiments was not found to affect the results except at high temperatures (500 °C). The mechanical compaction influenced slightly on the adsorption kinetics. The maximum amount adsorbed was not modified by compaction. However, the first state of compaction produced an increase of the half-sorption time. The Ca- and Mg-bentonite samples

reached the adsorption equilibrium more rapidly because the half-adsorption time estimated was less than the half-adsorption time estimated for Li-, Na-, and K-saturated bentonite samples.

2.9.4.2. ONE-DIMENSIONAL FINITE-ELEMENT PACKAGE

The commercial code “SoilCover” (Geo-Analysis 2000 Ltd, 2000) is a one-dimensional finite-element package that models transient liquid and water vapour flow, based on a theoretical model for predicting the rate of evaporation from soil surfaces [148,149] presented by Wilson et al [150]. The model is based on a system of equations for coupled heat and mass transfer in soil. The flow of water vapour and liquid water are described on the basis of Fick’s Law and Darcy’s Law as follows:

$$\frac{\partial h_w}{\partial t} = C_1 \frac{\partial}{\partial y} \left(k_w \frac{\partial h_w}{\partial y} \right) + C_2 \frac{\partial}{\partial y} \left(D_v \frac{\partial P_v}{\partial y} \right) \quad (2.49)$$

with

$$C_1 = \frac{1}{\rho_w g} \quad (2.50)$$

$$C_2 = \frac{P + P_v}{P \rho_w^2 g m_2} \quad (2.51)$$

$$D_v = \alpha \beta \left(D_{vap} \frac{W_v}{RT} \right) \quad (2.52)$$

where k_w is the unsaturated hydraulic conductivity, that depends on the suction value, h_w is the high of the column, t is the time, C_1 is the coefficient of consolidation with respect to the bulk phase, r_w is the mass density of water, g is the acceleration due to gravity, y is the position, C_2 is the coefficient of consolidation with respect to the water vapour phase, m_2 is the slope of the soil-water characteristic curve, P is the total gas pressure in the air phase, P_v is the partial pressure due to water vapour in the soil, D_v is the diffusion coefficient of water vapour through the soil, $\alpha = \beta^{2/3}$ is the tortuosity factor of soil, β is the cross-sectional area of soil available for vapour transfer, D_{vap} is the molecular diffusivity of water vapour in air, T is the temperature, W_v is the molecular weight of water, and R is the universal gas constant. The temperature T is evaluated on the basis of conductive and latent heat transfer as follows:

$$C_h \frac{\partial T}{\partial t} = \frac{\partial}{\partial y} \left(\lambda \frac{\partial T}{\partial y} \right) - L_v \left(\frac{P + P_v}{P} \right) \frac{\partial}{\partial y} \left(D_v \frac{\partial P_v}{\partial y} \right) \quad (2.53)$$

with

$$C_h = C_v \rho_s \quad (2.54)$$

where C_h is the volumetric specific heat of the soil as a function of water content, C_v is the specific heat of the soil, ρ_s is the mass density of the soil, λ is the thermal conductivity of the soil, and L_v is the latent heat of vaporization of water. SoilCover calculates the vapour pressure in the soil using the relationship provided by Edlefsen and Anderson, in which vapour pressure is calculated on the basis of the total suction in the liquid phase:

$$P_v = P_{sv} h_r \quad (2.55)$$

$$h_r = \exp \left(\frac{\Psi g W_v}{RT} \right) \quad (2.56)$$

where P_{sv} is the saturation vapour pressure of the soil at temperature T , h_r is the relative humidity of the soil surface as a function of total suction and temperature, and Ψ is the total suction in the unsaturated soil. Atmospheric coupling is achieved by calculating the soil evaporation flux. Soil evaporation flux is a function of the vapour pressure gradient between the cover surface and the atmosphere. A modified Penman formulation proposed by Wilson is used and is written as follows:

$$E = \frac{\Gamma Q + v E_a}{\Gamma + A v} \quad (2.57)$$

$$E_a = f(u) P_a \left(\frac{1}{h_a} - \frac{1}{h_r} \right) \quad (2.58)$$

$$f(u) = 0.35(1 + 0.15 U_a) \quad (2.59)$$

where E is the vertical evaporative flux, Γ is the slope of the saturation vapour pressure versus temperature curve at the mean temperature of the air, Q is the net radiant energy available at the surface, v is a psychrometric constant, E_a is a function dependent on wind speed, surface

roughness and eddy diffusion, U_a is the wind speed, P_a is the vapour pressure in the air above the evaporation surface, and h_a is the relative humidity of the air.

2.10. MOLECULAR SIMULATIONS

2.10.1. Overview

A central problem in the study of clay mineral surface chemistry is to deduce molecular mechanisms from experimental observations, that can easily be a source of interpretations. Techniques for the simulation of atomistic systems may provide insight into those mechanisms. The drawback is that all these calculations are based on various assumptions, depending on the level of description of the system, that influences their accuracy at describing the real phenomena, such that the results obtained have to be taken with caution.

The subsections 2.10.2 and 2.10.3 cover the application of simulation methods based on combining molecular dynamics with classical molecular mechanics, where interatomic interactions are expressed via empirical formulas. This approach is often called the force-field approach. Simulation methods based on classical mechanics consider each atom as a single entity and the forces between them are modelled by potential functions based on classical physics. There is no description of interactions at the sub-atomic scale. In addition to initial atomic positions, one must also provide a set of suitable parameters for the interaction potential functions, known as a force-field. Parameters for force-fields are derived from experimental data and/or quantum mechanical calculations on a finite set of systems. Therefore the question arises as to how well a force-field is able to model the properties of systems dissimilar to those from which it was derived; how a force-field is transferable to other systems. The use of simple inter-atomic potentials means that it is possible to handle up to millions of atoms and therefore model such larger and more “realistic” systems than quantum calculations treated in the subsection 2.10.4. A large number of publications dealing with the classical molecular dynamic simulations of smectite clays are based on a force-field model developed by Skipper *et al* [151,152] that considers the clay as a rigid structure with the same geometry as that of talc. The water is rigid as well, and the species interacts by pair-wise interactions between atoms represented as point charges. The simulations were found to be in semi-quantitative agreement with the swelling

curves measured experimentally with results depending on the models used to describe the water molecules (MCY, TIP4P, SCP). The approach of a rigid clay structure introduces an a priori distortion into the atomistic description of the structural and dynamic behaviour of surface and interlayer species that may influence the results obtained. Additionally, atomic charges in the rigid clay lattice are typically assigned values equivalent to their full formal charge, thus generating unreasonably large electrostatic potentials. Therefore flexible force-fields have been developed by Teppen *et al* [153] and Cygan *et al* [154]. In particular, the force-field of Cygan used interatomic potentials derived from parametrizations incorporating structural and spectroscopic data for a variety of simple hydrated compounds and deriving the partial charges of the coulomb terms by Mulliken and ESP analysis of DFT results on simple oxides. A flexible SPC-based water model was used to describe the water and hydroxyl behaviour. This force-field was used to simulate the hydration of a Na-montmorillonite and the results in terms of the swelling curve were reported to be in very good agreement with experiment. The model results were also in general agreement with previous theoretical descriptions of the swelling of smectite clays derived using rigid clay structures.

The microscopic picture of clay swelling derived from the classical simulations can be summarized as follows. Crystalline swelling is loosely attributed to the formation of molecular layers of interlayer solvent, but is in fact more closely associated with the solvation by stages of the interlayer counterions themselves. Taking as example the Na-montmorillonite, the swelling mechanism is as follows. In the starting configuration, the “one-layer hydrate” is visible with sodium ions forming inner-sphere surface complexes, where the sodium is bound to the clay surface, with the $\text{H}_2\text{O}/\text{Na}^+$ ratio was between 3 and 4. With increasing water vapor pressure the clay swells but the inner-sphere complexes are preserved, their distance to the clay mineral surface remaining almost constant. Concomitantly, this forces the water molecules to form two layers. The “two-layer hydrate” is attested from the double peak distribution of the water oxygens density profile in the direction perpendicular to the clay surface. However, the molecules do not form two well-defined lines of water molecules, and molecules are also found around the two maxima of the density profile. Also some simulations and experiments suggested the notion of water layer to be inappropriate for smectites with tetrahedral substitutions, because no water layers were observed, though these smectites show also stepwise adsorption. The key phenomenon in the transition occurs at a layer spacing close to 13.50 Å: part of the inner-sphere

sodium ions moves to the central plane of the interlayer. The driving force for this counterion flux is thought to be the energy associated with full hydration of these counterions. These hydrated sodium ions are referred to as outer-sphere complexes. This hydration is thought to be facilitated by the increased interlayer volume and the increased number of intercalated water molecules. Notably, the sodium ions move to the interlayer center for a ratio $H_2O/Na^+ \cong 6$. A further expansion of the clay leads to an increasing number of sodium ions in the center of the interlayer and concomitant adsorption of water molecules that hydrate these ions. In particular, it was observed that in the regime 14.25-15.0 Å the water oxygen atoms overlap with the sodium ions that were located close to the inner-sphere positions. The resulting constraint is relieved by a further expansion to a layer spacing of about 15.3 Å. In this final state, a large fraction of counterions are fully hydrated outer-sphere complexes in the central interlayer plane. These observations indicate that the swelling proceeded from the state of partially hydrated inner-sphere sodium ions (H_2O/Na^+ 3-4) to the state characterized by fully hydrated outer-sphere sodium ions with a smaller fraction of inner-sphere sodium ions ($H_2O/Na^+ \cong 8-9$). The ability of an ion to hydrate, and thereby to graduate from inner- to outer- to diffuse-complex, has been therefore identified as a key factor in the mobility of ions and the ability of clays to swell. The fraction of inner-sphere surface complexes was also found to be determined by the fraction of the layer charge arising from isomorphic substitutions in the tetrahedral sheet. This transition was also found to be associated with the increased mobility of cations and water molecules. In addition the simulations show also that confined water molecules form hydrogen bonds to each other and to the clay's surface, recreating the hydrogen-bonded network it enjoys in the bulk. Indeed, for the two-molecular layer hydrate the first nearest neighbour environment is remarkably close to that of bulk water and its molecular diffusion coefficient as well. However, the second nearest neighbour of the O-O radial distribution function suggested that the water suffers a longer-ranged perturbation to its tetrahedral network, leading to a small reduction in density relative to that of pure water, because packing of the molecules is less efficient.

In the section 2.10.2.2 a possible explanation for the hysteresis is given based on the results from classical molecular simulations. The free-energy of the clay-water systems at fixed relative humidity have been calculated to explain the hysteresis in the interlayer distance expressed as a function of the relative humidity, or chemical potential. Calculations have been performed on smectites with octahedral replacements. Results from the numerical calculations suggest that a

free-energy barrier separates the one- and two-layer hydrates, and swelling or shrinking occurs in the system is able to cross this free-energy barrier. As a result the system can be trapped in a meta-stable state. The origin of this free-energy barrier was interpreted in terms of the breaking of hydrogen bonds between the water molecules in each water layer and the formation of new bonds between the two layers of water molecules. However, as mentioned previously, the notion of layer hydrates is source of controversy. Moreover the curve of the interlayer distance expressed as the number of water content in the clay shows also hysteresis; at the same water content the adsorption isotherm does not show the same interlayer distance as the desorption curve. Since it appears at a fixed water content, it cannot be explained in terms of transition between layer hydrates. In addition the extent of hysteresis is dependent upon the type of counter ion; the hysteresis being more pronounced for the sodium form as compared the lithium and the calcium forms (see section 2.5.3.1). This is not taken into account when considering the breaking and formation of hydrogen bonds between and within layer hydrates. The stable interlayer distances appear also to be slightly dependent on the type of counterion. Since the swelling of the clay is strongly correlated with the hydration of the counter ions and its mobility, it would be expected that the hysteresis is also connected to the hydration of the counter ion.

As the number of atoms simulated continues to increase it is now becoming possible to consider simulating “real size” clay sheets without using periodic boundary conditions. The capabilities of large-scale atomic/molecular massively parallel (LAMMPS) codes have been exploited to simulate clay-polymer nanocomposite systems up to and beyond 1 million atoms, and approaching therefore the dimensions of clay sheets [155]. The group has observed that, for simulation cell sizes in excess of 250 000 atoms, undulations occur in the clay sheets. It still remains a challenge, however, to follow the evolution of a system beyond the timescale of 1-10 ns, even when using classical mechanics simulations. To access even larger simulation length and time scales, where the clay platelets themselves are embedded in a polymer matrix and thus are not constrained by periodic boundary conditions, it becomes necessary to employ a further type of dynamic simulation, meso-scale modelling, which is similar to molecular dynamics but at a coarse-grained level. The clay and the molecules are all represented by chains of spheres (beads), with the bonded interactions typically represented by simple harmonic functions. Using such techniques the diffusion of functionalized polymers into clay systems has been studied, showing that the

headgroups of the polymer remained at the edge of the clay interlayer while the backbone of the polymer is intercalated [156].

All of the force-fields currently used for describing interactions within clay-based materials are based on the “pair-wise” interaction approximation, in which the problem of calculating interactions for a many-body system is reduced to the treatment of pair-wise interacting bodies. This approximation still yields data in good agreement with bulk properties of clay systems. However, from the structural and vibrational analysis of talc and pyrophyllite, calculations using the CLAYFF forcefield were found to differ from *ab initio* calculations and experiments on hydroxyl bond length, Si-O-Si angle distribution, hydroxyl orientation angle, and Al₂OH vibration [157]. The choice of the pair-wise interaction potentials for the simulations of smectite clays is still a matter of debate, and studies into the microstructure of water molecules and hydrated cations using many-body force-fields have shown that to gain a more accurate understanding of the structure of water around strongly-polarising species, such as the cations present in the interlayer of hydrated cationic clays, many-body effects may need to be included within the simulations [158].

Section 2.10.4 represents papers in which quantum chemical methods are applied. Quantum mechanical simulations attempt to solve, to a good approximation, the fundamental equations of quantum mechanics, in order to model the interactions between the electrons and nuclei of a system of atoms. The advantage of quantum mechanical simulations is that they have an explicit representation of electrons. In addition, the only input data necessary is the atomic number and initial configuration of the nuclei and the total number of electrons. The major disadvantage of the method is the massive associated computational cost – at present, electronic structure calculations are limited to the study of hundreds of atoms, even when using large parallel computers. Due to the complex nature of clays, studies undertaken so far have mainly focused on the use of the cluster model approach [159,160,161,162,163]. This method consists of taking a small cluster of atoms from an extended clay structure to obtain a representative model for the study of interest. In particular, this approach was used to find a structure-property relationship for the interaction of substituted nitrobenzene molecules on montmorillonite and beidellite clusters. The global softness, which can be approximated by the inverse of the difference between the first ionization energy and the electron affinity of the molecule, was found to be a good descriptor for the affinity of those nitrobenzene compounds for the clay clusters, with limitations for molecules

where both electron-withdrawing and electron-releasing groups are strong. Usually, the inevitable dangling bonds that are generated by such a procedure have to be saturated by hydrogen atoms, producing undesired chemical properties. Another drawback of the cluster approach is that the finite-size effects can lead to misleading results.

To avoid such pitfalls, calculations using periodic boundary conditions have been recently undertaken. Although the Density-Functional Theory does not reach the so-called chemical accuracy yet (i.e. absolute errors on energetic that fall below 2 kJ/mol), this method is currently the only one that can predict acceptable estimates using realistic models. Results from *ab initio* DFT-based simulations of the hydration of montmorillonites with tetrahedral replacement provided the similar water structure and density profile in the direction perpendicular to the clay surface as obtained by previous classical MD calculations. In particular, the oxygen atoms showed a two peak distribution indicating the formation of a double-layer hydrate. At low hydration the water molecules were found to squeeze themselves in a flat orientation. With an increase in water content the water molecules formed stretched H-bonds with the clay surface. It was inferred from the nearest-neighbor coordination that the number of hydrogen bonds formed between water and clay is much smaller than the number between the water molecules themselves, showing the strong preference for intersolvent hydrogen bonding with only weak and short-lived hydrogen bonds to the silicate surface. The MD simulation showed that the formation of these hydrogen bonds is a dynamic process during which bonds are created and/or broken. The inner-sphere complex, where the sodium is coordinated to four water molecules and one basal oxygen atom, was found to be separated from the outer-sphere complex, where the sodium is coordinated by five water molecules, by an energy barrier of 1.2 kT. In this simulation the distance of the inner-sphere complex from the clay layer was different than that found in previous classical molecular dynamic simulations and no water adsorbed in the hexagonal cavity sites was observed, as opposed to previous classical molecular dynamic simulations.

DFT *ab initio* calculations have been also performed to study of the interaction between organic compounds and smectites. The MD simulation of anionic form of the pesticide 2,4-dichlorophenoxyacetic on a dry and hydrated calcium montmorillonite did not support the formation of cation bridge in the adsorption mechanism, but the formation of bidentate complexes on the dry clay and monodentate on the hydrated clay. The investigation of the initial stage in the *in situ* polymerization of methanal and ethylenediamide in the interlayer of sodium

montmorillonite showed that the catalysis occurred at the clay mineral lattice-edge where hydroxyl groups and exposed Al^{3+} ions act as strong Brønsted and Lewis acid sites, respectively.

2.10.2. Classical MD simulations with rigid clay structures

2.10.2.1. FORCE-FIELD MODEL DEVELOPED BY SKIPPER AND CO-WORKERS

A majority of classical molecular dynamic simulations on smectite clays that can be found in the literature are based on a force-field developed by Skipper and co-workers [151]. In order to describe molecular interactions in a swelling clay-water system, six sets of intermolecular potential functions had to be developed, viz., water-water, water-counterion (cation), cation-cation, water-clay mineral, cation-clay mineral, and clay mineral-clay mineral. The chosen representation of the interactions between water molecules or Na^+ and the clay mineral structure does involve significant approximations. Both the MCY and the TIP4P potential models have been used for the water-water interactions. The MCY model was developed by fitting *ab initio* quantum chemical calculations of the potential energy to the expression:

$$U = \sum_i \sum_j \left\{ \frac{q_i q_j}{r_{ij}} - A_{ij} \exp(-B_{ij} r_{ij}) + C_{ij} \exp(-D_{ij} r_{ij}) \right\}$$

The TIP4P model was developed by fitting experimental thermodynamic X-ray structural data for liquid water, in which intermolecular site-site interactions are described by the expression:

$$U = \sum_i \sum_j \left\{ 4\varepsilon_{ij} \left[\left(\frac{\sigma_{ij}}{r_{ij}} \right)^{12} - \left(\frac{\sigma_{ij}}{r_{ij}} \right)^6 \right] + \frac{q_i q_j}{r_{ij}} \right\}$$

The MCY model gives a too low water density, but is thought to have better transferability than the TIP4P model that gives the correct liquid water density. An advantage of the TIP4P model is that it is compatible with the OPLS force-field for organic molecules. Both models assume the water molecules to be rigid. For this reason, the dipole moment of the water molecules is about 2.2 D to 2.35 D, as compared to 1.8 D from experimental measurements. The *ab initio* model of Bounds 1985, which gives a good account of the aqueous solvation of Na^+ was selected for the water-sodium interaction. The clay layer is also rigid. Previous *ab initio* studies suggested that the valence electrons in OH, SiO_4 , and AlO_4 groups are centred on the O atoms and, therefore, that the latter dominates any short-range interaction with a clay mineral surface. This was taken as justification in representing the clay layer solely by O atoms saturated by two H atoms to make

use of the MCY and TIP4P models. To represent the siloxane surface, water molecules were placed at the sites of the O atoms on the basal planes of talc with the H atoms generally directed toward the cation positions in the tetrahedral sheet. Structural OH groups also were represented by water molecules, but with one H atom removed and the OH bond inclined approximately for a dioctahedral or trioctahedral mineral. Lastly, the apical O atoms in SiO_4 or AlO_4 tetrahedra were represented in the same way as the basal plane O atoms. Metals in the octahedral sheet were assigned unscreened ionic charges (Mg and Al are represented by point charges of $+2e$ and $+3e$). The charge was balanced by placing $-1e$ on each of the co-ordinating O atoms. The H atoms in structural OH groups were assigned the same positive charge as H in a water molecule. This charge was balanced by an equal opposite charge on the bonding O atoms. Semi-empirical estimates of the gross atomic charge on surface O atoms in uncharged silicate clusters suggested the value of $-0.8e$, which was adopted. Electroneutrality dictated a gross atomic charge of $+1.2e$ for Si. Negative charges resulting from isomorphic substitutions in the octahedral or tetrahedral sheets were placed on specific cation sites within the sheets, and the charge was reduced by $1e$.

2.10.2.1. TESTS OF THE FORCE-FIELD DEVELOPED BY SKIPPER AND CO-WORKERS

The force-field developed by Skipper and co-workers was used to investigate the swelling of Li-, Na, and K-montmorillonites of the Wyoming type with octahedral and tetrahedral replacements [164]. The curve of the layer spacing as a function of water content was found to be in semi-quantitative agreement with the experimental measurements (Fig. 2.30). The variation of the layer spacing with water content in the sodium- and lithium-montmorillonites took place in a monotonic, though stepwise manner, as observed experimentally (see section 2.5.3.1). The layer spacing for water contents around the step transition region fluctuated strongly. This was taken as an indication of the transition from monolayer to bilayer water structure. Indeed the density profiles of the water oxygens in the direction perpendicular showed a transition from a single peak distribution to a double-peak distribution with an increase in water content (Fig. 2.31), assigned to the “one-layer” and the “double-layer” hydrates, as suggested from previous experimental measurements (see section 2.5.3.2). However, we note that the density profile together with the snap shot of a double-layer hydrate (Fig. 2.32) show that the double-layer hydrate is not formed by two clearly separated layers, but contains water molecules between the two regions of higher water density. The ease of swelling was found to follow the energy of hydration of the cations, as observed experimentally (see section 2.5.3.3). As the water content

was increased, both the Li^+ and Na^+ were able to hydrate, and became detached from the surface. In contrast, it was found that the K^+ ions bound to the clay surface. The reduction of the K-montmorillonite to expand was therefore attributed to the reluctance of the K^+ ion to fully hydrate.

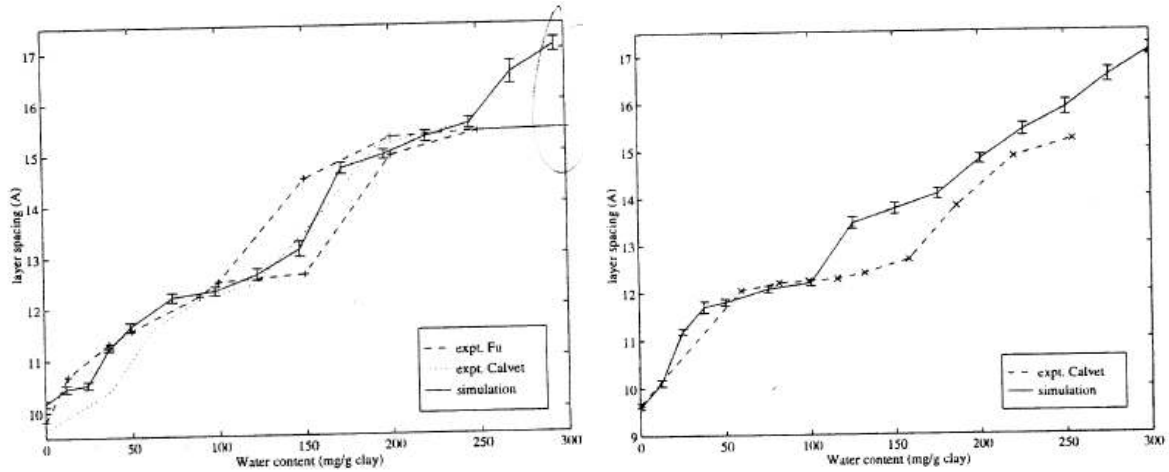


Fig. 2.30: (left) The interlayer spacing of Na-Wyoming montmorillonite as a function of increasing water content. (right) The interlayer spacing of Li-Wyoming montmorillonite as a function of increasing water content. (from [164]).

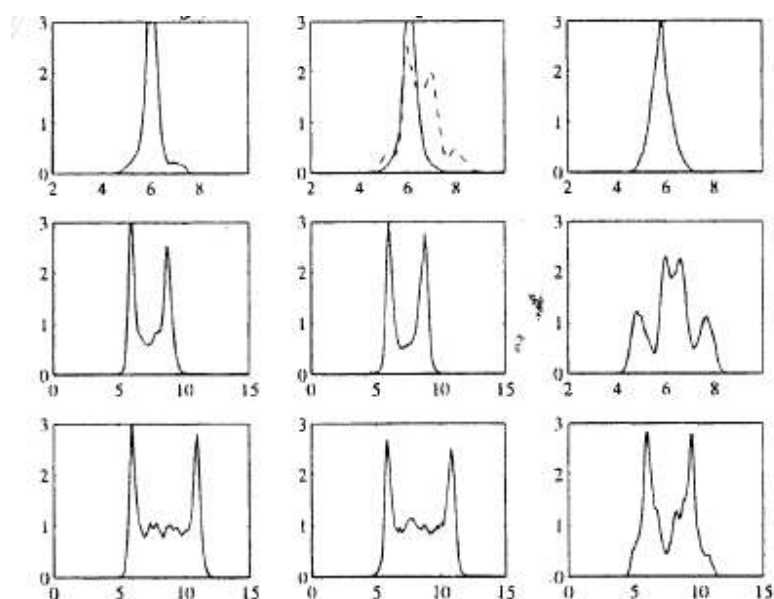


Fig. 2.31: Density profiles for Li⁺, Na⁺, and K⁺ counter ions, in the first, second, and third columns, respectively. The water content increases from 32 molecules, 64, to 96 water molecules, in the first, second, and third rows, respectively. Densities are calculated as a function of the distance perpendicular to the clay surface (from [164]).

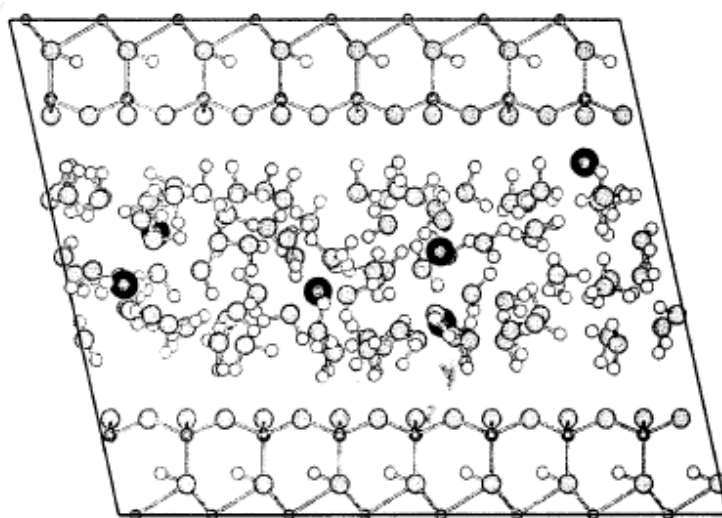


Fig. 2.32: Molecular model of sodium Wyoming montmorillonite as used in the Monte Carlo simulations. The simulation cell consists of two montmorillonite layers, 6 sodium ions (black), and 95 water molecules (from [164]).

The force-field developed by Skipper and co-workers was tested on talc, and Na-saturated Wyoming type montmorillonite and vermiculite using both the MCY and the TIP4P water models [152]. For talc, the layer spacing was found to be 2.7 % too small using the MCY model and 2 % too large using the TIP4P model. For the Wyoming montmorillonite and vermiculite, the

interlayer spacing were in agreement with experimental measurements within 0.2 % and 1.2 %. The interlayer distances obtained for a monolayer hydrate (experimental value: 12.2-12.5 Å) using the MCY and the TIP4P models were 12.1 Å and 11.6 Å for montmorillonite and 11.7 Å and 11.6 Å for vermiculite. It was concluded that the MCY models was more appropriate for the calculations with smectite clays compared to the TIP4P model.

However, simulation of water and cations in Wyoming montmorillonite (with both tetrahedral and octahedral replacements) and Arizona montmorillonite (with only octahedral replacements) performed by Tambach *et al* at varying relative humidity using the method of Skipper with both the MCY and the TIP4P water models lead to the opposite conclusion [165]. Density profiles showed significantly different interlayer structures depending on the type of clay and the models used. The four cation peak in the ion distribution of the Wyoming clay was attributed to the formation of inner-sphere complexes, where the counterion is bound to the surface, and outer-sphere complexes, where the counterion is fully hydrated and lies in the midplane of the clay interlayer. The inner-sphere complexes were formed with the cations that moved close to the surface and bound to tetrahedral substitutions. The spacing calculated with the TIP4P model were in better agreement with experimental data than the spacings calculated with the MCY model. The clay surface was also more attractive for Na⁺ counterions with MCY than with the TIP4P model. As a result, the cations were found to be in diffuse-layer and form outer-sphere complexes with the clay layers using the MCY model, whereas the TIP4P model predicted that cations are only present in the diffuse-layer. Therefore it was recommended to use the TIP4P model.

The method of Skipper *et al* was also used to investigate the dynamics of water and the counterions in the Wyoming Na-montmorillonite interlayer by monitoring their movement over 205 ps [85], which was reported to be long compared to the residence time of a water molecule in the bulk liquid (1 ps) or to that of a water molecule solvating Na⁺ in solution (10 ps). The Na⁺ density profiles showed that inner sphere surface complexes coexisted with outer-sphere surface complexes in all three hydrates. Some of the outer-sphere surface complexes dissociated from the siloxane surface to become diffuse-layer species in the multilayer hydrates. The fraction of inner-sphere surface complexes was determined by the fraction of the layer charge arising from isomorphic substitutions in the tetrahedral sheet. In the multilayer hydrates, the solvated counterions and water molecules were found to be relatively mobile (Table 2.14). In the one-layer hydrate, the water molecules resided mainly near the midplane because there was only one

water network, whereas in the two-layer hydrate, their number density was higher near the siloxane surface than near the midplane because there were two water networks at about 6.0 Å from the center of the octahedral sheets. In the three layer hydrate, the midplane water was found to be less well-structure than the near-surface water networks. The calculated molecular diffusion coefficients of water and the sodium counter ions in the clay interlayer were found to be somewhat reduced from their bulk values and to increase with increasing water content.

Table 2.14: Self-Diffusion coefficients of interlayer water molecules and sodium counter ions at 300 K. ^a D_w for one- and three-layer Li-montmorillonite hydrates; D_w for the two-layer hydrate of Na-montmorillonite; bulk water estimate is 2/3 of D_w at 298 K. ^b D_{Na} for Na-Wyoming montmorillonite hydrates, and 2/3 of the value of the infinite-dilution-limit D_{Na} in aqueous solution at 298 K (reproduced from [85]).

hydrate	$D_w(\text{MD})$ (m^2s^{-1})	$D_w(\text{exp})^a$ (m^2s^{-1})	$D_{Na}(\text{MD})$ (m^2s^{-1})	$D_{Na}(\text{exp})^b$ (m^2s^{-1})
one-layer	2.5×10^{-10}	2.5×10^{-10}	3.9×10^{-11}	1×10^{-12}
two-layer	1.4×10^{-9}	1×10^{-9}	5.1×10^{-10}	1×10^{-10}
three-layer	1.3×10^{-9}	1×10^{-9}	1.8×10^{-10}	2×10^{-10}
bulk water		1.5×10^{-9}		9×10^{-10}

2.10.2.1. POSSIBLE EXPLANATIONS OF THE SWELLING MECHANISMS

The semi-quantitative agreements between experimental observations and classical molecular dynamics simulations using the model developed by Skipper and co-workers allowed one to give possible explanations on the swelling mechanisms of water in smectite clays.

In particular, a series of grand isohear ensemble MC simulations were used to determine the free energy, enthalpy, and entropy of the swelling of Cs-, Na- and Sr-montmorillonites as a function of interlayer ion size and charge [166,167]. The interactions potentials were those of Skipper, but they used the SPC/E model for water. This model was reported to accurately reproduce the structural and dynamical properties of water, in particular its dielectric constant and diffusion coefficients, as well as describe the hydrogen bond dynamics in bulk water. Using the SPC/E model, we note though that the dipole moment of water is enhanced to 2.35 D as compared to experiments (1.85 D). Lennard-Jones (LJ) potential and partial charges on the atomic sites governed the intermolecular interactions. The disjoining pressure exhibited oscillations as a

function of layer spacing, indicating that swelling occurs in discrete steps (Fig. 2.33). The first minimum (“one-layer hydrates”) occurred for all the different ions in the range of 12.3 Å to 12.4 Å, whereas the position of the second minimum (“second-layer hydrate”) varied significantly with layer charge (14.8 Å to 15.4 Å). Disjoining pressures were found to be correlated with ion hydration numbers. This suggested that high swelling pressures results from hydrated ion “pillars” that push the clay layers apart. Similar behaviour was found upon variation of clay layer charge and interlayer ion hydration energy, suggesting that increasing the clay layer charge has a qualitatively similar effect to increasing the interlayer ion hydration energy. This suggested also that the ions may behave cooperatively such that increasing the number of ions in the interlayer has an effect similar to increasing the strength of individual ion-water interactions. Furthermore, decomposition of swelling free energies into enthalpic and entropic components indicated that energetic effects dominate the swelling process, with entropy playing an important yet smaller compensating role. Finally comparison of ion density profiles in two-layer hydrates of the three clays revealed an increasing tendency for formation of outer-sphere complexes as ion hydration energy increased.

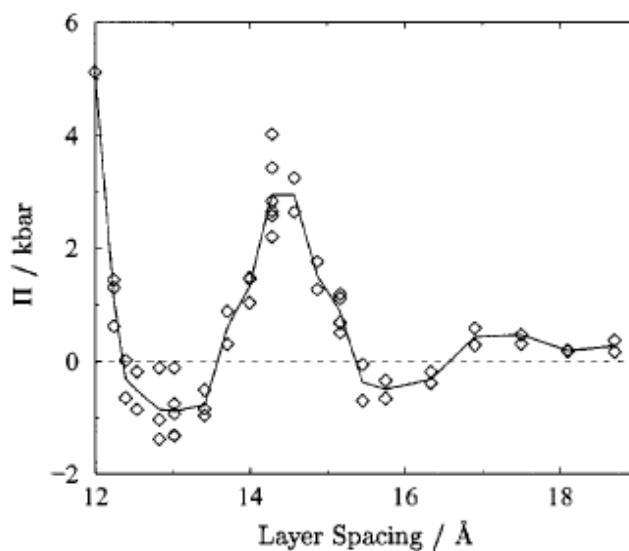


Fig. 2.33: Disjoining pressure for Na-montmorillonite. The solid line is the average of the individual pressure points (from [166]).

In another paper the method of Skipper *et al* and the TIP4P water model were used to reproduce the equilibrium sorption isotherm of water in a sodium-montmorillonite clay [168] and give a

detailed explanation on the swelling mechanisms. The stepwise nature of the clay swelling process is reproduced (Fig. 2.34) and the predicted stable states are reported to be in good agreement to experimentally observed ones with the computed interlayer water contents somewhat lower than experimental ones: dehydrates clay ($d \cong 10.0 - 10.4 \text{ \AA}$), a one-layer ($d \cong 12.0 - 12.5 \text{ \AA}$, $0.006-0.009 \text{ g}_{\text{water}}/\text{g}_{\text{clay}}$), two-layer ($d \cong 15 \text{ \AA}$, $0.16-0.19 \text{ g}_{\text{water}}/\text{g}_{\text{clay}}$), and three-layer hydrate ($d \cong 18-19 \text{ \AA}$, $0.2-0.25 \text{ g}_{\text{water}}/\text{g}_{\text{clay}}$). The computer simulations predict also the occurrence of hysteresis in layer spacing and clay water content. Information from the density profiles of the water molecules and the sodium counter ions, and the orientations of the water dipoles, as a function of relative humidity, have been used for a description of the clay swelling. In the starting configuration, the one-layer hydrate was clearly visible with sodium ions forming inner-sphere surface complexes (Fig. 2.35). In this regime, the $\text{H}_2\text{O}/\text{Na}^+$ ratio was between 3 and 4. The water molecules were positioned in the center of the interlayer. The water oxygen coordinated to a sodium counterion, while the water hydrogen atoms hydrogen-bond the clay surface oxygen atoms. With increasing water vapor pressure the clay swelled but the inner-sphere complexes were preserved, their distance to the clay mineral surface remaining almost constant. Concomitantly, this forced the water molecules to form two layers. The increase in layer spacing resulted in less confinement of the water molecules allowing them to orient themselves to the sodium counterions. This was derived from the change in the angle between the water dipole and the clay mineral surface normal vector. Such a result was interpreted as an increased orientation to the counterions and a decreased influence of hydrogen bonding to the clay mineral surface. It turned out that the water molecules close to one clay surface coordinated to sodium ions that were closest to the opposite one. The key phenomenon in the transition occurred at a layer spacing close to 13.50 \AA : part of the inner-sphere sodium ions moved to the central plane of the interlayer. The driving force for this counterion flux was the energy associated with full hydration of these counterions. These hydrated sodium ions are referred to as outer-sphere complexes. This hydration was thought to be facilitated by the increased interlayer volume and the increased number of intercalated water molecules. Notably, the sodium ions moved to the interlayer center for a ratio $\text{H}_2\text{O}/\text{Na}^+ \cong 6$. This ratio agrees well with the sodium coordination number of concentrated NaCl aqueous solutions [169]. A specific structural detail was that in the initial swelling stages the water molecules that have been positioned almost parallel to the clay sheets with their dipole vector were reoriented due to the increased counterion coordination. In this way,

they positioned themselves in a favorable orientation for full hydration in the central interlayer plane. It was suspected that this lowered the energy barrier for the transfer of sodium ions. A further expansion of the clay led to an increasing number of sodium ions in the center of the interlayer and concomitant adsorption of water molecules that hydrated these ions. Particularly, it was observed that in the regime 14.25-15.0 Å the water oxygen atoms overlapped with the sodium ions that were located close to the inner-sphere positions. The resulting constraint was relieved by a further expansion to a layer spacing of about 15.3 Å, allowing a further increase of the clay water content and the formation of inner-sphere surface complexes. In this final state, a large fraction of counterions were fully hydrated outer-sphere complexes in the central interlayer plane. These observations indicated that the swelling proceeded from a state of partially hydrated inner-sphere sodium ions ($\text{H}_2\text{O}/\text{Na}^+ \cong 3-4$) to a state characterized by fully hydrated outer-sphere sodium ions with a smaller fraction of inner-sphere sodium ions ($\text{H}_2\text{O}/\text{Na}^+ \cong 8-9$).

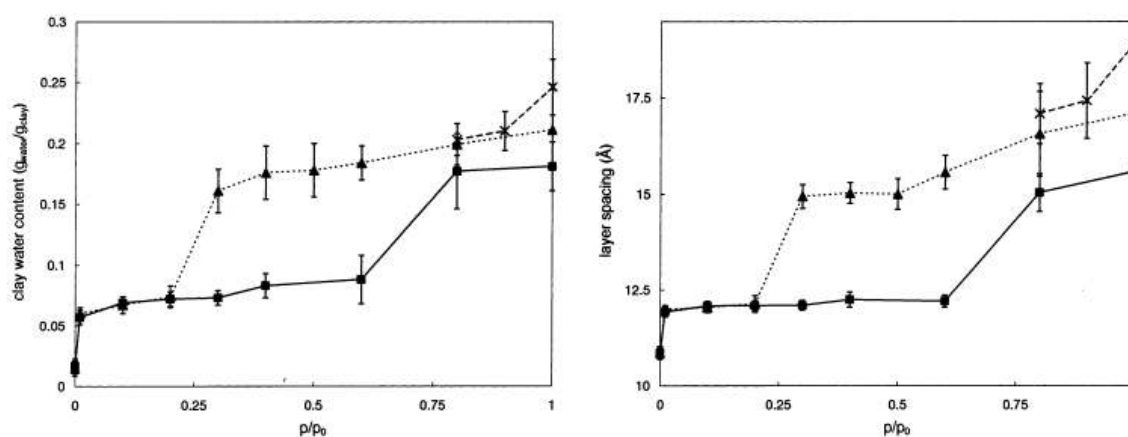


Fig. 2.34: Computed swelling curves for sodium montmorillonite: clay water content (left) and layer spacing (right) as a function of the water vapor pressure. The various branches relate to different starting configurations. Full lines: $d_0 = 12.5$ Å; dashed line: $d_0 = 15.0$ Å (from [168]).

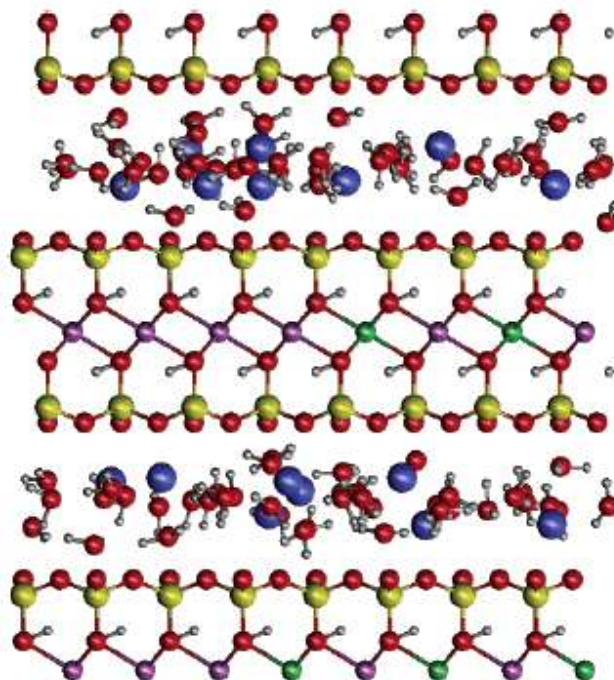


Fig. 2.35: Snapshot of the classical MD simulation for a one-layer hydrate at $p/p_0=0.3$ (from [168]).

2.10.2.1. POSSIBLE EXPLANATION OF THE SWELLING HYSTERESIS

Tambach *et al* [170] performed grand-canonical classical molecular simulations to study the molecular mechanism of clay swelling hysteresis as a function of the relative humidity. In particular, they focussed on the transition from the one- to the two-layer hydrate and the influence of three types of counterions (Li^+ , Na^+ , and K^+). The clay was an Arizona montmorillonite clay mineral with a unit-cell formula defined as $\text{M}_{1.0}[\text{Si}_{8.0}][\text{Al}_{3.0}\text{Mg}_{1.0}]\text{O}_{20}(\text{OH})_4$ where M represents a monovalent counterion. Two clay layers, each comprising eight unit cells, were used to build the model clay. The structure of the clay and the water molecules were rigid. For every fixed basal spacing and fixed chemical potential, the system was equilibrated for 50 ps and sampled for 250 ps. Results of the simulations showed that at certain relative humidities two local free-energy minima for the one- and two-layer hydrates are encountered. A free-energy barrier separates the one- and two-layer hydrate, and swelling or shrinking occurs if the system is able to cross this free-energy barrier. As a result, the system can be trapped in meta-stable state (Fig. 2.36). (If the system is trapped in the one-layer state, the relative humidity has to be increased until the free-energy barrier has (almost) disappeared, for the one-layer hydrate to swell to the two-layer hydrate). Experimentally, it is found that there is an increasing tendency for swelling with a decreasing cation size and increasing hydration energy [50,171,172]. This free-

energy barrier is attributed to the formation and breaking of hydrogen bonds between the one- and two-layer hydrates induced to the reorientation of the water molecules relative to the clay surface. A summary of the conclusions is illustrated in Fig. 2.37 giving a model of ideal interlayer structures. In the case of a one-layer hydrate, an increase of the relative humidity leads to an increase of water adsorption and therefore a small increase in basal spacing and a small rearrangement of the counterions and water molecules. This continues until a critical relative humidity is reached, depending upon the type of counterion. In the case of Arizona Na-montmorillonite the system swells and the counterions leave the clay surface. The final state is a two-layer hydrate. With the two-layer hydrate as starting point (Fig. 2.38), a decrease in the relative humidity induces desorption of water molecules from the interlayer space, followed by a relatively small decrease of basal spacing and small rearrangement of the counterions and water molecules. However, the reverse pathway requires that hydrogen bonds between the molecules in each water layer need to be broken and new bonds need to be formed between the two layers of water molecules, and therefore hysteresis occurs. However, we note that the water molecules at a water content corresponding to a “double-layer hydrate” do not form two well separated layers of water (Fig. 2.38). Especially, the domains where no counter ion is present clearly do not form a double water layer, so that the notion of water layers may be strongly dependent on the arrangement of the water molecules around the counter ions. Experiments and previous classical MD simulations showed the swelling to be significantly dependent upon the type of cation. Experiments showed also the extent of hysteresis to be dependent upon the type of cation. We would expect therefore the interaction between the water molecules and the counter ions to be involved in the energy barrier for the swelling hysteresis.

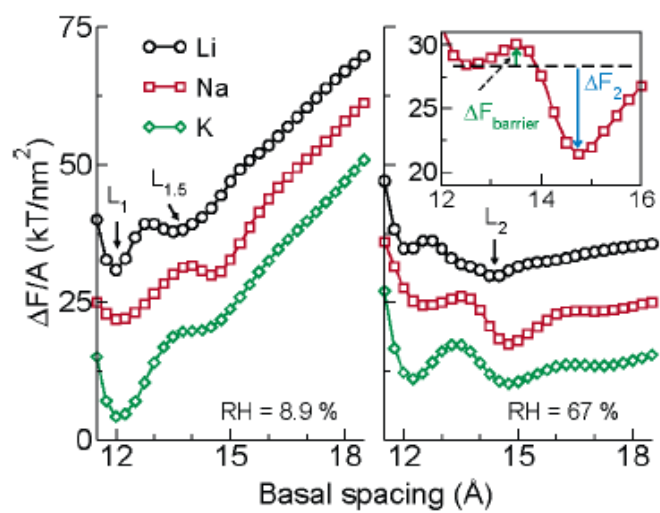


Fig. 2.36 : Simulated free-energy per clay platelet area ($\Delta F/A$) of an Arizona clay as a function of the basal spacing at low (left) and intermediate (right) relative humidity of 8.9 % and 67 % (from [173])

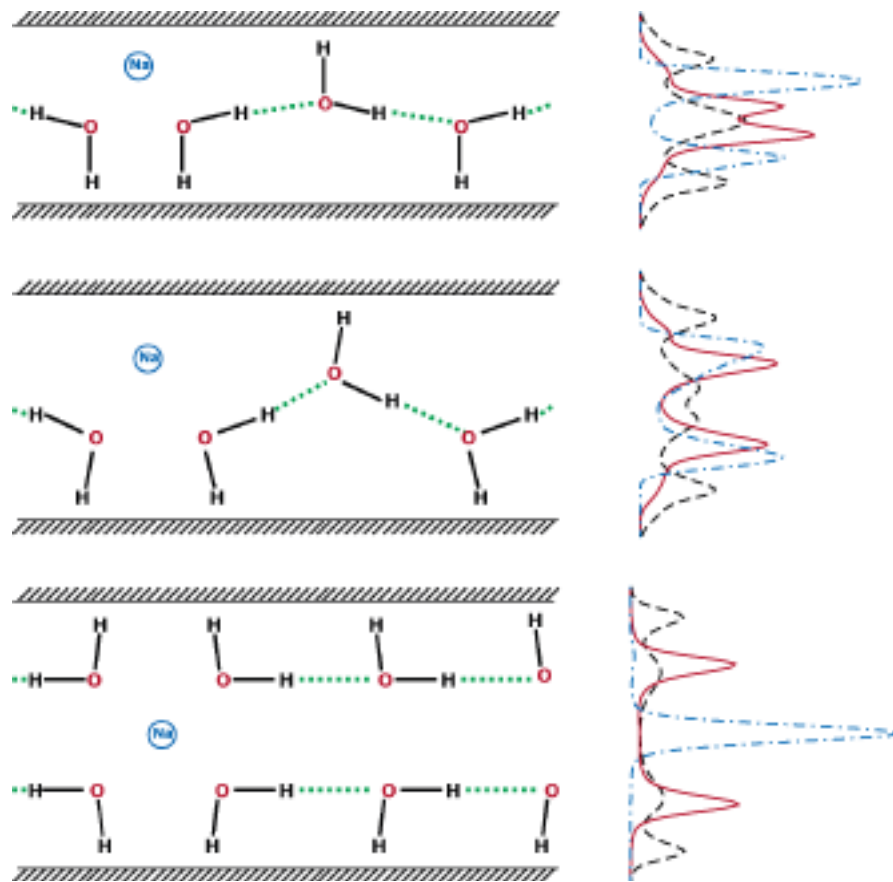


Fig. 2.37 : Illustration of the water orientation and arrangement of the counterion in the interlayer during swelling from a one- to a two-layer hydrate (from [173])

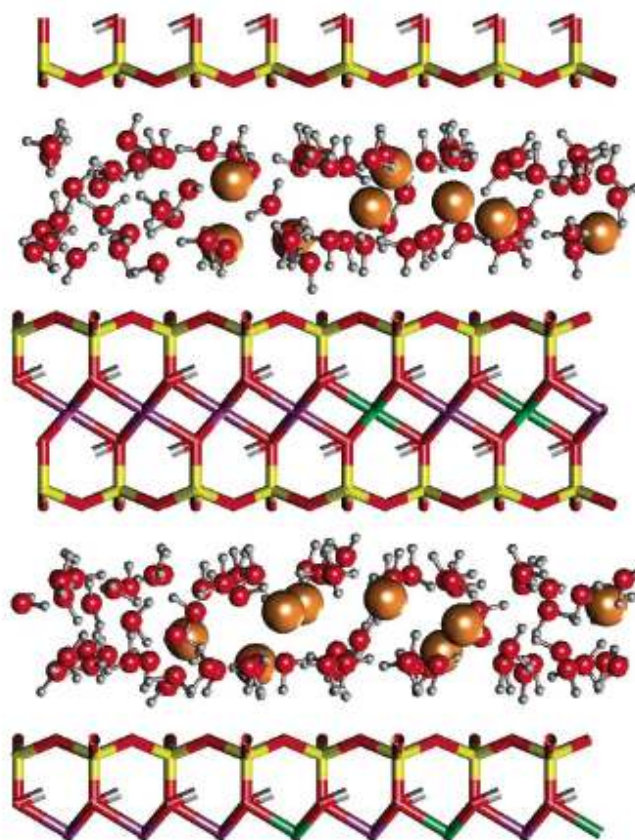


Fig. 2.38 : Snapshot of a two-layer hydrate of Arizona K-montmorillonite with a basal spacing of 14.75 Å at a relative humidity of 67 % (from [173])

2.10.2.1. THE CASE OF SAPONITE: MISLEADING NOTION OF WATER LAYERS?

The interaction of water with a synthetic saponite clay sample was investigated by Rinnert et al. [47] by following along water adsorption and desorption in the relative pressure range from 10^{-6} to 0.99 (i) the adsorbed amount by gravimetric and near-infrared techniques, (ii) the basal distance and arrangement of water molecules in the interlayer by X-ray and neutron diffraction under controlled water pressure, and (iii) the molecular structure and interaction of adsorbed water molecules by near-infrared (NIR) and Raman spectroscopy under controlled water pressure. The results thus obtained were confronted with Grand Canonical Monte Carlo (GC/MC) simulations, using a clay/water force field determined from semi-empirical periodic MINDO (Modified Intermediate Neglect of Differential Overlap) quantum calculations with block atomic wave functions coupled to perturbation theory for dispersion forces. The clay/water dispersion interaction was calculated in a self-consistent manner from the atomic polarizabilities estimated on the basis of the net atomic charges of the water molecules and the clay particle determined

from a Mulliken population analysis. The clay/sodium potentials were derived in the same manner by focusing on the leading contributions from the oxygen atoms of the clay network. The clay/water potential results from the sum of electrostatic, repulsive, and dispersive contributions. The atomic charge and geometry of the water molecules were those of the TIP4P water model. The simulation cell was composed from three clay lamellae, each containing 24 unit cells. The measured equilibrium sorption isotherms (Fig. 2.14a) was in semiquantitative agreement with the simulated one shown in Fig. 2.14b. Various well-distinct hydration ranges could be distinguished. In the case of saponite with tetrahedral substitution, where cation/water interactions are rather strong, swelling was initiated by cation/water interactions. However, the addition of at least three water molecules per cation was required to overcome the cation/layer interaction and displace the sodium cations toward the center of the interlayer region. The interlamellar spacing thus reached, around 12.3 Å, corresponded to what is classically referred to as a “one-layer hydrate,” whereas no water layer was present in the interlayer region. A filling of the interlayer at nearly constant spacing then occurred to reach a well-organized network of interlayer water molecules with significant interactions with the clay layer. The structure thus formed led to a complete extinction of the d_{001} line in D₂O neutron diffraction patterns, showing that the classically used notion of a one-layer state for clay minerals was misleading for describing such a system [47]. Upon further water adsorption, additional swelling was observed for $P/P_0 > 0.5$, and a network of liquidlike water molecules more structured than in bulk water was then present in the interlayer region, corresponding to the final swelling of the structure to reach d spacing values of 15.2 Å. The final hydration range at high relative pressure mainly corresponded to the filling of pores between clay particles.

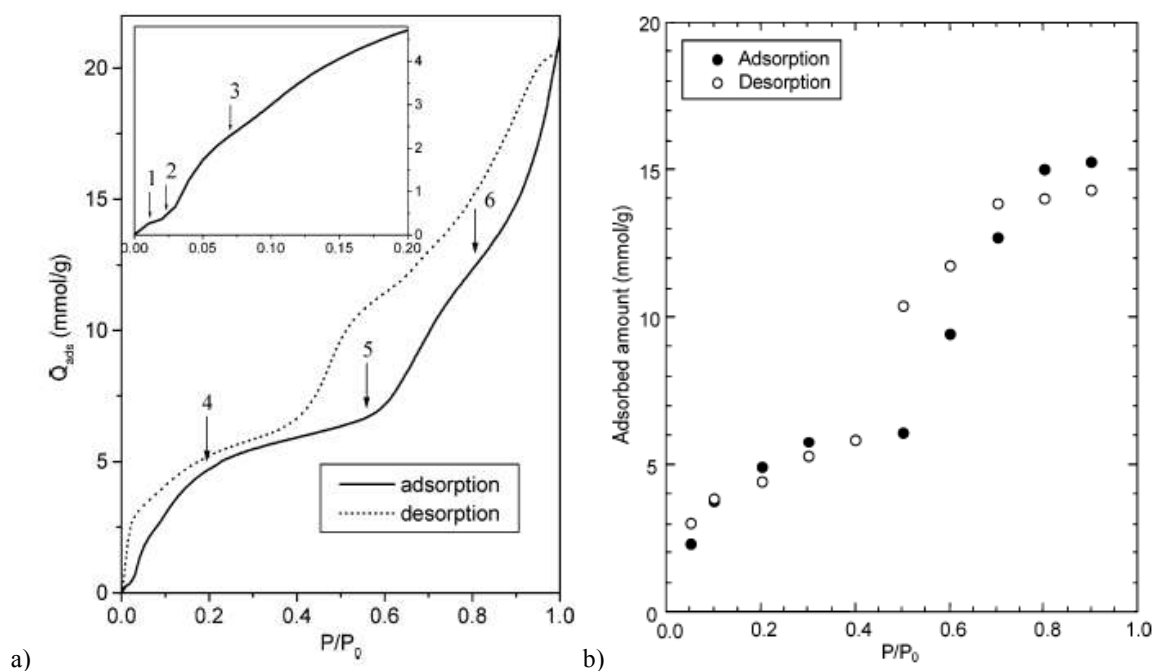


Fig. 2.39 : a) Measured adsorption-desorption isotherm obtained at 303 K on a synthetic saponite sample (from [47]).
 b) GC/MC simulations of the water adsorption-desorption isotherm of a synthetic saponite sample (from [47]).

2.10.3. Classical MD simulations with flexible clay structures

2.10.3.1. THE FORCE-FIELD MODEL DEVELOPED BY TEPPEN AND CO-WORKERS

The use of a rigid lattice can save substantial amounts of computer time. However, the exchange of energy and momentum among the interacting atoms of the clay substrate and the molecules of the interlayer or interfacial fluid is not possible. Thus, this approach introduces an a priori distortion into the atomistic description of the structural and dynamic behaviour of surface and interlayer species. Therefore, accurate representation of the dynamics of such processes as adsorption, surface hydration and complexation, and hydrogen bonding can be inherently limited if the atoms of the substrate layers are all considered as immobile. In particular, the surface diffusion of ions and water molecules can be overestimated and the structure of the aqueous layers at the interface can be distorted. Additionally, atomic charges in the rigid clay lattice are typically assigned values equivalent to their full formal charge, thus generating unreasonably large electrostatic potentials.

Teppen *et al.* [153] were successful in developing a new force field for clay phases that was based on a rigorous analysis of experimental X-ray diffraction data and charge assignment from MP2 quantum mechanics calculations of several small aluminosilicate molecules. The developed set of bonded interaction terms was successfully used to simulate several simple clay structures including gibbsite, kaolinite, and pyrophyllite, with the exception of hydroxyl orientation on kaolinite. However, bonds must be identified and evaluated for each metal-oxygen coordination, and the transferability of the force field remains a very important issue in practical implementation.

2.10.3.1. THE FORCE-FIELD MODEL OF DEVELOPED BY CYGAN AND CO-WORKERS

Cygan *et al.* [154] proposed an alternative approach to the development of a general force field for molecular simulations of hydrated crystalline compounds and their interfaces with fluid phases. The so-called CLAYFF was based on an ionic (nonbonded) description of the metal-oxygen interactions associated with hydrated phases. All atoms were allowed complete translational freedom within this force field framework. Metal-oxygen interactions were based on a simple Lennard-Jones (12-6) potential combined with electrostatics. The empirical parameters were optimized on the basis of known mineral structures, and partial atomic charges are derived from periodic DFT quantum calculations of simple oxide, hydroxide, and oxyhydroxide model compounds. The flexible SPC water model was used to describe the water and hydroxyl behaviour. Harmonic terms were included to describe the bond stretch and bond angle bend terms associated with water molecules, hydroxyls, and dissolved polyatomic molecules and ions. The structure of kaolinite and pyrophyllite could be successfully simulated using this force field. CLAYFF was also tested on the hydration of a sodium montmorillonite with octahedral and tetrahedral substitutions. The results of the simulations in the form of the swelling curve were in very good agreement with experiment (Fig. 2.40). The model results were in general agreement with previous theoretical swelling curves for smectite clays derived using rigid water and clay structures. The incorporation of a fully flexible force field was manifested in slightly more confined interlayer region. Series of “deswelling” simulations provided identical montmorillonite structures and basal spacings. This lack of hydration-dehydration hysteresis supported the attainment of fully equilibrated montmorillonite structures with the simulations.

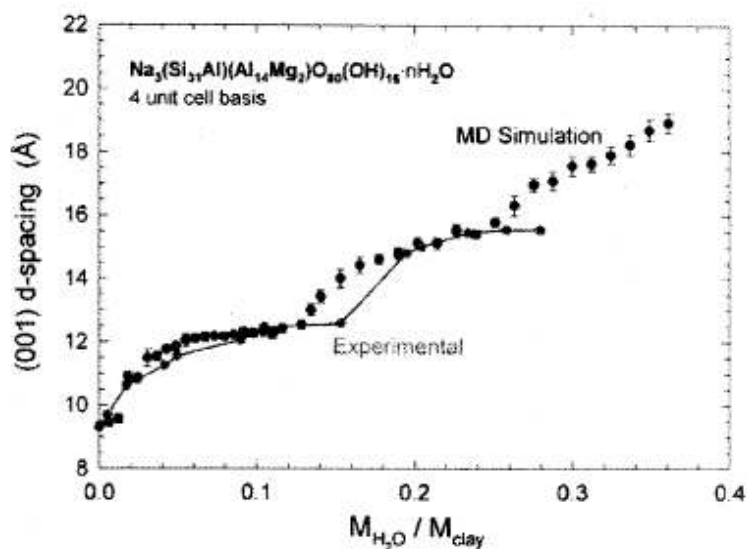


Fig. 2.40 : Measured adsorption-desorption isotherm obtained at 303 K on a synthetic saponite sample (from [154]).

2.10.4. Quantum calculations

2.10.4.1. HYDRATION OF A SMECTITES

Chatterjee *et al* [174,175] performed both localized and periodic calculations on a series of monovalent (Li, Na, K, Rb, Cs) and divalent (Mg, Ca, Sr, Ba) cations to monitor their effect on the swelling of montmorillonite and beidellite type of clays for one-, two-, and three-layer hydrates. The desired structures of montmorillonite and beidellite have been generated from the structure of pyrophyllite. The calculations have been carried out with periodic DFT using a gradient corrected functional BLYP, and DNP basis set. Becke-Perdew parametrization of the exchange-correlation functional was employed. The calculations were restricted to one special K point in the Brillouin zone, placed at (0,0,0). Kinetic cut-off energies between 600 and 1500 eV have been used. Hydrated phase calculations were performed with the minimum energy structures of the clays at the unhydrated phase. The interlayer structure was held fixed and the interlayer spacing was increased to accommodate the water molecule. For the hydrated phases, the cation and water in the interlayer space were relaxed but the lower part of the structure was kept fixed. Single-point calculations of the cation and anion of each molecule at the optimized geometry of the neutral molecule were also carried out to evaluate Fukui functions, global and local softness. The gross atomic charges were evaluated by using the technique of electrostatic potential (ESP) driven charges. At low hydration the water molecules were found to squeeze

themselves in a flat orientation. With an increase in water content the water molecules formed stretched H-bonds with the clay surface. The solvation energy at the first hydration shell of an exchangeable cation was computed, but the results did not correspond to the experimental d-spacing values. A novel quantitative scale was proposed with the numbers generated by the relative nucleophilicity of the active cation sites in their hydrated state through Fukui functions within the helm of the hard soft acid base principle, showing a match with the experimental trend in terms of d-spacing.

Boek and Sprik [176] performed *ab initio* molecular dynamic simulations (AIMD) to study the hydration of a sodium smectite clay with tetrahedral substitution. The simulation box contained 2 unit cells with one sodium counter ion. For the substitution site, a Si in the tetrahedral layer was replaced by Al. The finite size effects were checked by performing a MC force field simulation for the same model size. It appeared that the MC simulation yield approximately the same results for both the 8- and 2-unit-cell models. Electronic structures were computed using a plane wave pseudopotential implementation of Kohn-Sham DFT. The calculations were based on the BLYP energy functional. This functional was found to reproduce with sufficient accuracy the structure of the local environment and the self-diffusion coefficient of water. The Al and Na cations were modelled by regular semilocal norm-conserving pseudopotentials. The orbitals were expanded in plane waves up to an energy cutoff of 70 Ry in combination with medium-soft norm-conserving pseudopotentials according to the Trouiller-Martins (TM) scheme. The equations of motion for ions and orbitals were integrated using a fictitious electron mass of 1000 au and a time step of 7 au. The temperature was maintained at an average of 300 K. All calculations were carried out using the CPMD package. The wave function and geometry were optimized for the MD simulation. After equilibration, the MD run was continued for a period of 1 ps. This was just long enough to observe the reorientational motion distinguishing liquid water from ice. The sodium ion was found to be more strongly bound to the silicon-aluminum ring than the silicon ring by 14 kJ/mol, suggesting that charge localization on oxygens in the silicon-aluminium ring has relatively minor effect. The competing position above the Al tetrahedron was higher in energy by 43 kJ/mol. The AIMD and MC force field simulations gave very similar water structures (Fig. 2.41 and Table 2.15) and similar density profiles of the clay species perpendicular to the clay surface that showed a double peak distribution for the water oxygens (16), indicating the formation of a double layer hydrate. The simulation was begun with the cation in the midplane and remained at

this position during the simulation time (1 ps). The time may have been too short for the cation to form an inner-sphere complex, expected for tetrahedral substituted smectite clays. It was inferred from the nearest-neighbor coordination that the number of hydrogen bonds formed between water and clay is much smaller than the number between the water molecules themselves, showing the strong preference for intersolvent hydrogen bonding with only weak and short-lived hydrogen bonds to the silicate surface. Also, no water adsorbed in the hexagonal cavity sites, as reported experimentally for vermiculite, was observed.

In a later paper [177] they performed constrained dynamic simulations to study the adsorption of the sodium counter ion on the montmorillonite clay surface choosing the distance perpendicular to the clay surface as the reaction coordinate. The simulation showed that the Na^+ of the inner-sphere complex resides at a distance of 6.1 Å from the center of mass of the aluminium atoms, as opposed to 5.1 Å for previous classical simulations. In this case, the Na^+ is coordinated to four water molecules and one basal oxygen atom. The inner-sphere complex is separated to the outer-sphere complex, residing at a distance of 7.5 Å of the center of mass of the aluminium atoms (in the midplane), by an energy barrier of 1.2 kT. In the case of the outer-sphere complex, the Na^+ is coordinated to five water molecules. Only slightly less stabilization was found for adsorption onto Si_6 ring than adsorption onto the Si_5Al ring, though adsorption onto the clay surface without aluminium substitution was found to be unfavorable. It is shown also that the number of hydrogen bonds between water molecules is favoured compared with the hydrogen bonds between the water molecules and the basal oxygen atoms, and that it is increased when going from the outer-sphere complex to the inner-sphere complex.

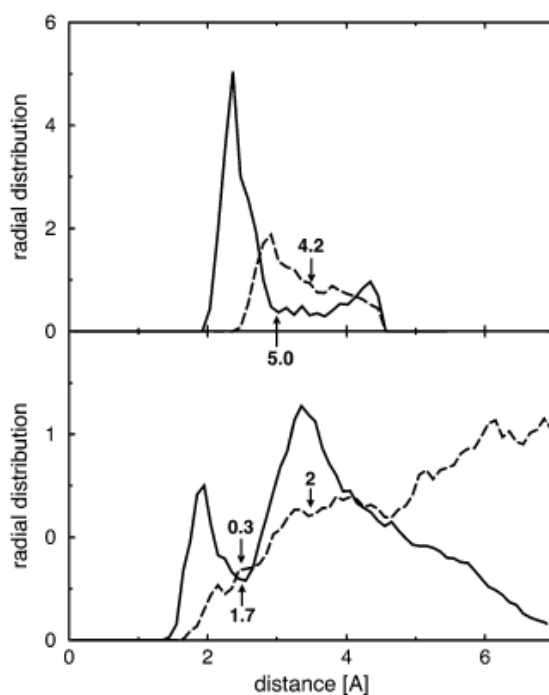


Fig. 2.41 : Radial distribution functions for water oxygen (O_w), water hydrogen (H_w), clay oxygen (O_c), and Na. Top graph: O_w - O_w .RDF (- -), Na- O_w RDF (-). Bottom graph: O_w - H_w RDF (-), O_c - H_w RDF(- -). The normalization of the RDF is relative to the value of the O_w - O_w RDF at $r=3.5$ Å (from [176]).

Table 2.15: Position of the first peak in RDF and coordination number of the first shell (and second shell for O_c - H_w) compared for the ab initio MD (AIMD) and classical MC results (from [176]).

	first peak in $g(r)$ (Å)		coordination no.			
	AIMD	MC	AIMD		MC	
Na- O_w	2.37	2.30	5.0		5	
O_w - O_w	2.92	2.80	4.2		4.4	
O_w - H_w	1.9	1.80	1.7		1.6	
O_c - H_w	2.14	1.90	0.3	2	0.3	2.7

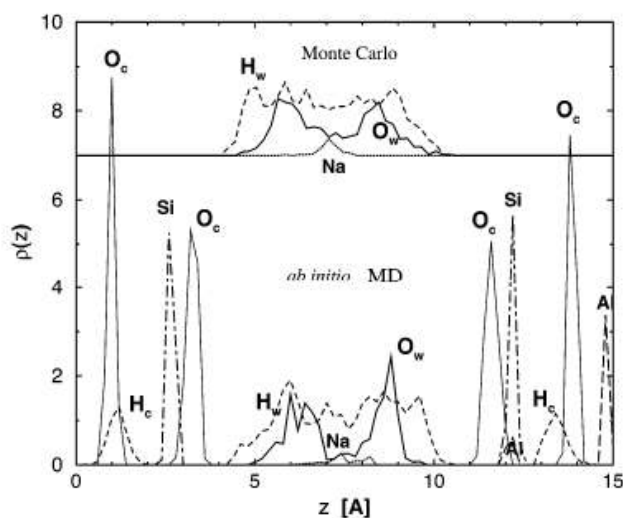


Fig. 2.42 : Density profiles for the clay species (Si, Al, water oxygen (O_w), water hydrogen (H_w), clay oxygen (O_c), and Na). Top: results from MC force field simulation. Bottom: ab initio calculations (from [176]).

2.10.4.1. SORPTION OF ORGANIC MOLECULES ON A CA-SMECTITE

Tunega *et al* [178] investigated the sorption of anionic form of the pesticide 2,4-dichlorophenoxyacetic acid on the dry and hydrated surface of a Ca-montmorillonite using short-time ab initio molecular dynamics (MD) simulation at room temperature. One Mg atom replaced one octahedral aluminium in the first type and one Al atom replaced one tetrahedral silicon in the second type. The supercell comprised 2 unit cells and one calcium counter ion. The ab initio DFT MD calculations were performed using the VASP package. The local density approximation (LDA) and the generalized gradient approximation (GGA) were used for the exchanged-correlation functional. The calculations were performed in a plane-wave basis set. The Brillouin-zone sampling was restricted to the Γ point. A plane-wave cut-off energy of 400 eV was used. The optimization of atomic positions was performed with a stopping criterion of 10^{-5} eV for the total energy. MD simulations were performed using a canonical ensemble with a Nosé thermostat procedure, maintaining a temperature of 300 K. The simulation times were 15-20 ps. The first 5-10 ps were reserved for the equilibration of initial configurations. The most stable of the calcium cations was found to be above the ditrigonal cavity. Without the presence of water, the pesticide was found to form stable bidentate outer surface complexes with the calcium cation. In the presence of the water molecules, water was found to form hydrogen bonds between each other, with the basal oxygen atoms, and with the pesticide. The MD simulation showed that the formation of those hydrogen bonds is a dynamic process during which bonds are created and/or

broken. In the presence of water the formation of monodentate complexes are preferred. The MD simulation did not support the formation of cation bridge in the adsorption mechanism.

Teppen *et al* [179] performed *ab initio* calculations of the initial stage in the situ polymerization of methanal and ethylenediamine within the interlayer of sodium montmorillonite, used experimentally for clay nanocomposites. Calculations on plane-wave density functional theory were performed with the CASTEP code. Ultrasoft pseudopotentials were employed. The energy cutoff for the plane wave expansion was 340 eV and just one k-point was allowed in the Brillouin zone, situated at (0.25,0,0). The form of the exchanged-correlation functional used adhered to the generalized gradient approximation (GGA). The optimized pyrophyllite unit cell was used as a template for the fabrication of the montmorillonites with different substitutions. Periodic models of montmorillonite that exhibited a lattice-edge were developed from the pyrophyllite and montmorillonite models. This was achieved by breaking all bonds that crossed the periodic plane created by the b and c lattice vectors. Oxygen atoms were then terminated with a hydrogen atom and non-oxygen atoms with a hydroxyl group, except for the exposed aluminium atom in the octahedral layer. No evidence was found for the dissociation of water in the hydration sphere of the sodium counterions. The optimized models showed that catalysis occurred at the clay mineral lattice-edge where hydroxyl groups and exposed Al³⁺ ions act as strong Brønsted and Lewis acid sites, respectively.

2.11. MALODOURS IN CAT URINE

Table 2.16 shows the possible organic compounds assigned in the mass spectra of cat [3,180,181,182] and bobcat urines [183]. The sensorial descriptions show that some of those compounds are potentially malodorous: hydrogen sulfide (putrid), methyl mercaptan (putrid), dimethyl disulfide (cabbage, cauliflower), dimethyl trisulfide (cabbage, cauliflower), 1-hexanol-2-ethyl (fermented), p-cresol (fecal) and indole (fecal). However, no sniffing experiments have been performed to determine the characteristic malodorous compounds in cat urine.

Table 2.16: Possible organic compounds found in cat urine. Retention index are given for a chromatographic polar column.

organic compounds	reference	retention index	sensorial
hydrogen sulfide	[3]	530	cooked egg, putrid
methylmercaptan	[3]	665	putrid, roasted, rotten, sulfurous, typical mercaptan
carbon disulfide	[3]	745	-
tetrahydro furan	[182]	860	-
dimethyldisulfide	[3]	1077	cabbage, cauliflower, onion, sulphury
pyrazine	[183]	1202	dusty, earthy, floral, narcotic, nuty, sweet
3-methyl-3-buten-1-ol	[183,180]	1255	-
methyl pyrazine	[183]	1255	meaty, musty, nutty, popcorn
benzene, 1-ethyl-2-methyl-	[182]	1257	-
3-hydroxy-2-butanone	[180]	1272	buttery, creamy, fatty, sour, vanilla
cyclohexanone	[182]	1301	ethereal, fresh, fruity, sweet
2-methyl-2-buten-1-ol	[180]	1311	ethereal, fresh, fruity, grape
2,5-dimethyl pyrazine	[180]	1316	nutty, raw potato, rusty
2,6-dimethylpyrazine	[183]	1324	cocoa, nutty
benzene, 1,2,3-trimethyl-	[182]	1338	gasoline, herbaceous, spicy
dimethyltrisulfide	[180]	1392	alliaceous, cabbage, cauliflower, cooked cabbage, cooling, garlic, mettalic, onion, sulphuric
trimethylpyrazine	[183]	1396	caramel, coca, coffe, earthy, roasted, roasty
1-hexanol-2-ethyl	[182]	1480	ethereal, fermented, rose, yeasty
dimethylsulfoxide	[180]	1556	-
3-mercapto-3-methyl-1-butanol	[183]	1631	meaty, soupy, spicy, sweet
dimethylsulfone	[183]	1889	-
1-dodecanol	[182]	1956	aldehydic coconut, earthy, fatty, honey, soapy, waxy
phenol	[183] [180]	1981	antiseptic, hyacinth, medicinal, phenolic
p-cresol	[180]	2066	cresylic, drain, fecal, medicinal, pigsty, stale
thymol	[180]	2172	aromatic, herbaceous, medicinal, spicy, terpenic, thyme
2-piperidinone	[183] [180]	2192	-
indole	[183]	2450	animal, cheese, faeces, mothballs, musk
hexadecanoic Acid	[180]	2889	oily
1-methylhydantoin	[183]	-	-
3-methylthio-3-methyl-butanol	[181]	-	-
4-mercapro-4-methyl-2-pentanone	[181]	-	-
4-methoxy-2-methyl-2-mercapto-butane	[181]	-	-
6-aza-5,7,12,14-tetrathiapentacene	[182]	-	-

CHAPTER 2 Literature Review

benzaldehyde, 2-hydroxy-6-methyl-	[182]	-	-
benzenemethanol, alpha, alpha-d	[182]	-	-
butanamide, 2,2,3,3,4,4,4-heptaflu	[182]	-	-
butanoic acid hexyl ester	[183]	-	-
carbonyl sulfide	[3]	-	-
cyclohexane, isothiocyanato-	[182]	-	-
hexanedioic acid, bis methylen	[182]	-	-
phenylacetamide	[183]	-	-

CHAPTER 3 THEORY

3.1. DIFFERENT TYPES OF PHYSICAL MODELING

Generally, simulation includes all methods that can reproduce the processes of a system in an analog or digital fashion. In numerical physical simulations, the evolution of the system obeys the physical laws that are expected to govern the real physical processes. They therefore focus on the physical content of the simulation and the results are intended to provide knowledge of background processes and promote physical understanding of the simulation region. Numerical simulations play an important role in the study of a broad range of physical and chemical phenomena, and provide a complement to experimental observations and analytical theoretical approaches. They give access to microscopic quantities that are not necessarily obtainable experimentally and are often a useful source of parameters for analytical or semi-analytical models. They may also better reflect the complexity of the real system used in an experiment than purely theoretical models. Moreover, numerical simulations may help to rationalize the observed experimental trends by understanding the effects of different parameters that may be difficult to study separately, or confirm the results of theoretical and experimental studies by using different description levels. They may be also predictive for conditions inaccessible to theoretical models or experiments (for example extreme pressure and temperature conditions, very short or very long time scales, etc.). The simulation methods used in the field of physical-chemistry are applied to problems ranging from the interaction between light and atomic structures at a sub-femto-second scale to the understanding of kinetic or hydrodynamic phenomena at time scales of up to several years.

Molecular simulation may be defined as the numerical study of physical and chemical behaviour in a system of discrete particles, with spatial scales ranging from the atomic to the macromolecular scale and time scales below the microsecond unit. Depending on the size of the system to be studied, the type of information sought, the required accuracy and the available calculation power, there exist different ways to describe the interactions between the particles of

the system. The quantum description of a system of atoms including electrons is based on the Schrodinger equation. An analytical solution of this equation exists only for a very limited number of cases and its numerical solution is rendered difficult by the large number of dimensions of typical systems. Three different so called *ab initio* or first-principle numerical methods are used: quantum Monte-Carlo (QMC) methods, quantum chemistry methods, and calculations based on density functional theory (DFT). The third method has been used in this thesis and will be described in more detail in section 3.3.

In the classical framework, the use of analytical interaction potentials, known as force-fields, allows one to evaluate the energy of the system and the forces at a much lower computational cost than quantum methods, therefore allowing one to study larger systems (around 10'000 atoms per cpu unit), or longer times (μ s). However, this provides a less detailed description of the system and may not be appropriate where the electronic structure of the system varies significantly (for example in chemical reactions). Moreover, the analytical potential contains parameters that must be adjusted according to quantum calculations or experimental results. The choice of the parameters generally results in a compromise between an accurate description of a system and its transferability, or ability to describe significantly different environments. The model chosen for the molecules (rigid, flexible, level of description of the molecule) and the form of the analytical interaction potential (coulomb interactions, dispersion interactions, dipolar interactions, polarisation) depend strongly on the nature of the system and the desired information. The level of description of the molecule may vary depending on whether one chooses an "all atomic" simulation, for which each atom is considered as a centre of force, a simulation for which each functional group is considered as a centre of force, or a mesoscopic simulation for which there is one centre of force per molecule or colloidal particle.

Finite element methods are used to find solutions to partial differential equations (PDE). They are generally applied to macroscopic physical laws that contain continuous variables (for example the Navier-Stokes equations, the diffusion equation, etc..). Because of the lower computational cost, due to the reduced number of dimensions, they provide results for larger space and time scales. However, they require materials input parameters (for example diffusion coefficients, partition coefficients, reaction rates, viscosity, etc..) that must be measured or calculated beforehand and do not provide a molecular description of the system. The results are also

dependent upon the choice of the physical macroscopic laws that are expected to govern the real processes. Finite element methods will be described in more details in section 3.2.

There exist also simulations combining the different level of descriptions, for which parts of the systems are treated in detail, whereas the surrounding environment is treated in a more global manner.

3.2. FINITE ELEMENT METHOD

3.2.1. Overview

The finite element method (FEM) is a numerical technique for solving boundary value problems which are described by partial differential equations. A domain of interest is represented as an assembly of subdomains (finite elements) and a continuous physical problem is transformed into a discretized finite element problem. The basic idea of finite elements is to use the exact operators of the differential equations, but to approximate the field variables by expanding them using basis functions over finite elements. To summarize in general terms how the finite element method works, the main steps of the finite element solution procedure are listed below.

- Choice of the partial differential equations (PDEs): The first step is to write down the differential equations that describe the problem.
- Discretization of the continuum: The second step is to divide the region of interest into finite elements and to interpolate the field variables over the elements using basis functions.
- The weak form: The partial differential equations are converted into a discretized system of equations using the Galerkin method.
- Choice of the boundary conditions: The boundary conditions are added to the discretized system of equations forming a discretized global system of equations.
- Solving of the global system of equations.

3.2.2. Choice of the PDE's

The behaviour of a fluid is modeled by the time-dependent Navier-Stokes equations, which have the form:

$$\rho \partial_t u - \eta \nabla^2 u + \rho(u \cdot \nabla)u + \nabla p = f \quad (3.60)$$

$$\nabla \cdot u = 0 \quad (3.61)$$

where ρ is the fluid density, u the fluid velocity, p the fluid pressure, η the fluid viscosity, and f an additional external force, e.g. gravitation or surface tension. The first equation is known as the momentum equation. This is a vector equation with the same dimensions n as the spatial dimension of the region under consideration, e.g. 2 in a coordinate system with cylindrical symmetry. The second equation is known as the continuity equation for an incompressible fluid. The field variables u and p that solve these equations represent the strong (or classical) solution and Eq. 3.60 and 3.61 are known as the strong form of the Navier-Stokes equations.

3.2.3. Discretization of the continuum

If the strong solution cannot be determined, the key to solving the problem is to discretize it. Nodes are used to break up the region under consideration into small finite elements such as shown in Fig. 3.43. As finite elements one may use triangles, squares or curvilinear polygons (or polyhedra for higher spatial dimensions). The field variables u and p are replaced by the following approximation:

$$u(x^{(1)}, \dots, x^{(n)}) \approx u^h(x^{(1)}, \dots, x^{(n)}) = \sum_i^{N_u} \begin{pmatrix} u_i^{(1)} \\ \dots \\ u_i^{(n)} \end{pmatrix} \psi_i(x^{(1)}, \dots, x^{(n)}) \quad (3.62)$$

$$p(x^{(1)}, \dots, x^{(n)}) \approx p^h(x^{(1)}, \dots, x^{(n)}) = \sum_i^{N_p} p_i \phi_i(x^{(1)}, \dots, x^{(n)}) \quad (3.63)$$

where $u_j^{(k)}$ is the k^{th} component unknown values corresponding to node i , N_u and N_p are the number of nodes in the triangulated region, ψ_i and ϕ_i are the basis functions that model the behaviour of the field variables at any point within the finite elements, $x^{(k)}$ is the k^{th} component of the spatial variable, and n is the spatial dimension of the region under consideration.

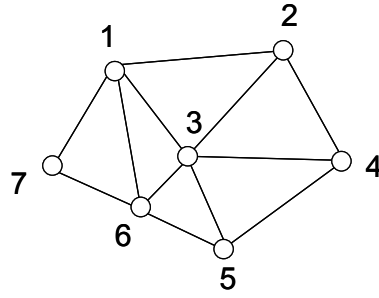


Fig. 3.43 : Example of a triangulated region with 7 nodes. Each node i is associated with n nodal values $u_i^{(k)}$ for the fluid velocity and 1 nodal value p_i for the pressure, where n is the spatial dimension of the region, i.e. 2 in this example.

For example, if the problem to be solved has cylindrical symmetry, the approximated field variables are given by:

$$u(r, z) \approx u^h(r, z) = \sum_i^{N_u} \begin{pmatrix} u_i^{(1)} \\ u_i^{(2)} \end{pmatrix} \psi_i(r, z) \quad (3.64)$$

$$p(r, z) \approx p^h(r, z) = \sum_i^{N_p} p_i \phi_i(r, z) \quad (3.65)$$

The basis functions ψ_i and ϕ_i take the value of one at the node i , and zero at all other nodes. They can be any kind of interpolation function. However, polynomial functions are generally used because of their ease of derivatization and integration.

3.2.4. The weak form

After substituting the interpolated field variable into the Navier-Stokes equations, the differential equation takes the following approximate form:

$$\rho \partial_t u^h - \eta \nabla^2 u^h + \rho (u^h \cdot \nabla) u^h + \nabla p^h - f = R_1 \quad (3.66)$$

$$\nabla \cdot u^h = R_2 \quad (3.67)$$

where R_1 and R_2 are nonzero residuals because of the approximate representation of the field variables. The Galerkin method provides residual minimization by multiplying the terms of the above equations by so-called test functions, integrating over the finite element and equating to

zero. When the test functions are also the basis functions used to represent the solutions u and p , the method is called the Petrov-Galerkin method, and the following weak form of the Navier-Stokes equations is obtained:

$$\int_{\Omega} (\rho \partial_i u^h - \mu \Delta u^h + \rho (u^h \cdot \nabla) u^h + \nabla p^h) \psi_i d\Omega = \int_{\Omega} f \psi_i d\Omega \quad (3.68)$$

$$\int_{\Omega} (\nabla \cdot u^h) \phi_i d\Omega = 0 \quad (3.69)$$

u^h and p^h that satisfy the integrated equations for all test functions ψ_i and ϕ_i in a reasonably large space, such as the space of all polynomials, are necessarily close to the strong solution. On the other hand, with this integral form of the equations, the solution functions have much more freedom to misbehave; there may be points at which the functions are undefined, or tend to infinity, and the derivatives may not exist. Therefore, in order to reduce the freedom to misbehave, the order of derivativization of the solution function u^h is reduced by applying integration by parts to the Laplacian operator in the weak momentum Eq. (3.68). The weak form of the Navier-Stokes equations then become

$$\int_{\Omega} \mu \nabla u^h \nabla \psi_i + (\rho \partial_i u^h + \rho (u^h \cdot \nabla) u^h + \nabla p^h) \psi_i d\Omega - \int_{\partial\Omega} \frac{\partial u}{\partial n} \psi_i ds = \int_{\Omega} f \psi_i d\Omega \quad (3.70)$$

$$\int_{\Omega} (\nabla \cdot u^h) \phi_i d\Omega = 0 \quad (3.71)$$

The test function is associated with the node i . If the node i is not on the boundary, the function is zero and the boundary term in the momentum equation disappears. The pair of functions u^h and p^h that satisfy the weak Navier-Stokes equations for all test functions ψ_i and ϕ_i from a given set, are called the weak solutions of the Navier-Stokes equations.

The test functions for the momentum equations are the set of velocity basis functions ψ_i and the test functions for the continuity equation are the set of pressure basis functions ϕ_i . The solutions of Eq. (3.70) and (3.71) contain $nN_u + N_p$ unknown coefficients, where n is the spatial dimension of the momentum equation: The weak Navier-Stokes equations are formed by multiplying the (vector) momentum equation by each of the N_u velocity basis functions ψ_i , and the continuity

equation by each of the N_p basis functions ϕ_i , and the number of unknown coefficients matches the number of equations.

3.2.5. The boundary conditions

The boundary conditions, i.e. the values that the solution must attain at certain points on the boundary of the region, may be specified. For the fluid velocity, the “no-slip” condition implies that the flow is exactly zero along the boundary. The “slip” condition only implies the velocity component normal to the wall to be zero. Another condition on the fluid velocity is the inflow boundary condition, which defines the value of both components of the velocity vector along the interfacial boundary. For the pressure, it is common to specify a single value at one point.

In order to maintain the size of the weak Navier-Stokes system of equations, the equations associated with the nodal values for which boundary conditions are specified are replaced by the information provided by the boundary condition. By writing the weak Navier-Stokes equations outside the specified boundaries as $F(u,p) = f$ and the boundary conditions as $G(u,p) = g$, the whole system of equations may be written in the following form:

$$X \equiv \begin{pmatrix} u^{(1)} \\ \dots \\ u^{(n)} \\ p \end{pmatrix} \quad (3.72)$$

$$H(X) \equiv \begin{pmatrix} F(u^{(1)}, \dots, u^{(n)}, p) - f \\ G(u^{(1)}, \dots, u^{(n)}, p) - g \end{pmatrix} = 0 \quad (3.73)$$

3.2.6. Solving the nonlinear system of equations

Without the non-linear term in the weak momentum equation, the Stokes equations would form a linear system of equations that could be solved in a relatively straightforward manner using the matrix formalism. In the case of the Navier-Stokes equations, Newton’s method for solving a system of nonlinear equations of the form $H(X)=0$ can be used. In this method the function $H(X)$ is approximated by a Taylor expansion about X_0 up to the linear term:

$$H(X) \approx H(X_0) + H'(X_0)(X - X_0) \quad (3.74)$$

$$X \approx X_0 - (H'(X_0))^{-1} H(X_0) \quad (3.75)$$

Where H' is the derivative of H . The Newton iteration consists of repeatedly evaluating the right hand side of equation (3.76) and using the results as the new estimate of the root.

$$X^{k+1} \approx X^k - (H'(X^k))^{-1} H(X^k) \quad (3.76)$$

3.3. AB INITIO CALCULATIONS

3.3.1. Overview

This section provides a short theoretical introduction on the *ab initio* calculations used in this thesis. In the Born-oppenheimer approximation, the motion of the electrons is first separated from that of the nuclei treated in a classical manner (section 3.3.2), so that the quantum problem simplifies by considering only the structures of electrons in the atomistic system. In Density Functional Theory (DFT), initially proposed by Hohenberg and Kohn, all ground state properties of the system are determined by the electron density that is therefore the central variable (section 3.3.3), as opposed to the many-body electronic wavefunction in quantum chemistry methods. In particular, the total energy E of a system including the kinetic energy of the electrons, the electron-electron interactions in the presence of static external potential $v(r)$ (for example, the atomic nuclei) is a unique functional of the electron density. One commonly used approach to draw conclusions about real systems using this information is the one developed by Kohn and Sham who converted DFT into a practical tool for rigorous calculations (see section 3.3.4). Within the framework of the Kohn-Sham DFT, the intractable many-body problem of interacting electrons in a static external potential is reformulated into a tractable problem of non-interacting electrons moving in an effective potential, that includes the external potential and the exchange functional (the difference between the kinetic energy of the non-interacting system and that of the interacting system, which is assumed to be small) and the correlation functional (the difference between the electron-electron repulsion energy and the classical coulomb energy) of the Coulomb interactions between the electrons. Modeling the latter two interactions becomes a problem within Kohn-Sham DFT. The most popular model for this exchange-correlation functional being the Perdew-Burke-Ernzerhof (PBE) based on the Generalized Gradient Approximation (GGA)

that includes the gradient of the electron density (section 3.3.5). The Kohn-Sham orbitals are represented in terms of a plane waves basis set that offer a number of advantages when using periodic boundary conditions (periodically repeated simulation cells) (section 3.3.6). In order to reduce computational costs the pseudopotential approximation is introduced (section 3.3.7). Here the electrons are partitioned between core and valence states. The core electrons and ionic potential are replaced with a pseudopotential that acts on a set of pseudo orbitals. The Born-Oppenheimer dynamics and the Car-Parinello dynamics are described in section 3.3.8. In the former, the nuclei are moved according to the classical equations of motion, the forces on the nuclei being given by the spatial derivative of the converged Kohn-Sham energy. In the latter, a term, that can be assigned to a fictitious electronic temperature, is added to the classical Lagrangian to include the electron dynamics in a classical manner. The equations used to model the data are presented in section 3.3.9.

3.3.2. Born-Oppenheimer Approximation

In general, the heavy nuclei can be assumed to move more slowly than the light electrons because of their large difference in masses so that to a first approximation, the motions of the electrons can be separated from that of the nuclei; this is the Born-Oppenheimer approximation. Since the nuclei have a high mass, their movement can be approximately treated in a classical manner and changed according to the classical Lagrange equations of motions. This is a very good approximation as long as the properties studied are not related to the motion of light atoms (i.e. hydrogen) or vibrations with a frequency ν greater than $h\nu > kT$. The problem is therefore simplified by considering only the structure of electrons in the atomistic system.

3.3.3. Density functional theory

In quantum chemistry methods, the description of the electronic system is given by the so-called Schrodinger differential equation.

$$\hat{H}_{el}\Psi(R,r) = E\Psi(R,r) \quad (3.77)$$

where

$$\hat{H}_{el} = - \underbrace{\sum_{i=1}^N \frac{1}{2m_e} \nabla_{r_i}^2}_{T_{el}} - \underbrace{\sum_{\alpha,i} \frac{Z_{\alpha}}{|R_{\alpha} - r_i|}}_{V_{ne}} + \underbrace{\sum_{i<j}^N \frac{1}{|r_i - r_j|}}_{V_{ee}} \quad (3.78)$$

Where m_e is the mass of the electrons, Z are the charge of the nuclei, and r and R are the positions of the electrons and the nuclei, and E is the energy of the system. This equation includes the kinetic energy operator T_{el} of the electrons, the electron-nucleus attraction energy V_{ne} , and the electron-electron repulsion energy V_{ee} . In this description, the state of the system is defined by a 3N-dimensional wave function Ψ that is a solution to the Schrodinger differential equation. This wave function represents the probability density of finding the electrons and nuclei of the system in a particular state. Properties of the systems are determined by this wave function. In particular the total energy $E = E[\Psi]$ and the electron density $\rho[\Psi]$ are functionals of the wave function.

In Density Function Theory (DFT), initially proposed by Hohenberg and Kohn, the problem of finding the electronic wave function Ψ of the system is reduced to the problem of finding the electron density ρ . Hohenberg and Kohn proved that the total energy E of a system including that of the many body effects of electrons (exchange and correlation) in the presence of static external potential $v(r)$ (for example, the atomic nuclei) is a unique functional of the electron density

$$E = E[\rho] = T[\rho] + V_{ext}[\rho] + V_{ne}[\rho] + V_{ee}[\rho] = \int v(r)\rho(r)dr + F_{HK}[\rho] \quad (3.79)$$

where

$$F_{HK}[\rho] = T[\rho] + V_{ee}[\rho] \quad (3.80)$$

$$v(r) = v_{ne}(r) + v_{ext}(r) \quad (3.81)$$

It includes the kinetic energy functional $T[\rho]$, the nuclei-electron attractive potential energy functional $V_{ne}[\rho]$, the electron-electron repulsive energy functional $V_{ee}[\rho]$, and the external potential $V_{ext}[\rho]$.

The second Hohenberg-Kohn theorem provides a variational principle to find the ground state energy. It states that for any given non-negative trial density $\rho(r)$, that integrates to the correct number of electrons $\int \rho(r)dr = N$, the true ground state energy is a minimum of the energy

functional. It requires that the ground state density satisfies the variational principle with μ as Lagrange multiplier

$$\delta\left(E[\rho] - \mu\left[\int \rho(r)dr - N\right]\right) = 0 \quad (3.82)$$

The variational principle of Hohenberg-Kohn provides a way to obtain solutions to the problem if T , V_{ne} and V_{ee} are known functionals. Unfortunately, only V_{ne} is known exactly. The problem remains of how to calculate T , and how to calculate the nonclassical part of V_{ee} .

3.3.4. The Kohn-Sham method

Kohn and Sham invented an ingenious indirect approach to the kinetic-energy functional $T[\rho]$, the Kohn-Sham method. They hence converted DFT into a practical tool for rigorous calculations. They proposed reintroducing the electron orbital wave functions φ_i instead of just the density into the problem in such a way that the kinetic energy can be computed simply and to good accuracy. The Kohn-Sham electron orbitals φ_i are simply a way of representing the density ρ ; they are not an approximation of the quantum chemical electron wavefunction Ψ . The idea of Kohn and Sham is to reformulate the interacting problem so that its kinetic component is now defined to be the kinetic component $T_s[\rho]$ of a non-interacting reference system in an effective potential $v_{eff}(r)$ containing the interactive part of the kinetic energy.

$$[T_s + v_{eff}(r)]\varphi_i = \varepsilon_i\varphi_i \quad i=1 \text{ to } N \quad (3.83)$$

$$\rho(r) = \sum_i^N |\varphi_i(r)|^2 \quad (3.84)$$

where

$$v_{eff}(r) = v(r) + \int \frac{\rho(r')}{|r-r'|} dr' + \frac{\delta E_{xc}[\rho]}{\delta \rho(r)} \quad (3.85)$$

$$E_{xc}[\rho] = T[\rho] - T_s[\rho] + V_{ee}[\rho] - J[\rho] \quad (3.86)$$

The effective potential is then given by using the Hohenberg-Kohn variational principle. The exchange-correlation energy $E_{xc}[\rho]$ contains the difference between $T[\rho]$ and $T_s[\rho]$ (exchange

part) which is assumed to be small, and the difference between the electron-electron repulsion energy $V_{ee}[\rho]$ and the classical coulomb energy $J[\rho]$ (correlation part). The Kohn-Sham formulation succeeds in transforming the N-body problem into N single-body problems, each coupled via the Kohn-Sham effective potential $v_{eff}(r)$. These equations are nonlinear and are thus solved by a self consistent iterative procedure. The major advantage of DFT is that the requirements for the basis set used to construct the orbitals φ_i are far more modest than the more conventional quantum chemical correlation methods used to solve the Schrodinger equation. The Hohenberg-Kohn theorem is only rigorously proven for the ground state. Despite this, DFT is being applied successfully to excited states, systems that are subjected to an external magnetic field, systems that are polarized, systems where relativistic effects are important, and to open shell systems.

3.3.5. Choice of the exchange-correlation functional : PBE functional

The Kohn-Sham equations, while exactly incorporating the kinetic energy $T_s[\rho]$, still leave the question of the exchange-correlation functional $E_{xc}[\rho]$ unresolved . Numerous forms exist for the functional. The principle of the local density approximation (LDA) of the functional is to calculate the exchange and correlation energies per particle of the homogenous electron gas as a function of the density. The LDA is applicable to systems with slowly-varying densities but cannot be formally justified for highly inhomogenous systems such as atoms or molecules. The essential justification for its use in atoms and molecules comes from its successful numerical application to isolated molecules. However, poor accuracy accompanies the oversimplified model, especially for condensed phases, and LDA is known to overbind. In this thesis we used the Perdew-Burke-Ernzerhof (PBE) functional, which is today the most popular functional. It is based on the Generalized Gradient Approximation (GGA). In this approximation, the gradient of the electron density $\nabla\rho$ is included as a new variable in the functional.

$$E_{xc}^{GGA}[\rho] = \int f(\rho, \nabla\rho) dr \quad (3.87)$$

The PBE does not contain any parameters that are neither fundamental constants nor determined to satisfy some specified quantum mechanical relation. The strength of DFT is that it represents an optimal compromise between accuracy and feasibility. However, it is not systematically

improvable and the computational cost, although lower than quantum chemical methods, is still high relative to empirical methods. Actual deficiencies, such as the self-interaction of electrons and the complete absence of long range dispersion forces (Van-der-Waals forces), are due to the spatial locality in most density functionals. This means an accuracy of the calculated energies of the order of 1-2 kcal/mol. The ultimate goal is to find a non-local density functional which yields so called “chemical accuracy”. This essentially means that the method should be able to quantitatively predict chemical properties within the standard deviation offered by the best experimental methods.

3.3.6. Choice of the basis set : Plane waves

The Kohn-Sham orbitals φ_i may be represented in terms of any complete basis set. The use of a plane wave basis set (e^{ikr}) offers a number of advantages: (i) the same basis set can be used for all atomic species, (ii) convergence toward completeness can easily be tested, (iii) plane waves do not depend on nuclear positions so, unlike localized basis sets, correction terms are not needed for the calculation of forces, (iv) simple calculation of energy and forces. In general, the representation in plane wave basis set would require an infinite basis set. However, the imposition of boundary conditions allows the use of Bloch’s theorem, whereby the orbitals φ_i of an electron within a periodic potential may be written as the product of a cell periodic part $u_j(r)$, that can be expanded in terms of a Fourier series, and a wavelike part e^{ikr} (where k are the wave vectors). The problem of the infinite number of electrons has now been mapped onto a problem of expressing the wavefunction in terms of an infinite number of plane waves in the first Brillouin zone, defined as all the vectors $k \leq 1/2G$, where G are reciprocal lattice vectors from the Fourier series. In principle this Fourier series is infinite. However, the series can be truncated. The coefficients $c_{j,k+G}$, for the plane waves have a kinetic energy $E_{kin} = (\hbar^2 / 2m) |k + G|^2$ (where m is the electron mass and \hbar is the Planck constant). Plane waves with high kinetic energy have less contribution than those of low kinetic energy, so that a plane wave cutoff energy E_c can be introduced to reduce the basis set to a finite size. Plane wave basis sets can also be applied to non-periodic systems such as isolated molecules. To accomplish this, the molecule is placed at the centre of a periodic supercell. If the supercell is large enough, the interactions between the molecules in neighbouring cells become negligible.

3.3.7. Use of pseudopotentials

Although the Kohn-Sham equations are tractable when plane waves are used to expand the electron wavefunctions, an all-electron calculation including both core and valence electrons, along with the full Coulombic potential of the nuclei would still be prohibitively expensive. This is because the tightly bound core orbitals and the highly oscillatory nature of the valence electrons require that a high energy cutoff E_c value should be used, and hence a high number of plane waves. However, it is possible to partition the electrons between core and valence states. Such a partition is possible because the majority of physical properties of solids depend upon the valence electrons. It is for this reason that the pseudopotential approximation is introduced. The core electrons and ionic potential are replaced with a pseudopotential that acts on a set of pseudo wave functions. The pseudopotentials are usually generated from all-electron calculations by self-consistently solving the all-electron Schrödinger equation for the atom associated with the pseudopotential. The pseudopotential is not unique. However, it must obey the following criteria: (i) The pseudo wavefunction must be the same as the all-electron wavefunction outside a cutoff radius. (ii) The pseudo wavefunctions must be continuous at the cutoff radius, as must be the first and second derivatives. (iii) The valence all-electron and pseudopotential eigenvalues must be equal. (iv) The pseudopotential is also constructed such that the scattering properties of the pseudo wavefunctions are identical to the scattering properties of the ion and the core electrons. In general, this will be different for each angular momentum component of the valence wavefunction. Therefore the pseudopotential will be angular momentum dependent, and is called a “non-local” pseudopotential. If the same core charges are produced by the real and pseudo wavefunctions the pseudopotential is called norm-conserving and ensures that the pseudo atom produces the same scattering properties as the ionic core. The pseudo orbitals and pseudopotentials of the oxygen atom using Martins-Trouiller norm-conserving form of pseudopotentials are shown for example in Fig. 3.44 and Fig. 3.45.

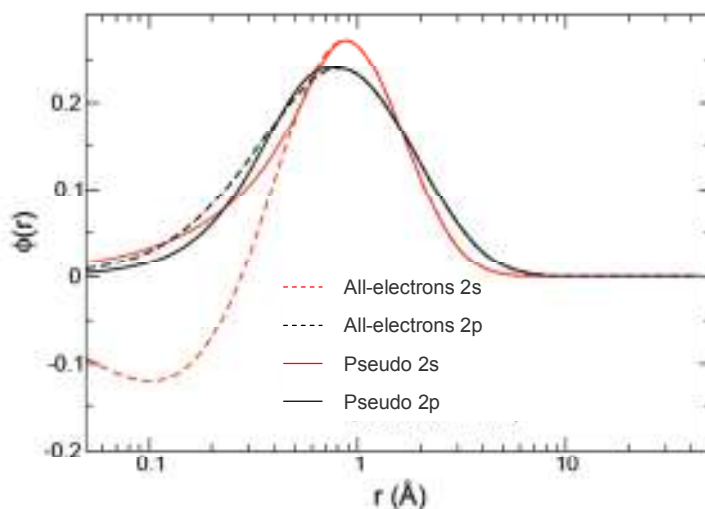


Fig. 3.44: All-electrons and pseudo 2s and 2p orbitals of the oxygen atom using Martins-Trouiller pseudopotentials with a cutoff radius $r_c=1.05$ Å. 1s electrons are core electrons.

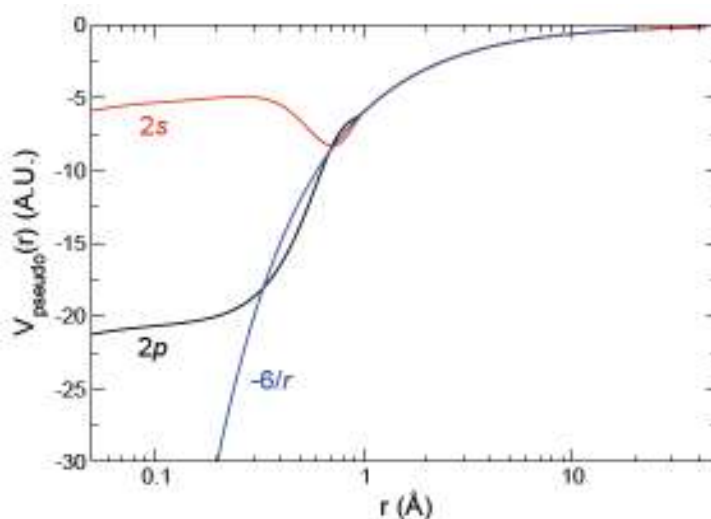


Fig. 3.45: Martins-Trouiller pseudopotentials 2s and 2p of the oxygen atom with a cutoff radius $r_c=1.05$ Å. 1s electrons are core electrons. The point charge core potential $-6/r$ is shown for comparison.

3.3.8. Born-Oppenheimer and Car-Parrinello dynamics

In a computer experiment it is not possible to generate the true trajectory of a system with a given set of initial positions and velocities. Numerical techniques based on a discretization of time, and a repeated calculation of the forces on the particles, are used instead. However, the method should have the following properties: (i) long time energy conservation, (ii) short time

reversibility to reflect the reversibility of the original differential equations. The numerical trajectory will exponentially diverge from the true trajectory but as the energy is conserved the same phase space will be sampled. In this thesis two methods have been used for the calculation of the trajectories: a) Born-Oppenheimer dynamics and b) Car-Parrinello dynamics. Both methods can be formulated in the Lagrangian description of classical mechanics. The trajectories are obtained by integration of the Lagrange equations of motion

$$\frac{d}{dt} \frac{\partial L}{\partial \dot{R}_\alpha} = \frac{\partial L}{\partial R_\alpha} \quad (3.88)$$

where $L=T-V$ is the Lagrangian, and T and V are the kinetic and potential energies of the system.

In the case of the Born-Oppenheimer dynamics the kinetic term is given by the movements of the nuclei and the potential term (the Born-Oppenheimer surface energy) includes the nuclei repulsion and the converged Kohn-Sham energy of the electronic system.

$$T = \sum_{\alpha} \frac{1}{2} m_{\alpha} \|\dot{R}_{\alpha}\|^2 \quad (3.89)$$

$$V_{BO} = \sum_{\alpha < \beta} \frac{Z_{\alpha} Z_{\beta}}{|R_{\alpha} - R_{\beta}|} + \min \{ E_{el}^{KS}(\varphi_i, R) \} \quad (3.90)$$

When the Kohn-Sham energy is minimal, that is when the wavefunctions are completely converged, the partial derivative of the total energy with respect to atomic position gives the force felt by the atom. This is the Hellman-Feynman theorem. The error in the force is first order with respect to error in the wavefunction, and thus in the energy, so that the Hellman-Feynman theorem can only be implemented when the wave functions are very close to self-consistency. The advantage of the Born-Oppenheimer dynamic is that relatively large time steps can be chosen. However the wave functions have to have converged for each time step, which is computationally expensive.

In the case of the Car-Parrinello dynamics, the classical Lagrangian is extended to include the electron dynamics in a classical manner

$$L = \sum_i \frac{1}{2} m_{\alpha} \|\dot{R}_{\alpha}\|^2 + \sum_i \mu \langle \dot{\varphi}_i | \dot{\varphi}_i \rangle - E^{KS}(\varphi_i, R_{\alpha}) + \sum_{ij} \Lambda_{ij} \left(\int \varphi_i^*(r) \varphi_j(r) - \delta_{ij} \right) \quad (3.91)$$

A second term, that can be assigned to a fictitious electronic temperature, is added to the classical kinetic term. The last term in the Lagrangian can be thought as an additional force of constraint that maintains orthonormality of the wavefunctions, with Δ_{ij} as Lagrange multipliers. The electronic subsystem is close to its instantaneous minimum energy, i.e. close to the exact Born-Oppenheimer surface, if the fictitious mass and the time step are small enough. A way to keep the time step large and still increase the fictitious mass in order to keep the energy close to the Born-Oppenheimer surface is to choose heavier nuclear masses. This depresses the largest phonon or vibrational frequency of the nuclei that determines the maximum fictitious mass that can be chosen.

3.3.9. Analysis of the data

Various properties can be calculated from the trajectories. In this thesis the following properties have been calculated:

The average temperature T is calculated from the average kinetic energy of the system

$$\langle E_{kin} \rangle = \frac{1}{2} k_B T \quad (3.92)$$

The diffusion coefficient D is calculated from the mean squared displacement of the atomic positions relative to a reference initial configuration, chosen after thermalization of the system.

$$D = \frac{1}{6t} \langle (R(t) - R(0))^2 \rangle \quad (3.93)$$

The radial distribution function (RDF) is calculated from the interatomic distances R_{ij} .

$$g(r) = \left\langle \sum_i \sum_{j \neq i} \delta(r - R_{ij}) \right\rangle \quad (3.94)$$

The dipole distribution function is calculated from the orientation θ_i of the dipoles.

$$g(\theta) = \left\langle \sum_i \delta(\theta - \theta_i) \right\rangle \quad (3.95)$$

CHAPTER 4 CHOICE OF THE MATERIALS AND EXPERIMENTAL PROCEDURES

4.1. CHOICE OF THE MATERIALS

A sodium Kunipia-F smectite clay, obtained from Kunimine (Japan) was selected for this study because of its high purity in terms of smectite content and percentage of sodium counter ions (see CHAPTER 6). It has further advantages of being a raw clay, being therefore more representative of smectite clays used for the cat litter, and the sodium counter ions are easier to exchange than in the case of a calcium clay. A disadvantage of this clay is that it contains iron replacements in its octahedral layer, that restrict the possibility of measuring the diffusion coefficients of water in its interlayer by NMR measurements. This clay has also a large distribution of platelet's sizes (see CHAPTER 6), rendering the modelling of effective diffusion much more complicated. The synthetic Laponite sodium smectite has been also considered because of its absence of iron cations in the octahedral layer and its well defined platelet dimensions. However, uncertainties remained on the composition in terms of amorphous impurities.

The 6 model volatiles (Table 4.17) selected for the study were chosen according to their stability, their vapour pressure (ranging from 1723 Pa to 12616 Pa at 25 °C), their difference in chemical functionalities (hydroxyl group, carbonyl group, ether group, pyridyl group, aromatic group, electro negative atom, polar, apolar), the availability of their physical data in terms of density and gas diffusion coefficient (ranging from 0.62×10^{-5} to 2.71×10^{-5} m²/s), and their commercial availability.

The Kunipia-F sodium smectite was ion exchanged with small organic ammonium cations differing in their sizes and number of carbons (Table 4.18) and with metallic cations (Li⁺, Ca²⁺).

Table 4.17. List of the model volatiles. Oxygen atoms are in red, hydrogen atoms are in white, carbon atoms are in grey, and nitrogen atoms are in blue.


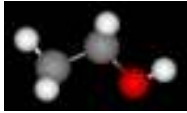
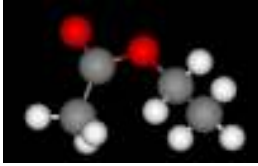

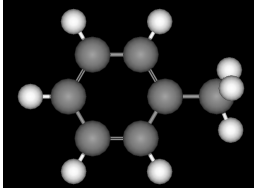
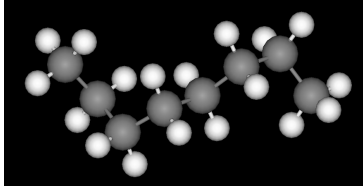
volatile	chemical formula	structure
water (for chromatography, Merck)	H ₂ O	
ethanol (absolute GR for analysis, Merck)	CH ₃ CH ₂ OH	
ethyl acetate (GR for analysis, Merck)	CH ₃ COOCH ₂ CH ₃	
pyridine (Assay > 99 % (GC), Fluka)	C ₅ H ₅ N	
toluene (GR for analysis, Merck)	C ₆ H ₅ CH ₃	
n-octane (Assay > 96 % (GC), Fluka)	C ₈ H ₁₈	

Table 4.18. List of organic cations

organic cation	abbreviation	structure
pentyl trimethyl ammonium	PTMA	
hexyl trimethyl ammonium	HTMA	
tetraethyl ammonium	TEA	
N,N'-dipentyl-diazabicyclooctane	DPDBCO	
phenyl trimethyl ammonium	PHTMA	

4.2. CLAY CHARACTERIZATIONS

X-Ray diffraction spectroscopy (XRD) measurements were performed on clay films using a Siemens Kristalloflex 805 diffractometer ($\lambda=1.54 \text{ \AA}$) at room temperature and room relative humidity. The measurement range used for the full spectrum ranged from 2° to 70° . The step angle was 0.02° and the acquisition time per angle was 3 s. The interlayer distance was measured using a clay film dried for 1 day at 50°C with a P_2O_5 adsorbent under a vacuum of 70 Torr. In this case a measurement range from 4° to 8° was used, with a step angle of 0.04° and an acquisition time per angle of 4 s, in order to minimize sorption due to ambient relative humidity. Clay films used for XRD measurements were fabricated from the as-received material and the purified clay by the evaporation at room temperature of 1wt% clay dispersions on polyethylene substrates. The clay was dispersed in water with the aid of ultrasonic treatment. Purification of the clay was carried out by allowing a 2 wt% aqueous clay solution to sediment for 3 days. The supernatant 2 cm above the surface of the clay solution was collected and allowed to sediment for a further 3 days. The remaining supernatant was then used for characterization.

For transmission electron microscopy (TEM) measurements a 0.1 wt% clay/water dispersion was prepared. One drop of the clay suspension was placed on a copper formvar-carbon coated grid and let to dry for 5 minutes. The grid was then transferred to a Philips CM12 transmission

electron microscope. Images were taken using a Gatan Multiscan numerical camera model 794. The diameter distribution of the clay platelets were obtained from the maximal and minimal diameters of 5786 clay platelets imaged by TEM on 6 different grids.

Visualization of the clay granules by SEM was carried out in a Quanta 200F FEG microscope (FEI company Eindhoven), operated at 8 kV in Low Vacuum mode. The clay granules were mounted on sample holders with double-sides adhesive tape and cut with a razor blade in 2 parts to reveal the internal structure.

The apparent density of the clay was measured by helium gas pycnometry using a commercial Accupyc 1330 instrument from Micromeritics. Prior to measurements the clay was dried for 1 day at 50 °C with a P₂O₅ adsorbent under a vacuum of 70 Torr.

For the elemental analysis, the clay was first dried for 2 h at 105 °C and then calcined at 1050 °C. 1.2121 g of the crushed calcined clay was diluted with 6 g of lithium tetraborate. The mixture was melted at 1250 °C. After cooling, the sample was transferred to a Philips 2400 X-ray fluorescence spectrometer for analysis.

The granules were prepared from a clay slurry. The clay slurry was first rolled such as to form spherical granules, and then dried under a fume hood in a rolling container. The samples were dried at 50 °C using a P₂O₅ adsorbent under vacuum.

4.3. CLAY MODIFICATIONS

The sodium (Na) smectite was modified with calcium (Ca), phenyl trimethylammonium (PHTMA), pentyl trimethyl ammonium (PTMA), N,N'-Dipentyl-diazabicyclooctane (DPDBCO), hexyl trimethylammonium (HTMA), tetraethylammonium (TEA), by ion exchange using a batch method. The organic ammonium salts were purchased from Fluka, except for the PTMA and the DPTMA, which were synthesized in house. The clay was first dried for 2 days at 60 °C under a vacuum of 70 Torr using a P₂O₅ adsorbent. 1 g of the dried clay was then dispersed into 100 ml of a 50 % water/methanol solution by means of ultrasonic treatments. The modifier was dispersed in 50 ml of a 50 % water/methanol solution in a proportion of 1.2 times the molar amount of the clay cation exchange capacity (CEC). The clay solution was then poured into a flask containing 250 ml of a 50 % water/methanol solution, and the modifier solution subsequently added. The

solution was mixed for a further 15 min with a high-performance dispersing instrument (Ultra-Turrax) and stirred for 24 h under reflux at 60 °C. After centrifugation of the mixture, the supernatant was removed and 400 ml of methanol added and subjected to a 3 min treatment with the Ultra-Turrax. The mixture was centrifuged again and the supernatant removed. This procedure was repeated once with methanol and twice with ethanol, after which the clay was left to dry in a fume hood. The interlayer distance of the modified clays was measured by X-Ray diffraction spectroscopy (XRD) using a Siemens Kristalloflex 805 diffractometer ($\lambda = 1.54 \text{ \AA}$) on films of the modified clays (Table 4.19). The clay films used for XRD measurements were fabricated by room temperature evaporation of 1 wt% clay dispersions on polyethylene substrates. Prior to XRD measurements the clay films were dried for 2 days at 60 °C with a P_2O_5 adsorbent under a vacuum of 70 Torr. The measurements were made at room temperature and ambient relative humidity. The interlayer distances, d_{001} , of the modified clays showed the substitute cations to intercalate between the clay layers (Table 4.19). For comparison, the measured interlayer distance of the sodium smectite at ambient relative humidity was 1.23 Å.

Table 4.19. Interlayer distances (d_{001}) of the modified clays measured at room temperature and ambient relative humidity.

organic cation	d_{001} (nm)
PTMA	1.37
HTMA	1.37
TEA	1.40
DPDBCO	1.41
PHTMA	1.46

The clay was also modified with lithium (Li) by column ion exchange. 40 g of dried clay aggregates was introduced to a capillary column. An aqueous solution of 15 wt% lithium chloride was poured onto the clay and allowed to flow through the clay in the column at a rate of 2 L per day for 5 days. The clay was then washed with ethanol at 2 L per day for 5 days. The clay was then allowed to dry in a fume hood. Lithium (^7Li) and sodium (^{23}Na) NMR spectra of the clay exchanged with lithium showed a peak for lithium and no peak for sodium indicating that the sodium cation was exchanged.

4.4. SYNTHESIS OF THE ORGANIC SALTS

Synthesis of the organic cations have been performed by Dr. Lorenz Meier. For the preparation of the pentyl trimethyl ammonium bromide 33 ml of trimethyl amine solution 45 % in water (Aldrich) were mixed with 41,5 g of 1-Bromopentane in closed flask and stirred at 60 °C over night. The solution was dried in a rotavapor to give the white product.

For the preparation of the N,N'-dipentyl-diazabicyclooctane dibromide 14.02 g Diazabicyclooctane and 41.5 g 1-bromopentane were dissolved in 45ml DMSO and stirred over night in closed flask at 60 °C. The solvent was evaporated. 200 ml bidistilled water and 0.5 g of activated charcoal were added, heated up to boiling temperature for 30 minutes. The activated charcoal was filtered off. The product was recrystallised from 100 g NaBF₄ in 800 ml of water. The yield was 29.4 g. The products were checked by NMR.

4.5. DETERMINATION OF THE EQUILIBRIUM SORPTION ISOTHERMS

4.5.1. Sorption isotherms with DVS instrumentation

A Dynamic Vapour Sorption (DVS-2000) instrument from SMS (Surface Measurements System, UK) was used to measure the desorption isotherm of water from the clay. Prior to experiments the clay was dried at 0 %RH. Dry nitrogen gas with a purity of 99.995 % was used as the carrier gas. The clay was then equilibrated at relative humidities starting from 95 down to 0 %RH through 5 %RH steps, by regulating the ratio of dry and saturated gas flows, the latter being calibrated with NaCl, MgCl₂, and LiCl salt solutions.

The clay was assumed to be equilibrated when the variation of the weight did not exceed 0.0002 %/min of the dry mass over 10 minutes. About 50 mg of material was used for each measurement. Heating the sample up to 105 °C a residual water content of 0.6 wt% after DVS drying was attributed. This was taken into consideration for the calculations of the water contents.

The desorption isotherms of ethanol, ethyl acetate and toluene were determined with the DVS-advantage instrument (Surface Measurements Systems, UK) adapted for use with organic

volatiles. The partial pressure of the vapor was controlled by adjusting the flow ratio of saturated and dry carrier gas (dried air, cleaned with an adsorption filter (pure gas products) $H_2O < 15$ ppb).

The vapor concentration was measured with a dew point analyzer. The clay was equilibrated at relative activities from about 90 % to 0 %. The clay was assumed to be equilibrated when the variation of the weight did not exceed 0.001 % of the actual mass per minute over 10 minutes. 15 to 30 mg samples were used.

4.5.2. Desorption isotherms with Knudsen thermogravimetry

The desorption isotherms were also measured by Knudsen thermogravimetry (KTGA) using a combined thermobalance-DSC Setaram (France) TG-DSC111. When the standard pans of balance are replaced with Knudsen cells (Fig. 4.46), which communicate with a low external pressure p_{ext} (10^{-4} Pa) through a 20 μ m orifice, an isothermal drying process can be triggered by means of a turbomolecular pump. Under these conditions the driving force sucking volatile molecules out of the cell is the drop of volatile partial pressure, p , across the orifice. Since p_{ext} is always at least two-order of magnitude lower than p_{int} within the cell, the loss rate of volatiles dm_v/dt is practically proportional to p_{int} , namely [184]:

$$\frac{dm}{dt} = K(p_{int} - p_{ext}) \cong K p_{int} \quad (4.96)$$

Where K is constant for a given gas escaping through the Knudsen orifice of a given geometrical size and at a given temperature.

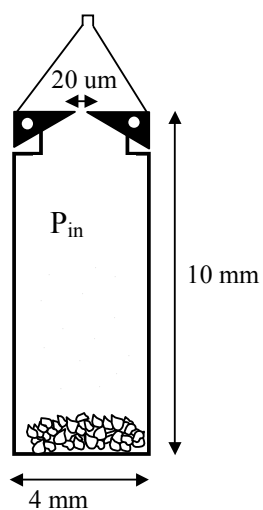


Fig. 4.46. Schematic of the Knudsen cell.

The ratio between the mass loss rate (dm_v/dt) from a given material and the mass loss rate $(dm_v/dt)^*$ from the pure volatile liquid, at the same temperature and with the same Knudsen cell, gives the trend of the relative vapour pressure a_v of the volatile in the material considered:

$$\frac{\frac{dm}{dt}}{\left(\frac{dm}{dt}\right)^*} \cong \frac{Kp_{\text{int}}}{Kp_{\text{int}}^*} = \frac{p_{\text{int}}}{p_{\text{int}}^*} = a_v \quad (4.97)$$

where p_{int}^* is the saturated vapour pressure of the pure volatile.

Since the ratio p/p^* involves the whole desorption run collected from the thermobalance, the corresponding desorption isotherm is a continuous trace.

Prior to measurements, the clay was dried at 50 °C with a P_2O_5 adsorbent under vacuum, and then mixed with the volatile liquid to form a clay slurry.

This method has been already applied on foodstuffs and clay materials [184,185].

4.6. DETERMINATION OF WATER CONTENT AT 43 %RH BY SATURATED SALT SOLUTIONS

In addition to the DVS and Knudsen measurements the water content in the clay at 43 %RH and 25 °C was checked using saturated solutions. The clay was equilibrated at 97 %RH and 25 °C using a saturated solution of K_2SO_4 . After one month the clay was equilibrated for another month at 43 %RH using a saturated solution of K_2CO_3 . The clay was then dried for 2 days at 50 °C with a P_2O_5 adsorbent under a vacuum of 70 Torr.

4.7. MEASUREMENT OF THE RELEASE KINETICS

The release kinetics of the volatiles were analysed by thermogravimetry (TG) and 3D differential scanning calorimetry (DSC) using a commercial TG-DS-MS Sensys instrument from Setaram (Fig. 4.47 and Fig. 4.48), France. 5 mm diameter and 1 cm tall aluminum crucibles were used as sample holders. The sample and reference crucibles were placed at the center of each of the two 7 mm diameter columns of the thermostatted DSC chamber. The crucibles were subjected to a dry nitrogen carrier gas flow ranging from 5 ml/min to 100 ml/min per column. The measurement chamber was surrounded by a plastic bag under dry nitrogen gas over pressure in order to minimize pollution by external air during loading (Fig. 4.48). The quality of the dry nitrogen atmosphere inside the thermostatted chamber was checked by using a mass spectrometer coupled to the output flow of the DSC instrument.

The measurements were performed under isothermal conditions at 25 °C and 35 °C and by ramping the temperature from 23 °C to 200 °C. For the temperature scans, 5 μ l droplets of the volatile liquids were deposited on cylindrical samples and a different clay sample was used for each experiment. The scanning rate was 2 K/min and duplicate measurements were performed for each type of volatile and each type of clay.

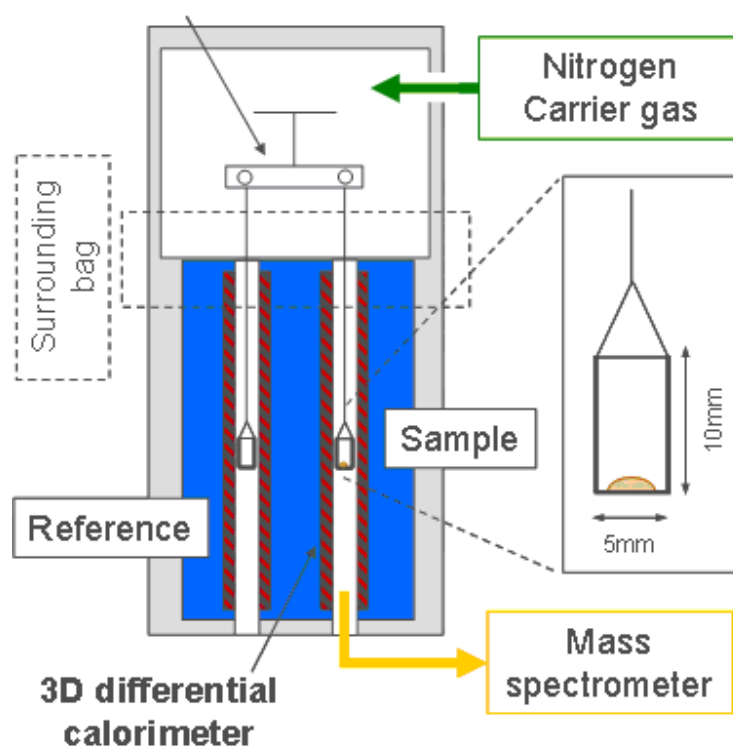


Fig. 4.47. Schematic of the TG-DSC-MS instrumentation

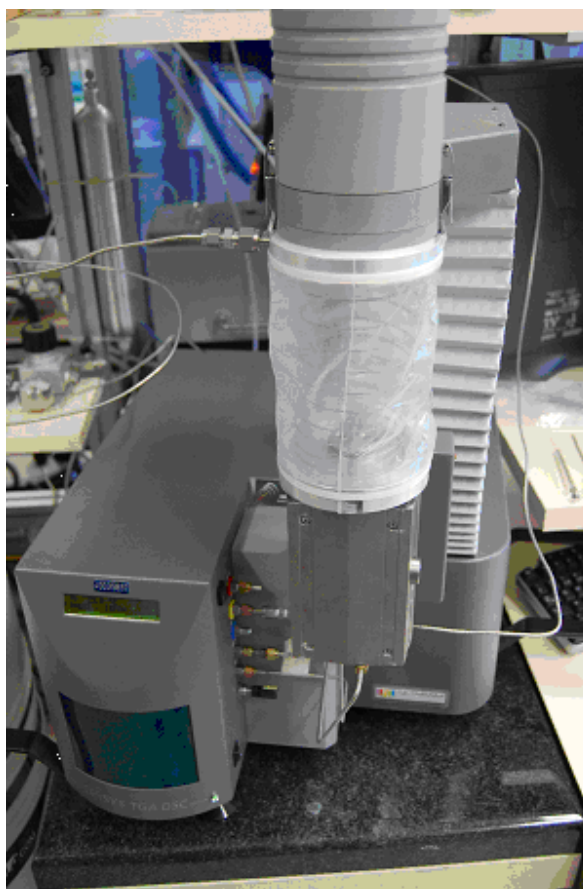


Fig. 4.48. Picture of the TG-DSC-MS instrumentation showing the surrounding bag with the nitrogen gas input.

4.1. URINE EXTRACTION

100 ml of urine, 30 g of NaCl, and 30 ml of dichloromethane were mixed and shaken for 30 seconds. After settling of the mixture for 15 minutes, the bottom phase was collected. The procedure was repeated three times with the collected liquid. Na₂SO₄ was added to the collected liquid to adsorb the remaining water. The mixture was then filtered and rinsed with dichloromethane. The extraction was finally obtained from the evaporation of the liquid down to 10 ml.

CHAPTER 5 NUMERICAL METHODS

5.1. FINITE ELEMENT METHODS

5.1.1. Physical equations and boundary conditions

Finite element methods (FEM) (see section 3.3.3 for a theoretical background) were used for the numerical calculation of the rate of release. The same geometry as that of the TG-DSC-MS Sensys instrumentation (see section 4.7) was used for the calculations, i.e. a cylindrical column of 7 mm diameter and 100 mm height, a cylindrical crucible of 5 mm in diameter and 10 mm in height, at the center of the column, and a sample placed at the bottom of the crucible.

The isothermal rate of evaporation of the bulk liquid was separated into two processes: (i) Gas/condensed phase adsorption and desorption; (ii) Diffusion and convection of the volatiles in the gas phase. The isothermal rate of release of the volatile from the clay was separated into three processes: (i) Internal diffusion of the volatile in the sample; (ii) Gas/condensed phase adsorption and desorption of the volatile onto surface of the sample; (iii) Diffusion and convection of the volatile in the gas phase.

The transfer rate across the gas/condensed phase interface is a molecular process that has a typical time of 10^{-10} s, whereas the process of diffusion of molecules in air has a typical time of 10^{-5} s [186]. The water vapor concentration at the surface of the liquid adjusts therefore rapidly compared with the time required for droplet evaporation [187], so that local instantaneous equilibrium conditions could be assumed between the rate of gas/condensed phase desorption and the rate of gas/condensed phase adsorption. The local pressure at the sample surface was therefore assumed to be in instantaneous equilibrium with the local adsorbed volatile concentration at the sample surface. The gas/condensed phase partition coefficients were given by the saturated vapour pressure in the case of the evaporation of the volatile liquids and by the equilibrium desorption isotherm in the case of the release of water from the clay.

The diffusion/convection process in the gas phase was calculated using the convection diffusion equation, the Navier-Stokes equation, and the continuity equation given by Eq. (5.98), (5.99), and (5.100):

$$\partial_t c = \nabla D_{gas} \nabla c + u \nabla c \quad (5.98)$$

$$\rho(\partial_t u + (u \cdot \nabla)u) = -\nabla p + \eta \nabla^2 u \quad (5.99)$$

$$\nabla \cdot u = 0 \quad (5.100)$$

Where t is the time, c is the gas concentration of the volatile in the gas phase, D_{gas} is the diffusion coefficient of the volatile in the gas phase, u is the velocity of the gas, p is the pressure of the gas, and ρ and η are the density and the viscosity of the carrier gas. The internal diffusion process was calculated using the diffusion equation:

$$\partial_t c = \nabla D_{eff} \nabla c \quad (5.101)$$

Where t is the time, c is the concentration of water in the clay, D_{eff} is the effective diffusion coefficient of water in the clay.

The weight loss is calculated from the total normal evaporating gas flux at the sample surface. A constant flux boundary condition was applied to the top of the column to simulate the rate of the carrier gas flow. A constant pressure condition was applied to the bottom of the column. The temperature was assumed to be constant in the whole system. The concentration of volatiles in the gas phase was initially set to zero. The evaporation of the water droplet was solved under steady state conditions, changing the droplet height, and assuming a constant bottom surface. The shape of the droplet was considered to be a spherical cap, because of the decrease in contact angle observed during evaporation [187]. The number of mesh grid elements on the boundaries was increased as the dependence of the numerical results on the division became negligible. Increasing the number of element in the domains did not improve the results. No slip condition was used at the sample boundary. Slip boundary conditions provided the same result, though with slower convergence (Fig. 5.49). The system of equations was solved by finite element methods with the help of a commercial COMSOL software package in 2D cylindrical coordinates.

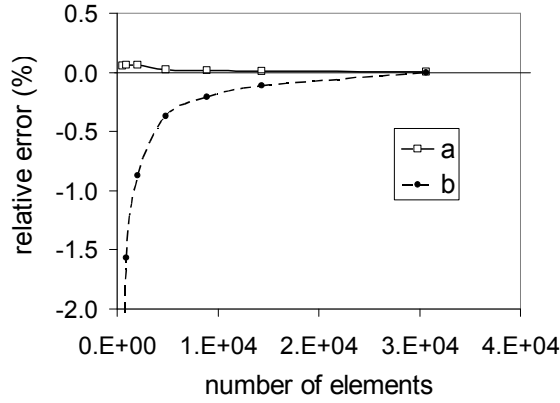


Fig. 5.49. Error on the calculated initial rate of evaporation R of a $5\ \mu\text{l}$ droplet relative to the converged value as a function of the number of mesh elements on the boundaries. Boundary conditions on the walls: a) slip; b) no slip.

5.1.2. Physical input parameters

The physical input parameters used for the finite element calculations are described hereafter. Using the Chapman-Enskog first approximation for low density binary gas mixtures [188], and the fact that the logarithm of the gas diffusion coefficient is approximately linearly proportional to the temperature [189,190,191], the dependence of the gas diffusion coefficients D_{gas} on pressure and temperature can be expressed by:

$$D_{gas} \sim \frac{T^n}{p_{tot}} \quad (5.102)$$

Where p_{tot} is the total pressure, n is the temperature proportionality constant, and T is the temperature. Table 5.20 shows the values of the gas diffusion coefficients of the volatile liquids in air or nitrogen determined by linear regression of the literature data [188,189,190,191,192,193,194,195,196,197,198,199,200,201,202] using Eq. (5.102).

Table 5.20: Average gas diffusion coefficients for different gas mixtures used in this study. The values were obtained from linear regression of the literature data.

gas mixture	average diffusion coefficient ($10^{-5} \text{ m}^2/\text{s}$)	
	25 °C	35 °C
water / nitrogen	2.47	2.64
water / air	2.71	2.87
ethanol / air	1.19	1.24
ethyl acetate / air	0.86	0.92
pyridine / (air, nitrogen)	1.06	
toluene / air	0.90	0.95
n-octane / air	0.62	

The saturated vapor pressures p_s of the volatile liquids (Table 5.21) were calculated from the Antoine equation (Eq. (5.103)). The constants of the Antoine equation were taken from literature data [203,204,205,206,207,208,209,210,211].

$$\log(p_s) = A - \frac{B}{C + T} \quad (5.103)$$

Where T is the temperature, and A , B , and C are material constants.

Table 5.21: Saturated vapour pressures of the liquid volatiles used in this study. The values were obtained from the literature data using the Antoine equation

chemical species	saturated vapour pressure (Pa)		
	10 °C	25 °C	35 °C
water	1227	3167	5624
ethanol	3141	7877	13757
ethyl acetate	5802	12616	20119
pyridine		2757	
toluene		3800	6239
n-octane		1723	

The effective diffusion coefficient of water in the smectite clay can be modeled using the definition of the effective diffusion coefficient and the tortuosity models of Fricke and Bharadwaj given in section 2.7.4. The model of Gusev and Luti could not be used because it gave a tortuosity factor larger than those for the water contents of interest in this study.

5.2. AB INITIO CALCULATIONS

5.2.1. Computational approach

The *ab initio* calculations were based on Density functional theory (DFT) [212] in the plane wave – pseudopotential scheme of the Car-Parrinello Molecular Dynamic (CPMD) software [213] (see section 3.3 for a theoretical background).

In all calculations the structures were represented by a periodically repeated supercell. Core electrons, considered as frozen, were not treated explicitly in this approach and pseudopotentials represent their interaction with the valence electrons. The local term and pseudoradii of the pseudopotentials are shown in Table 5.22. Electronic valence wavefunctions were expanded in plane waves up to a certain kinetic energy cutoff E_c . If not otherwise mentioned the equilibrium structures were calculated with a threshold of 10^{-7} a.u. for the largest off-diagonal component G_w of the energy gradient in the wavefunction optimization and 10^{-5} a.u. for the largest off-diagonal component G_g of the energy gradient in the geometry optimization.

Table 5.22. Local term and pseudoradii of the pseudopotentials.

atom	local orbital	pseudoradii		
		s	p	d
Oxygen (O)	p	1.05	1.05	
Hydrogen (H)	s	0.94		
Silicon (Si)	d	1.9	2.1	2.1
Magnesium (Mg)	p	1.95	3.2	
Aluminium (Al)	d	1.8	1.8	1.8
Sodium (Na)	d	2.3	2.3	1.9603
Carbon (C)	p	1.2	1.2	
Nitrogen (N)	p	1.12	1.12	

For the exchange-correlation functional the generalized gradient approximation (GGA) was used and in particular the Perdew-Burke-Ernzerhof (PBE) [214] parametrization. Spin-polarization was accounted for all open shell systems. As atomic (norm-conserving) pseudopotentials both those derived with the Martins-Trouiller’s (MT) [215] procedure with factorization of the non-local part in the Kleinman-Bylander scheme [216] and those obtained from Goedecker’s method [217] were tested.

The sodium pseudopotential includes non-linear core corrections to the exchange-correlation functional to account for the non-negligible overlap of the valence and the core shells [218]. It was tested on the bond lengths, ionization potentials and binding energies of Na_2 , NaH , NaO ,

and NaOH and the binding energies and radii of hydration of a sodium cation surrounded by one to six water molecules (section 5.2.2.4). The other atomic pseudopotentials used in this work have been successfully applied to many different systems in previous studies.

The example of talc was used to decide on the most convenient scheme to use, in terms of fastest convergence of energy and forces as a function of the plane wave cutoff (section 5.2.2.1). On this basis MT pseudopotentials were used. We verified that $E_c=100 Ry$ was sufficient for the plane wave expansion of the electron wavefunctions. Then, convergence of the internal atomic coordinates was tested and also their dependence on the size of the supercell both for talc and pyrophyllite (section 5.2.2.2), for which detailed experimental data are available [219,220]. However the lattice constant of the unit cell was kept fixed to the experimental value.

The initial structures of talc and pyrophyllite were taken from X-ray experimental determinations [219,220]. Lattice parameters of the two clays are shown in Table 5.23. Older experimental data on the pyrophyllite structure are also shown for comparison [221].

Table 5.23. Measured lattice parameters of talc and pyrophyllite. Lengths are in Å and angles in degrees.

	a	B	c	α	β	γ
talc [219]	5.291	9.46	5.29	98.68	119.9	85.27
pyrophyllite [220]	5.16	8.966	9.347	91.18	100.46	89.64
pyrophyllite [221]	5.161	8.957	9.351	91.03	100.37	89.75

We considered also all the model volatiles investigated experimentally, namely water, ethanol, ethyl acetate, pyridine, toluene, n-octane, and nitrogen dimer. Their initial structures were obtained from geometry optimization made with the so-called UNIVERSAL force-field (UFF) [118] included in the CERIU2 software. The electronic structure, dipole moment, ionization potential, and polarizability of the isolated volatiles were calculated using MT pseudopotentials and compared with experimental values (section 5.2.2.3). A cubic periodic box of 30 Å length was used to weaken the interaction between volatiles in adjacent boxes.

The initial model structure of sodium smectite was generated from that of a pyrophyllite supercell by random substitutions of aluminum atoms with magnesium atoms in the octahedral sheet and random substitutions of silicon atoms by aluminum atoms in the tetrahedral sheet. More details on the building of the bulk and slab clay models are given in sections 8.2 to 8.4. The supercell approach was used and only the $k=0$ Bloch functions were taken into account; in this way, provided the supercell is appropriate, one generally obtains a

reliable representation of the charge density of the system. This choice was especially important in preparation of the study of adsorption that induces structural relaxation. Both Car-Parrinello molecular dynamics [222] and Born-Oppenheimer molecular dynamics calculations have been performed on the clay models. Details on these calculations are given in the CHAPTER 8.

5.2.2. Validation of the DFT approach

5.2.2.1. GEOMETRY OPTIMIZATION OF TALC: CHOICE OF THE PSEUDOPOTENTIALS

The results of the optimized structures of talc as a function of the plane wave cutoff and as a function of the size of the supercell using Goedecker pseudopotentials are shown in Table 5.24, and the ones using MT pseudopotentials are given in Table 5.25. When using the Goedecker pseudopotentials, the structure is converged at $E_c = 180$ Ry for a 222 supercell. Bond length differences between experiment and calculations become smaller than 0.03 Å, and bond angles differences smaller than 2 degrees. When using the MT pseudopotentials, the structure has converged by $E_c = 100$ Ry for a 222 supercell. Bond length differences between experiment and calculations become smaller than 0.06 Å, and bond angles differences smaller than 3 degrees. The largest discrepancies arise from the bond length and bond angles that involve a magnesium atom. However, it is also important to note that a geometry optimization represents a hypothetical structure at 0 K, whereas crystallographic X-ray data refer to room temperature and represent a real space average. It is worth noting that the surface of talc has a low corrugation and that all the calculated O_bSiO_a angles of the tetrahedron are that of a perfect tetrahedron. Fig. 5.50 shows also that the hydroxyls are aligned in a direction perpendicular to the clay surface.

Results for the 222 supercell obtained using Goedecker pseudopotentials are somewhat closer to experimental data than those obtained using MT pseudopotentials. However, because a higher plane-wave cutoff is necessary (see Fig. 5.51), calculations using Goedecker pseudopotentials are much more expensive in terms of computational time than those using MT pseudopotentials. Since MT pseudopotentials guarantee the needed accuracy they were used in all calculations.

When starting the geometry optimization from two different spatial configurations, one finds two different optimized structures with energies differing by only 0.1 eV for a unit cell, with symmetric arrangement with respect to the plane formed by the silicon atoms and the apical oxygen atoms as shown in Fig. 5.52. The position of the basal oxygen atom obtained from

experimental data at room temperature lies closer to the plane formed by the two silicon atoms and the apical oxygen atoms than the position obtained from geometry optimization. Since experimental measurements are averages over all the configurations accessible to the talc structure at room temperature, the basal oxygen atoms are expected to oscillate between the two configurations shown in Fig. 5.52a and Fig. 5.52b. In order to verify this hypothesis, a Car-Parrinello molecular dynamics simulation was performed with temperature rescaling below 500 K and above 700 K and a time step of 0.73 fs. However, over 0.150 ps, the basal oxygen atom did not cross the plane formed by the two silicon atoms and the two apical oxygens, thus indicating the existence of an energy barrier for the virtual system.

Table 5.24. Structural parameters of talc using Goedecker pseudopotentials for a 111 cell for various E_c and for various size of the supercell for $E_c = 180$ Ry. Ts.th. is the thickness of the tetrahedral sheet, Os.th. is the thickness of the octahedral sheet, ΔZ is calculated as the standard deviation around the plane formed by the basal oxygen atoms and gives an indication of the corrugation of basal oxygens along [110], $d(A-B)$ is the average angle between atom A and atom B, $\angle(A-B-C)$ is the average angle between the atoms A, B and C. O_b stand for the basal oxygens, O_a for the apical oxygens, and O_h for the oxygen of the clay hydroxyl.

supercell		111			111	222
E_c		70	180	250	180	
	Exp [219]					
Ts.th.	2.16	2.13	2.11	2.11	2.11	2.17
Os.th.	2.20	2.36	2.26	2.26	2.26	2.23
ΔZ	0.01	0.01	0.03	0.02	0.03	0.01
$d(\text{Si}-O_b)$	1.62	1.69	1.67	1.67	1.67	1.63
$d(\text{Si}-O_a)$	1.62	1.63	1.62	1.63	1.62	1.63
$d(\text{Mg}-O_a)$	2.08	2.12	2.10	2.09	2.10	2.08
$d(\text{Mg}-O_h)$	2.05	2.07	2.04	2.05	2.04	2.07
$d(O_h-H)$		0.99	0.97	0.97	0.97	0.97
$\angle(O_b-Si-O_b)$	109.5	111.9	112.0	112.0	112.0	109.4
$\angle(Si-O_b-Si)$	140.5	130.1	132.2	132.4	132.2	139.0
$\angle(O_b-Si-O_a)$	109.4	107.0	106.9	106.8	106.9	109.5
$\angle(\text{Mg}-\text{Si}-O_a)$	121.9	123.8	122.6	122.7	122.6	122.4
$\angle(O_a-\text{Mg}-O_a)$	94.6	92.0	93.4	93.8	93.4	94.5
$\angle(O_h-\text{Mg}-O_a)$	95.3	93.7	95.2	95.2	95.2	94.9
$\angle(\text{Mg}-O_h-\text{Mg})$	96.1	95.1	96.4	97.0	96.4	96.3
$\angle(\text{Mg}-O_h-H)$	120.9	121.6	120.6	120.1	120.6	120.7

Table 5.25. Structural parameters of talc using MT pseudopotentials for a 111 cell for various E_c and for various size of the supercell for $E_c = 100$ Ry. Ts.th. is the thickness of the tetrahedral sheet, Os.th. is the thickness of the octahedral sheet, ΔZ is calculated as the standard deviation around the plane formed by the basal oxygen atoms and gives an indication of the corrugation of basal oxygens along [110], $d(A-B)$ is the average angle between atom A and atom B, $\angle(A-B-C)$ is the average angle between the atoms A, B and C. O_b stand for the basal oxygens, O_a for the apical oxygens, and O_h for the oxygen of the clay hydroxyl.

supercell		111			111	222	333
E_c		70	100	180	100		
	Exp [219]						
Ts.th.	2.16	2.12	2.11	2.11	2.11	2.17	2.18
Os.th.	2.20	2.44	2.43	2.43	2.43	2.39	2.39
ΔZ	0.01	0.02	0.02	0.02	0.02	0.03	0.03
$d(Si-O_b)$	1.62	1.68	1.68	1.68	1.68	1.64	1.64
$d(Si-O_a)$	1.62	1.63	1.63	1.63	1.63	1.63	1.63
$d(Mg-O_a)$	2.08	2.14	2.14	2.14	2.14	2.13	2.13
$d(Mg-O_h)$	2.05	2.10	2.09	2.09	2.09	2.11	2.11
$d(O_h-H)$		0.97	0.97	0.97	0.97	0.96	0.96
$\angle(O_b-Si-O_b)$	109.5	112.0	112.0	112.0	112.0	109.5	109.3
$\angle(Si-O_b-Si)$	140.5	130.8	131.6	131.6	131.6	137.9	138.2
$\angle(O_b-Si-O_a)$	109.4	106.9	106.8	106.8	106.8	109.5	109.6
$\angle(Mg-Si-O_a)$	121.9	124.7	124.6	124.6	124.6	124.1	124.1
$\angle(O_a-Mg-O_a)$	94.6	90.8	91.0	91.0	91.0	91.7	91.7
$\angle(O_h-Mg-O_a)$	95.3	92.2	92.4	92.4	92.4	92.3	92.3
$\angle(Mg-O_h-Mg)$	96.1	93.7	93.9	93.9	93.9	93.1	93.0
$\angle(Mg-O_h-H)$	120.9	122.6	122.4	122.4	122.4	123.1	123.1

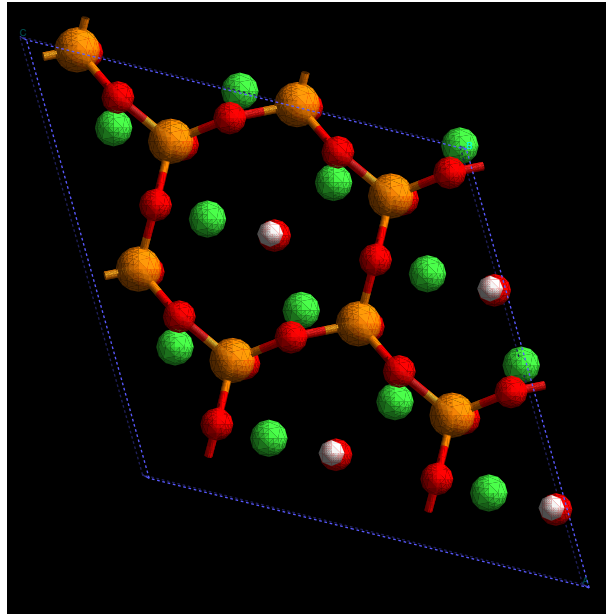


Fig. 5.50. Top view of a talc layer. Oxygen atoms are in red, silicon atoms are in orange, hydrogen atoms are in white, and magnesium atoms are in green

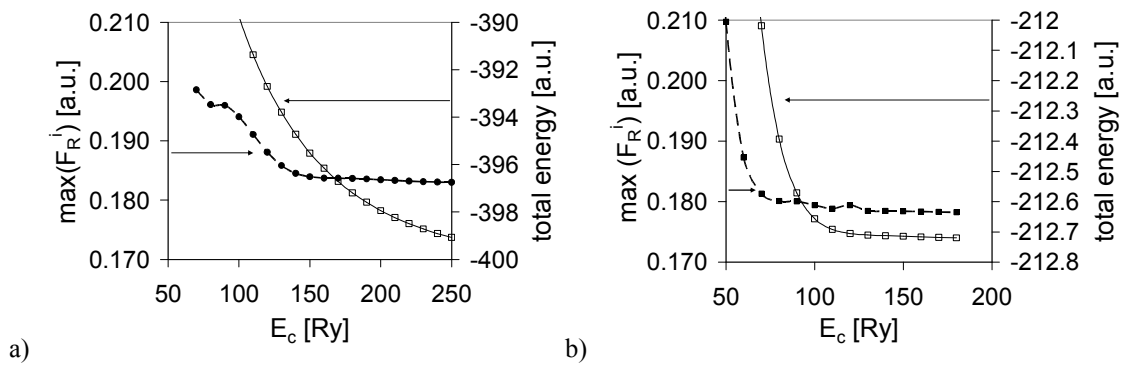


Fig. 5.51. Total energy and maximum component F_R^i of the virtual force (energy gradient) as a function of E_c for the wave function optimization of talc using a) Goedecker pseudopotentials and b) MT pseudopotentials.

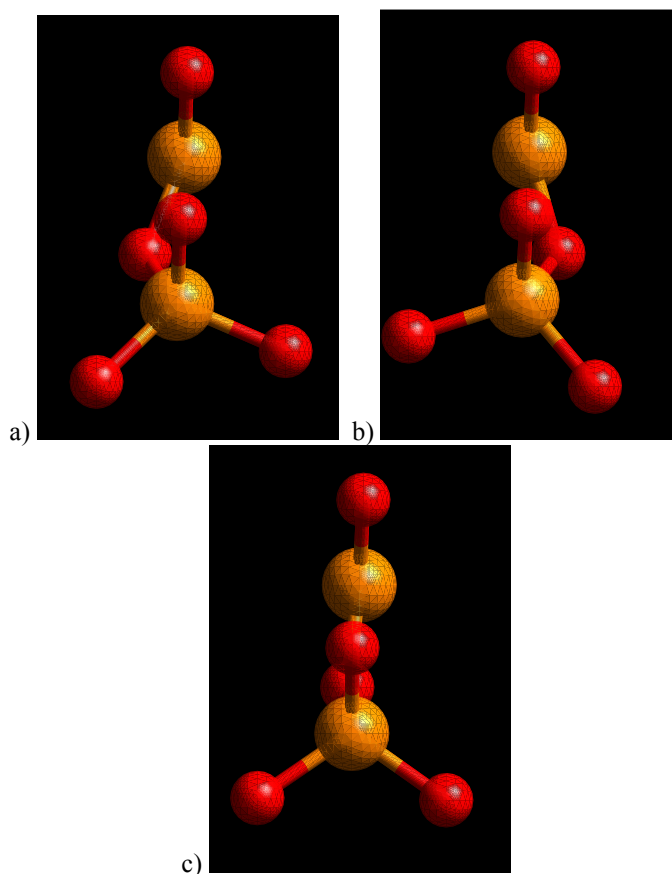


Fig. 5.52. Structures of Talc calculated at 180 Ry from two different initial configurations with final energies of (a) -212.8185 Hartree and (b) -212.8148 Hartree, and c) experimental structure. Silicon atoms are in orange and oxygen atoms in red. The two apical oxygens can be seen at the top of the sketches.

5.2.2.2. GEOMETRY OPTIMIZATION OF PYROPHYLLITE

The results of the optimized structures of pyrophyllite as a function of the plane wave cutoff and as a function of the size of the supercell are shown in Table 5.26. The structure has converged by $E_c = 100$ Ry and for a 211 supercell. Bond length differences between experiment and calculations become smaller than 0.02 Å, and bond angles differences smaller than 3 degrees. However, as mentioned above, it is also important to note that a geometry optimization would represent the structure at 0 K, whereas experimental data have been obtained at room temperature, and represent a real space average.

In Table 5.27 the results (221 cell; 100 Ry) are compared to experiment and to those of previous theoretical studies obtained with other computational schemes, also based on DFT. In particular, Larentzos *et al.* [157] used a 212 supercell, the projector-augmented wave (PAW) approach [20] with plane-wave expansion for the $k = 0$ valence wavefunctions and the Perdew-Wang [21] exchange-correlation functional. Both Refson *et al.* [223] and Sainz-Diaz *et al.* [224] performed calculations on a 111 cell in the pseudopotential framework. A plane-

wave expansion of the valence wavefunctions sampled over the Brillouin Zone was considered in [223], whereas only the Γ point was taken into account in [224], which used localized functions as the basis set. In all cases the lattice parameters were optimized (Table 5.28). Table 5.27 shows that our calculations are within expected deviations, namely analogous to those found between experimental data from different sources.

Table 5.26. Structural parameters for a 111 cell of pyrophyllite at various E_c and at $E_c = 100$ Ry for various size of the supercell. Ts.th. is the thickness of the tetrahedral sheet, Os.th. is the thickness of the octahedral sheet, ΔZ is calculated as the standard deviation around the plane formed by the basal oxygen atoms and gives an indication of the corrugation of basal oxygens along [110], Ψ , where $\cos(\Psi) = \text{Os.th.}/2(\text{Al-O})$ is the octahedral flattening angle, $d(\text{A-B})$ is the average angle between atom A and atom B, $\angle(\text{A-B-C})$ is the average angle between the atoms A, B and C. O_b stand for the basal oxygens, O_a for the apical oxygens, and O_h for the oxygen of the clay hydroxyl.

supercell			111			111	211	221	222	333
E_c			70	100	180	100				
	Exp [220]	Exp [221]								
Ts.th.	2.15	2.15	2.15	2.14	2.14	2.14	2.17	2.17	2.17	2.17
Os.th.	2.13	2.08	2.16	2.16	2.16	2.16	2.15	2.14	2.14	2.14
ΔZ	0.25	0.16	0.32	0.32	0.32	0.32	0.27	0.26	0.26	0.26
Ψ	56.4	57.8	56.3	56.2	56.2	56.2	56.2	56.3	56.3	56.3
$d(\text{Si-O}_b)$	1.61	1.61	1.64	1.64	1.64	1.64	1.63	1.63	1.63	1.63
$d(\text{Si-O}_a)$	1.63	1.62	1.64	1.64	1.64	1.64	1.64	1.64	1.64	1.64
$d(\text{Al-O}_a)$	1.92	1.95	1.95	1.94	1.94	1.94	1.93	1.93	1.93	1.93
$d(\text{Al-O}_h)$	1.89	1.94	1.89	1.89	1.89	1.89	1.90	1.90	1.90	1.90
$d(\text{O}_h\text{-H})$			0.97	0.97	0.97	0.97	0.96	0.96	0.97	0.96
$\angle(\text{O}_b\text{-Si-O}_b)$	109.6	109.5	110.5	110.5	110.5	110.5	109.5	109.5	109.5	109.4
$\angle(\text{Si-O}_b\text{-Si})$	131.6	132.3	127.2	127.7	127.6	127.7	129.5	129.6	129.6	129.7
	144.7	140.7	138.1	138.9	139.0	138.9	141.9	141.7	141.7	141.8
$\angle(\text{O}_b\text{-Si-O}_a)$	109.4	109.4	108.4	108.4	108.4	108.4	109.4	109.5	109.5	109.5
$\angle(\text{Al-Si-O}_a)$	123.3	121.8	124.1	124.1	124.2	124.1	123.6	123.5	123.6	123.6
	128.1	125.8	127.9	127.8	127.8	127.8	128.2	128.0	128.0	128.0
$\angle(\text{O}_a\text{-Al-O}_a)$	92.5	94.0	91.6	91.8	91.8	91.8	92.1	92.2	92.2	92.2
$\angle(\text{Al-O}_a\text{-Al})$	102.1	100.2	101.1	101.3	101.3	101.3	101.7	101.5	101.6	101.6
$\angle(\text{O}_h\text{-Al-O}_a)$	94.5	94.2	95.8	95.8	95.9	95.8	93.9	94.0	94.0	94.0
	92.7	94.1	92.4	92.5	92.4	92.5	92.3	92.4	92.4	92.5
$\angle(\text{Al-O}_h\text{-Al})$	103.5	100.2	103.0	103.1	103.2	103.1	103.0	102.9	102.9	102.9
$\angle(\text{Al-O}_h\text{-H})$			122.7	122.9	122.9	122.9	121.8	121.4	121.3	121.4

Table 5.27. Experimental and calculated structural parameters of pyrophyllite. Ts.th. is the thickness of the tetrahedral sheet, Os.th. is the thickness of the octahedral sheet, ΔZ is calculated as the standard deviation around the plane formed by the basal oxygen atoms and gives an indication of the corrugation of basal oxygens along [110], Ψ , where $\cos(\Psi) = \text{Os.th.}/2(\text{Al-O})$ is the octahedral flattening angle, $d(\text{A-B})$ is the average angle between atom A and atom B, $\angle(\text{A-B-C})$ is the average angle between the atoms A, B and C. O_b stand for the basal oxygens, O_a for the apical oxygens, and O_h for the oxygen of the clay hydroxyl.

	Exp [220]	Exp [221]	This work	Th. [157]	Th. [223]	Th. [224]
T.th.	2.15	2.15	2.17		2.18	2.17
Oc.th.	2.13	2.08	2.14		2.13	2.13
ΔZ	0.25	0.16	0.26		0.21	0.31
ψ	56.4	57.8	56.3		56.9	56.7
$d(\text{Si-O}_b)$	1.61	1.61	1.63	1.62	1.64	1.67
$d(\text{Si-O}_a)$	1.63	1.62	1.64	1.63	1.66	
$d(\text{Al-O}_a)$	1.92	1.95	1.93	1.92	1.95	1.94
$d(\text{Al-O}_h)$	1.89	1.94	1.90	1.89	1.91	1.90
$d(\text{O}_h\text{-H})$			0.96	0.97		0.98
$\angle(\text{O}_b\text{-Si-O}_b)$	109.6	109.5	109.5	109	109.5	110.1
$\angle(\text{Si-O}_b\text{-Si})$	131.6	132.3	129.6	130		
	144.7	140.7	141.7	144		
$\angle(\text{O}_b\text{-Si-O}_a)$	109.4	109.4	109.5	109		108.6
$\angle(\text{Al-Si-O}_a)$	123.3	121.8	123.5	126		
	128.1	125.8	128.0			
$\angle(\text{O}_a\text{-Al-O}_a)$	92.5	94.0	92.2	92	94.8	
$\angle(\text{Al-O}_a\text{-Al})$	102.1	100.2	101.5	102		
$\angle(\text{O}_h\text{-Al-O}_a)$	94.5	94.2	94.0	94		
	92.7	94.1	92.4			
$\angle(\text{Al-O}_h\text{-Al})$	103.5	100.2	102.9	103		
$\angle(\text{Al-O}_h\text{-H})$			121.4			

Table 5.28. Experimental and calculated literature values of the the cell parameters of pyrophyllite.

	Exp [220]	Exp [221]	Th. [157]	Th. [223]	Th. [224]
a	5.16	5.161	5.119	5.239	5.15
b	8.966	8.957	8.911	9.024	8.98
c	9.347	9.351	9.065	9.964	9.21
α	91.18	91.03	90.77	89.732	88.96
β	100.46	100.37	100.96	101.419	99.8
γ	89.64	89.75	89.91	98.558	90

Fig. 5.53 shows top view of the structure of a pyrophyllite layer and Fig. 5.54 shows the top and side views of the silicon-oxygen ring of pyrophyllite. Compared to the talc structure, the number of cations in the octahedral layer is reduced from 3 to 2. As a result, the apical oxygen

atoms are not surrounded by 3 cations, but by 2 aluminum atoms, breaking the 3-fold symmetry found in the talc structure for the 3 magnesium atoms surrounding the apical oxygen atom. The average O_bSiO_a angles of the tetrahedron is that of a perfect tetrahedron. However, we note that the angle involving the basal oxygen atom farther away from the two aluminum atoms is larger than the 109.5 degrees, whereas those involving the two other basal oxygen atoms, closer to the aluminum atoms, are smaller than the 109.5 degrees. This may be explained by the fact that the apical oxygen atom is oriented in the direction of the two aluminum atoms because of the broken 3-fold symmetry. One can see that the basal oxygen atoms are oriented alternatively outward and inward of the hexagonal structure formed by the silicon atoms. This alternative orientation may be explained by the rotation of the tetrahedra as a result of the orientation of the apical oxygen atoms toward the aluminum atoms and the common basal oxygen atoms between the tetrahedral that constrain the structure. As a result, one can see that the hydrogen atom of the hydroxyl does not point perpendicular to the sheet surface, but have a preferential direction toward the basal oxygen atom farther away from the two aluminum atoms. Another consequence is the increase in the corrugation compared to talc.

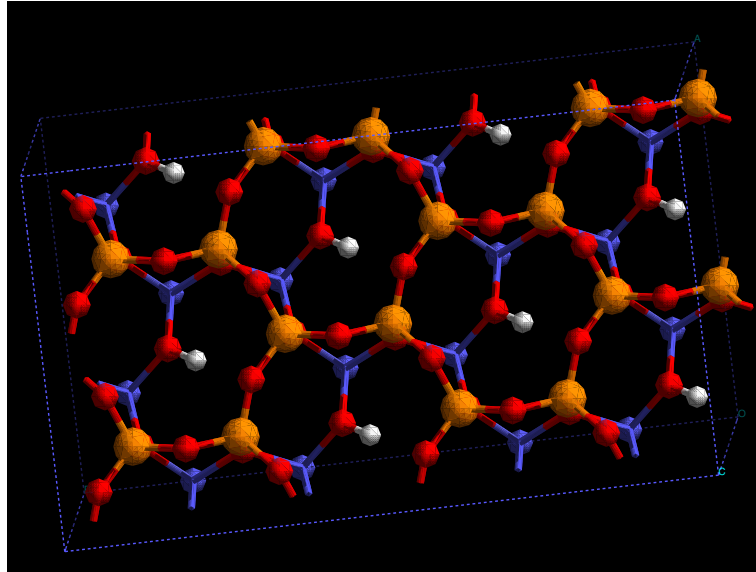


Fig. 5.53. Top view of the tetrahedral sheet of a pyrophyllite layer. Oxygen atoms are in red, silicon atoms are in orange, hydrogen atoms are in white, and aluminum atoms are in blue.

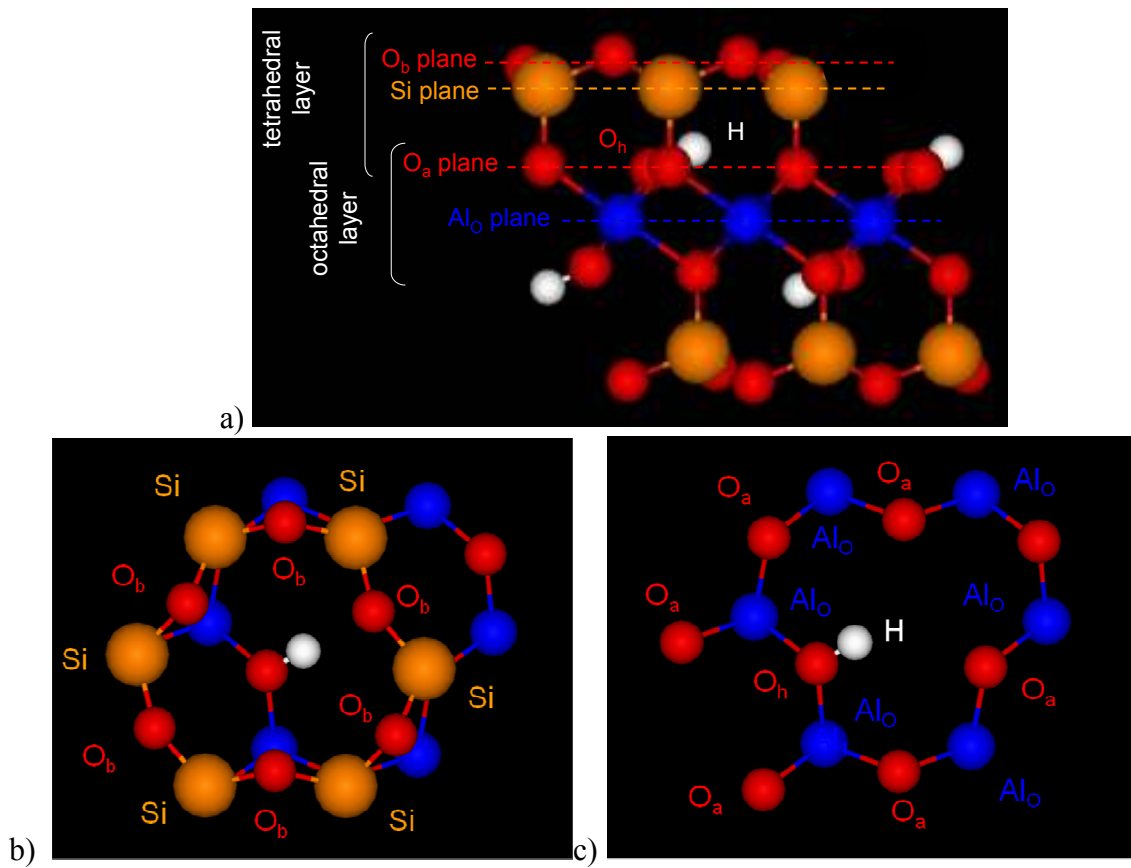


Fig. 5.54 : Structure of pyrophyllite. a) Side view of the silicon-oxygen ring showing the planes of basal oxygen atoms (O_b), silicon atoms (Si), apical oxygen atoms (O_a), and octahedral aluminum atoms (Al_o). Hydroxyl oxygen (O_h) and hydrogen atoms are also indicated. b) Top view of the silicon-oxygen ring showing the labels of the silicon atoms and the basal oxygen atoms. c) Top view of the silicon-oxygen ring showing the labels of the apical oxygen atoms, the aluminum atoms, the hydrogen atom and the hydroxyl oxygen atom. Oxygen atoms are in red, hydrogen atoms in white, silicon atoms in orange, and the aluminum atom in blue.

5.2.2.3. STRUCTURE OPTIMIZATION OF THE VOLATILES AND SOME OF THEIR ELECTRONIC PROPERTIES

Table 5.29 to Table 5.35 show the comparison between calculations and experimental results for the structure and the electronic properties of the single volatile molecules used in the experiments (water, ethanol, ethyl acetate, pyridine, toluene, n-octane, and the nitrogen dimer). In general calculations are in good agreements with experimental data with differences (marked in bold) lower than 0.02 \AA in bond lengths, lower than 2° in angles, and lower than 5 % for the ionization potentials, dipole moments and polarizabilities. Exceptions are the ionization potential of the nitrogen dimer which is 7 % higher than the experimental value, the dipole moments of ethanol, ethyl acetate and toluene which differ by 9-15 % from experiment, and the polarizability of water which differ by 17 % from experiment. The experimental data we have on n-octane are the one of an n-octane crystal, whereas in our calculations all volatile molecules were treated as isolated molecules, so that some discrepancies can be found between calculations and experimental data of n-octane.

Table 5.29. Experimental and calculated structural features and electronic properties of one water molecule (lengths in \AA , angles in degrees, ionization potentials in eV, and dipole moments in Debye). The experimental data are taken from Ref [225].

		Th.	Exp.
Bond length	OH	0.975	0.9575
Bond angle	HOH	103.7	104.51
Ionization potential	adiabatic	12.532	12.612 \pm 0.01
	vertical	12.532	
Dipole moment		1.795	1.854
Polarizability		1.60	1.45

Table 5.30. Experimental and calculated structural features and electronic properties of ethanol (lengths in Å, angles in degrees, ionization potentials in eV, and dipole moments in Debye). The experimental data are taken from Ref [225].

		Th.	Exp.
Bond length	CO	1.447	1.431
	C _a H	1.105	1.100
	OH	0.974	0.971
	C _b H	1.098	1.090
	CC	1.518	1.512
Bond angles	CCO	107.8	107.8
	C _b C _a H	110.5	111.0
	COH	107.6	105.0
	C _a C _b H	110.3	110.0
Ionization potential	adiabatic	9.87	10.47 ± 0.02
	vertical	10.12	
	average		
Dipole moment	average	1.53	1.69
	trans		1.44
	gauche		1.68
Polarizability	average	5.27	5.41
	trans		5.11

Table 5.31. Experimental and calculated structural features and electronic properties of ethyl acetate (lengths in Å, angles in degrees, ionization potentials in eV, and dipole moments in Debye). The experimental data are taken from Ref [225], except for the bond lengths and bond angles that are taken from Ref [226].

		Th.	Exp.
Bond length ^[225]	C ₃ -H ₇	1.097	1.105
	C ₁ =O ₂	1.221	1.203
	C ₁ -C ₃	1.510	1.508
	C ₁ -O ₄	1.363	1.345
	O ₄ -C ₅	1.467	1.448
	C ₅ -C ₆	1.514	1.515
Bond angles	O ₂ C ₁ C ₃	125.5	124.1
	O ₂ C ₁ O ₄	123.5	124
	C ₁ O ₄ C ₅	115.0	115.7
	O ₄ C ₅ C ₆	107.6	108.2
	C ₁ C ₃ H	109.9	107.7
	C ₅ C ₆ H	110.6	108.1
Ionization potential [225]	adiabatic	9.55	10.01 ± 0.05
	vertical	9.83	
Dipole moment		2.03	1.78
Polarizability		9.22	9.7

Table 5.32. Experimental and calculated structural features and electronic properties of pyridine (lengths in Å, angles in degrees, ionization potentials in eV, and dipole moments in Debye). The experimental data are taken from Ref [225].

		Th.	Exp
Bond length	N-C _a	1.341	1.34
	C _b -C _c	1.397	1.394
	C _b -H _b	1.090	1.081
	C _a -C _b	1.395	1.395
	C _a -H _a	1.094	1.084
	C _c -H _c	1.091	1.077
Bond angles	C _a NC _a	117.0	116.8
	C _a C _b C _c	118.5	118.5
	NC _a H _a	116.0	115.9
	NC _a C _b	123.7	123.9
	C _b C _c C _b	118.5	118.3
	C _c C _b H _b	121.2	121.3
Ionization potential	adiabatic	8.80	
	vertical	9.25	
			9.25
Dipole moment		2.234	2.215
Polarizability		9.63	9.5

Table 5.33. Experimental and calculated structural features and electronic properties of toluene (lengths in Å, angles in degrees, ionization potentials in eV, and dipole moments in Debye). The experimental data are taken from Ref [225].

		Th.	Exp.
Bond length	CC (ring)	1.399	1.399
	CH (average)	1.094	1.11
	CH diff	0.007	0.01
Ionization potential	adiabatic	8.52	
	vertical	8.68	
			8.82 ± 0.01
Dipole moment		0.433	0.375
Polarizability		12.51	12.26 - 12.3

Table 5.34. Experimental and calculated structural features and electronic properties of n-octane (lengths in Å, angles in degrees, ionization potentials in eV, and dipole moments in Debye). The experimental data are taken from Ref [227].

		Th.	Exp.
Bond length	C ₁ H ₁	1.100	0.93 ± 0.04
	C ₂ H ₄	1.099	1.07 ± 0.04
	C ₂ H ₅	1.100	1.15 ± 0.04
	C ₁ H ₇	1.103	1.03 ± 0.04
	C ₁ H ₈	1.103	1.08 ± 0.04
	C ₆ H ₉	1.104	1.02 ± 0.04
	C ₆ H ₁₀	1.104	1.03 ± 0.04
	C ₁₁ H ₁₃	1.103	0.97 ± 0.04
	C ₁₁ H ₁₄	1.104	1.12 ± 0.04
	C ₁ C ₂	1.531	1.534 ± 0.07
	C ₁ C ₂	1.531	1.522 ± 0.07
	C ₂ C ₃	1.532	1.529 ± 0.07
	C ₃ C ₄	1.532	1.516 ± 0.07
Bond angles	H ₃ C ₂ H ₄	107.5	104.0
	H ₃ C ₂ H ₅	107.7	118.0
	H ₄ C ₂ H ₅	107.6	110.0
	H ₇ C ₁ H ₈	106.0	113.0
	H ₉ C ₆ H ₁₀	105.8	108.0
	H ₁₃ C ₁₁ H ₁₄	105.9	115.0
	C ₂ C ₁ C ₆	113.1	114.4
	C ₁ C ₆ C ₁₁	114.0	113.3
	C ₆ C ₁₁ C ₁₂	113.3	112.2
Ionization potential	adiabatic	8.96	
	vertical	9.50	9.82
Dipole moment		0.00374	
Polarizability		15.98	15.9

Table 5.35. Experimental and calculated structural features and electronic properties of the nitrogen dimer (length in Å, ionization potentials in eV)

		Th.	Exp.
Bond length	N-N	1.107	1.098
Ionization potential	adiabatic	16.39	
	vertical	16.76	15.5808
Dipole moment		0	0
Polarizability		1.82	1.7403

5.2.2.4. TESTS OF THE SODIUM PSEUDOPOTENTIAL

In this section calculated and experimental values for the characteristics of molecules containing sodium cations are compared. We emphasize that non-linear core corrections (NLCC) [218] to the exchange-correlation functional are mandatory for a good approximation to the pseudopotential of elements like sodium when treated as a one-electron system, because there is non negligible overlap between the $n=2$ core shell and the valence shell. Therefore in general calculations without this correction are less valid. The major effect of ignoring NLCC is the shrinking of the atomic radius; better agreement found with this approximation for whatever quantity must be considered fortuitous. It is true however that even the NLCC is an approximation and should be tested against semi-core or accurate all-electron calculations.

The pseudopotentials for sodium were tested on the bond lengths, ionization potentials and binding energies of Na_2 , NaH, NaO, and NaOH and the binding energies and radii of hydration of a sodium cation surrounded by 1 to 6 water molecules. Experimental data were taken from Ref [225], except for the ionization potentials of NaO and NaOH that were taken from Ref [228], and the binding energies of water on the sodium cation from Ref [229]. Table 5.36 to Table 5.39 show that calculations using NLCC are in good agreement with experimental values with bond length errors lower than 0.02 \AA , and errors in ionization potentials and binding energies lower than 5 %. We note also that the results from the calculations without the use of NLCC are not as good as the one using non-linear core correction, with a maximal error of 0.18 \AA for the bond length of Na_2 , and a maximal error of 35 % for the ionization potential of Na_2 . The limited accuracy of the pseudopotential emerges in the value of the binding energy of NaH as expected in view of the small size of hydrogen. Comparison of the present calculations of the hydration energies and binding radii of water molecules around a sodium cation with calculations from the literature are within expected deviations

Table 5.36. Experimental and calculated ionization potentials of the sodium atom using (Values are given in eV).

	Exp. [230]	Th.		
		All electrons	with NLCC	without NLCC
First ionization potential	5.139	5.143	5.372	5.143

Table 5.37. Experimental and calculated structural features and electronic properties of Na₂, NaH, NaO, and NaOH (bond length in Å, angles in degrees, ionization potentials in eV, and binding energies in kJ/mol). Experimental data are from [225], except for the ionization potentials of NaO and NaOH, which are from [228]. The experimental binding energies are given at 0 K and the Zero point energies (ZPE) are indicated.

Chemical	Properties		Exp. [225]	Th. (this work)	
				with NLCC	without NLCC
Na ₂	Bond length		3.0789	3.070	3.253
	Ionization potential	adiabatic	4.88898 ± 0.00016	5.036	4.601
		vertical		5.142	4.699
Binding energy		69.9	71.7	47.9	
NaH	Bond length		1.8873	1.888	1.969
	Binding energy		181.97 ± 0.25 (ZPE 7.0)	177	166
NaO	Bond length		2.052	2.065	2.137
	Ionization potential	adiabatic	7.41 ^[228]	7.77	7.43
		vertical		7.99	7.68
Binding energy		252.4 ± 16.7 (ZPE 2.9)	266	260	
NaOH	Bond length	Na-O	1.93	1.94	2.013
		OH	0.97	0.965	0.965
	Bond angle		179	179	179.1
	Ionization potential	adiabatic	7.89 ^[228]	7.82	7.57
vertical		8.04		7.79	

Table 5.38. Experimental and calculated binding energies of the additional water molecules for one to six water molecules around a sodium cation.

	Numer of water molecules	Exp. [229] [kcal/mol]	Th. [176] [kcal/mol]	Th. (This work)		
				with NLCC		without NLCC
				[kcal/mol]	[kJ/mol]	[kcal/mol]
Binding energy of the last molecule	1	24.0	24.1	24.3	101.6	21.1
	2	19.8	20.8	21.8	91.1	19.2
	3	15.9		18.0	75.2	16.3
	4	13.8	14.1	12.5	52.5	12.3
	5	12.2		12.2	51.0	11.5
	6	10.6		9.0	37.7	9.0

Table 5.39. Calculated radii of hydration (Na-O interatomic distances), in Å, of water molecules around a sodium cation.

	Numer of water molecules	Th. [176]	Th. (This work)	
			with NLCC	without NLCC
Radius of hydration	1	2.215	2.20	2.30
	2	2.244	2.21	2.31
	3		2.24	2.34
	4	2.368	2.30	2.39
	5		2.33	2.41
	6		2.37	2.44

CHAPTER 6 EVAPORATION OF PURE LIQUIDS

6.1. INTRODUCTION

This chapter presents the results on the measurements of the evaporation of bulk volatile liquids using the TG-DSC-MS Sensys instrumentation. The evaporation is measured as a function of temperature, carrier gas flow rate and the type of volatile. The experimental data are compared with FEM calculations and with calculations using a semi-analytical model. The results provide a validation of the experimental and modeling approach.

6.2. SEMI-ANALYTICAL MODEL

Fig. 6.55 shows the evaporation of a 5 μl water droplet at 25 $^{\circ}\text{C}$ under a dry nitrogen carrier gas flow rate of 5 ml/min. The droplet was deposited at the bottom of the cylindrical crucible of the TG-DSC-MS instrument. Comparison between the finite element method calculations (Fig. 6.55c) and experimental results (Fig. 6.55b) shows the calculation to be in good agreement with the experimental values.

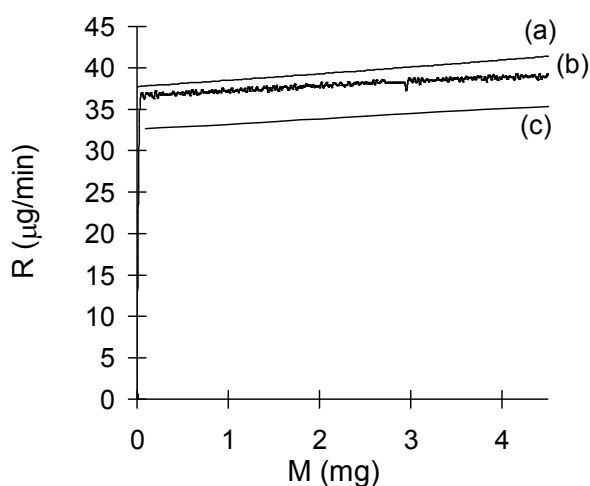


Fig. 6.55. Rate of evaporation R of a 5 μl water droplet at 25 $^{\circ}\text{C}$ under a dry nitrogen carrier gas flow rate of 5 ml/min as a function of the amount of water M left in the crucible. (a) Semi-analytical solution, (b) Experimental data, (c) Finite element simulation

The results of the simulations in terms of convective flux intensity and gas concentration of the water vapor can be used to develop a semi-analytical equation for the rate of evaporation. This model will be used to explain the dependence of the rate of evaporation on material, environmental and geometrical parameters and for rationalizing the release of water from sodium smectite clay granules. In particular, the results (Fig. 6.56) showed that, inside the crucible, the intensity of the convective flux is significantly stronger than the diffusive flux, and that the gas phase concentration is approximately constant along a line of constant height below the top of the crucible. This means that, to a first approximation, the evaporation may be considered as 1-dimensional diffusion inside the crucible and that the evaporated molecules may be considered to be diluted in the carrier gas flow at the top of the crucible.

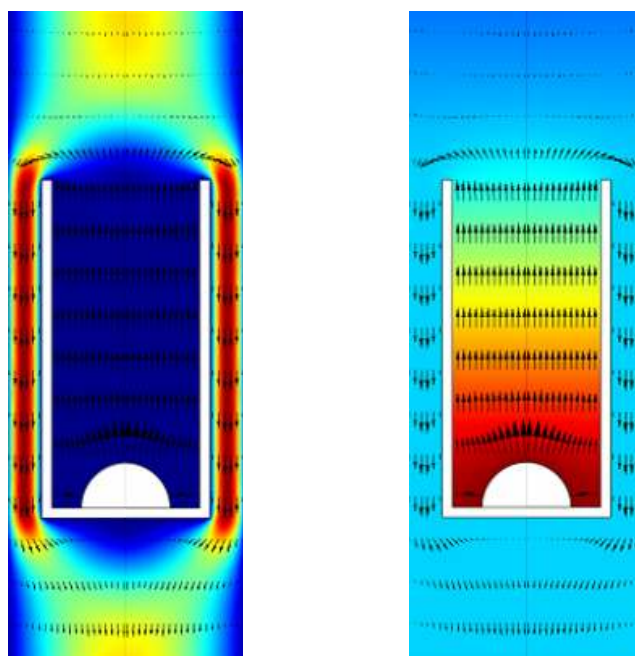


Fig. 6.56. Convective flux (left) and concentration (right) in the column and crucible of the TG-DSC-MS instrument calculated by FEM for the evaporation of a 5 μl water droplet.

Based on the conclusions and Fick's second law, one may derive from Eq. (6.104) an approximate one dimensional semi-analytical solution for the rate of evaporation, given by Eq. (6.105) and (6.106):

$$\begin{aligned}
 R &\cong -S_0 J = -S_0 D_{gas} \nabla c \cong -S_0 D_{gas} \frac{\Delta c}{h} \\
 &= -S_0 D_{gas} \frac{c_s - c_{top}}{h} = -S_0 D_{gas} \frac{c_s - \frac{p_{tot}}{kT} \frac{|R|}{|R|+F}}{h} = -S_0 D_{gas} \frac{\frac{p_s}{kT} - \frac{p_{tot}}{kT} \frac{|R|}{|R|+F}}{h}
 \end{aligned} \tag{6.104}$$

$$\Rightarrow R = \frac{-b + \sqrt{b^2 - 4ac}}{2a} \tag{6.105}$$

where

$$\begin{aligned}
 a &= \frac{kTh}{S_0 D_{gas}} \\
 b &= \frac{kThF}{S_0 D_{gas}} - p_s + p_{tot} \\
 c &= -p_s F
 \end{aligned} \tag{6.106}$$

where R is the rate of evaporation, h is the height between the top of the droplet and the top of the crucible, S_0 is the surface of the base of the crucible, J is the evaporation flux, k is the Boltzmann constant, T is the temperature, c_s is the equilibrium partial vapour concentration at the surface of the sample, c_{top} is the partial vapour concentration at the top of the crucible, p_s is the equilibrium partial vapour pressure at the surface of the sample, p_{tot} is the total pressure, and F is the carrier gas flow rate. c_s and p_s are given by the saturated vapour concentration and saturated vapour pressure in the case of a liquid.

Results of the semi-analytical solution for the evaporation of the 5 μl water droplet, plotted in Fig. 6.55a, is in good agreement with the experimental curve. The better agreement of the semi-analytical calculation with the experimental data, compared to the finite element calculation is fortuitous. The higher rate of release calculated with the semi-analytical solution, compared to the one obtained from finite element calculations, is due to the fact that the diffusion of the water molecules in the gas phase extends above the dilution line at the top of the crucible defined above, increasing therefore the concentration gradient and, by Eq. (6.104), the rate of release.

The true droplet shape is close to that of a spherical cap, because of the decrease of the contact angle with evaporation. However, for simplicity, its mass can be reasonably well approximated by considering a half oblate spheroid. Using this approximation and assuming strong dilution and small droplet height compared to the height of the crucible, a linear

relationship is obtained between the rate of evaporation R and the mass M of the droplet, in agreement with the curves shown in Fig. 6.55:

$$\begin{aligned}
 R &\cong -S_0 D \frac{c_s - c_{top}}{h} \cong -S_0 D_{gas} \frac{c_s}{h} \\
 &= -\frac{S_0 D_{gas} c_s}{h_0} \frac{1}{1 - \frac{M}{\rho \frac{2}{3} \pi r_0^2 h_0}} \cong -\frac{S_0 D_{gas} c_s}{h_0} \left(1 + \frac{M}{\rho \frac{2}{3} \pi r_0^2 h_0}\right)
 \end{aligned} \tag{6.107}$$

where V is the volume of the half oblate spheroid, ρ is the density of the droplet, r_0 is the bottom radius and h_0 is the height of the crucible.

6.3. EFFECT OF TEMPERATURE

The temperature dependence of the pressure p_s at the sample surface can be obtained from the Clausius-Clapeyron equation:

$$p_s = A e^{-\frac{\Delta H}{kT}} \sim e^{-\frac{\Delta H}{kT}} \tag{6.108}$$

Where A is a prefactor and ΔH is the enthalpy of vaporization of the chemical. The enthalpy of vaporization was assumed to be constant over the temperature range considered. Using Eq. (6.104) and (6.108), and the temperature and pressure dependence on the gas diffusion coefficient (Eq. (5.102)), and assuming strong dilution, the approximate dependence of the rate of evaporation on the temperature and total pressure is then given by:

$$R \sim \frac{T^{n-1} e^{-\frac{\Delta H}{kT}}}{P_{tot}} \tag{6.109}$$

The heat of vaporization of water measured with the DSC during the evaporation of the water droplet was found to be 43.9 kJ/mol \pm 0.3 kJ/mol, which is the same as the reported value of the enthalpy of vaporization of water, i.e. 43.99 kJ/mol at 25 °C. Eq. (6.109) was used to calculate the rates of evaporation of water at 20 °C, 30 °C and 35 °C from one experimental data curve at 25 °C. The results, shown in Fig. 6.57, were in very good agreement with experimental data, with a decrease of the rate of evaporation of around 25 % for a decrease in temperature of 5 °C.

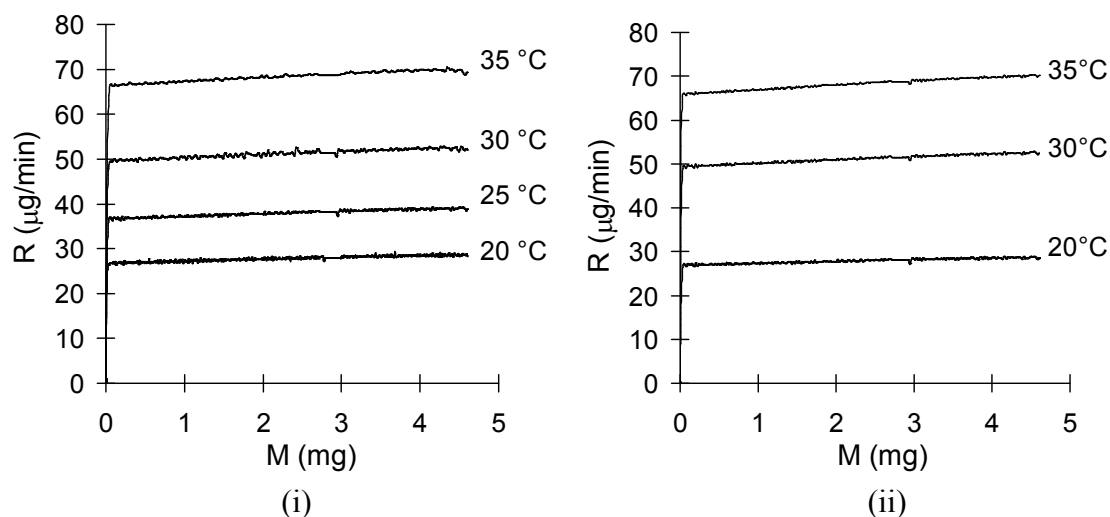


Fig. 6.57. (i) Experimental data for the rate of evaporation R of a $5 \mu\text{l}$ water droplet at 20°C , 25°C , 30°C , and 35°C under a dry nitrogen flow rate of 5 ml/min as a function of the amount of water M left in the crucible. (ii) Numerical calculations of the rate of evaporation of a $5 \mu\text{l}$ water droplet at 20°C , 30°C , and 35°C , using the experimental data at 25°C .

6.4. EFFECT OF CARRIER GAS FLOW RATE

The effect of the carrier gas flow rate on the initial rate of evaporation of a $5 \mu\text{l}$ water droplet is shown in Fig. 6.58. Here again, semi-analytical calculations and finite element simulations are in good agreement with the experimental measurements. We observe an increase in the rate of evaporation with increased carrier gas flow rate due to the stronger pressure gradient, as may be seen from Eq. (6.104). We note that even for this simple case, the approximate semi-analytical solution is already relatively complex and specific to the environmental geometry.

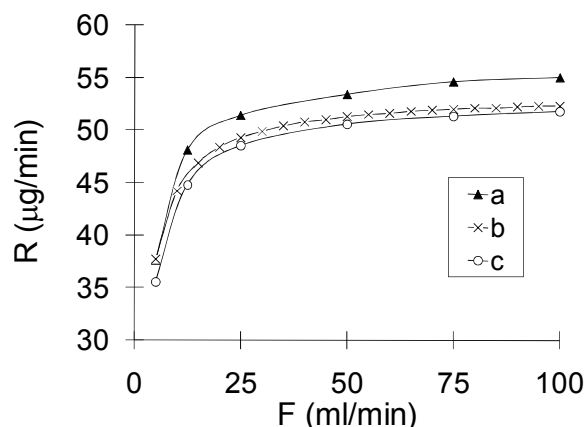


Fig. 6.58. Initial rate of evaporation R of a $5 \mu\text{l}$ water droplet at $25 \text{ }^\circ\text{C}$ as a function of the dry nitrogen carrier gas flow rates F . a) analytical calculation, b) experimental data, c) finite element simulation

6.5. EFFECT OF THE TYPE OF CHEMICAL

The effect of the type of chemical on the rate of evaporation was measured using 6 liquid volatiles (pyridine, ethyl acetate, ethanol, water, toluene, and n-octane) with different shapes and functional groups. The results of finite element method calculations, shown in Fig. 6.59, were in agreement with the experimental behaviours, for rates of evaporations ranging from around $0.5 \mu\text{mol}/\text{min}$ to $4.6 \mu\text{mol}/\text{min}$. A comparison between finite element method calculations and experimental results shows that the curves calculated by finite element methods are systematically lower than the measured values by 17.3 %, on average, reproducing the trends observed experimentally. This shift is not well understood, but errors on input parameters, like the carrier gas flow rate, the pressure, and the dimensions of the instrumentation can influence the results in a systematic way. If numerical values of the rate of evaporation relative to the values for water are considered, the average error between calculations and experiments decreases to 7.4 %. This error can be attributed to errors on material constants, like vapour pressures and gas diffusion coefficients.

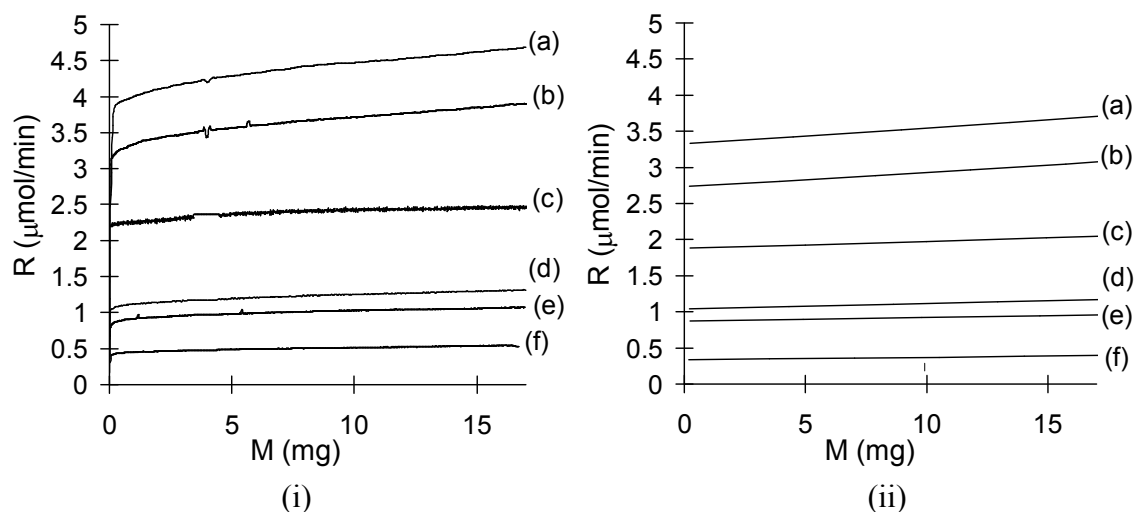


Fig. 6.59. (i) Experimental data and (ii) finite element simulations of the rate of evaporation R of (a) ethyl acetate, (b) ethanol, (c) water, (d) toluene, (e) pyridine, and (f) n-octane, at 25 °C under a dry nitrogen carrier gas flow rate of 5 ml/min as a function of the amount of volatiles M left in the crucible

6.6. CONCLUSION

The evaporation of bulk volatile liquids was analyzed by thermogravimetry and differential calorimetry using the TG-DSC-MS Sensys instrumentation. The results were in satisfactory agreement with FEM calculations (average relative error of 7.4 %) and with calculations using a semi-analytical model derived from the FEM calculations. The evaporation is dominantly diffusive inside the crucible and convective outside it. The rate of evaporation is determined by the equilibrium pressure at the surface of the volatile liquid, i.e. the saturated vapour pressure, by the gas diffusion coefficient of the volatile inside the crucible, by the carrier gas flow rate outside the crucible and by the geometry of the instrumentation. Comparison between experimental data and calculations allowed one to rationalize the effect of the temperature, carrier gas flow rate and type of volatile on the rate of evaporation. In particular, the dependence on the temperature could be modeled by an Arrhenius-type of equation derived from the semi-analytical model, and a decrease of the rate of the temperature of 5 % led to a decrease of the rate of evaporation of around 25 %. The heat of vaporization measured during the evaporation of water was found to be the same as the enthalpy of vaporization of water. This was taken as an indication that the surface vapour pressure is the equilibrium saturated vapour pressure, suggesting adequate use of boundary conditions.

For such relatively simple thermodynamic conditions, this semi-analytical model takes already a complex form and is specific to the geometry of the instrumentation, which raises

questions as to the general use of an analytical approach to modeling similar real release systems, and hence the general use of phenomenological models. The conditions used in the semi-analytical model are not specific to bulk volatile liquids only, but can be applied to the release of volatiles from an adsorbent assuming homogenous concentration of the volatile inside the adsorbent. In this case, the surface equilibrium pressure will be given by the equilibrium desorption isotherm of the volatile on the adsorbent.

CHAPTER 7 CHARACTERIZATION OF THE CLAY

7.1. INTRODUCTION

This chapter presents results on the characterization of the Kunipia-F clay. The clay is characterized in terms of elemental analysis, from which one obtains the chemical formula of the clay necessary for the modeling of the clay by *ab initio* calculations for the investigation of the interactions between the volatiles. Also comparison between the structure and elemental analysis of the as-received and the purified clay allows one to check the purity of the clay in terms of smectite content and type of counter ion. The morphology of the clay aggregates and the clay platelets are also characterized for the modeling of the tortuosity between clay platelets.

7.2. ELEMENTAL ANALYSIS AND PURITY OF THE CLAY

Table 7.40 summarizes the measured properties of the clay. The chemical formula of the clay was calculated from the elemental analysis of the as-received and the purified clay. Table 7.41 shows properties of the clay calculated using the unit cell chemical formula of the purified clay as given in the table. For the calculations, the unit cell of the clay was assumed to have the same lattice dimensions as that of pyrophyllite [231], except for the length of the c-axis that was taken as the average value of the interlayer distances of dry Na-smectites found in the literature [46,232,233,44,234,235,236,237,70,52], i.e. $9.86 \text{ \AA} \pm 0.16 \text{ \AA}$.

Table 7.40: Measure clay properties

Property	Value
Unit cell chemical formula from elemental analysis of the as-received clay	$\text{Na}_{0.94}\text{Ca}_{0.06}[(\text{Si}_{7.76}\text{Al}_{0.24})\text{O}_{20}(\text{OH})_4\text{Al}_{3.32}\text{Fe}_{0.22}\text{Mg}_{0.64}]$
Unit cell chemical formula from elemental analysis of the purified clay	$\text{Na}_{0.84}\text{Ca}_{0.08}[(\text{Si}_{7.8}\text{Al}_{0.2})\text{O}_{20}(\text{OH})_4\text{Al}_{3.06}\text{Fe}_{0.22}\text{Mg}_{0.68}]$
Cation content of the purified clay	Na+ (91%), Ca2+ (9%)
Measured apparent density (g/cm^3)	2.62
Peak of the measured distribution of the platelets diameter (nm)	120
Mean of the measured distribution of the platelets diameter (nm)	566

Table 7.41: Clay properties calculated from the chemical formula of the purified clay

Property	Value
Molecular weight per unit cell chemical formula of the Kunipia F clay (g/mol)	746.38
Volume of a unit cell of Na-smectite (\AA^3)	463.95
Basal plane surface area of Na-smectite (\AA^2)	92.53
Density calculated from chemical formula and unit cell volume of Na-smectite (g/cm^3)	2.76
Calculated specific total surface area (m^2/g)	747
Mean van der Waals radius of a water molecule (\AA)	1.41
Total number of water molecules per unit cell chemical formula	11.64
Number of oxygen sites per unit cell chemical formula	12

The elemental analysis of the non-purified clay was in agreement with results from Nakashima [238]. The as-received clay and the purified clay show very similar XRD spectra with clearly visible high order reflection peaks (Fig. 7.60) indicating good purity of the clay, as previously reported [103,239]. The elemental analysis of the two clays was also very similar, with low ferric content and sodium as the main counter-ion, again suggesting high purity. Moreover the calculated density was close to the measured density. Assuming that a unit cell of the clay has the same surface area as the unit cell of pyrophyllite, one finds a specific surface area of $747 \text{ m}^2/\text{g}$. By dividing the surface area per unit cell into squares of width equal to the Van der Waals diameter of a water molecule (1.41 \AA [240]), it may be shown that each unit cell could ideally accommodate around 12 water molecules, which is also the same as the number of oxygen sites on the clay surface per unit cell. There is also about one charge, or one sodium counter ion, per unit cell chemical formula.

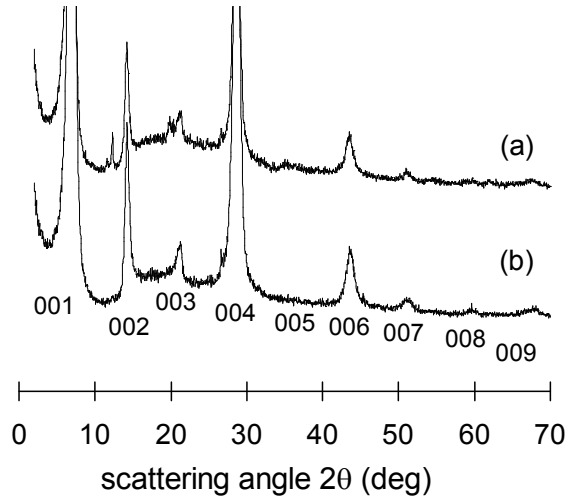


Fig. 7.60. XRD measurements on a) as-received clay, and b) purified clay. The different reflection planes are labeled from 001 to 009.

7.3. MORPHOLOGY AND SIZE DISTRIBUTION OF THE CLAY

7.3.1. Dimensions of the smectite platelets: Light scattering measurements

Static light scattering measurements were performed on smectite aqueous solutions of the Kunipia-F clay at scattering angles of 20° to 130° in steps of 10° . For each scattering angle, distributions of diffusion coefficients R_H of the clay platelets were obtained from fits of the experimental intensity correlation functions g_i (Fig. 7.61) by minimization of Eq. (7.110) using the CONTIN code [241] and using the Stocks-Einstein equation (Eq. (7.111)).

$$\left\| \sum_i \left(g_i - e^{D_i q^2 t} \right) \right\|^2 + \alpha^2 REG \quad (7.110)$$

$$R_H = \frac{kT}{6\pi\eta D} \quad (7.111)$$

$$q(\theta) = \frac{n4\pi \sin(\theta/2)}{\lambda} \quad (7.112)$$

where D are the diffusion coefficients of the platelets, t is the time, q is the scattering vector given by Eq. (7.112), k is the Boltzmann constant, T is the temperature, η is the viscosity of the solvent (i.e. water), n is the reflection index of the solvent, θ is the scattering angle, and λ is the wavelength of the laser light. The regularizer REG penalizes the fit for deviations from

behavior expected on the basis of statistical prior knowledge or parsimony. The relative strength of the regularizer is determined by α , the regularizer parameter.

The distribution functions of hydrodynamic radius are shown in Fig. 7.62 and Fig. 7.63.

It is worth noting that Hansen [242] calculated an approximate formula for the translation friction coefficient of cylinders by approximating the shape of the cylinder by small spheres, such that the diameter of the cylinders d_c can be obtained from knowledge of the hydrodynamic radius R_H by solving Eq. (7.113).

$$\frac{R_H}{R_s} = 1.0304 + 0.0193x + 0.06229x^2 + 0.004x^3 + 0.00166x^4 + 2.66x10^{-6}x^7 \quad (7.113)$$

$$x = \ln(L/d_c) \quad (7.114)$$

where L is the thickness of the cylindrical clay platelet, and R_s is the radius of a sphere with equivalent volume as that of the cylinder.

However the formula was given for aspect ratios L/d_c between 0.01 and 100. In the case of the clay platelets with $L=9.86$ nm, this corresponds to R_H values lower than 30, which is significantly lower than the range of values shown in Fig. 7.62 and Fig. 7.63. Fig. 7.62 shows also that the regularizer parameter α do not change significantly the peak position of the calculated distributions. However, the distribution changes significantly with the scattering angle (Fig. 7.63). This dependence is due to the fact that the scattered intensity depends on the mass of the scattered object, and thus on the size of the platelets. This is therefore a clear indication that the real distribution of platelet diameters has a large polydispersity. In these conditions, the distributions obtained by light scattering measurements cannot be considered as the real distribution of the average platelet diameters.

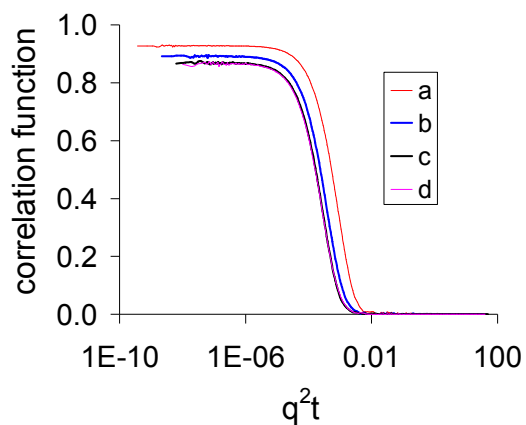


Fig. 7.61. Intensity correlation function as a function of q^2t for scattering angles of a) 20° , b) 50° , c) 90° , and d) 130° . q is the scattering vector and t is the time.

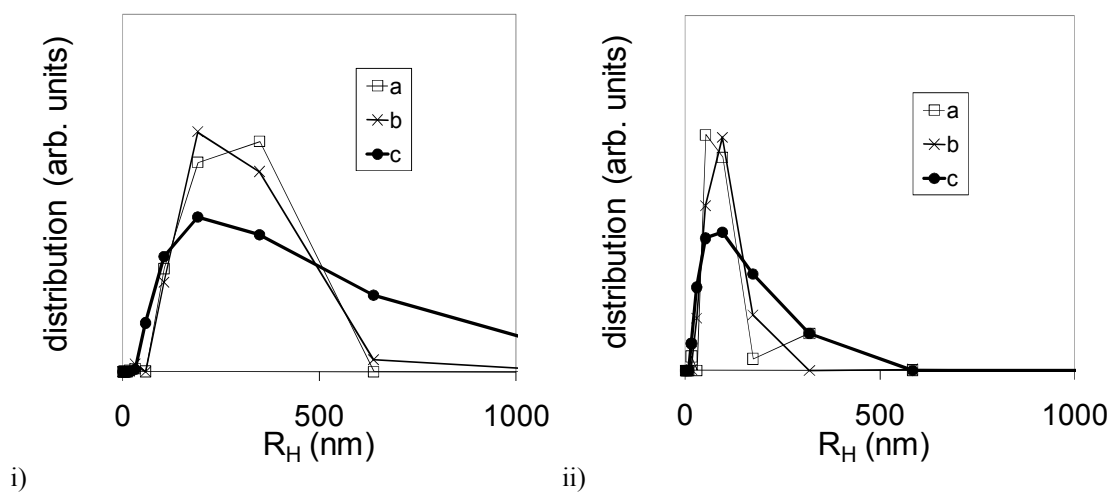


Fig. 7.62. Distributions of hydrodynamic radius R_H for scattering angles of i) 20° and ii) 130° , and values of α equal to a) 0, b) 0.01, and c) 1.

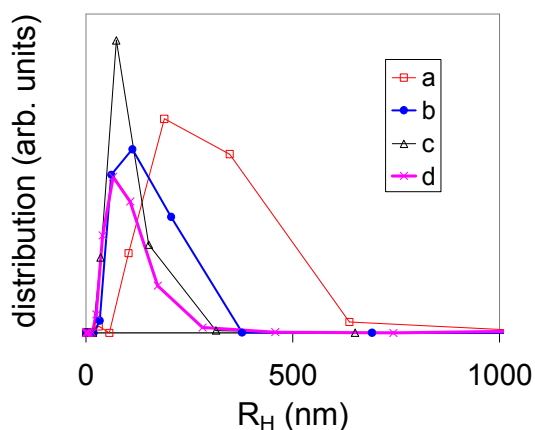


Fig. 7.63. Distributions of hydrodynamic radius R_H for $\alpha=0.01$ and scattering angles of a) 20° , b) 50° , c) 90° , and d) 130° .

7.3.2. Dimensions of the smectite platelets: TEM measurements

As alternative to the light scattering measurements, image analysis on TEM micrographs were performed. Fig. 7.64 shows the heterogeneous polygonal polydispersed clay platelets and Fig. 7.65 shows the distribution of platelets diameter of the clay, obtained from micrographs, with a peak at 120 nm and a mean value of 566 nm. The measured values could be approximated by a lognormal distribution function, which is the most commonly observed crystal size distribution generated by a proportionate (size-dependent) crystal growth [243].

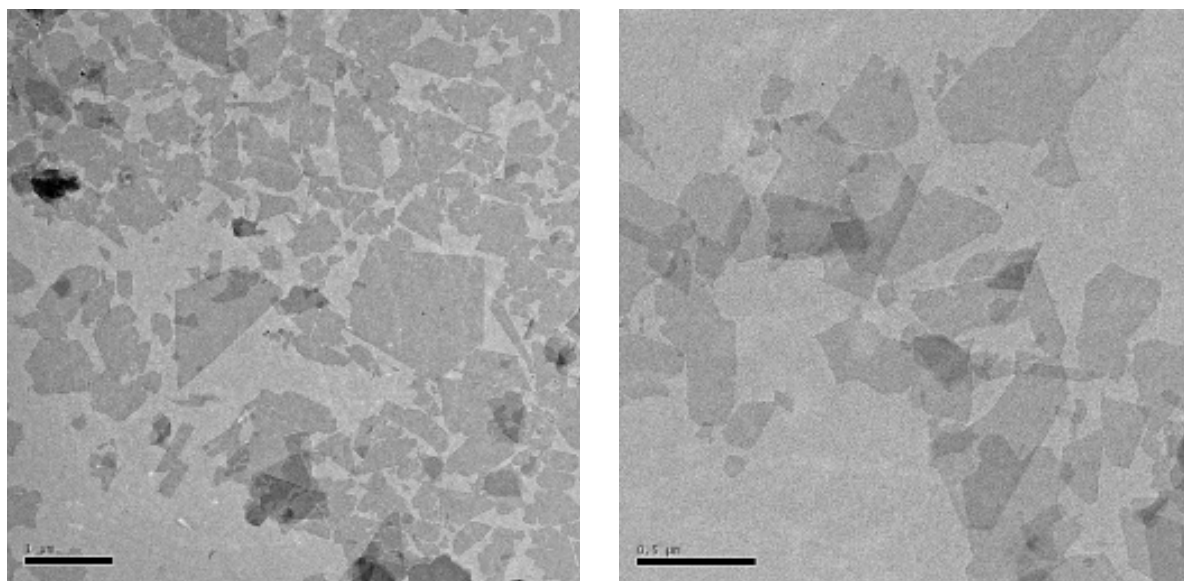


Fig. 7.64. TEM micrograph of the clay platelets. The dimensions of the scale bars are $1\ \mu\text{m}$ (left) and $0.5\ \mu\text{m}$ (right).

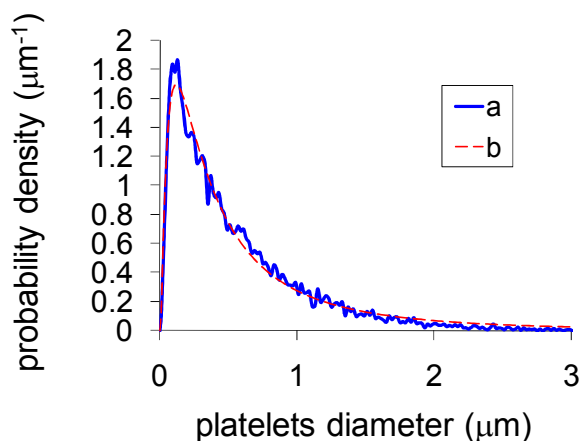


Fig. 7.65. a) Distribution of the averaged clay platelet diameters obtained from TEM micrographs and b) fit of the measured values with a lognormal distribution function (mean value = 566 nm; peak value = 120 nm)

7.3.3. Morphology of the powder aggregates

Fig. 7.66 shows micrographs of the Kunipia-F smectite clay powder. The aggregates have a plate like morphology. They show sheet-like structures on their surface that follow the curvatures of the aggregates. These apparent sheets may be formed by the parallel stacking of the clay platelets.

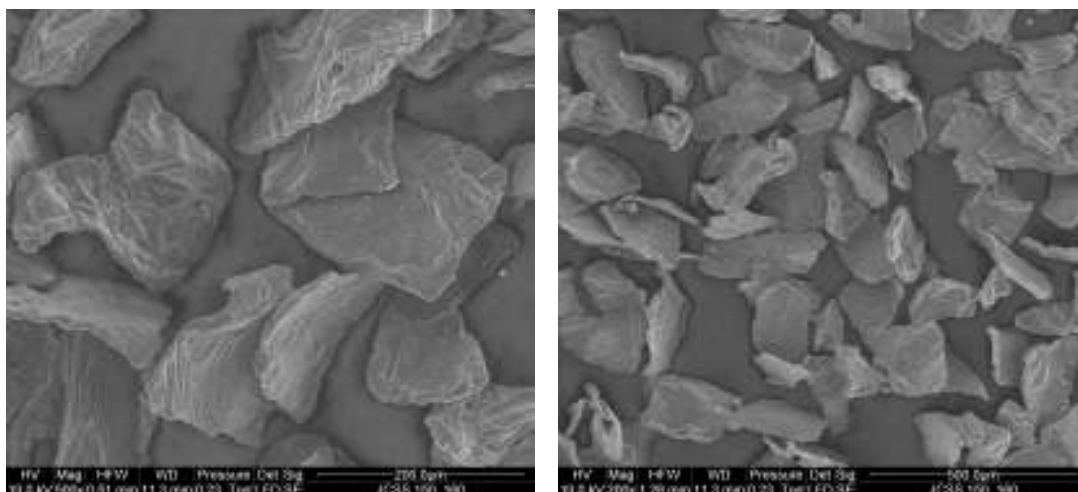


Fig. 7.66. SEM micrographs of the Kunipia-F powder.

7.1. CONCLUSION

The elemental analysis of the Kunipia-F clay showed the high purity of the clay in terms of smectite content and sodium counter ions. The distribution of the average clay platelet

diameters obtained by image analysis of TEM micrographs was a broad lognormal distribution with a mean value of 566 nm and a peak at 120 nm.

CHAPTER 8 *INTERACTIONS BETWEEN VOLATILES AND THE SODIUM SMECTITE*

8.1. INTRODUCTION

The binding and dynamics of the volatile molecules on the clay are expected to influence their release from the clay. In a first step clay models are built according to the chemical formula of the Kunipia-F clay (sections 8.2-8.4). A slab clay model representing the surface of the clay is used to investigate the binding of the volatile molecules used in the experiments on the clay (section 8.5), and a bulk clay model representing the interlayer gallery of the clay is used to investigate the dynamics of water molecules in the clay interlayer (section 8.6). In section 8.7, an attempt is made to rationalize the hysteresis observed in the equilibrium sorption isotherm of water on the clay by studying the energetics of the clay-water system as a function of the position of the counter ions in the interlayer gallery for various interlayer distances.

8.2. BUILDING OF THE SODIUM SMECTITE MODELS

The bulk material was represented by a 222 and a 211 supercells of the Kunipia-F sodium smectite. The surface material was represented by a 221 supercell of the Kunipia-F sodium smectite. In this case, in order to drastically weaken the interactions between the clay layers in the direction perpendicular to the surface of the clay layer the length of the c-axis was increased from 9.347 Å to 25 Å. The 222 model contains ten counter ions, the 221 model contains four counter ions, and the 211 model contains 2 counter ions. In these models all iron atoms of the chemical formula of the raw Kunipia-F sodium smectite (Table 7.40) were replaced by aluminum atoms. This choice makes calculations somewhat easier and guarantees the needed accuracy. The chemical formula per unit cell of the 222, 221, and 211 smectite models of the Kunipia-F sodium smectite are shown in Table 8.42.

Table 8.42: Chemical formula the model clays. The chemical formula of talc, pyrophyllite are shown for comparison.

clay	model	Chemical formula per crystal unit cell	Charge per unit cell
talc		$\text{Si}_8\text{O}_{20}(\text{OH})_4\text{Mg}_6$	0
pyrophyllite		$\text{Si}_8\text{O}_{20}(\text{OH})_4\text{Al}_4$	0
Kunipia-F	222	$(\text{Si}_{7.75}\text{Al}_{0.25})\text{O}_{20}(\text{OH})_4\text{Mg}_{0.625}\text{Al}_{3.25}$	-1.25
	221	$(\text{Si}_{7.75}\text{Al}_{0.25})\text{O}_{20}(\text{OH})_4\text{Mg}_{0.75}\text{Al}_{3.25}$	-1
	211	$(\text{Si}_{7.5}\text{Al}_{0.5})\text{O}_{20}(\text{OH})_4\text{Mg}_{0.5}\text{Al}_{3.5}$	-1

Mulliken population analysis was performed on the optimized geometries of the model smectites without sodium counter ions and the initial configuration of the sodium atoms has been chosen according to the lowest negative Mulliken charges of the basal oxygen atoms and to homogeneity considerations. Car-Parrinello molecular dynamic simulation have been then performed with the model smectites with sodium counter ions with temperature rescaling ($400 \text{ K} \pm 200 \text{ K}$) and a time step of 0.73 fs. For each model, three structures corresponding to the energy minima obtained during the dynamic calculations have been selected for geometry optimizations. After geometry optimization, for each model, the structure with the lowest energy was chosen as the initial configuration for further studies of the interactions between the model volatiles and the sodium smectite.

8.3. EQUILIBRIUM INTERLAYER DISTANCE OF THE DRY SMECTITE

Fig. 8.67 shows the energy of the 222 Kunipia-F supercell as a function of the length of the c-axis lattice parameter, keeping the other two dimensions fixed. The calculations have been computed with a threshold of 10^{-3} a.u. for G_g , except for the calculation at 20.2 Å for which an attempt to lower the threshold to 10^{-4} a.u. The 11 last points were fitted with the Murnaghan equation of state given by Eq. (8.115), resulting in an optimum value of 20.36 Å for the c-axis of the 222 supercell. This corresponds to a value of 10.18 Å for the c-axis of a unit cell, or the interlayer distance, which is greater by about 0.4 Å than the experimental value (section 7.2), but in the expected deviation.

$$p = \frac{2k_0}{k_0' (1+h) - (1-h)v^{-hk_0'}} \frac{v^{-hk_0'} - 1}{v^{-hk_0'}}, \quad hk_0' = \sqrt{D} \quad (8.115)$$

where

$$D = k_0'^2 - 2k_0''k_0 \quad (8.116)$$

and $k_0^{(n)}$ is the n^{th} derivative of the bulk modulus. V and p denote volume and pressure, respectively, and v is the specific volume defined by $v=V/V_0$, V_0 being the volume at the reference thermodynamic condition usually taken to be atmospheric pressure and room temperature.

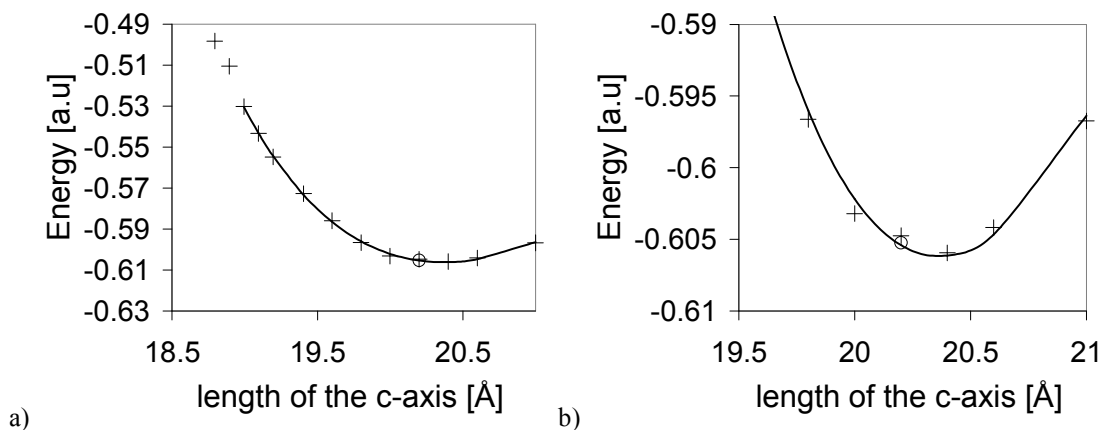


Fig. 8.67. Calculated energy of the bulk model of the Kunipia-F as a function of the length of the c-axis lattice parameter of the 222 supercell. The zero of the energy scale is -3420 a.u.

8.4. THE 221 SURFACE MODEL OF THE SODIUM SMECTITE

8.4.1. Positions of the counter ions

A top view of the silicon-oxygen plane of the 221 surface model of the Kunipia-F sodium smectite is shown in Fig. 8.68. The counter ions are positioned on the rings A, B, E, and F, the rings C and D remaining empty. A top view of those rings containing a sodium counter ion (Na) is shown in Fig. 8.70 and the corresponding side view of a ring, showing the planes of basal oxygen atoms (O_b), the plane of silicon atoms (Si) with possible aluminum substitutions (Al_T) in the tetrahedral layer, the plane of apical oxygen atoms (O_a) and the plane of octahedral aluminum atoms (Al_O) with possible magnesium substitutions (Mg), is pictured in Fig. 8.69. The labels of the atoms are summarized in Table 8.43.

The nearest environment of both A and B positions contains an aluminum substitution, that of E and F does not. E and F stand above the magnesium substitutions in the octahedral structure. The close environment of A differs from that of B in the direction of the structural hydroxyl relative to the position of the aluminum substitution. The structural hydroxyl of structure A points in the direction of a basal oxygen atom linked to the aluminum substituted atom, which is not the case for the structure B. E and F differ in the distance of the sodium to the nearest

magnesium atoms, as can be seen in Table 8.44. One can see also, qualitatively, that for each ring, the basal oxygen atoms point alternatively inward and outward to the respective sodium cations.

Table 8.43. Description of the labels for the silicon, oxygen, hydrogen, aluminum, magnesium and sodium atoms.

label	description
Si	tetrahedral silicon
O _b	tetrahedral basal oxygen
O _a	octahedral apical oxygen
O _h	hydroxyl oxygen
H	hydroxyl hydrogen
Al _T	tetrahedral aluminum
Al _O	octahedral aluminum
Mg	octahedral magnesium
T	tetrahedral cation
M	octahedral cation
Na	sodium counter ion

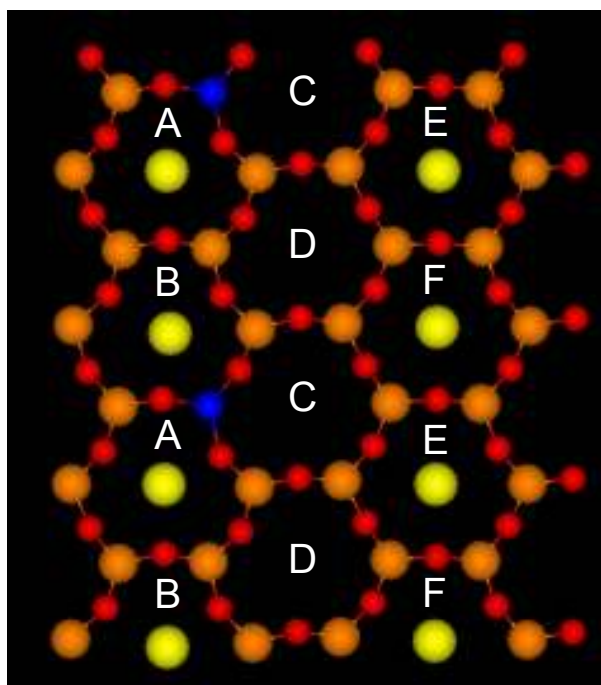


Fig. 8.68 : Top view of the silicon-oxygen plane of the 221 surface model of the Kunipia-F sodium smectite. Sodium counter ions above the surface are also shown. Oxygen atoms are in red, hydrogen atoms in white, silicon atoms in orange, sodium atoms in yellow, and the aluminum atom in blue. The silicon-oxygen rings are labeled from A to D.

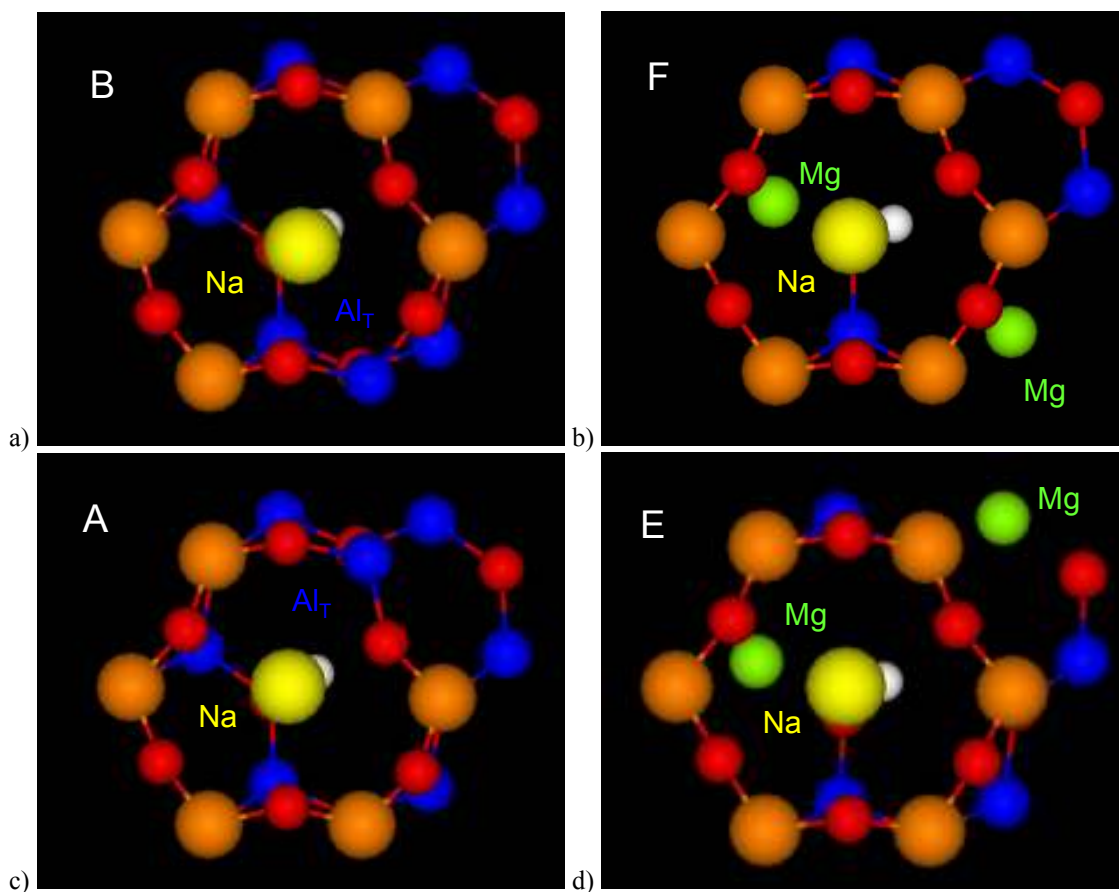


Fig. 8.69 : Structure of the 221 charged clay slab model. a) Top view of the ring B showing the labels of the aluminum substitution. b) Top view of the hexagonal ring F showing the labels of the aluminum substitution. c) Top view of the hexagonal ring A showing the labels of the aluminum substitution. d) Top view of the hexagonal ring E showing the labels of the aluminum substitution. Oxygen atoms are in red, hydrogen atoms in white, silicon atoms in orange, magnesium atoms in green, the aluminum atom in blue, and the sodium atoms are in yellow.

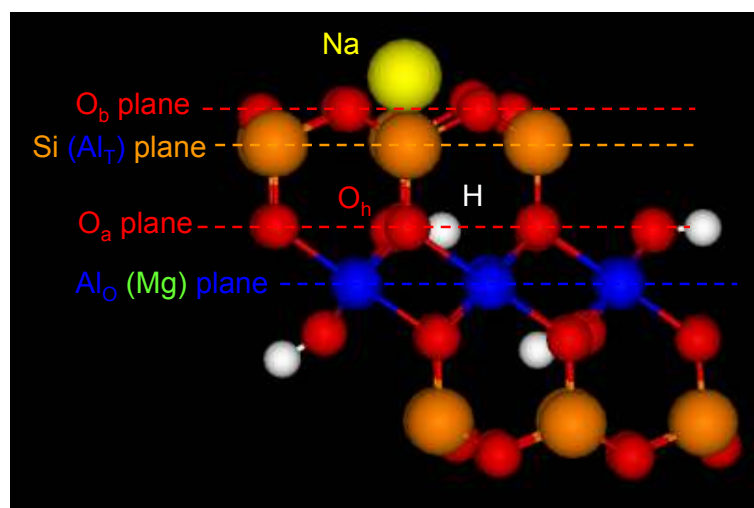


Fig. 8.70 : Side view of an hexagonal ring in the 221 charged clay slab model showing the plane of basal oxygen atoms (O_b), the plane of silicon atoms (Si) with a substitution by an aluminum (Al_T) atom for the hexagonal rings A and B, the plane of apical oxygen atoms (O_a), and the plane of aluminum atoms (Al_O) with substitutions by magnesium atoms (Mg) for the hexagonal rings E and F. Hydroxyl oxygen (O_h) and hydrogen atoms are also indicated. Oxygen atoms are in red, hydrogen atoms in white, silicon atoms in orange, sodium atoms in yellow, and the aluminum atoms in blue.

Table 8.44 : Distances from the sodium cations of structures E and F and their respective 3 nearest neighbour magnesium atoms.

position of the sodium cation	Na-Mg interatomic distances		
	1	2	3
E	4.04	5.08	5.93
F	4.01	5.81	5.94

8.4.2. Structural features and sodium counter ion adsorption energies

8.4.2.1. STRUCTURAL CHANGES AS COMPARED TO PYROPHYLLITE

The 221 surface model of the Kunipia-F sodium smectite shows changes in structural distances and angles compared to the case of pyrophyllite calculated in section 5.2.2.2 (Table 8.45 and Table 8.46).

Sodium-hydroxyl hydrogen repulsion

Fig. 8.71 shows that the hydroxyl hydrogen moves away from the clay surface in the direction of the octahedral layer. As a result the Al_O-O_h-H angle (see Table 8.43 for the definition of the atom labels, and Fig. 5.54 and Fig. 8.71 for their positions) of the 221 surface model is

decreased by about 11° for the rings with tetrahedral substitution (rings A and B) and by about 15° for the rings with octahedral substitutions (rings E and F). The larger decrease of the rings with octahedral substitutions, as compared to the ones with tetrahedral substitutions, corresponds to a closer distance of the sodium counter ion to the clay surface. Therefore the movement of the hydroxyl hydrogen can be attributed to the repulsion between the sodium and the hydroxyl hydrogen. The interaction with the sodium counter ion results also in an increase of about 0.06 \AA of the bond distance between the octahedral cation and the hydroxyl oxygen.

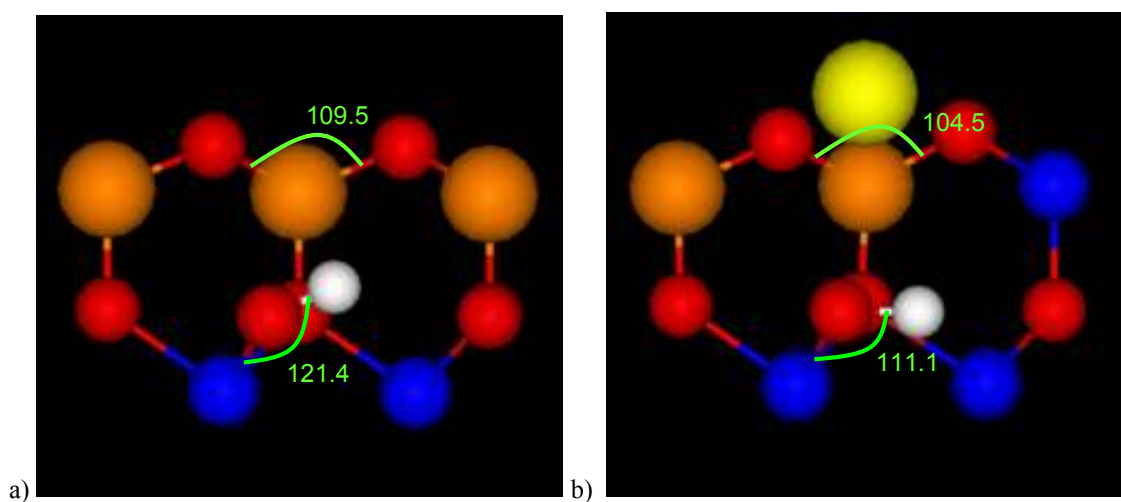


Fig. 8.71 : Side view of the pyrophyllite (a) and the hexagonal ring A of the charged clay slab (b) showing the change in $O_b\text{-Si-O}_b$ and $Al\text{-O}_h\text{-H}$ angles. Oxygen atoms are in red, hydrogen atoms in white, silicon atoms in orange, magnesium atoms in green, the aluminum atom in blue, and the sodium atoms is in yellow.

Distorsion of the tetrahedra

The dioctahedral structure of pyrophyllite gives rise to a rotation of the tetrahedra out of the (001) plane resulting in a ditrigonal ring and a corrugation of the basal oxygen atoms [220]. The ditrigonal structure is also observed for the charged clay. Indeed, one out of two basal oxygen atom is found to be closer to the sodium counter ion, independently of the type of substitution (Table 8.45). The average tetrahedral and octahedral thicknesses are increased by about 0.08 \AA and 0.05 \AA , respectively. In addition the averaged $O_b\text{-Si-O}_a$ angles of the charged clay are decreased by about 5° for the rings with tetrahedral substitutions and by about 6.5° for the rings with octahedral substitutions. However, the $Si\text{-O}_b$ distances of the charged clay remain very similar to the ones of pyrophyllite. This suggests a rotation of the basal oxygens around the silicon-silicon axes. We observe also a change in the corrugation that decreases for the rings A, E and F, and increases for the ring B. For the ring B, the basal oxygens O_b^1 and O_b^2 linked to the aluminum substitution are significantly above the average

plane of basal oxygens (0.13 Å and 0.17 Å). For the two basal oxygen atoms of the hexagonal ring A, linked to the aluminum substitution, only the basal oxygen O_b^4 is significantly above the average plane of basal oxygens (0.13 Å); the atom O_b^3 is closer to the plane of basal oxygens (0.01 Å). We note that the atom O_b^3 of the ring A points inwards of the ring A, whereas the atom O_b^2 of the ring B points outwards of the ring B.

Aluminum replacements

Except for the averaged O_b -T- O_a angle, the angles involving an aluminum substitution are decreased by about 2° to 3°, and the bond distances between the tetrahedral cation and the oxygen atoms are increased by about 1.2 Å, as compared with the non-substituted silicon atoms. The octahedral atoms substituted by magnesium atoms, show pronounced changes in the averaged O_h -M- O_a angle (about +8 °) and averaged M- O_h -H angle (about -8 °), and an increase in the bond distances to oxygen atoms of about 2 Å; also the averaged O_a -M- O_a and M- O_a -M angles are increased, respectively decreased, by about 2 °, as compared to the non-substituted aluminum atoms.

Table 8.45. Distance (in Å) parameters for a 221 cell of pyrophyllite, and the A, B, E and F hexagonal rings of the 221 charged clay slab model. Ts.th. is the thickness of the tetrahedral sheet, Os.th. is the thickness of the octahedral sheet, ΔZ is calculated as the standard deviation around the plane formed by the basal oxygen atoms and gives an indication of the corrugation of basal oxygens along [110], Ψ , where $\cos(\Psi) = \text{Oct. th.}/2(\text{Al-O})$ is the octahedral flattening angle, $d(A-B)$ is the average angle between atom A and atom B. The subscripts T and O stand for tetrahedral and octahedral.

	pyrophyllite	221 model (Na counter ions)			
		A	B	E	F
Ts.th.	2.17	2.27	2.26	2.24	2.23
Os.th.	2.14	2.17	2.18	2.21	2.23
ΔZ	0.26	0.18	0.29	0.16	0.12
ψ	56.3	56.5	56.0	57.4	56.9
$d(\text{Si-O}_b)$	1.63	1.64	1.64	1.65	1.65
$d(\text{Al}_T\text{-O}_b)$		1.76	1.76		
$d(\text{Si-O}_a)$	1.64	1.63	1.65	1.61	1.60
$d(\text{Al}_T\text{-O}_a)$		1.74	1.74		
$d(\text{Al}_O\text{-O}_a)$	1.93	1.96	1.95	1.97	1.94
$d(\text{Mg-O}_a)$				2.14	2.15
$d(\text{Al}_O\text{-O}_h)$	1.90	1.94	1.95	1.95	1.98
$d(\text{Mg-O}_h)$				2.19	2.18
$d(\text{O}_h\text{-H})$	0.96	0.97	0.97	0.97	0.97
$d(\text{Na-T}_{\text{plane}})$		1.30	1.29	0.92	0.92
$d(\text{Na-O}_b)$		2.32	2.34	2.41	2.39
		2.95	2.95	2.74	2.75

Table 8.46. Angle (in deg) parameters for a 221 cell of pyrophyllite, and the A, B, E and F hexagonal rings of the 221 charged clay slab model.. $\angle(A-B-C)$ is the average angle between the atoms A, B and C. The subscripts T and O stand for tetrahedral and octahedral.

	pyrophyllite	221 model (Na counter ions)			
		A	B	E	F
$\angle(O_b-Si-O_b)$	109.5	104.5	104.7	102.8	102.9
$\angle(O_b-Al_T-O_b)$		101.8	101.7		
$\angle(Si-O_b-Si)$	129.6	126.7	125.5	129.3	130.6
	141.7	137.9	137.9	137.9	135.5
$\angle(Al_T-O_b-Si)$		124.3	124.4		
		130.7			
$\angle(O_b-Si-O_a)$	109.5	111.7	111.8	112.9	113.3
$\angle(O_b-Al_T-O_a)$		112.0	110.8		
$\angle(Al_O-Si-O_a)$	123.5	124.7	125.3	124.3	125.7
	128.0	129.4	128.5	127.5	125.4
$\angle(Al_O-Al_T-O_a)$		121.7	121.7		
		129.5	129.5		
$\angle(O_a-Al_O-O_a)$	92.2	91.2	90.9	90.7	90.2
$\angle(O_a-Mg-O_a)$				91.2	93.8
$\angle(Al_O-O_a-Al_O)$	101.5	99.1	99.4	97.2	96.5
$\angle(Mg-O_a-Al_O)$				94.3	95.6
$\angle(O_h-Al_O-O_a)$	94.0	92.8	94.0	87.6	87.3
	92.4	90.8	91.2	85.0	85.8
$\angle(O_h-Mg-O_a)$				97.4	96.0
				93.0	90.9
$\angle(Al_O-O_h-Al_O)$	102.9	99.1	99.4		
$\angle(Mg-O_h-Al_O)$				91.6	89.5
$\angle(Al_O-O_h-H)$	121.4	111.1	110.2	108.4	104.4
$\angle(Mg-O_h-H)$				96.6	99.7

8.4.2.1. BINDING ENERGY OF THE SODIUM COUNTER IONS

The sodium atoms were positioned alternatively in A, B, E and F to determine the corresponding binding energies. Table 8.47 shows the binding energies of sodium in the four sites and the sodium to silicon plane distances. A and B correspond to a lower binding energy than E and F by ~ 15 kJ/mol, and a larger distance of the sodium to the silicon plane by ~ 0.3 Å. The cation in A has a slightly lower binding energy than in B, and similarly when in E it has a slightly lower binding energy than in F. These lower binding energies correlate with a larger sodium to silicon plane distance. The larger binding energy on E and F, as compared to A and

B, correspond also to lower Mulliken charges on the basal oxygen atoms calculate from Mulliken population analysis on the smectite without counter ions (Table 8.48), and therefore to a stronger attraction between the oxygens and the sodium counter ion.

Table 8.47 : Binding energies (in kJ/mol) of the cations and sodium to silicon plane distances (in Å) in A, B, E and F.

position	binding energy	Na-(T plane) distance
A	732	1.30
B	734	1.26
E	748	0.93
F	751	0.89

Table 8.48 : Average Mulliken charges at the surface of the sodium smectite without counter ions.

	O _b	Si/Al	Si only
A	-0.628 ± 0.004	1.503 ± 0.153	1.565 ± 0.018
B	-0.628 ± 0.004	1.502 ± 0.152	1.563 ± 0.020
E	-0.632 ± 0.002	1.574 ± 0.009	1.574 ± 0.009
F	-0.631 ± 0.002	1.572 ± 0.007	1.572 ± 0.007

8.5. BINDING OF VOLATILES ON THE 221 SURFACE MODEL

8.5.1. Binding of one water molecule

8.5.1.1. BINDING ENERGIES AND CONFIGURATIONS OF THE WATER MOLECULES

Table 8.49 shows the binding energies, sodium to water oxygen interatomic distances, water hydrogen to basal oxygen interatomic distances, of one water molecule above the structures A, B, E, and F for different configurations. Note however that energy differences < 4kJ/mol (~1 kcal/mol) are beyond the general accuracy of the calculations.

The binding energies of the water molecules bound to the cations in A and B are significantly higher than those to cations in E and F (~10 kJ/mol). This is the inverse order as that obtained for the binding energies of the sodium cations on the clay surface. One can see that the water molecule forms hydrogen bonds with basal oxygen atoms (Fig. 8.72). In the case of configuration B-a, the binding energy is especially higher than for all other configurations. Here, the water forms a hydrogen bond with a basal oxygen atom O_b linked to the substituted aluminum atom (Fig. 8.72a). We note also that this basal oxygen atom points outwards from the cation B, and inwards to the structure C, that does not contain any cation. The hydrogen bond distance (1.9 Å) is also especially shorter than for the other configurations. In the

configurations A-b and A-d (Fig. 8.72b and c), the water molecule also forms a hydrogen bond with a basal oxygen atom linked to the substituted aluminum atom. However the binding energies are lower than for the configuration B-a, especially for the configuration A-d that has a binding energy lower than all the other configurations. In the case of the configuration A-b, the basal oxygen atom points inwards in the direction of the cation A. In the case of the configuration A-d, the basal oxygen atom points outwards in the direction of the cation B.

For the configurations related to the cations E and F, the water molecule tends to form a hydrogen bond with the basal oxygen atom pointing outwards in the direction of a structure that contains no sodium cation, but not with the basal oxygen atoms pointing inwards in the direction of the respective sodium cation (Fig. 8.72d). Except for the configurations B-a and A-d, for the same ring structure, there is no significant difference in binding energy between the configuration with a water molecule directly on top of a sodium cation (Fig. 8.72e), and the configuration with a water molecule forming a hydrogen bond with a basal oxygen atom (Fig. 8.72d).

Except for the configuration B-a, we note that the binding energy of one water molecule on the sodium counter ion differs from the calculated binding energy of two times the binding energy of hydrogen bond between an isolated water dimer (43.6 kJ/mol) by only a few kJ/mol.

The water molecule was also positioned on structures C and D, that do not contain any counter ion. The molecules were positioned with their oxygen atom pointing in the direction of the hydrogen of the clay hydroxyl. The structures were first calculated with a threshold of 10^{-5} au for G_w and 10^{-3} au for G_g . The 'binding energies' of one water molecule on structures C and D are of the order of one hydrogen bond or lower (12 to 22 kJ/mol). Note that the oxygen of the water molecules did not remain directed towards the clay hydroxyl. The same calculations, restarted with a threshold of 10^{-6} au for G_w and 10^{-4} au for G_g , converged to the configurations B-a and A-a, showing also that the C and D positions do not correspond to local minima. Rather the corresponding 'binding energies' provide an estimate of the energy barriers to diffusion. These turn out to be at least 20 kJ/mol. Therefore at low temperature a water molecule on the clay surfaces is easily trapped by a sodium ion in whatever position and there is no bond between the water molecule and the clay hydroxyl, which is expected from the large distance between the hydrogen of the clay hydroxyl and the plane formed by the basal oxygen atoms (~ 2.34 Å).

Table 8.49 : Binding energies, sodium to water oxygen O_w interatomic distances, and hydrogen water H_w to basal oxygen O_b interatomic distances for one water molecule around cations A, B, E and F for different configurations. Binding energies are in kJ/mol and interatomic distances are in Å.

position	configuration	binding energy	distance	
			Na- O_w	H_w - O_b
A	a	54	2.30	2.12
	b	53	2.27	2.50
	c	51	2.29	2.44
	d	46	2.26	2.01
B	a	60	2.27	1.90
	b	52	2.28	3.35
	c	49	2.30	2.42
E	a	46	2.28	3.42
	b	45	2.30	2.47
F	a	45	2.28	3.10
	b	44	2.30	2.53

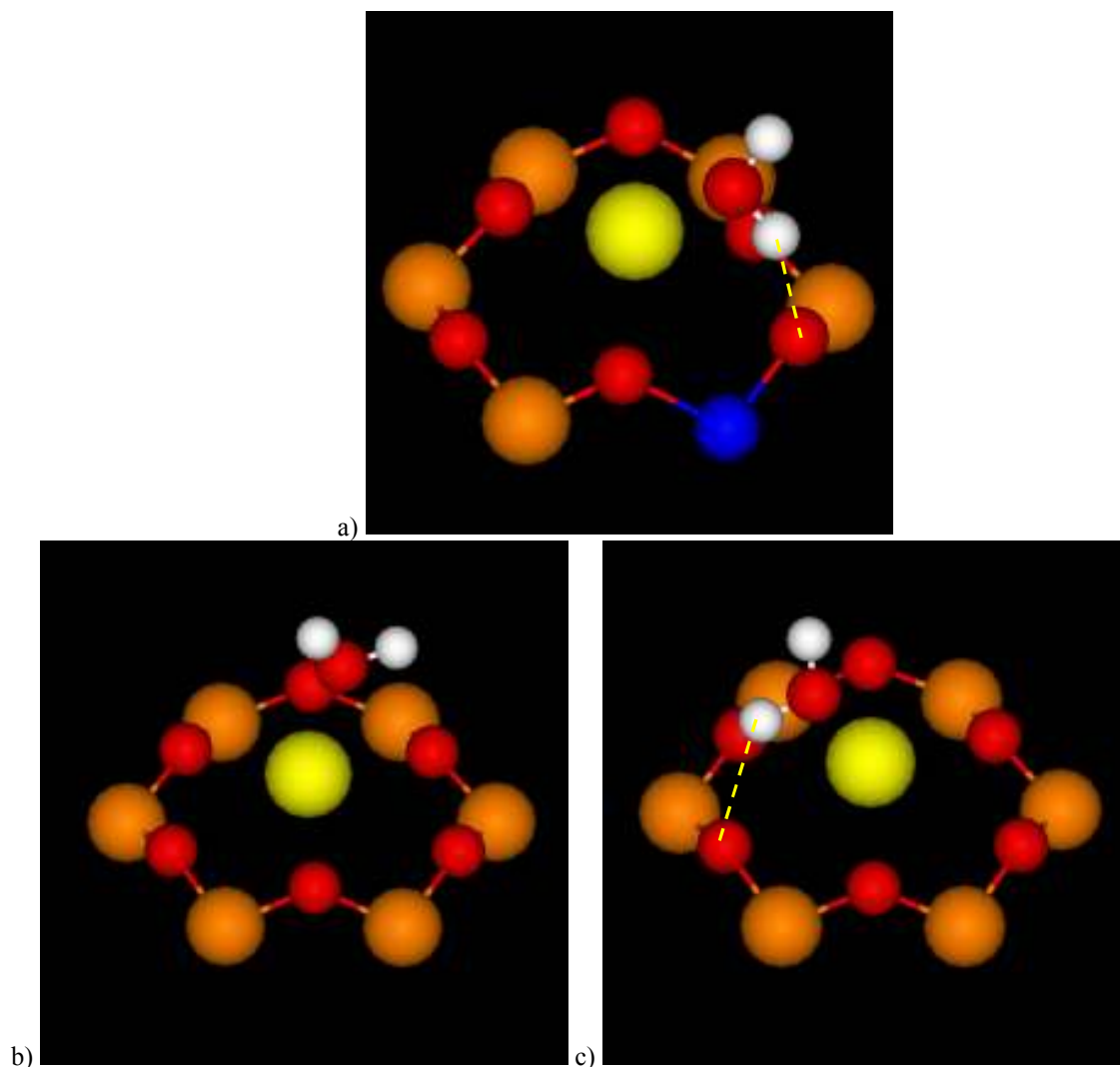


Fig. 8.72 : One water molecule configurations around the counter ions. a) configuration B-a. b) configuration F-a. c) configuration F-b Oxygen atoms are in red, hydrogen atoms in white, silicon atoms in orange, sodium atoms in yellow, and the aluminum atom in blue. The yellow dashed lines denote hydrogen bonds.

8.5.1.2. STRUCTURAL CHANGES

The energy loss E_L of the substrate due the structural changes induced by water adsorption and the bond length and bond angles of the smectite structure were also calculated. E_L do not seem to be very significant (in Table 8.50). Also, for each specific cation position there is no clear correlation between them and the binding energy differences of different arrangements of the molecule. However, Table 8.50 shows that the distance between the sodium counter ion and the silicon plane, and the distance between the sodium and the basal oxygens, increase by 0.21 to 0.34 Å and by 0.07 to 0.10 Å, respectively, indicating that the sodium moves away from the smectite surface with the adsorption of one water molecule. Therefore, part of the binding energy of the water molecule may be the energy to move the cation away from the smectite surface. We note also a slight increase in the $AlO-O_h-H$ angle. This may indicate a

decrease of repulsion of the sodium on the hydrogen hydroxyl of the smectite, in agreement with the observations made between pyrophyllite and the dry smectite in the preceding section. No significant changes were observed for the other structural features.

Table 8.50 : Deformation energy E_L , and increase in the sodium to silicon to plane distances, the sodium to basal oxygen O_b interatomic distances, and the $Al-O-H$ angle, with respect to the dry smectite, for one water molecule around cations A, B, E and F for different configurations. Binding energies are in kJ/mol and interatomic distances are in Å.

position	configuration	E_L	Na-(T-plane)	Na- O_b		$\angle(Al-O-H)$
A	a	6	0.28	0.10	0.08	2
	b	3	0.22	0.08	0.07	1
	c	4	0.26	0.09	0.08	2
	d	6	0.24	0.08	0.06	2
B	a	7	0.28	0.07	0.10	2
	b	3	0.21	0.06	0.07	2
	c	6	0.34	0.14	0.10	2
E	a	3	0.25	0.04	0.04	1
	b	5	0.32	0.05	0.06	1
F	a	3	0.22	0.05	0.04	1
	b	4	0.27	0.06	0.05	1

8.5.2. Binding of other single volatiles

8.5.2.1. CONFIGURATIONS OF THE VOLATILES

Geometry optimization of the 221 model of the Kunipia-F sodium smectite with different volatile molecules on the surface was performed. The volatiles considered were ethanol, ethyl acetate, toluene, pyridine, and n-octane. A single molecule was positioned above cation A, located close to an aluminum replacement, and cation F, located above magnesium replacements.

Results for water are reported for reference, and in particular in configurations F-a and F-b, and A-a and A-c described in the previous section. In the initial configurations, the molecules were given specific orientations that changed only slightly after optimization. The ethanol molecule (Fig. 8.73a) was positioned with its oxygen atom directed towards the sodium counter ion. For ethyl acetate two configurations were considered, of which (Fig. 8.73b) corresponds to the case where the oxygen atom on the resonant bond is directed towards the sodium cation, and (Fig. 8.73c), to the case where the other oxygen atom is directed towards the sodium cation. The pyridine molecule was positioned with the aromatic plane lying perpendicular to the clay surface and the nitrogen atom directed towards the sodium cation

(Fig. 8.73d). The latter was also obtained as result of geometry optimization starting from a configuration with the plane of the aromatic ring lying parallel to the clay surface. The toluene molecule (Fig. 8.73e) was positioned with its aromatic ring lying parallel to the clay surface. The n-octane molecule (Fig. 8.73f) was positioned with its axes lying parallel to the smectite surface and perpendicular to the line formed by the A and B, or the E and F positions.

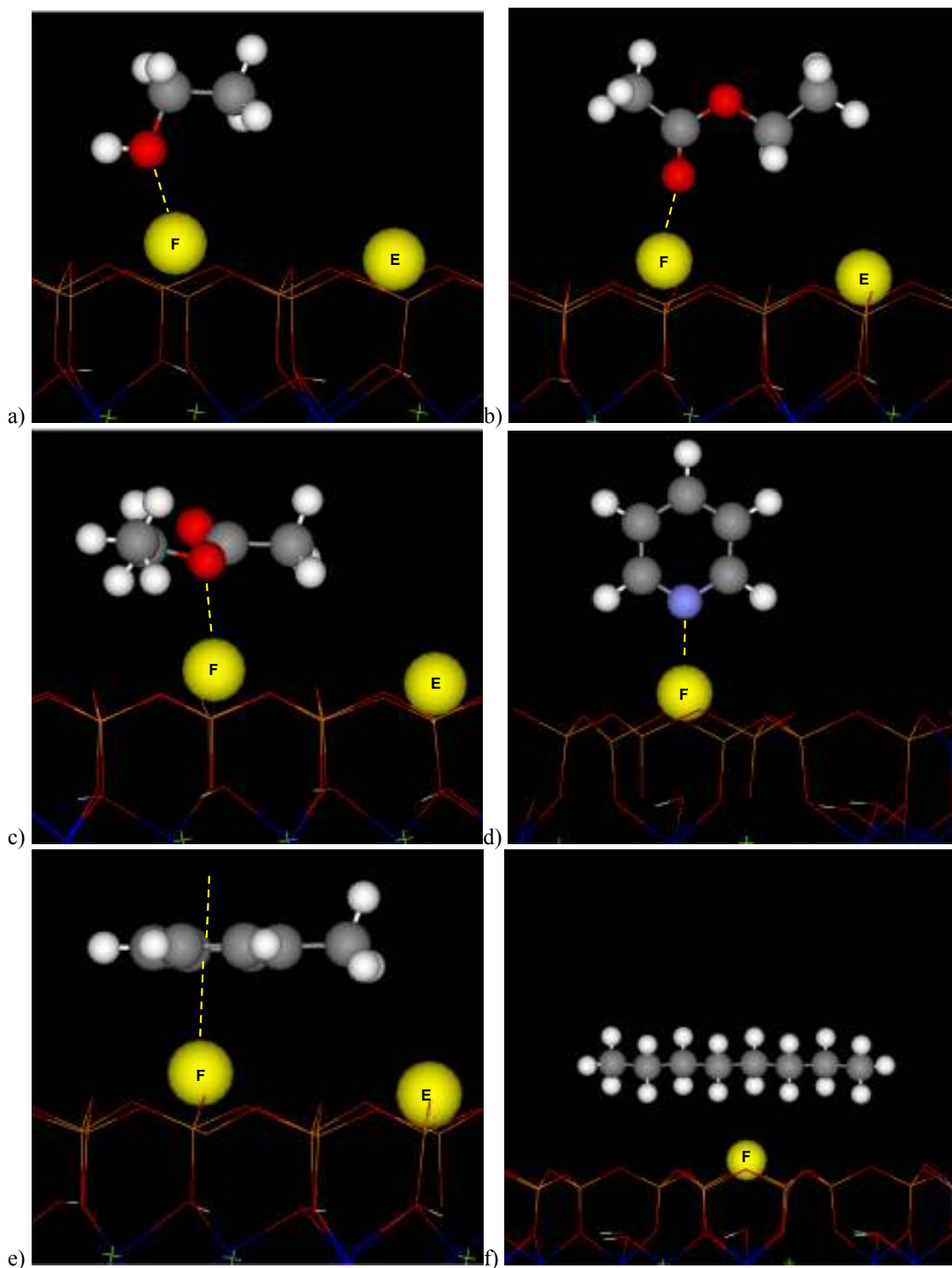


Fig. 8.73 : Volatile molecules at the F site: a) ethanol, b) ethyl acetate (i), c) ethyl acetate (ii), d) pyridine, e) toluene, f) n-octane. The yellow dashed lines denote bonds between the electronegative atoms and the sodium cation (a-d), and the bond between the cation and the aromatic electron cloud of toluene (e).

8.5.2.1. BINDING ENERGIES

Table 8.51 shows the binding energy of each volatile at different locations and configurations on the smectite surface, and the distance between the sodium cation and the electronegative element of the volatile. One can note that the binding energies, and the sodium to silicon plane distances, are systematically higher on the cation in A than on the cation in F. As already pointed out, the A position is above a ring containing a substituted aluminum, while F is, above magnesium. In analogy with the case of water, structures C and D are weaker attraction centers for the molecules considered here. Energy minimization was achieved only within $G_g \sim 10^{-4}$ a.u. and provided an estimate of the binding energy which is ~ 10 kJ/mol lower than for positions above the cations in F or A .

Except for water and for the ethyl acetate in the configuration (b), the smallest distance between the hydrogens of the volatiles to the basal oxygens is larger than 3 Å, Therefore, they cannot form hydrogen bonds with the basal oxygen atoms and at the same time bind to the sodium cation, in contrast to water. In the case of ethyl acetate in the configuration (b), the distance between the two non-methyl hydrogens and the nearest basal oxygens are about 2.65 Å.

Table 8.51 : Binding energies of different volatiles on the clay slab, distances between the sodium cation and the electronegative element of the volatile, and sodium to silicon plane distances. The superscripts refer to the corresponding configurations.

volatile	binding energy		Na-O or Na-N	
	above A	above F	above A	above F
water	54 ^(a)	45 ^(a)	2.30	2.28
	51 ^(c)	44 ^(b)	2.29	2.30
ethanol	54	48	2.28	2.27
ethyl acetate	59	52 ^(a)	2.21	2.22
		23 ^(b)		2.44
pyridine	72	63	2.37	2.39
toluene	35	25		
n-octane	15	9		

Table 8.52 shows the largest binding energy found, and the ionization potential, dipole moment, and polarizability of the isolated molecules. The differences in binding energies on cation F between water, ethanol, ethyl acetate, and pyridine, correlate well with the ionization potentials (Table 8.52), which can in turn be related to the electronegativity of the oxygen or nitrogen atom. We note that it does not correlate well with the ion-dipole interaction energies calculated from the dipole moments of the molecules (Table 8.52). Water is a special case because it also forms a hydrogen bond with a basal oxygen atom, which is stronger in A than

in F. The larger binding energy of ethyl acetate over ethanol, on the other hand, can be explained by the presence of an excess electron on the carboxylate moiety. The binding energy of toluene is of the order of the binding energy of a hydrogen bond; this is consistent with the nature of the interaction, namely between the cation and the π -electronic system of the molecule. The much lower binding energy of n-octane is consistent with the nature of its interaction, which is dominated by the ion-induced dipole component. On the other hand, the latter is significant because, due to its elongated structure, n-octane has a high polarizability (Table 8.52). The sodium to silicon plane distance is also lower in the case of n-octane than for the other volatiles.

Table 8.52 : Largest binding energies of different volatiles on the clay slab and some characteristics of the isolated molecules (ionization potential, dipole moment and polarizability) Compared with experiment. Energies are given in kJ/mol, ionization potential in eV, dipole moment in Debye.

properties		pyridine	ethyl acetate	ethanol	water	toluene	n-octane
largest binding energy	Th. cation A	72	59	54	54	35	15
	cation F	63	52	48	45	25	9
ionization potential	Th. adiabatic	8.80	9.55	9.87	12.53	8.52	8.96
	vertical	9.25	9.83	10.12	12.53	8.68	9.50
	Exp [225]	9.25	10.01	10.47	12.612	8.82	9.82
dipole moment	Th.	2.23	2.03	1.53	1.79	0.43	0.00
	Exp [225]	2.215	1.78	1.69	1.854	0.375	
charge-dipole energy	Th. cation A	114.5	105.2	93.8	101.3		
	cation F	111.8	104.5	94.5	103.1		
polarizability	Th.	9.63	9.22	5.27	1.60	12.51	15.98
	Exp [225]	9.5	9.7	5.41	1.45	12.28	15.9

8.5.2.1. STRUCTURAL CHANGES

Table 8.53 shows the increase in the sodium to silicon-plane distances, in the sodium to basal oxygen distances, and in the $AlO-O_H-H$ angles, with respect to the dry smectite. As for the case with water, as results of the adsorption of the volatiles on the smectite, the sodium counter ion moves away from the surface. The rise of the counter ion is less pronounced for the n-octane than for the other volatiles. The lower binding energy of the n-octane molecule on the sodium cation may partially account for this. However, the rise of the sodium cation is the strongest for the toluene molecule, though the binding of the toluene molecule on the sodium cation is not the strongest. Here again the average $AlO-O_H-H$ angles increase by 1 to 2 ° probably due to the lower repulsion between the sodium atom and the hydroxyl hydrogen. The other distances and angles do not significantly change.

Table 8.53 : Increase in the sodium to silicon to plane distances, the sodium to basal oxygen O_b interatomic distances, and the $Al-O_h-H$ angles, with respect to the dry smectite, for one volatile molecule around cations A, and F for different configurations. Binding energies are in kJ/mol and interatomic distances are in Å. Superscripts in parenthesis denote the labels of the respective configurations.

volatile	Na-(T-plane)		Na- O_b				$\angle(Al-O_h-H)$	
	above A	above F	above A		above F		above A	above F
water	0.28	0.22	0.10	0.08	0.05	0.04	2	1
	0.26	0.27	0.09	0.08	0.06	0.05	2	1
ethanol	0.26	0.26	0.08	0.08	0.06	0.05	2	1
ethyl acetate	0.28	0.35	0.09	0.09	0.07	0.07	2	2
		0.23			0.04	0.05		1
pyridine	0.22	0.26	0.07	0.07	0.06	0.05	1	1
toluene	0.32	0.40	0.11	0.10	0.08	0.08	2	2
n-octane	0.16	0.06	0.05	0.05	0.02	0.01	1	1

8.5.3. Binding of two to six water molecules

8.5.3.1. BINDING OF TWO WATER MOLECULES ON TWO DIFFERENT SODIUM COUNTER IONS

Table 8.54 shows the binding energies and sodium to water oxygen interatomic distances of two water molecules bound to sodium cations located at different positions (A through F). Table 8.54 reports the results obtained by positioning each molecule on specific configurations and then relaxing the structure. These allow us to extract a quantitative estimate of the presence of the other molecule on the adsorption energy. The total binding energy is lower than the sum of those of the isolated molecules by only 2 kJ/mol, showing that the two processes are essentially independent. We observe again that the B and A positions are the most attractive centers for water.

Table 8.54 : Total binding energies B.E., binding energy of the last molecule b.e. taking as reference the configurations of molecule 2, and sodium to basal oxygen distance. Binding energies are in kJ/mol and distances are in Å. The single molecule configurations refer to Table 8.49.

positions		binding energies		Na- O_w distance	
Mol 1	Mol 2	B.E.	b.e.	Mol 1	Mol 2
B-a	A-a	113	54	2.27	2.31
B-a	E-a	105	46	2.27	2.28
B	E-a	95	45	2.28	2.29
A	E-a	95	45	2.28	2.29
A	F-a	94	46	2.28	2.29
B	F-a	94	46	2.28	2.29
E-a	F-a	88	45	2.31	2.32

8.5.3.2. BINDING OF TWO WATER MOLECULES ON ONE SODIUM COUNTER ION

Table 8.55 shows the binding energies, the sodium to water oxygen interatomic distances, and the water hydrogen to basal oxygen interatomic distances, of two water molecules on the same cation (A through F). The total binding energies of the water molecules on cations in A and B are higher by at least 15 kJ/mol than those relative to cations in E and F. Except for the configuration A-2b, in each configuration the two water molecules form a hydrogen bond with a basal oxygen atom O_b (two dimers). In the A-2b configuration, one of the two water molecules forms a hydrogen bond with a basal oxygen atom and another hydrogen bond with the other water molecule (one dimer). This configuration has the lowest binding energy of the configurations on the cations A and B. In the B-2a configuration, one molecule is in the most energetically favorable for a single molecule, bound to the basal oxygen atom, linked to the (replacing) aluminum atom (Fig. 8.74a) (B-a of Table 8.49). Therefore the total binding energy is again much higher than that of the other configurations. Taking the corresponding single- molecule adsorption configurations as reference, we calculated the binding energy of the additional molecule (Table 8.57). This turns out to be lower by around 10 kJ/mol in all cases. Clearly structures with two molecules on different cations are thermodynamically more stable.

The energy losses E_L of the substrate due the structural changes induced by water adsorption were also calculated (Table 8.56). The latter are more significant than in the case of a single- molecule adsorption and involve much larger E_L values. In particular, Na moves further away from the surface as shown when comparing Table 8.56 with Table 8.49.

Table 8.55 : Total binding energies, sodium to water oxygen O_w interatomic distances, and hydrogen water H_w to basal oxygen O_b interatomic distances, of two water molecules around cations A, B, E and F. Binding energies are in kJ/mol and interatomic distances are in Å. Note that in A-2b, an H-bond (1.934 Å) exists between the water molecules having a O_w-O_w distance of 2.751 Å.

position / configuration	binding energy	Na- O_w distance			H_w-O_b distance		O_wH_w distance	
		Mol 1	Mol 2	mean	Mol 1	Mol 2		
A	2a	96	2.32	2.31	2.32	2.12	2.39	1.93
	2b	92	2.27	2.73	2.50	1.82		
B	2a	106	2.26	2.28	2.27	1.94	1.96	
	2b	95	2.32	2.32	2.32	2.17	2.76	
E-2	81	2.33	2.30	2.32	2.17	2.23		
F-2	79	2.34	2.31	2.33	2.12	2.31		

Table 8.56 : Deformation energy E_L (in kJ/mol) due to changes in the smectite structure and sodium to silicon plane distance (in Å) for two water molecules around cations A, B, E and F.

position / configuration	E_L	Na-(T-plane) distances	
A	2a	21	1.91
	2b	12	1.66
B	2a	29	2.10
	2b	23	1.98
E-2	30	1.77	
F-2	31	1.73	

Table 8.57 : Total binding energies B.E., binding energy of the last molecule b.e. calculated from the reference single molecule configurations (see Table 8.49), for 2 water molecules around cations A, B, E and F. Binding energies are in kJ/mol and interatomic distances are in Å.

two molecules configuration	reference single molecule configuration	binding energy		
		B.E.	b.e.	
A	2a	A-a	96	42
	2b	A-c	92	41
	2b	A-b	92	40
B	2a	B-a	106	46
	2b	B-b	95	43
E-2		E-b	81	36
F-2		F-b	79	35

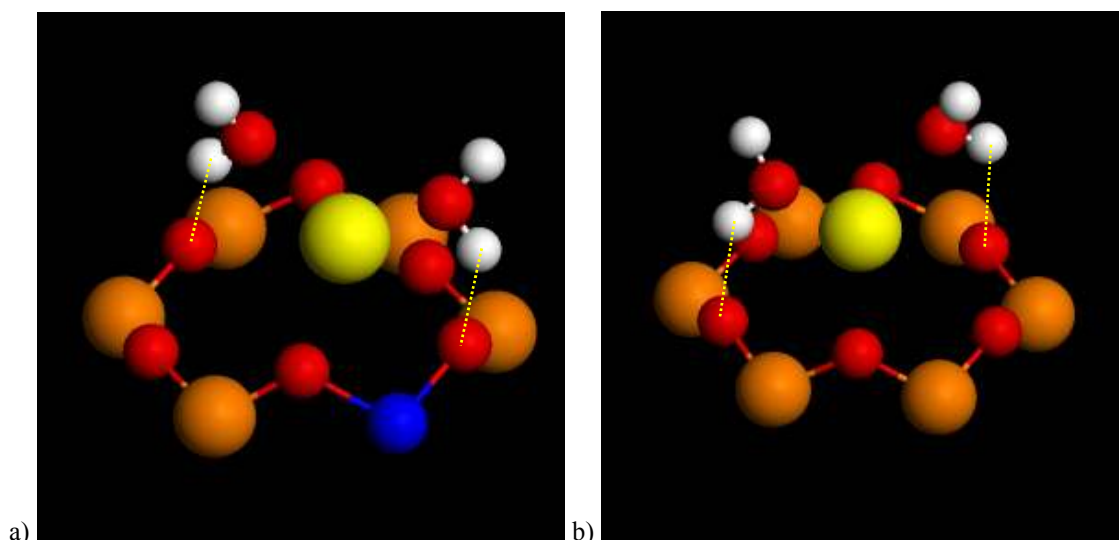


Fig. 8.74 : Configurations of two water molecules around the sodium counter ions. a) configuration B-2a. b) configuration F-2. Oxygen atoms are in red, hydrogen atoms in white, silicon atoms in orange, sodium atoms in yellow, and the aluminum atom in blue. The yellow dashed lines denote hydrogen bonds.

8.5.3.3. BINDING OF THREE WATER MOLECULES ON ONE SODIUM COUNTER ION

Table 8.58 shows the binding energies, the sodium to water oxygen interatomic distances, the water hydrogen to basal oxygen interatomic distances, and the water hydrogen bond distances, of three water molecules on the cations A, B, E, and F for different configurations. Positions A and B are more favorable also in this case.

Two different types of configurations (α and β) were found.

- In α (Fig. 8.75a) the three molecules are bound to the cation and form hydrogen bonds with three different basal oxygen atoms (three monomers), of which two belong to the same hexagonal silicon-oxygen structure, and the other to an adjacent one (belonging to the domain of a different ion position as indicated in square brackets). This type of configuration was observed for all four different cation positions A through F. A[B]- α 1 has a total binding energy especially higher than the others because one of the water molecules forms a hydrogen bond with a basal oxygen atom linked to the (replacing) aluminum atom (Fig. 8.75a) (as in B-a in Table 8.49).
- In β (Fig. 8.75b) the adsorbate is a trimer in which one molecule forms an H-bond with a basal oxygen and one is farther from the counterion than the others (2.5-2.6 Å). The values of the binding energies show that the intermolecular interaction starts to be competitive with the surface adsorption. This configuration was not found for the cations in A and F.

The energy loss E_L due the structural changes of the substrate induced by water adsorption was also calculated (Table 8.59). The latter are more significant than in the case of a two-molecules adsorption and involve much larger E_L values. Here again, Na moves further away from the surface as shown when comparing Table 8.59 with Table 8.49.

For the β configurations the sodium to silicon plane distance is shorter than for the α configurations, corresponding to a higher number of hydrogen bonds with the basal oxygen atoms. This shorter sodium to silicon plane distance correlates with a lower E_L . The same is true for the E[F] and F[E] configurations but not for the two A[B] ones. One can thus identify another relevant feature, namely the distance between the sodium cation and the replacing aluminum which is shorter for A[B]- α 1 than for A[B]- α 2 (see Table 8.59), and about the same as for the non-hydrated smectite consistent with a lower E_L value. The same effect is observed between the B[A] configurations.

Table 8.58 : Total binding energies, sodium to water oxygen O_w interatomic distances, hydrogen water H_w to basal oxygen O_b interatomic distances, and water-water hydrogen bond distances (between molecules 2 and 3, and, 1 and 3), of three water molecules around cations A, B, E and F. Binding energies are in kJ/mol and interatomic distances are in Å. [X] denotes hydrogen bonding with a basal oxygen atom located on X.

position / configuration	binding energy	Na- O_w distances			H_w - O_b distances			O_w - H_w (O_w - O_w) distances		
		Mol 1	Mol 2	Mol 3	Mol 1	Mol 2	Mol 3			
A[B]	α 1	156	2.24	2.29	2.29	1.77	1.862	1.91		
	α 2	130	2.22	2.25	2.47	1.78	1.846	2.01		
B[A]	α 1	143	2.29	2.30	2.45	1.83	1.95	2.10		
	α 2	140	2.24	2.25	2.30	1.75	1.86	1.88		
B	β	135	2.34	2.41	2.50	1.80			1.96 (2.75)	2.05 (2.80)
E[F]	α 1	123	2.25	2.27	2.31	1.87	1.86	1.91		
	α 2	116	2.26	2.27	2.31	1.89	1.919	1.97		
E	β	118	2.32	2.37	2.57	1.78			1.95 (2.75)	1.98 (2.75)
F[E]	α 1	118	2.27	2.29	2.30	1.78	1.95	1.98		
	α 2	120	2.24	2.26	2.30	1.90	1.91	1.94		

Table 8.59 : Deformation energy E_L (in kJ/mol) due to changes in the smectite structure and the sodium to silicon plane distance (in Å) of three water molecules around cations A, B, E and F. The distance between the tetrahedral aluminum substitution and the sodium are also indicated (increased distances with respect to the dry clay are written in brackets). [X] denotes hydrogen bonding with a basal oxygen atom located on X.

position / configuration		E_L	Na-(T-plane) distances	Na- Al_T distances
A[B]	$\alpha 1$	97	2.89	3.33 [0.10]
	$\alpha 2$	136	2.87	5.07 [1.84]
B[A]	$\alpha 1$	86	2.71	3.09 [0.01]
	$\alpha 2$	121	2.93	4.46 [1.38]
B	β	40	2.28	3.03 [-0.05]
E[F]	$\alpha 1$	116	2.83	
	$\alpha 2$	113	2.81	
E	β	62	2.19	
F[E]	$\alpha 1$	113	2.72	
	$\alpha 2$	138	3.02	

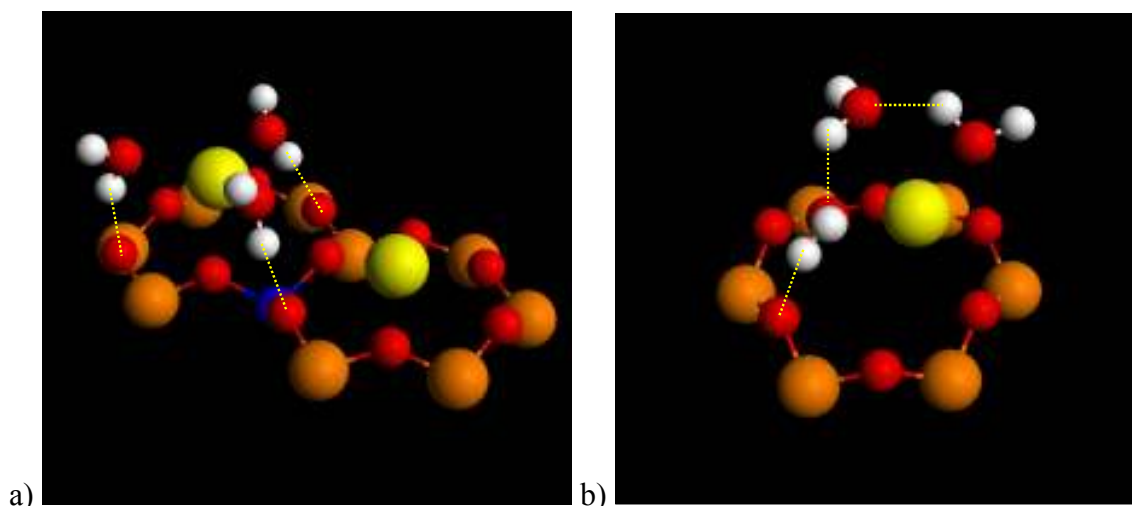


Fig. 8.75 : Configurations of three water molecules around the counter ions. a) configuration A[B]- $\alpha 1$, b) configuration E- β . Oxygen atoms are in red, hydrogen atoms in white, silicon atoms in orange, sodium atoms in yellow, and the aluminum atom in blue. The yellow dashed lines denote hydrogen bonds.

8.5.3.4. SHORT DYNAMICS OF FOUR WATER MOLECULES ON THE SMECTITE SURFACE

In order to explore probable molecular configurations on the complicated surface of the clay and their stability, an ultra-short DFT (Car-Parrinello) molecular dynamics calculations was performed with four water molecules on the surface of the 221 clay model. The time of the simulation (1.5 ps) allowed us only to explore whether the configuration determined through optimization was highly unstable around room temperature (279 ± 13 K) and also to possibly identify other relevant ones. As an initial configuration, we considered the structure obtained after optimization with the molecules clustering around the cation in F. There was a specific

reason for this choice. From the chemical formula of the Kunipia-F sodium smectite, about one out of thirty surface silicon atoms is replaced by an aluminum atom. As a result, three out of sixteen hexagonal rings are affected by the aluminum replacement. Therefore the environment of cation F, located above magnesium, for the dynamic calculations, was considered to be more representative of the smectite behavior than the one of cation A, located close to aluminum.

Fig. 8.76 show the behavior of the water molecules #1 to #4 in terms of interatomic distances. Fig. 8.77 are snap shots of the simulation at $t=0$ (after thermalization) and at the end of the simulation ($t=1.488$ ps). At $t=0$ (Fig. 8.77a) molecule #4 forms a hydrogen bond with molecule #2, that is bound to the sodium counter ion located above the hexagonal structure F, and forms also a hydrogen bond with one basal oxygen atom. Molecule #3 is also bound to the cation in F, but molecule #1 is not. During the simulation the molecule #4 detaches from molecule #2 and forms a bond with the sodium counter ion located above the structure E (Fig. 8.76a). The molecule #1 moves away from the hexagonal structure F to the structure E and forms a hydrogen bond with the molecule #4 (Fig. 8.76a). Along its trajectory the molecule #1 is found to form a short hydrogen bond with a basal oxygen atom (Fig. 8.76a). The molecules #2 remained bound to the cation located above the structure F and the molecule #3 come closer to the molecule #2 (Fig. 8.76b). At the end of the simulation the molecules #3 and #1 are hydrogen bonded to the molecules #2 and #4, respectively, that are bonded to the cations F and E, respectively.

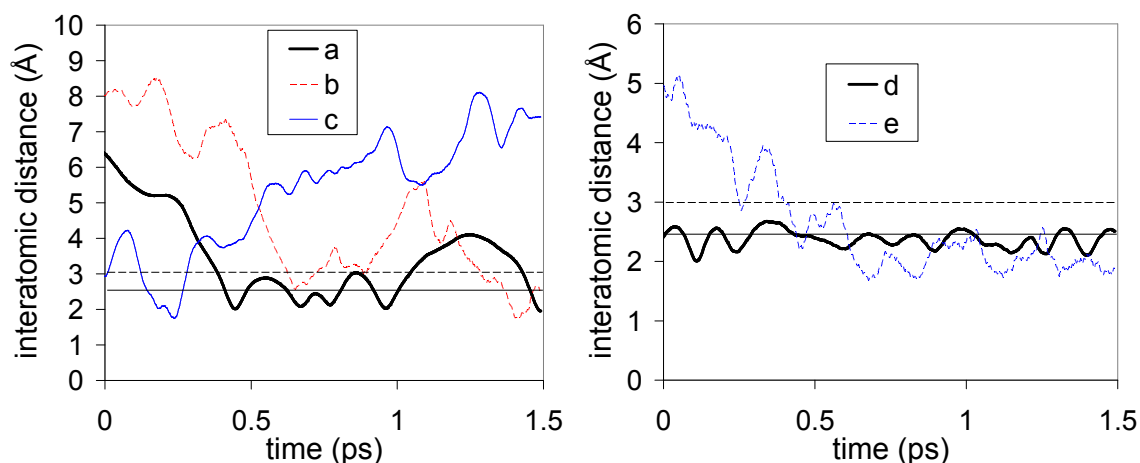


Fig. 8.76 : Interatomic distances between the water molecules #1 to #4 during the MD simulation. Distances between a) the oxygen of water molecule #4 and the cation located in the hexagonal structure E, b) the hydrogen of water molecule #1 and the oxygen of water molecule #4, c) the hydrogen of water molecule #1 and the basal oxygen atom O₁, d) the oxygen of water molecule #2 and the cation located in the hexagonal structure F, and e) the hydrogen of water molecule #3 and the oxygen of water molecule 2. The straight horizontal full line corresponds to the binding radius of one water molecule on a sodium atom in vacuum. The straight horizontal dashed line corresponds to the maximal length of an hydrogen bond

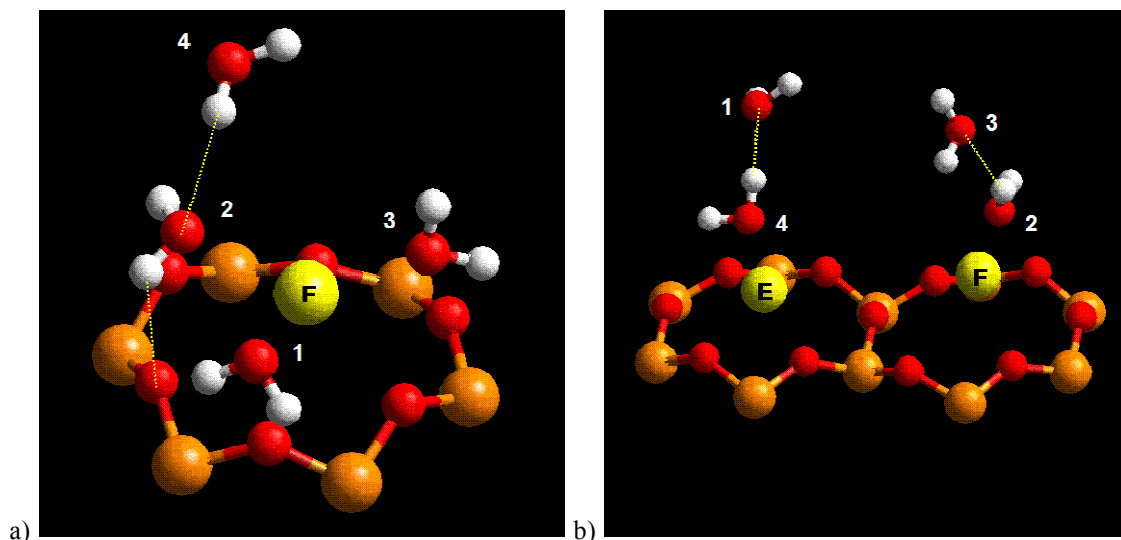


Fig. 8.77 : Snap shot of the dynamic molecular simulation of 4 water molecules on the 221 clay slab model. a) initial configuration ($t=0$). b) final configuration ($t=1.488$ ps). Oxygen atoms are in red, hydrogen atoms in white, silicon atoms in orange, and sodium atoms in yellow. The yellow dashed lines represent hydrogen bonds.

8.5.3.5. BINDING OF FOUR WATER MOLECULES

Most of the results in Table 8.60 correspond to geometry optimization started from a cluster of molecules located around one cation. Instead the E&F configuration was the configuration obtained in the previous section from quenching from a trajectory obtained with Car-Parrinello molecular dynamics. One can identify three most relevant types, depending on the number of molecules directly bound to the counterions: four, three, or two water molecules bound to the sodium cation.

The presence of an aluminum replacement in the tetrahedral sheet continues to render A more hydrophilic than F. The competing role of the surface (counterion and basal oxygens) and the water-water interaction in attracting water molecules emerges clearly from inspection of Table 8.60 and Fig. 8.78.

The two water arrangements in A are clearly different but are degenerate within the accuracy of the calculations. Indeed in A[B] (Fig. 8.78a) four monomers are adsorbed separately, with

three out of them being H-bonded to the basal oxygen atoms (two bound to Al), whereas in A (Fig. 8.78b) the adsorbate can be described as three (distant) molecules bound both to the counterion and to an extra off-plane molecule. In contrast, the three configurations we calculated on the F domain differ significantly in the binding energy. In both F[E]a and F[E]b one molecule is also relatively close to the E site (2.5 Å). However the two structures are quite different: water is adsorbed in the form of a dimer and two monomers in F[E]a (Fig. 8.78c) and in that of four monomers in F[E]b (Fig. 8.78d); the latter is similar to the case of A[B] but with weaker H-bonds to the surface as reflected in the large energy difference (~30 kJ/mol). In F (Fig. 8.78e) one can recognize a monomer and a trimer; the latter has only one molecule connected to the surface and one acting as bridge between those bound to the counterion. Interestingly, the case of two dimers separately adsorbed on the E and F domains (Fig. 8.78f) (O_w-O_w distance ~ 3.6Å) is also an energetically competitive configuration.

Taking as reference the 3 water molecules configuration F[E]- β (Table 8.58), the energy of the additional molecule for the configuration F[E]a is 50.4 kJ/mol.

The energy loss E_L of the substrate due the structural changes induced by water adsorption was also calculated. A comparison between Table 8.60 and Table 8.58 show that the Na moves further away from the surface if the four molecules are bound to the counter ion. Here again a lower energy loss correlates well with a shorter sodium to silicon plane distance. Also, the higher the number of bonds formed between the hydrogen atoms of the water molecules and the basal oxygen atoms, the larger is the distance between the sodium cation and the silicon plane.

Table 8.60 : Total binding energies, sodium to water oxygen O_w interatomic distances, hydrogen water H_w to basal oxygen O_b interatomic distances, and water-water hydrogen bond distances, of four water molecules. Binding energies are in kJ/mol and interatomic distances are in Å. The energy loss E_L due to changes in the smectite structure and the sodium to silicon plane distance are also given. Binding sites are written in brackets. The configurations are sorted by the number of water molecules bound to the sodium counter ion. [X] denotes hydrogen bonding with a basal oxygen atom located on X.

number of molecules bound to the cation	4			3		2
position / configuration	A[B]	F[E] (a)	F[E] (b)	A	F	E&F
binding energy	184	171	153	180	164	159
Na- O_w distance	2.24 [A] 2.25 [A] 2.32 [A] 2.37 [A]	2.29 [F] 2.28 [F] 2.39 [F] 2.42 [F]	2.25 [F] 2.33 [F] 2.35 [F] 2.36 [F]	2.33 [A] 2.35 [A] 2.44 [A] 3.45 [A]	2.27 [F] 2.27 [F] 2.33 [F] 3.56 [F]	2.27 [F] 4.67 [F]
		2.52 [E]	2.51 [E]			2.32 [E] 4.48 [E]
H_w - O_b distance	1.70 [A] 1.78 [A] 1.84 [B]	1.90 [E] 1.93 [F] 1.99 [F] 2.15 [F] 2.71 [F] 2.71 [F]	1.83 [E] 2.01 [E] 2.11 [F] 2.42 [F] 2.44 [F] 2.92 [F]	1.90 [A] 2.52 [A]	1.78 [F] 1.89 [F] 2.71 [F]	2.64 [F] 2.94 [EF]
O_w - H_w distance		1.97	2.81	1.82 1.91 2.02	1.73 1.83	1.81 1.83 2.62
O_w - O_w distance		2.73	3.17	2.74 2.81 2.81	2.68 2.76	2.81 2.79 3.59
E_L	210	160	177	55	123	12
Na-T-plane distance	3.88	3.07	3.26	2.30	2.80	1.24 [F] 1.16 [E]

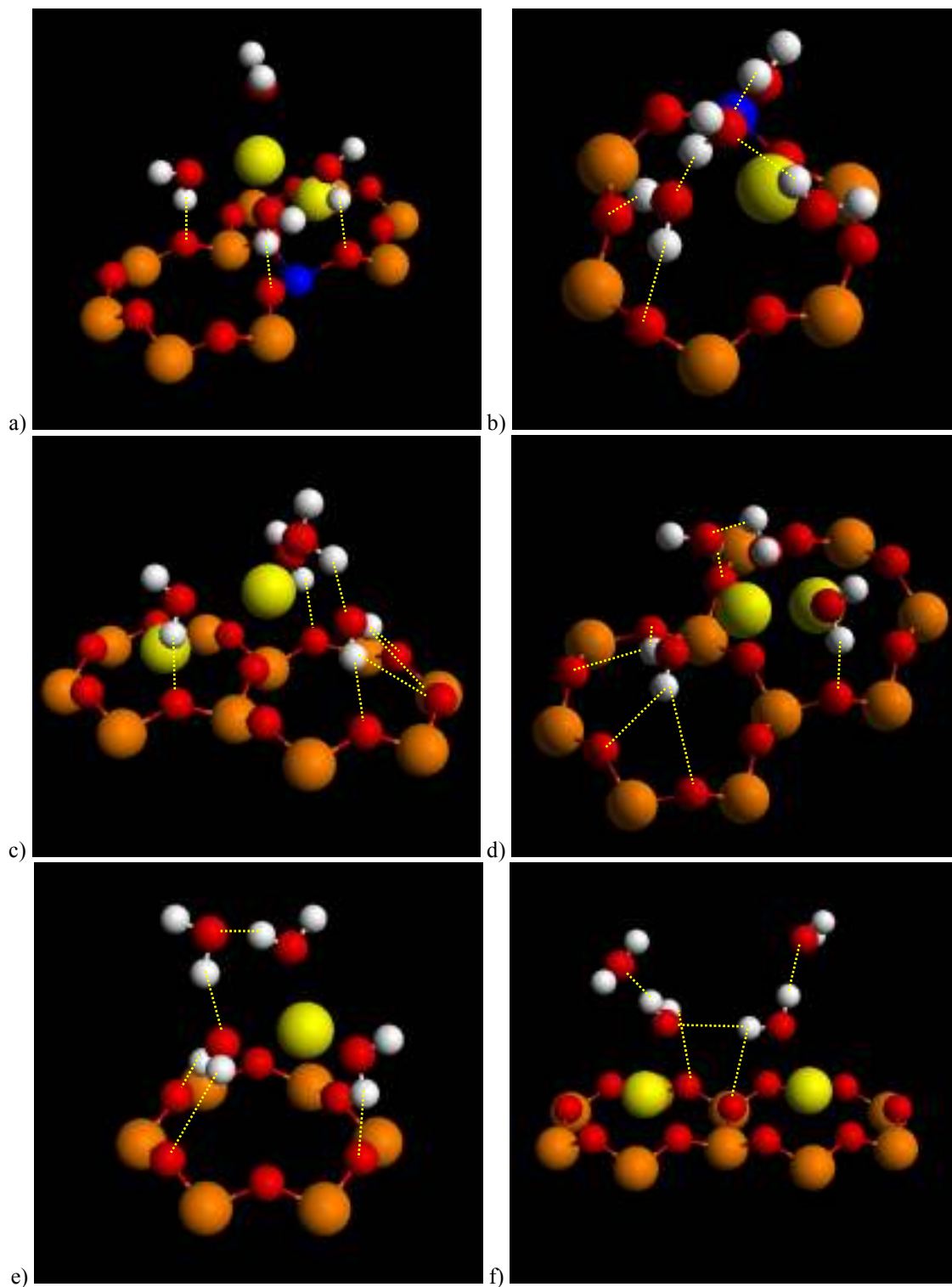


Fig. 8.78 : Configurations of four water molecules. a) configuration A, b) configuration A[B], c) configuration F[E]a, d) configuration F[E]b, e) configuration F, and f) E&F. Oxygen atoms are in red, hydrogen atoms in white, silicon atoms in orange, sodium atoms in yellow, and the aluminum atom in blue. The yellow dashed lines denote hydrogen bonds.

8.5.3.6. SHORT DYNAMIC OF SIX WATER MOLECULES ON THE SMECTITE SURFACE

Another ultra-short DFT (Car-Parrinello) molecular dynamics calculations was performed, though with six water molecules on the surface of the 221 clay model. Here again the time of the simulation (0.62 ps) allowed us only to explore whether the configurations determined through optimization were highly unstable around room temperature (270 ± 14 K) and also to possibly identify other relevant ones. As for the dynamic simulation with four water molecules, as initial configuration, we considered the structure obtained after optimization with the molecules clustering around the cation in F.

Initially ($t=0$) (Fig. 8.79b), molecules #1, #2, #4 and #5 form a hydrogen bond network, and only two molecules (#1 and #3) are bound to the sodium ions, in F and E respectively. Molecule #6 is free, not bound to any other water molecule or basal oxygen atom. At the end of the simulation ($t=0.672$ ps) (Fig. 8.79a) one clearly sees that a closed hydrogen network has formed, driven by the rotation of molecule #3; its hydrogen atom, which was linked with the oxygen atom of molecule #2 is now linked with that of molecule #6. Molecules #1 and #3 remained bound to the cations F and E, respectively.

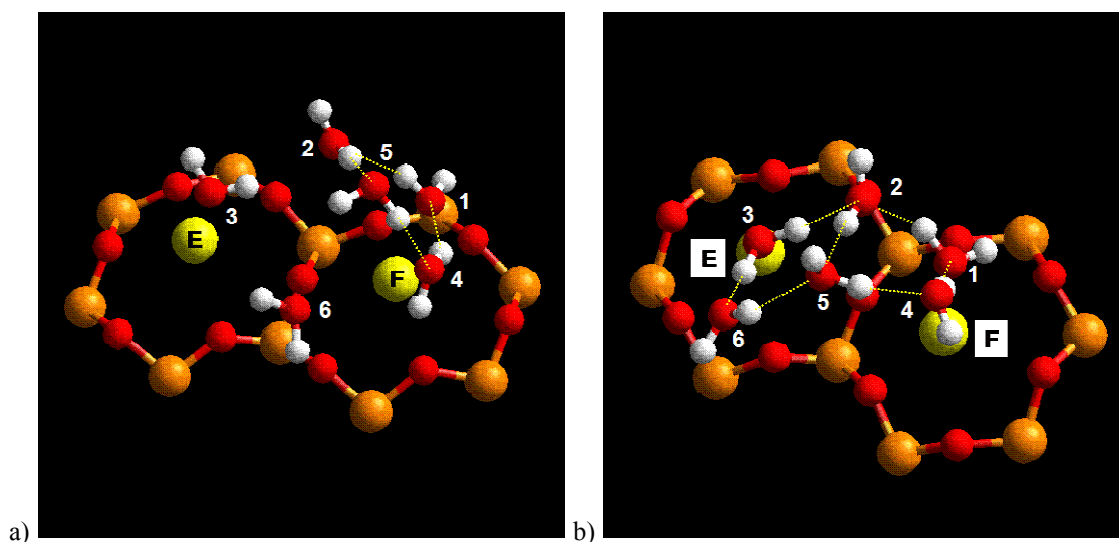


Fig. 8.79 : Snap shots of the dynamic molecular simulation of 6 water molecules on the 221 clay slab model. a) initial configuration ($t=0$). b) end configuration ($t=0.672$ ps). Oxygen atoms are in red, hydrogen atoms in white, silicon atoms in orange, and sodium atoms in yellow. The yellow dashed lines represent hydrogen bonds.

8.5.3.7. BINDING OF SIX WATER MOLECULES

The configurations determined with either geometry optimization (configurations A[B], F[E], and F) or quenching from molecular dynamics trajectories (configuration E&F from the previous section) have been sorted according to the number of molecules bound to one cation

(Table 8.61): five, three, or one water molecule(s) bound to the sodium cation. There is apparently no possibility for six molecules to bind to a single counterion located at the surface. Five is the upper limit both for the A and F cations, with one however significantly farther away (2.47-2.48 Å), and also not too distant from a closer cation (B or E) and H-bonded to a basal oxygen of its ring. In the A[B] arrangement (Fig. 8.86a), the adsorbate can be described as composed of two monomers (one bound to the B-ring via a strong H-bond) and a chain of four (intra-chain O_w-O_w distances ranging from 2.75 to 2.84 Å), out of which three form H-bonds with basal oxygens. In F[E] (Fig. 8.86b), a single monomer coexists with a complex of five (O_w-O_w distances ranging from 2.74 to 2.82 Å) of which only two are H-bonded to the O_b 's.

In the F-case (Fig. 8.86c), only three molecules are bound to the counterion; one is adsorbed as a monomer, also H-bonded to the surface, whereas the other two are part of a pentamer (O_w-O_w distances ranging from 2.69 to 2.91 Å). Of these, one forms four H-bonds to the surface and acts as the (off-plane) cap of a quasi-planar four-fold ring.

The most interesting configuration is the one designated as E&F (Fig. 8.86C) to clarify that each cation is directly bound to only one molecule. One can recognize (see Fig. 8.86d) a water hexamer, formed by two planes in V-shape joint by the two central molecules, with one relatively long H-bond (3 Å) and two molecules bound to an O_b with (also) relatively weak H-bonds. This cluster has a significantly higher binding energy than the others, thus showing that at this stage the intermolecular attraction starts to gain over that of the clay in determining the energetically favored structures for the adsorbates. In this way, the E and F domains start to offer a more favorable adsorption center than the A and B domains.

The sodium to T-plane distances (Table 8.61) follow the trends already identified in the previous sections. Fig. 8.81 shows that, for the configurations of one to six water molecules on the smectite considered in this study, the energy loss E_L is associated with an increased distance of the sodium counter ion to the clay surface. However, there is not a full correlation between sodium to silicon plane distance and energy loss, such that other factors are responsible for the energy loss. In parallel, the Al-O-H angle shows a tendency to increase up to a plateau with the movement of the sodium counter ion away from the surface (Fig. 8.81). This may be attributed to the decreased repulsion between the sodium counter ion and the hydrogen hydroxyl. However this change is small.

Table 8.61 : Total binding energies, sodium to water oxygen O_w interatomic distances, hydrogen water H_w to basal oxygen O_b interatomic distances, and water-water hydrogen bond distances, of 6 water molecules around cation A, around cation F (for configurations a and b), and around cations E and F. Binding energies are in kJ/mol and interatomic distances are in Å. The energy loss E_L due to changes in the smectite structure and the sodium to silicon plane distance are also given. Binding sites are written in brackets. The configurations are sorted according to the number of water molecules bound to the sodium counter ion. [X] denotes hydrogen bonding with a basal oxygen atom located on X.

number of water molecules bound to the sodium	5		3	1
position / configuration	A[B]	F[E]	F	E&F
binding energy	289	243	249	295
Na- O_w distance	2.31 [A] 2.31 [A] 2.32 [A] 2.37 [A] 2.48 [A] 3.72 [A]	2.32 [F] 2.33 [F] 2.35 [F] 2.36 [F] 2.47 [F] 3.42 [F]	2.26 [F] 2.27 [F] 2.34 [F] 3.53 [F] 3.95 [F] 4.03 [F]	2.32 [F] 3.93 [F] 4.96 [F] 5.17 [F]
	2.41 [B] 2.53 [B]	2.53 [E]		2.24 [E] 4.10 [E]
H_w - O_b distance	1.65 [B] 1.68 [A] 1.83 [A] 2.06 [A]	1.79 [F] 1.82 [E] 1.85 [F]	1.77 [F] 2.03 [F] 2.59 [F] 2.62 [F] 2.72 [F]	2.68 [E] 2.85 [F]
O_w - H_w distance	1.81 1.89 1.91	1.82 1.91 1.93 1.98	1.73 1.78 1.78 1.81 2.03	1.64 1.74 1.74 1.77 1.86 1.89 2.09
O_w - O_w distance	2.76 2.75 2.84	2.74 2.79 2.74 2.82	2.69 2.74 2.75 2.78 2.91	2.64 2.72 2.71 2.76 2.81 2.85 3.01
E_L	282	244	126	13
Na-(T plane) distance	4.010	4.020	2.080	1.03 [F] 1.37 [E]

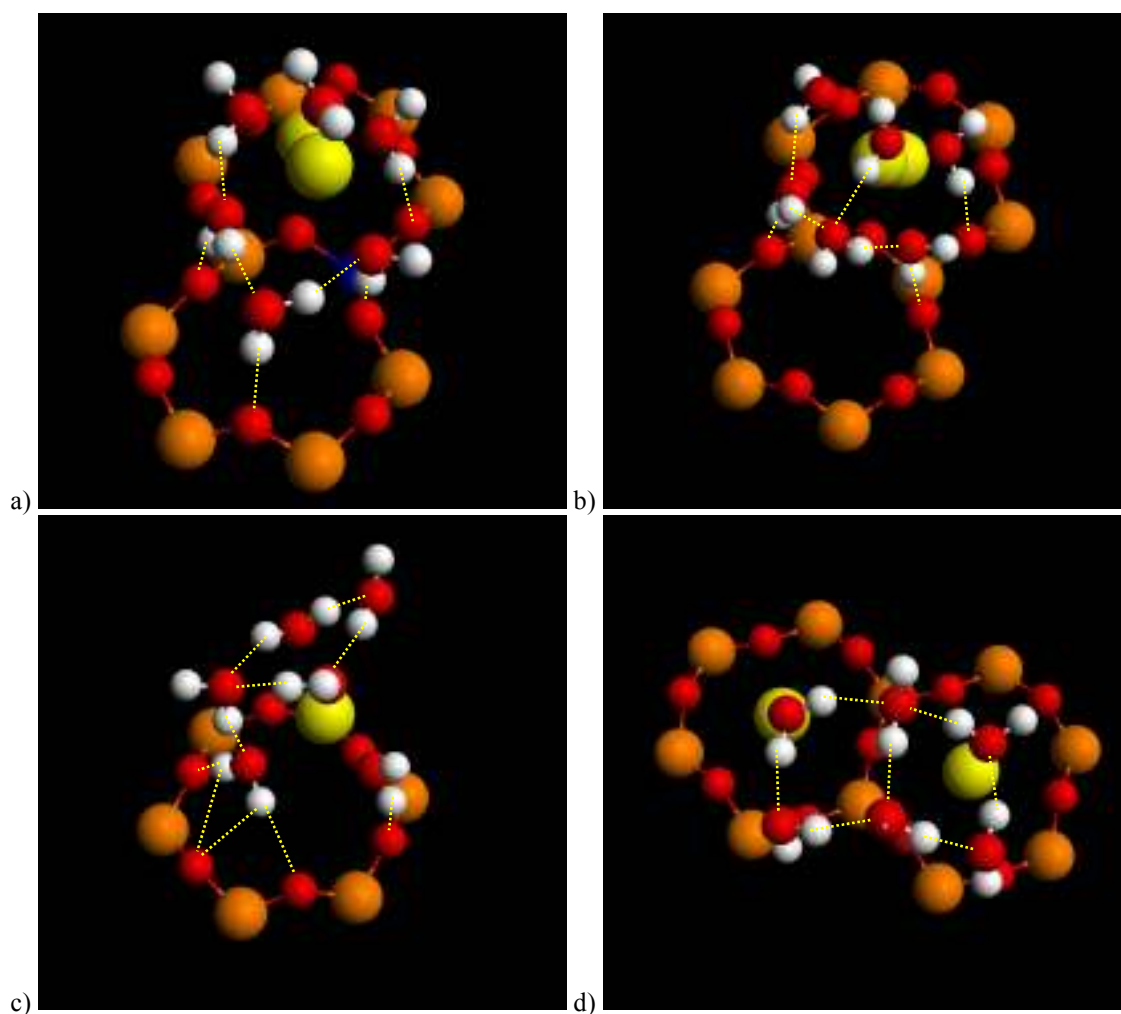


Fig. 8.80 : Configurations of six water molecules a) configuration A[B], b) configuration F[E], c) configuration F, and d) E&F. Oxygen atoms are in red, hydrogen atoms in white, silicon atoms in orange, sodium atoms in yellow, and the aluminum atom in blue. The yellow dashed lines denote hydrogen bonds.

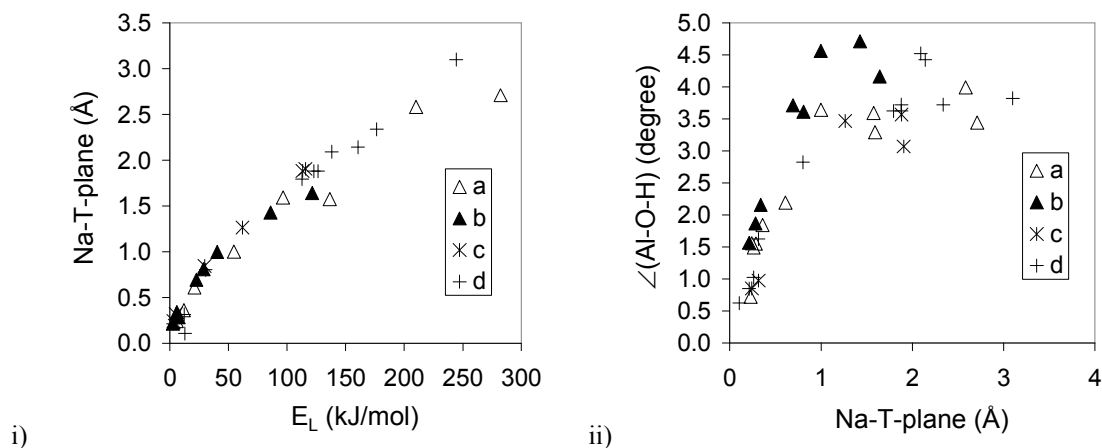


Fig. 8.81 : i) Increased sodium to silicon plane distance relative to the dry clay as a function of the “distortion” energy. ii) Increased in Al-O-H angle relative to the dry clay as a function of the increased sodium to silicon plane distance relative to the dry clay. The data are shown for all the configurations from one to six water molecules around cations a) A, b) B, c) E, and d) F.

8.6. DYNAMICS OF WATER IN THE SMECTITE INTERLAYER

8.6.1. Introduction

Here we attempt a characterization of the diffusion of water within the 211 smectite model considered in this thesis. A 11.77 ps Car-Parrinello molecular dynamics simulation was performed on the 211 supercell bulk model of the Kunipia-F sodium smectite containing 2 sodium counter ions and 24 water molecules for one fixed interlayer distance of 15.2 Å. The initial stage of the simulation of the hydrated system consisted of classical molecular dynamics runs using the COMPASS force field [244] and keeping the clay structure, including counter ions, fixed, thus giving the possibility to the water molecules to rearrange more rapidly while avoiding undesirable changes of the smectite geometry deriving from the use of the empirical potential. This system was thermalized at room temperature. The final configuration was then reoptimized within the DFT scheme and used as initial step of the *ab initio* MD using rescaling of particles velocities until stabilization of the system about room temperature.

8.6.2. Configuration of the sodium cations

From the initial configuration (Fig. 8.82) both cations moved fast (in only 2 ps) close to the midplane, away from the basal oxygen atoms (see Fig. 8.83) with the cation A less centered in the interlayer gallery than cation B. The sodium to water oxygen radial distribution function (RDF) (Fig. 8.84) shows a first peak at 2.32 Å (first coordination shell) (and a second at 4 Å) for both cations. This value is in agreement with the trend found in the calculations of Na-water complexes (section 0); almost full hydration is predicted for both cations, being the average values of the coordination number 5.57 and 5.83 Å for cations A and B, respectively. Other details are in Table 8.62. During the simulation, four specific molecules were permanently bound to both cations. Configurations formed with six water molecules simultaneously coordinated to each cation, of which one shared between them (#20) were observed.

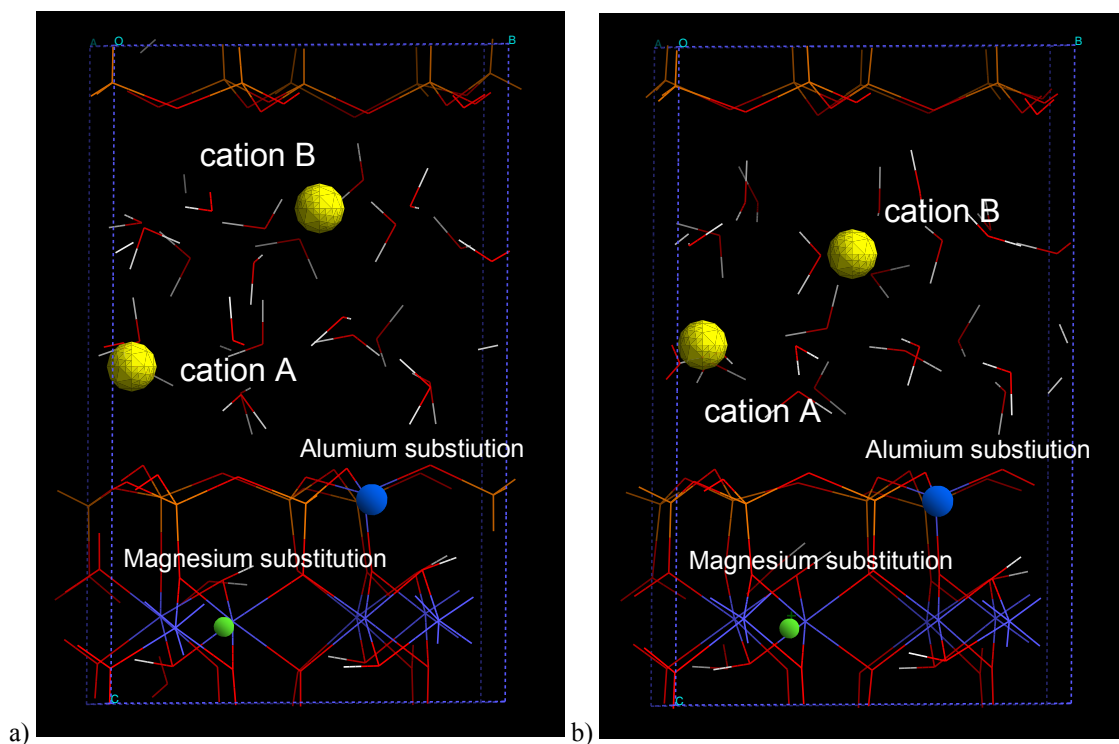


Fig. 8.82 : Snap shot of the dynamic simulation a) after thermalization ($t=0$), and at the end of the MD simulation ($t = 11.77$ ps).

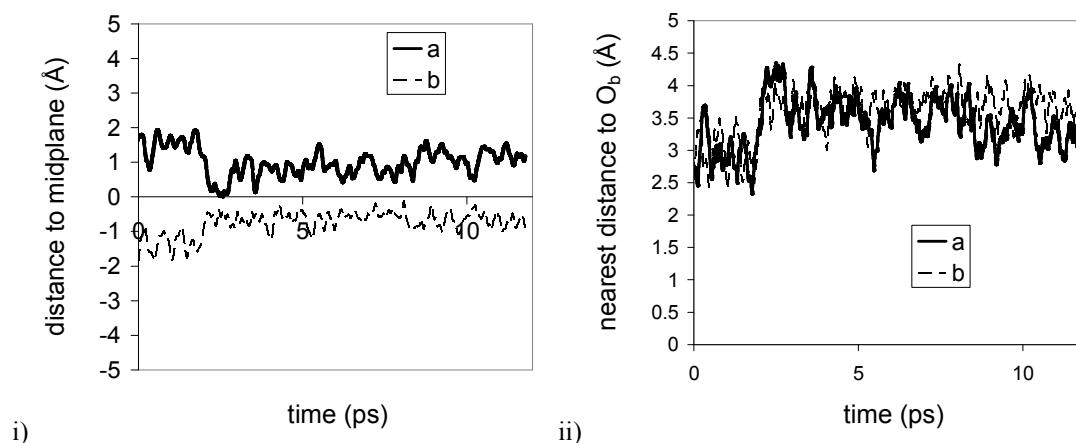


Fig. 8.83 : Distance from the cations (a) A and (b) B to (i) the midplane and (ii) the nearest basal oxygen O_b .

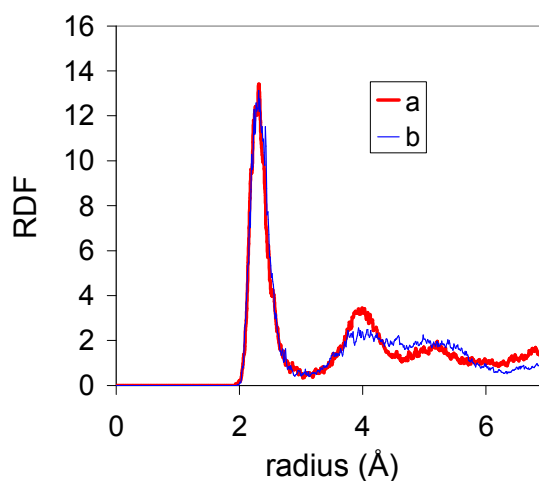


Fig. 8.84 : Sodium to water oxygen $Na-O_w$ radial distribution functions (RDF) for cations (a) A and (b) B.

Table 8.62 : Water molecules bound to the sodium counter ions and relative bond-lengths (in Å) Molecules not permanently bound are denoted in bold.

cations	number of water molecules bound to Na	$Na-O_w$ distances	labels of the water molecules
A	4 to 6	2.311; 2.550; 2.351; 2.290	1, 8, 9, 20, 24, 21
B	4 to 6	2.415; 2.329; 2.4192; 2.290	2, 19, 17, 20, 13, 24

8.6.3. Configuration of the water molecules

We calculated the oxygen-oxygen RDF and corresponding density of the water molecules. The curve averaged over the 24 water molecules (Fig. 8.85i) shows a first peak at 2.66 Å (first coordination shell), and a maximal density of 1.05 g/cm³ at 3.53 Å. The curve averaged over

the water molecules bound to the cations (Fig. 8.85ii) shows – as expected – a broadened and almost bimodal distribution in the first coordination shell (with an additional peak at 3.14 Å.) The water hydrogen to water oxygen RDF (Fig. 8.86a) has a first peak at 0.98 Å (the chemical bond) and a second at 1.72 Å (the hydrogen bond), which is ~ 0.2 Å shorter than in bulk water, whereas the water hydrogen to basal oxygen RDF (Fig. 8.86b) peaks at 1.97 Å (Table 3) showing that these H-bonds are weaker than those of the water network. Also, the number of H-bonds between the basal oxygen and the water molecules is significantly smaller (about four times less) than that between the water molecules themselves.

We calculated the angles between the water dipoles and the normal to the closest clay surface. The angle distribution function of the water molecules shows preferential orientations at 57 ° and 119 ° (Fig. 8.87). The water molecules bound to the cations are preferentially oriented with an angle of 57 ° to the clay surface (Fig. 8.87b). This confirms interpretations from previous NMR measurements (see section 2.4.3).

Based on the calculated distributions we propose a possible average arrangement of the water molecules in the smectite interlayer where one water molecule is orientated with its hydroxyl group almost perpendicular to the smectite surface and its dipole oriented in the direction of the sodium counter ion (Fig. 8.88). Another water molecule is oriented with its dipole moment directed to the first water molecules. However, at this water content, studies usually report a double peak water oxygen distribution, corresponding to a double layer hydrate. Rinnert *et al* already suggested the notion of water layer to be inappropriate for saponite samples (see section 2.5.3.2). We note also that the double peak distribution of water oxygens contains water molecules at the center of the interlayer. The double peak distribution may be the result of the arrangement of water molecules around the sodium cation as long as the cations are found at the center of the interlayer and show therefore a single peak distribution. In our simulation, the cations show a double peak distribution that may create a different distribution of the water molecules in the interlayer due to their arrangement around the cations.

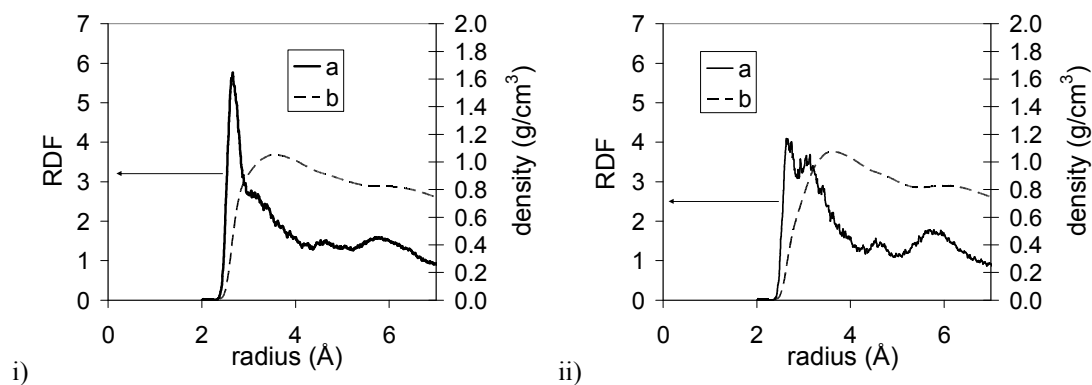


Fig. 8.85 : (a) Water Oxygen-oxygen O_w-O_w radial distribution and (b) corresponding density of water as a function of radial distance. (i) for all water molecules and (ii) for those bound to the cations.

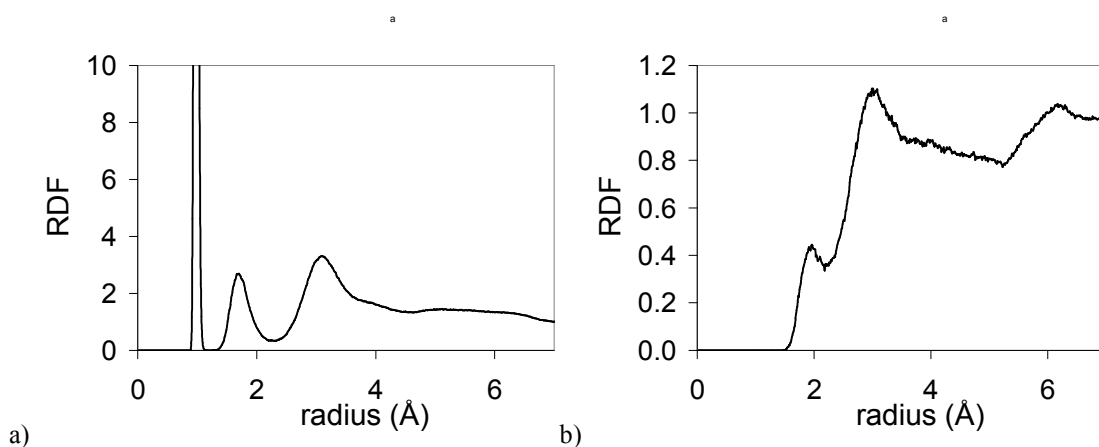


Fig. 8.86 : Radial distribution function of a) the water oxygen to water hydrogen (O_w-H_w) interatomic distances and b) the basal oxygen to water hydrogen (O_b-H_w) interatomic distances.

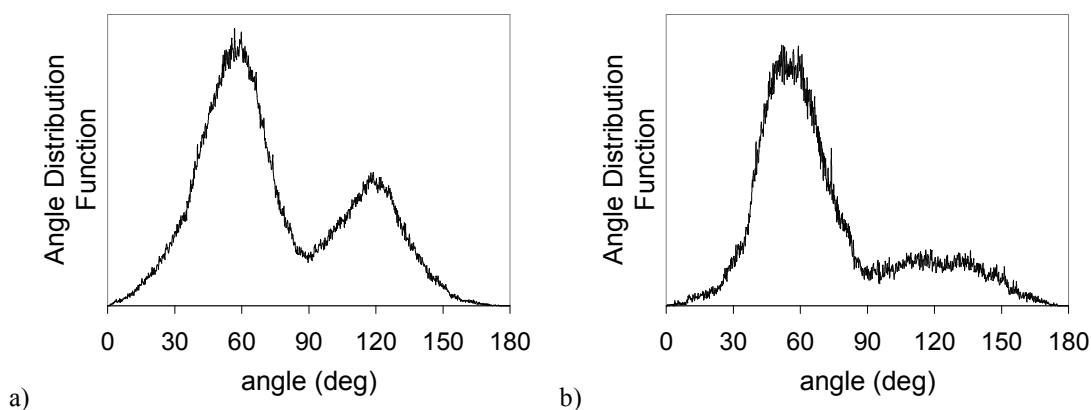


Fig. 8.87 : Distribution function of the angles between the water dipoles and the clay surface for (i) all water molecules, and (ii) the water molecules bound to the cations.

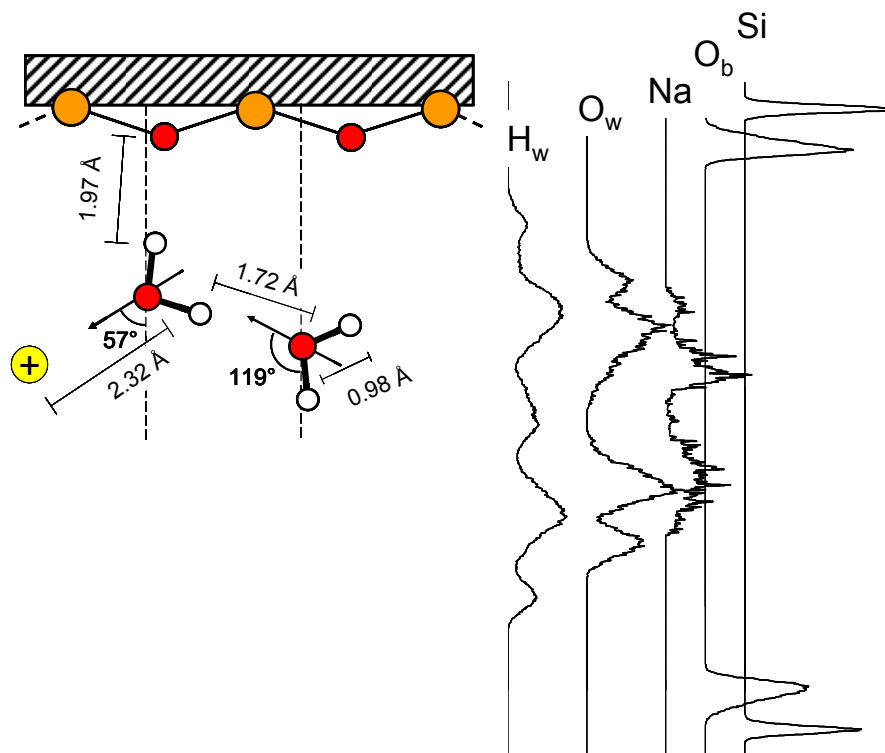


Fig. 8.88 : Density profile for the smectite species (Si, basal oxygen O_b , Na, water oxygen O_w , and water hydrogen H_w) along the direction perpendicular to the smectite surface and illustration of a possible average arrangement of the smectite species in the interlayer. Silicon atoms are in orange, oxygen atoms are in red, hydrogen atoms are in white, and the sodium cation is in yellow.

8.6.4. Diffusion of the water molecules

The values of the radial maximum displacements of each of the 24 water molecules are shown in Fig. 8.89a. The values ranged from 1.22 to 3.26 Å. As can be seen from Fig. 8.89b, no distinction is found between the maximal displacement of the water molecules bound to the cations and the maximal displacement of those never in contact with the cations. Also, no correlation was found between the distance from the water molecules to the smectite layer and their maximal radial displacements. The average displacements was decomposed into two directions parallel to the smectite surface, one of them being in the direction of the line formed by the two counter ions (y -direction), and a direction perpendicular to the surface. From the decomposition, it is clear however that higher mobility is along the y -direction where restrictions imposed from the smectite structure and the presence of the counterions is minimal.

From a linear fitting over the last ~ 10 ps of the Car-Parrinello molecular dynamic simulation we obtain a qualitative value of the self-diffusion coefficient and its components (Table 8.63). We note that the estimate we obtain for the average diffusion coefficient of water at room

temperature is significantly reduced (by a factor of 5) from the value calculated [245] for bulk water ($1.0 \times 10^{-5} \text{ cm}^2/\text{sec}$) within a very similar computational scheme (the latter is smaller than the experimental datum by a factor of 2). The decreased mobility is consistent with the shrinking observed above for the H-bonds in the water network that in turn is related to the strong interaction existing with the counterions. Therefore it can be concluded that the role of the counterions in determining the structural organization and mobility of the water confined within the smectite layers is indeed crucial.

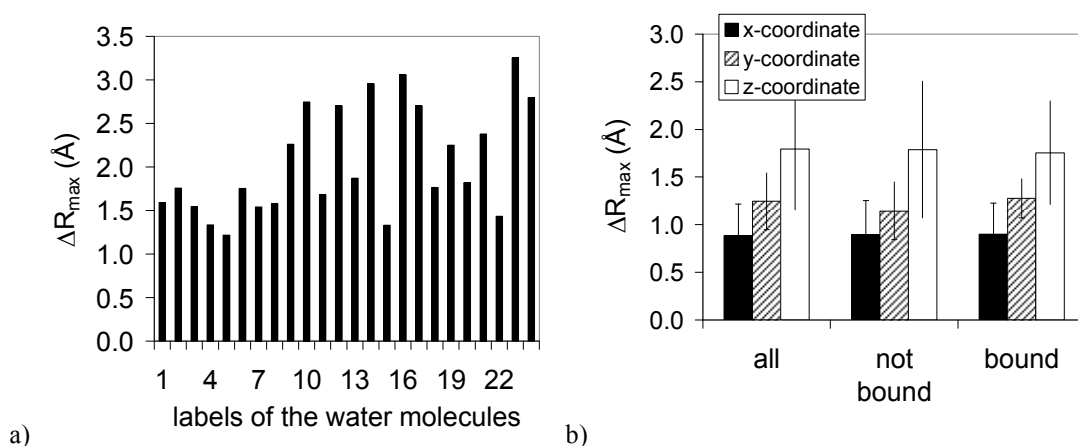


Fig. 8.89 : a) Maximal radial displacements of the 24 water molecules. b) Average maximal displacements of the water molecules in the x-, y-, z- directions: for all , those bound to the cations, and those never in contact with the cations.

Table 8.63 : Diffusion coefficients of the water molecules in the x-, y-, z-directions, and radial average (isotropic value).

	diffusion coefficients ($10^{-10} \text{ m}^2/\text{s}$)
x-direction	1.2
y-direction	2.1
z-direction	1.2
radial average	5.2

8.7. POSSIBLE EXPLANATION FOR THE SWELLING HYSTERESIS

8.7.1. Introduction

Previous studies suggested the hysteresis in smectite swelling to be associated with trapping of the system in metastable “swelling” states separated by a clear free energy barrier. It was suggested that the swelling of the smectite could be attributed to the formation and breaking

of hydrogen bonds between and within layer hydrates (see section 2.6). However, this explanation is not satisfactory because it does not explain the dependence of the hysteresis on the type of counter ion (see section 2.5). The swelling of the clay is also strongly associated with the hydration of the counter ion (see sections 2.5 and 2.10). Moreover, as seen in the previous section, the notion of layer hydrate is controversial. Experience gained in the previous calculations suggested to consider another hypothesis for the origin of the hysteresis, related to the occurrence of different microscopic configurations of the sodium-water complexes.

The higher is the hydration energy of the counter ion, the easier it is for the smectite to swell. It seems reasonable to postulate that the full hydration of the counter ion is necessary for the smectite to swell by the increase in osmotic pressure pertained to its increase mobility, and therefore that the two different interlayer distances in the smectite hysteresis correspond to two different states of hydration of the counter ion: a fully hydrated state for the expanded smectite and a partially hydrated state for the non-expanded smectite. Indeed, the expansion of the sodium smectite platelets and the hysteretic region appear at around 6 water molecules per sodium counter ion (see section 2.5), which corresponds to the coordination of a fully hydration sodium counter ion in bulk water [169]. In previous calculations (section 8.5), we observed different configurations for the same number of water molecules on the smectite surface due to the tendency of the water molecules to form hydrogen bonds between each others, and, to a lower extent, with the smectite surface. We can therefore envisage that, in the hysteretic region, at the same water content, the non-expanded state corresponds to a configuration where the counter ion is partially hydrated with the water molecules not bound to the counter ion forming hydrogen bonds between each other and with the smectite surface. The extent of the hysteresis would therefore depend upon the difference in energy between the two possible configurations, as far as a lower difference in energy would correspond to a larger hysteresis. Indeed, for the sodium smectite the binding energy of one water molecule on the sodium counter ion differs from the energy of two hydrogen bonds by only a few kJ/mol (section 8.5.1.1). The difference being expected to be higher for the lithium and the calcium cations because of their greater hydration energies, this may explain the experimental observation that the hysteresis is more pronounced for the sodium smectite than for lithium and the calcium smectites (see section 2.5).

To investigate this view, two sets of simulations were performed, differing in the initial configuration of the sodium ions: in one (sample I) they were all close to the smectite surface (Fig. 8.90a) to mimic the initial stage of the “incremental” adsorption while in the other

(sample II) they were all located near the midplane of the interlayer gallery to represent the initial stage of “incremental” desorption (Fig. 8.90a). The aim is to see how these two initially different states evolve in correspondence to different interlayer distances d for fixed water content. Therefore calculations were performed for eight d -values, regularly spaced in the range from 12.2 to 15.7 Å. The structural model for the dry smectite is the 221 supercell. The system contains four sodium counter ions and twenty-four water molecules, thus allowing in principle for full hydration. The first stage of each simulation consisted of classical MD using the COMPASS force field [244], up to thermalization at 300K, which provided an initial configuration for the Car-Parrinello MD runs. Rescaling of particles velocities was applied until the temperature of the system established itself also around room temperature. The duration of these simulations ranged from 3.1 ps to 13.2 ps. This was indeed sufficient to distinguish the behavior of the system dependent of the interlayer distance. Moreover, in order to estimate the dependence of the relative energy of the two “final” states on the interlayer distance, (ultra-short) Born-Oppenheimer (BO) simulations, which, by quenching the electron system to the ground state, give more accurate energy values. Deuterated water was considered, so as to increase the time step (from 0.073 ps to 0.097 ps) of the MD integration.

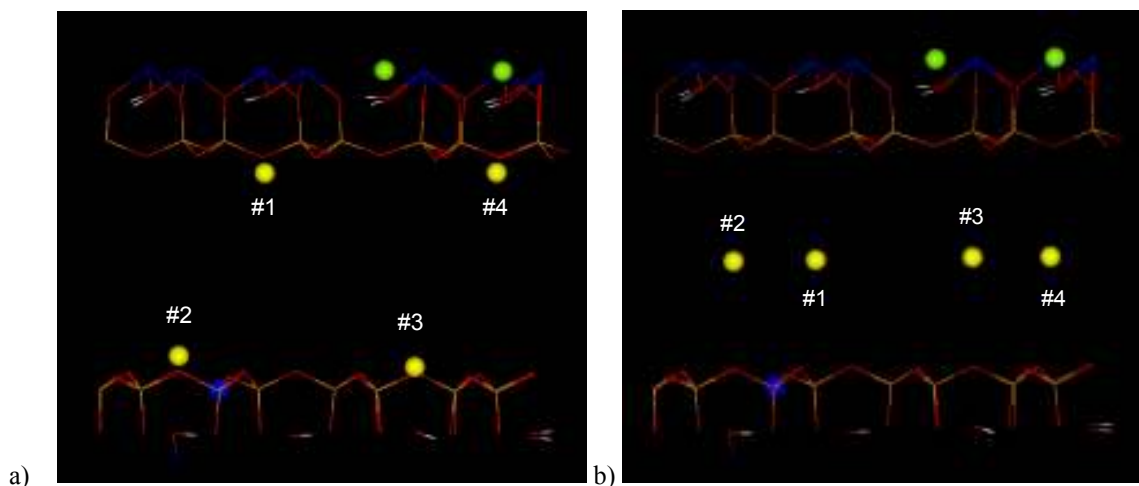


Fig. 8.90 : Position of the sodium cations (in yellow) #1 to #4 above the smectite surface for a) sample I and b) sample II. The aluminum atom is in blue. The magnesium atoms are in green. The basal oxygen atoms are in red. The silicon atoms are in orange.

8.7.2. Results

The cations were sufficiently mobile in both samples (at all interlayer distances) to move away from the initial configurations. Fig. 8.91 reports the behavior of the cation distances from the midplane (i) and from the basal oxygen atom (ii), averaged over time, as a function

of the interlayer distance. Values calculated for the sodium to mid-plane distances and the sodium to the nearest basal oxygen in the two samples are found to overlap within the error bars. As one can see by comparison with Fig. 8.91iii, the displacement of the cations relative to the midplane correlates with the number of water molecules in the first solvation shell (coordination number CN) of the cations, that have been calculated from the sodium to the water oxygen RDF. The sodium ions are always only partially hydrated at the concentration we considered. CN values range from a minimum of 1.7 water molecules for a cation close to the smectite surface, to a maximum of 5 per cation, for a cation close to the midplane of the interlayer gallery.

A distinct behavior of the two samples can be recognized in correspondence of interlayer distances 15.7 Å and 15.2 Å: the average values of the sodium to mid-plane distances is lower for sample II, the average values of the sodium to the nearest basal oxygen are accordingly higher, and also the CN are clearly higher.

Fig. 8.92 and Fig. 8.93 show the total energies obtained from averaging over the Car-Parrinello and Born-Oppenheimer simulations. Again a clear distinction is observed only for interlayer distances of 15.7 Å and 15.2 Å and the sample with higher sodium-water coordination becomes energetically favored. The position of the energy minimum shows the swelling effect; the optimal range of interlayer distances also occurs in the region corresponding to experimental observation. While for small values the two states tend to collapse, in that region the two “final” states are energetically degenerate but the “state of order” of Na-water complexes in particular is different. This can be interpreted as a symptom of hysteresis.

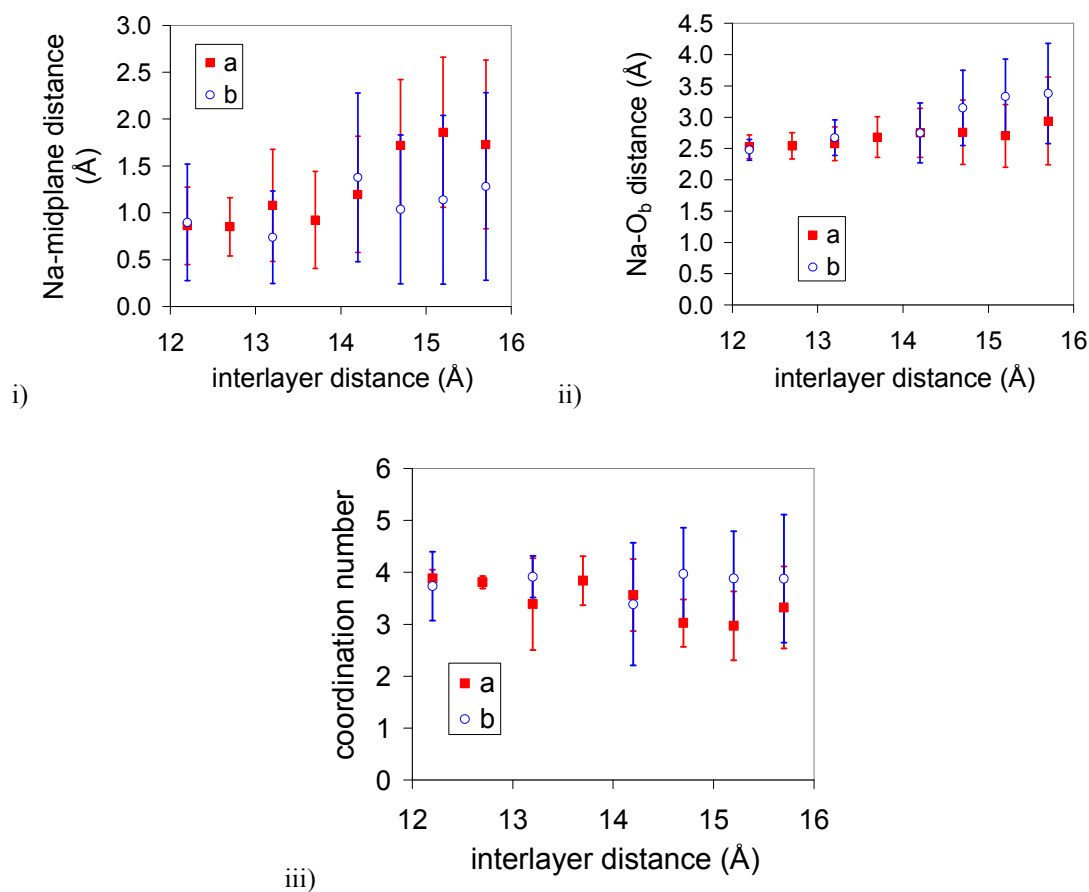


Fig. 8.91 : (i) Average distance of sodium from (i) midplane and (ii) nearest basal oxygen distance; and (iii) average Na-water coordination number, as a function of the interlayer distance. From Car-Parrinello simulations. a) sample I and b) sample II.

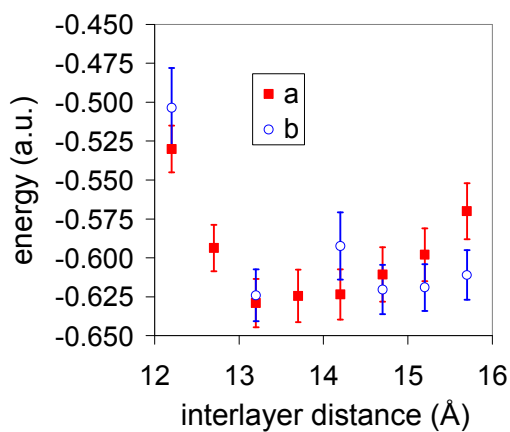


Fig. 8.92 : Average energies from the Car-Parrinello simulations as a function of the interlayer distance. a) sample I and b) sample II. The zero of the energy scale is -2123 Hartree.

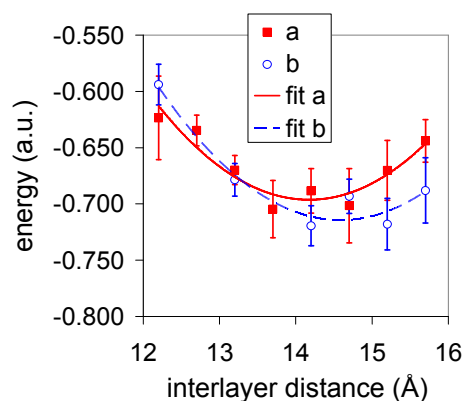


Fig. 8.93 : Average values energies from the Born-Oppenheimer simulations as a function of the interlayer distance. a) sample I and b) sample II. The zero of the energy scale is -2123 Hartree. The curves represent second order polynomial fits.

8.8. CONCLUSION

Geometry optimizations have been performed for the adsorption of single volatile molecules of ethanol, ethyl acetate, pyridine, toluene, n-octane and for the adsorption of one to six water molecules on the surface of a Kunipia-F clay model. The model contained one aluminum substitution in the tetrahedral layer and three magnesium substitutions in the octahedral layer. As a result, the model contained four charge balancing sodium counter ions, two of which were located above silicon-oxygen rings with tetrahedral substitution, and two were located above rings with magnesium substitutions. Comparison with the structure of the neutral pyrophyllite and the Kunipia-F clay model showed a repulsion effect between the sodium counter ions and the hydrogen atom of the clay hydroxyls. The following conclusions were obtained for the binding of the single volatiles on the clay surface.

- Sites with the tetrahedral substitution were found to be more attractive centers (~ 10 kJ/mol) than that with magnesium substitutions for the binding of all the volatile molecules on the sodium counter ions.
- A greater binding energy of the volatile on the sodium cation corresponded to a weaker binding of the sodium cation with the clay surface.
- The rings that contained no counter ion were found to be significantly weaker adsorption centers, so that a volatile molecule can be easily trapped on the counter ions (estimated barrier for diffusion ~ 10 kJ/mol).
- The sodium cation binding sites were found to be essentially independent.

- An inverse correlation was found between the ranking of the binding energies of the volatiles containing an electronegative atom (O or N) on the sites with magnesium substitutions (pyridine (63 kJ/mol) > ethyl acetate (52 kJ/mol) > ethanol (48 kJ/mol) > water (45 kJ/mol)) and the ranking of their ionization potential. The binding energy of toluene was found to be about the same as that of a hydrogen bond and that of n-octane was found to be significantly lower than for the other volatiles, consistent with the nature of its interaction, which is dominated by the ion-induced dipole component.
- For water, H-bonds with basal oxygen atoms helped stabilizing the binding. This was especially true when the basal oxygen atom is linked to the tetrahedral substitution.
- The possibility of water molecules to form H-bonds between each others lead to different configurations of the water molecules on the clay surface for the same number of molecules. The configurations varied in the number of water molecules bound to the sodium counter ion, the number of H-bonds with the basal oxygens, and the number of H-bonds between each others (formation of monomers, dimers, trimers, etc.). With increasing number of water molecules, the intermolecular interaction became gradually more effective than the sodium-water interaction thus limiting the number of sodium-bound molecules to five (no full hydration). At the level of six molecules, the onset of a structural transition is observed for the adsorbate (water 3D-ring) showing that water-water interaction starts to dominate over the clay (counterions and basal oxygens) in determining its configuration.
- An increase in the number of molecules bound to the counterion corresponded to its progressive detachment from the surface (0.2 Å - 4 Å) and was found to be related to energy losses in the clay structure (3 kJ/mol - 282 kJ/mol).
- Ultra short Car-Parrinello dynamic calculations showed the formation of the H-bonds to be a dynamic process.

A 11.77 ps Car-Parrinello dynamics simulation was run on the Kunipia-F clay model with 24 water molecules and two sodium counter ion in the clay interlayer. The water molecules formed both hydrogen bonds between each other and with the basal oxygens, though the latter were found to be weaker and much less present than the former. The counter ions moved close to the center of the interlayer gallery and were found to be hydrated by almost six water molecules. The density profile of the clay species along the direction perpendicular to the clay surface showed that the water molecules did not form a “two-layer” hydrate. This was attributed to their arrangement around the two counter ions that also did show a single peak

density profile and could explain the controversy on the layer hydrates found in the literature (see section 2.5.3.2). The water molecules were found to be oriented, on average, with their hydroxyl group almost perpendicular to the clay surface. Restrictions imposed by the clay surface and the counter ions showed the average diffusion coefficient of the water molecules to be reduced by a factor two compared with that of bulk water.

As an attempt to explain the molecular origin of the hysteresis observed in the equilibrium sorption isotherm of water on smectite clays, two sets of simulations were performed, differing in the initial configuration of the sodium ions in the clay interlayer: in one they were all close to the smectite surface to mimic the initial stage of the “incremental” adsorption while in the other they were all located near the midplane of the interlayer gallery to represent the initial stage of “incremental” desorption. The calculations were performed for a content of six water molecules per sodium counter ion and eight d-values, regularly spaced in the range from 12.2 to 15.7 Å. Unfortunately, the cations were sufficiently mobile in both samples to move away from their initial configurations, and a clear distinction was observed only for the highest interlayer distances at 15.7 Å and 15.2 Å where the sample with higher sodium-water coordination became energetically favored. The two states at the energy minimum, representing the swelling effect, were energetically degenerate but the “state of order” of Na-water complexes was different. This was interpreted as a symptom of hysteresis.

CHAPTER 9 EQUILIBRIUM SORPTION ISOTHERMS OF VOLATILES ON SMECTITE CLAYS

9.1. INTRODUCTION

In CHAPTER 6, we used the values of the surface pressure, to calculate the rate of evaporation of pure liquids. In the case of the clay the surface pressure is given by the equilibrium desorption isotherm and will therefore be used as input parameters to model the release of the volatiles from the clays in the next chapter. In this chapter we present the results on the equilibrium desorption isotherms of water, ethanol, ethyl acetate and toluene on the Kunipia-F clay and its derivatives modified by ion exchange with small organic cations and metallic cations. Two techniques are used for these measurements: Dynamic vapour sorption (DVS) and Knudsen Thermogravimetry (KTGA).

9.2. EQUILIBRIUM DESORPTION ISOTHERMS OF VOLATILES ON THE SODIUM SMECTITES

9.2.1. Reproducibility of the equilibrium desorption isotherms measurements

9.2.1.1. DVS

The DVS equilibrium desorption isotherms for water (at 25 °C), and for ethanol, ethyl acetate and toluene (at 35 °C) are shown in Fig. 9.94, in which the data have been represented by plotting the weight fraction, w_f (Eq. (9.117)) versus a_v (Eq. (9.118)),

$$w_f = \frac{m_v}{m_c} \quad (9.117)$$

$$a_v = \frac{p_v}{p_v^*} \quad (9.118)$$

where m_v and m_c are the mass of adsorbed volatile and the clay dry mass, respectively, p_v is the pressure of the volatile above the clay, and p_v^* is the saturated vapour pressure of the pure volatile liquid at the same temperature.

The desorption isotherms of water and ethanol showed good reproducibility, but those of ethyl acetate and toluene were associated with 1 - 2 % and 0.5% errors respectively. The

desorption isotherm of water showed two distinct steps, whereas the ethanol, ethyl acetate and toluene desorption isotherms were more reminiscent of a Langmuir isotherm. The two step isotherm is generally associated with the hydration of the clay counter ion and the displacement of the clay layers, the interlayer spacing reaching values characteristic of a double solvation layer (see section 2.5.3 and 2.10). The lack of evidence for two steps in ethanol, ethyl acetate and toluene and the relatively low maximum amounts of sorbed volatile suggest that the counter ions were not fully solvated and the clay layers did not expand beyond the equivalent of a monolayer coverage.

It is significant that the amount of water sorbed at $a_v=0.95$ was about 30 wt%, i.e. almost 3 times the amount of ethanol and ethyl acetate sorbed at the same a_v . The maximum amount of sorbed toluene was even lower, i.e., about 10 times less than that of water. This may be attributed to the difficulty of toluene being able to migrate within the clay interlayer galleries, its adsorption occurring mainly at the external surface (see section 2.8). The increase in adsorption observed at higher volatile loadings may be attributed to the filling of micropores by capillary action (see section 2.5.3)

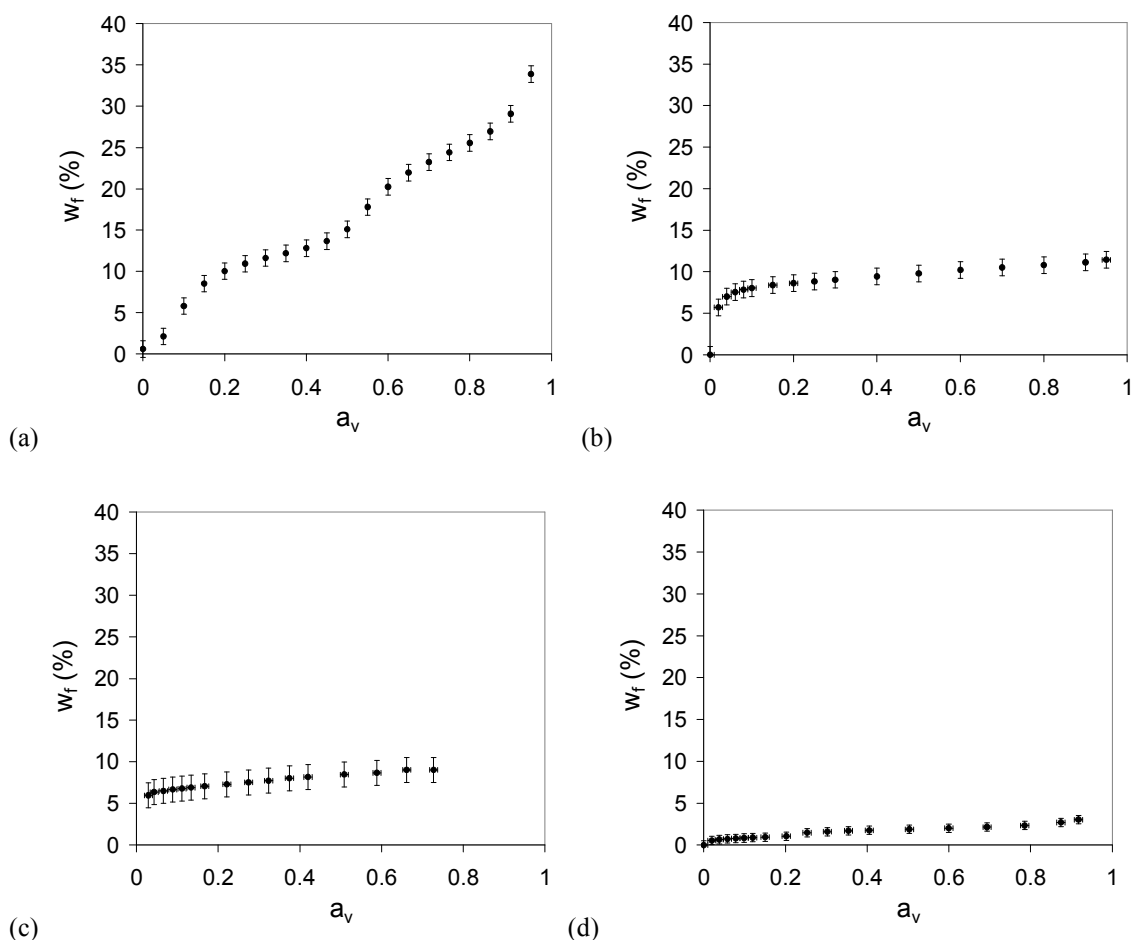


Fig. 9.94. DVS measurements of the desorption isotherms of the volatiles from smectite clay. The weight fraction of the volatiles w_f is plotted as a function of the volatile activity a_v : (a) water (at 25 °C), (b) ethanol, (c) ethyl acetate, (d) toluene (all at 35 °C).

9.2.1.2. KTGA

The KTGA desorption isotherms for bulk water at 25 and 10 °C, and bulk ethanol and ethyl acetate at 10 °C, are given in Fig. 9.95. In these experiments the main uncertainty was associated with residual volatile in the clay at the end of each run. To determine the amount of residual volatile, the cell was heated to 70 °C. Satisfactory reproducibility was observed for water and ethanol, but the results for ethyl acetate showed more uncertainty. Two steps were again present in the desorption isotherms of water, but were less in evidence for the ethanol and ethyl acetate, consistent with the results from the DVS measurements.

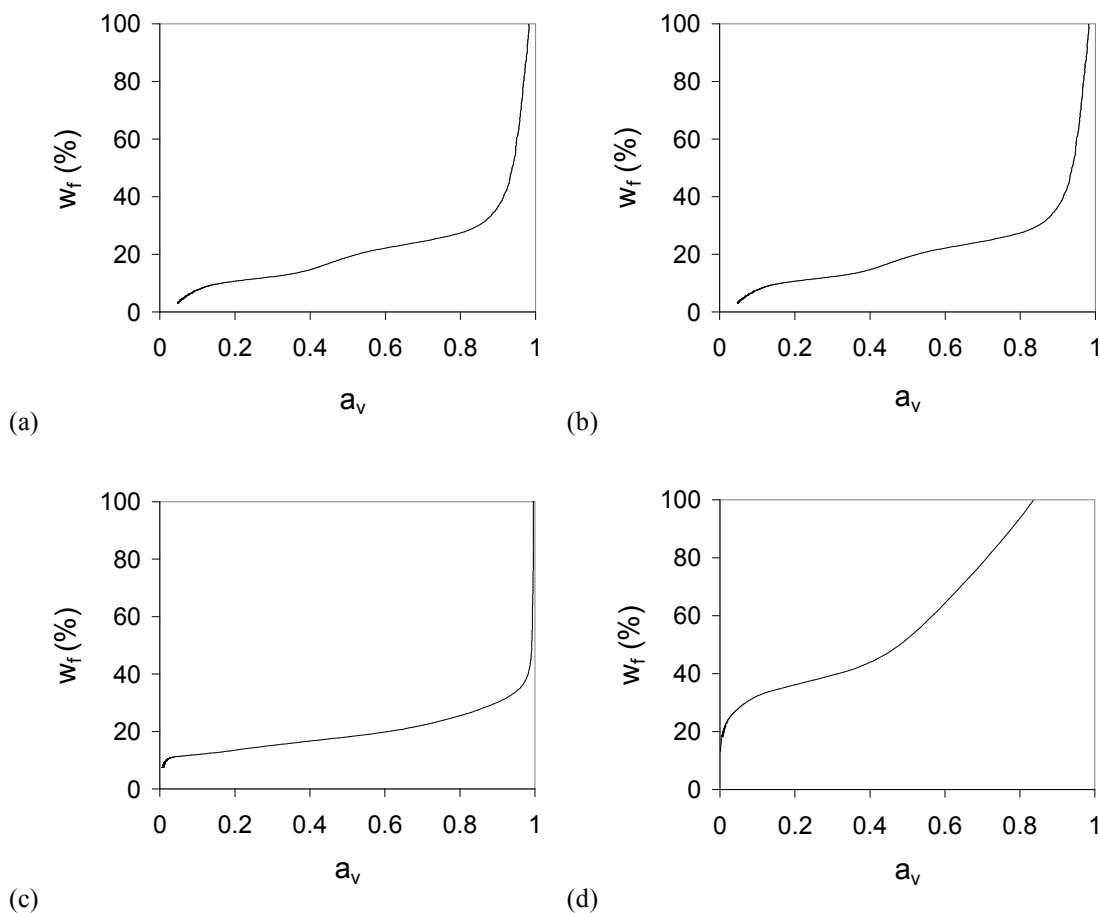


Fig. 9.95. KTGA measurements of the desorption isotherms of volatiles from smectite clay. The weight fraction of the volatiles w_f is plotted as a function of the volatile activity a_v : (a) water at 25 °C, (b) water at 10 °C, (c) ethanol at 10 °C, (d) ethyl acetate at 10 °C.

9.2.2. Comparison between the KTGA and DVS measurements for water

In the KTGA method, the data provide a continuous record of the desorption process, and the acquisition time for a complete desorption isotherm is about 10 times shorter than for the DVS method. However, the desorption isotherms could only be obtained at relatively low temperatures in the present case (10 °C), because the evaporation rates of water, ethanol and ethyl acetate were too rapid at higher temperatures, and the technique was not suitable for toluene because of the intrinsic limitations of the available Knudsen cells (O-ring sealing sensitive to toluene vapor). On the other hand data could only be obtained at relatively high temperatures by DVS, because equilibrium could not be reached at low temperatures over reasonable periods of time.

Both the KTGA and the DVS methods also have limitations at very low vapor pressures. In the case of DVS, low vapor pressures are difficult to control and measure owing to the limited accuracy of the flow control and the dew point analyzer. In the case of the KTGA method, the

volatile cannot be fully removed from the sample at the measurement temperature, so that the evaluation of m_v requires additional quantification of the residual volatile.

Fig. 9.96 shows the desorption isotherms of water obtained with the two methods at 25°C. The two trends are in substantial agreement, the main discrepancies being observed in the ranges of a_v corresponding to large changes in slope, i.e. at very low and very high water contents, and at the transition between the two pseudo-plateaus. These discrepancies may be accounted for in terms of the dynamic nature of Knudsen desorption, which implies steady migration of the solvent towards the head space and then through the orifice of the Knudsen cell. The system requires a certain time to achieve the steady state characterized by Eq. (4.97). A slower suction rate, e.g., use of a narrower orifice, usually improves performance, but increases the measurement time. The Knudsen cell used in the present case was designed for foodstuffs [184] that necessitate relatively rapid measurements because of their tendency to degrade. The orifice size therefore represents a compromise between the suction rate and the experimental time, and hence the sensitivity to changes in the desorption rate. The differences between the Knudsen and DVS isotherms were nevertheless limited to around 2.4 wt% in the range of most relevance for applications, i.e. for RH of the order 45 %, in which the results from the DVS were also consistent with those obtained from saturated salt solutions.

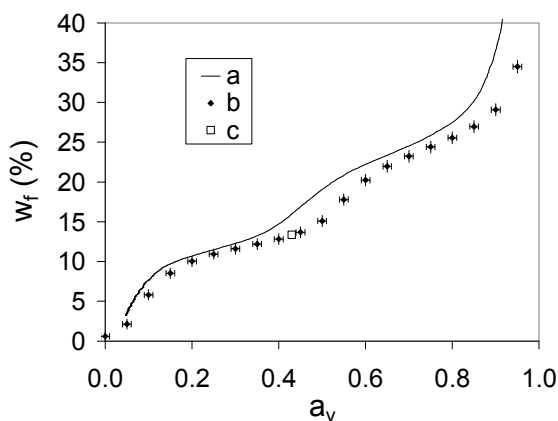


Fig. 9.96. Equilibrium desorption isotherms of water at 25 °C: (a) KTGA method, (b) DVS method, (c) equilibration with saturated salt solutions.

9.2.3. Effect of temperature on water desorption isotherm

Fig. 9.97 shows the desorption isotherms of water obtained at different temperatures with DVS and KTGA. Reasonable agreement was again obtained. In general, the changes in a_w with temperature are expected to reflect the difference in binding strength between water

molecules in the bulk and water molecules in the clay-water system. However, in the present case, the temperature had little effect on water desorption (at least within the experimental detection limits). The experimental results therefore suggest that the binding strength is of the same order for the two types of interaction, which is consistent with our previous results of *ab initio* calculations (section 8.5.1).

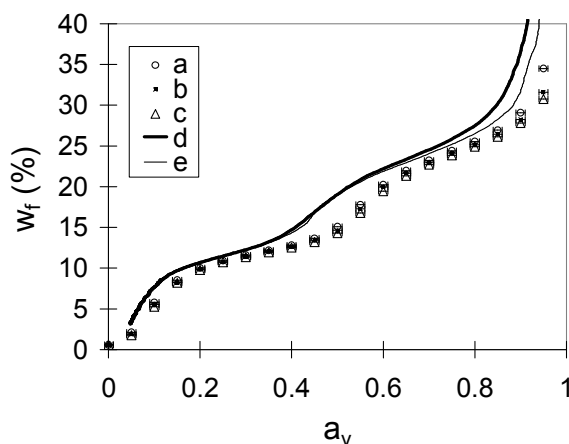


Fig. 9.97. Equilibrium desorption isotherm of water on the clay measured by the DVS method at a) 25 °C, b) 30 °C and c) 35 °C, and by the KTGA method at d) 25 °C and e) 10 °C.

In order to provide a better indication of the effect of changes of temperature on the gas/condensed phase partition, the same desorption data have been plotted as function of the water concentration in the gas phase, c , calculated according to Eq. (9.119), (expressed in mol m^{-3}), as shown in Fig. 9.98.

$$c = \frac{p_v}{RT} = a_v \frac{p_v^*}{RT} \quad (9.119)$$

At high water contents, the equilibrium concentration of water in the gas phase above the sample approaches the saturated water vapor concentration. As the water content is decreased, the water concentration in the gas phase decreases owing to sorption of the water molecules in the clay. There is hence a transition from a state similar to that of the bulk liquid to a state dominated by the interactions of the water molecules in the clay-water system. This transition is clearly independent of the temperature in the range considered, but decreasing the temperature decreases the gas phase concentration owing to the lower kinetic energy of the molecules.

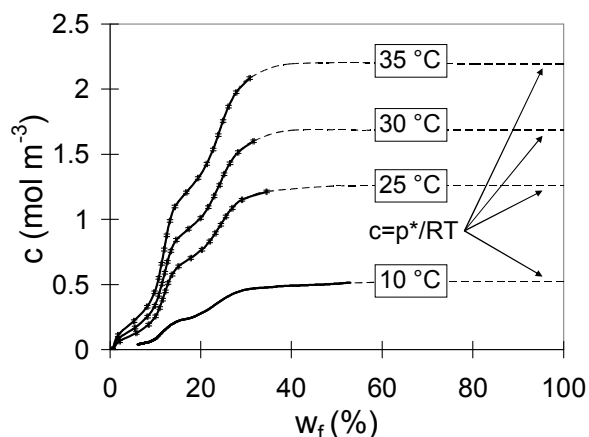


Fig. 9.98. Equilibrium desorption isotherm of water from smectite clay measured by DVS at 25 °C, 30 °C and 35 °C and by KTGA method at 10 °C.

9.2.4. Comparison between volatiles

To facilitate comparison of the desorption of different volatiles, the desorption data have been plotted as a function of the coverage θ , defined by,

$$\theta = \frac{m_{\text{solvent}}}{m_{\text{clay}}} \frac{M_{\text{clay}}}{M_{\text{solvent}}} \quad (9.120)$$

where m and M are the mass and molar mass, respectively, the molar mass of the clay referred to the crystalline unit cell corresponding to the chemical formula of the clay (746 g/unit cell (section 7.2)). Fig. 9.99(i) to (iv) show the trends observed at 10 and 35 °C. At large θ , all the curves attain or approach a plateau. The minimum θ at which saturation is reached with water is almost 12 molecules per unit cell, while lower values are predicted for the other volatiles. The details of the desorption at lower θ , i.e. when the interaction with the clay counter ions dominates (this depends on temperature, but usually occurs at $\theta < 2$) are shown in Fig. 9.99 (iii) and (iv), for 10 and 35 °C, respectively. One unit cell contains on average about one sodium counter ion, so that data corresponding to $\theta < 2$ reflect the interaction of the volatile molecules with the clay counter ion. The trends for the four volatiles indicate that their thermodynamic activities follow the order: ethyl acetate > ethanol > water > toluene, according to the data at 10 °C. There is more uncertainty in the data at 35 °C, because the larger volatility reduces the detectability at low θ . Nevertheless, the behavior of toluene remains distinct from that of the other volatiles.

Our aim is to compute how the thermodynamic activity a_v depends on the adsorption energy of the volatile on the smectite surface. Equilibrium is reached when the chemical potential

μ_{gas} of the adsorbate in the gas phase equals the chemical potential μ_{surf} of the adsorbate on the surface,

$$\mu_{surf} = \mu_{gas} \quad (9.121)$$

and μ_{gas} is related to a_v by:

$$\mu_{gas} = \mu^* + kT \ln\left(\frac{p_v}{p_v^*}\right) = \mu^* + kT \ln(a_v) \quad (9.122)$$

where μ^* is the standard state chemical potential at $p = p^*$. μ_{surf} is calculated from the derivative of the free energy F by the number of sorbed volatiles:

$$\mu_{surf} = \left(\frac{\partial F}{\partial N}\right)_{A,T} \quad (9.123)$$

where

$$F = U - TS \quad (9.124)$$

where S is the entropy and U the energy of the volatile molecules sorbed on the surface. The simplest treatment of adsorption and binding is a statistical approach of the Langmuir lattice model. We consider the surface of the solid to be a two-dimensional lattice having M independent sites. In the case of the smectite, the A sites represent the A sodium counter ions on the smectite surface, since we showed in the previous section that the sodium counter ions are the main binding sites at very low coverage and that those sites are essentially independent. Each of the N sorbed volatile molecule occupy one site. The coverage of the adsorbate on the surface is:

$$\theta = \frac{N}{A} \quad (9.125)$$

S is calculated from the number of arrangements W of the volatiles on the surface lattice and the Boltzmann relation:

$$S = k \ln W \cong -N \ln\left(\frac{N}{A}\right) - (A - N) \ln\left(\frac{A - N}{N}\right) \quad (9.126)$$

where

$$W = \frac{A!}{N!(A - N)!} \quad (9.127)$$

where k is the boltzamnn constant. If each of the N volatiles is sorbed on the surface with a binding energy ε , the adsorption energy is given by:

$$U = -N\varepsilon \quad (9.128)$$

If the internal degrees of freedom of the particle also change because particle orientations become restricted upon binding, or because new modes of vibrations are created in the surface, there is an additional contribution to the free energy, $-NkT \ln(q_{surf})$, where q_{surf} is the internal partition function of the volatile on the surface. The relationship between the volatile activity, a_v , and the binding energy of the volatile on the sodium cation, ε , is finally given by:

$$a_v = \frac{1}{q_{surf}} \left(\frac{\theta}{1-\theta} \right) e^{-\varepsilon/kT} \quad (9.129)$$

It follows from Eq. (9.129) that the trends observed for the thermodynamic activities of the four volatiles at low coverage θ imply an opposite ranking of the interaction strength, in so far as a larger thermodynamic activity should correspond to a weaker interaction. Further uncertainties remain for ethyl acetate. Given its lower ionization potential and its higher dipole moment ethyl acetate is expected to bind to the sodium counter ion more strongly than ethanol. This trend is consistent with the results of our *ab initio* calculations of the binding of the single volatile molecules to the sodium counter ion, taking into account also the fact that domains with tetrahedral substitutions are more frequent than those with magnesium substitutions and thus more representative of the system behavior (section 8.5.2).

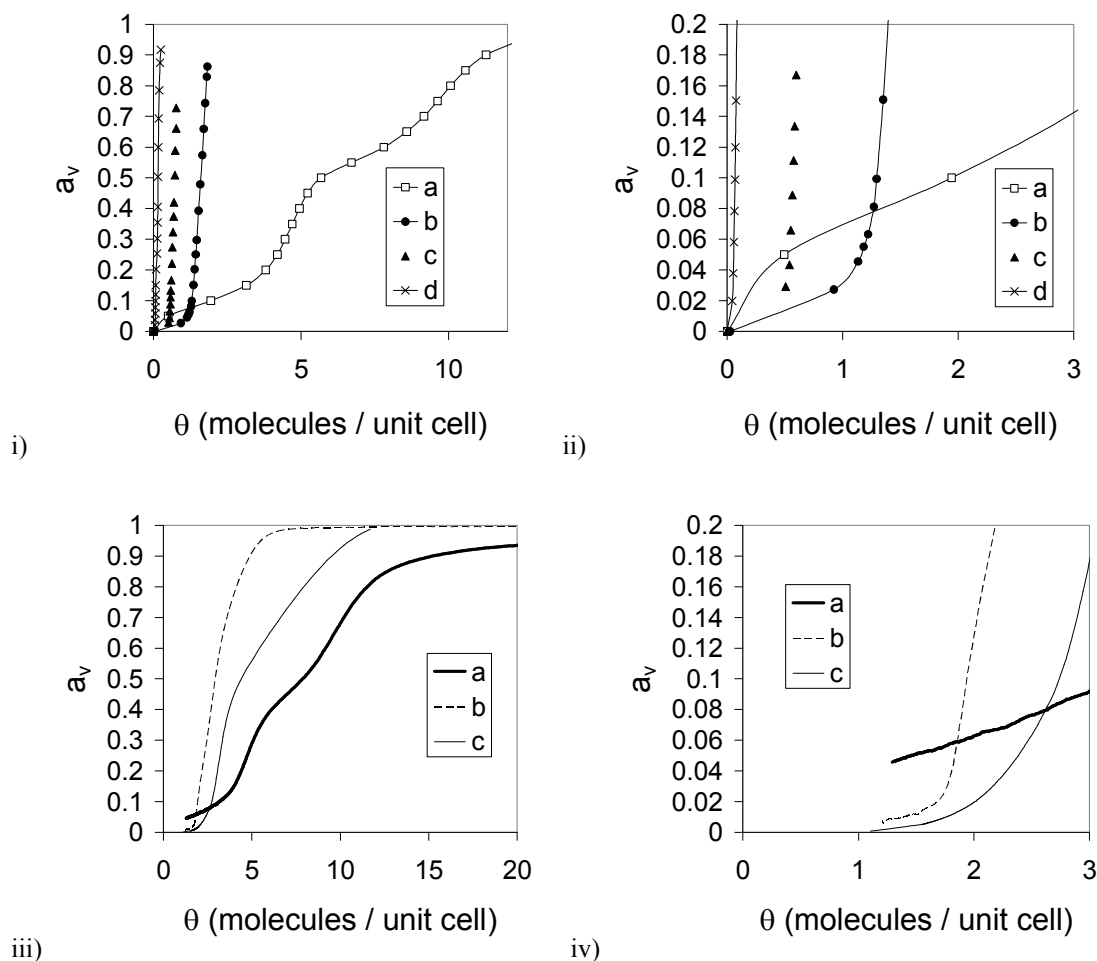


Fig. 9.99. (i) and (ii) DVS measurements at 35 °C of the equilibrium desorption isotherm of the volatiles on the clay. (iii) and (iv) KTGA measurements at 10 °C of the equilibrium desorption isotherm of the volatiles on the clay. a) water. b) ethanol. c) ethyl acetate. d) toluene.

Fig. 9.100(i) to (iv) show the equilibrium desorption isotherms plotted in terms of plane c and θ . The plateau attained at high coverage is related to the vapour pressure of the pure volatile (see Eq. (9.118)) p_v^* , that are given in section 5.1.2 for each volatile. At high coverage the gas phase concentrations follow therefore the order: ethyl acetate > ethanol > toluene > water. At $\theta < 2$ (Fig. 9.100 (ii) and (iv)), the ranking order of c is the same as for the corresponding a_v (see Fig. 9.99 (ii) and (iv)), which is not necessarily true for any given set of volatiles since, from Eq. (9.118), different p^* can lead to different ranking of c (see Table 5.21 section 5.1.2).

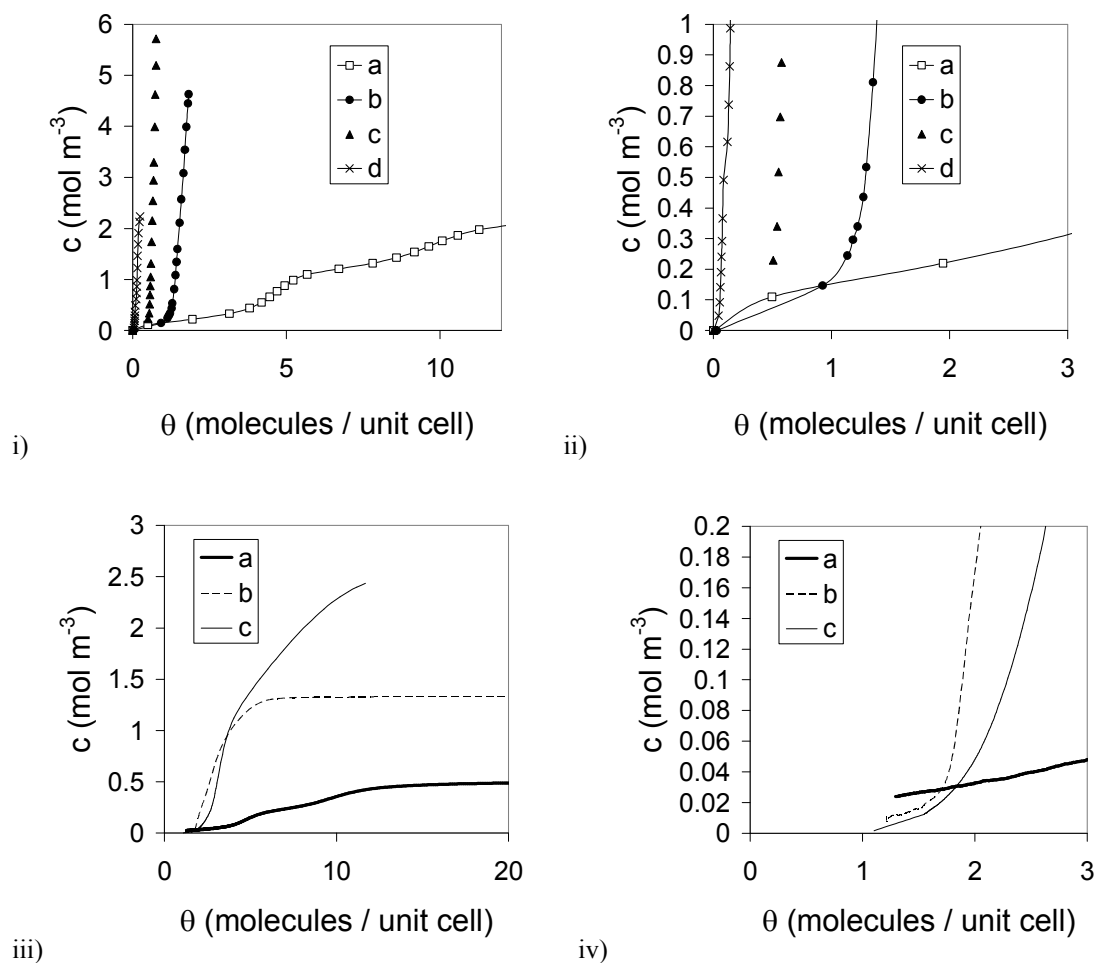


Fig. 9.100. (i) and (ii), DVS measurements at 35 °C of the equilibrium desorption isotherm of the volatiles on the clay; (iii) and (iv), KTGA measurements at 10 °C of the equilibrium desorption isotherm of the volatiles on the clay: (a) water, (b) ethanol, (c) ethyl acetate, (d) toluene.

9.3. EQUILIBRIUM SORPTION ISOTHERM OF WATER ON THE MODIFIED SMECTITES

Water equilibrium desorption isotherms of water measured at 25 °C on the smectites with various metallic and small organic cations are shown in Fig. 9.102. Both the calcium and the sodium clays show steps in the equilibrium desorption isotherms (Fig. 9.102) as previously observed for similar smectites (see section 2.5.3). The figure shows that c for a given value of θ , is higher for the sodium clay than for the calcium clay, except at very high θ . The first step is related to a first expansion of the smectite layer attributed to the partial hydration of the cations due to the penetration of the water molecules inside the layers. The cations remain in contact with the smectite layer, forming inner-sphere surface complexes with water in a horizontal plane (see section 2.5.3). At low θ , corresponding to the first step in the equilibrium desorption isotherm, the lower gas phase concentration for the calcium smectite

can be explained through Eq. (9.129) and Eq. (9.119) by the larger affinity of water for the calcium cation than for the sodium cation, which is in agreement with the higher hydration energy of calcium (-1577 kJ/mol) as compared to sodium (-406 kJ/mol).

The second step is linked to a further expansion of the layers possibly due to the detachment of the fully hydrated cations forming outer-sphere complexes. Therefore, at intermediate θ , corresponding to the second step in the equilibrium desorption isotherm, the difference in c for the calcium and the sodium smectites can be attributed to the ease of the counter ion to be fully hydrated, or equivalently, to the ease of formation of outer-sphere complexes (see section 2.5.3 and 2.10.2.1).

There were no marked difference between the equilibrium desorption isotherms of the smectites modified with small organic cations (Fig. 9.101). However, the maximum amount of water adsorbed by the organic smectites was about half the maximum amount adsorbed by the sodium and the calcium smectites, and the sorption isotherm did not show a double-step sorption. Following the previous argumentation, the organic cations are therefore assumed not to be fully hydrated by the water molecules, acting as swelling inhibitors.

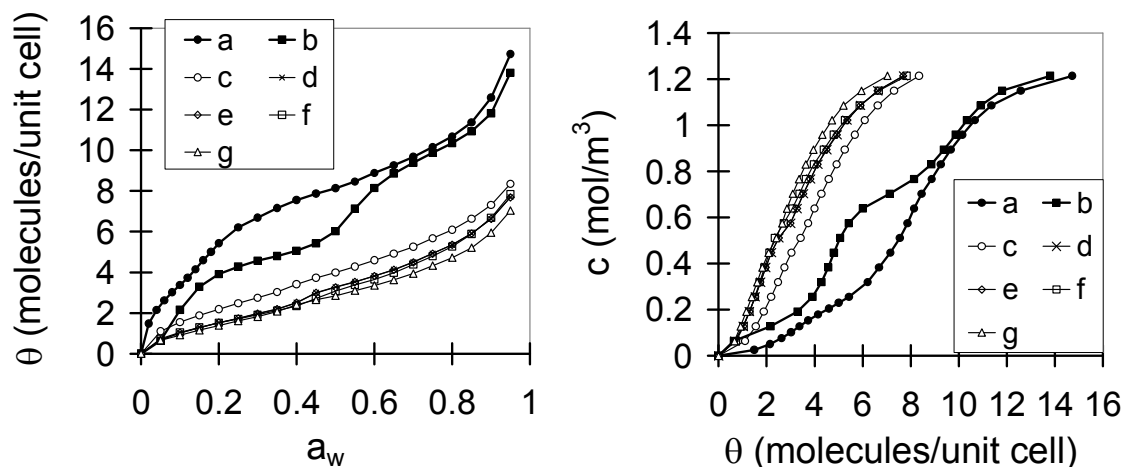


Fig. 9.102. Equilibrium desorption isotherms of water at 25 °C on the Kunipia-F clay with different counter ions. (a) Ca; (b) Na; (c) PHTMA; (d) PTMA; (e) DPDBCO; (f) HTMA; (g) TEA. (left) The coverage, θ as a function of the water activity, a_w . (right) Gas phase concentration, c , as a function of θ .

9.4. CONCLUSION

Dynamic vapour sorption (DVS) measurements and Knudsen thermogravimetry (KTGA) yield very similar shapes for the desorption isotherm of water from clay at 25 °C, with a

maximal variation of 2.5 %RH. These results support the substantial complementary nature of the two methods and justify their use to compare the behaviour of other volatiles, namely, ethanol, ethyl acetate and toluene, which were compatible with either approach.

The relevant results allowed the following conclusions:

- at high coverage the desorption behaviour observed reflects the bulk properties, and the different volatilities, of the four volatiles;
- at low coverage ($\theta < 2$), where the prevailing process is the interaction with the sodium counter ions of the clay, the desorption trends allow ranking the volatiles according to the relevant strength of interaction, namely, ethyl acetate > ethanol > water > toluene.

These conclusions are in agreement with our previous *ab initio* calculations (section 8.5). The differences observed between the equilibrium desorption isotherms of water on the modified smectites could be explained in terms of the binding strength of the counter ion and its tendency to be fully hydrated.

CHAPTER 10 RELEASE KINETICS OF VOLATILES FROM SMECTITE CLAYS

10.1. INTRODUCTION

This chapter presents the results on the measurements of the release of water, ethanol, ethyl acetate, and toluene from the Kunipia-F clay and its derivatives modified by ion exchange with small organic cations and metallic cations. The rates of release are measured using the TG-DSC-MS Sensys instrumentation. The experimental data are compared with FEM calculations and with calculations using the semi-analytical model developed in CHAPTER 6 taking as input the equilibrium desorption isotherms measured in CHAPTER 9.

10.2. RELEASE KINETICS OF WATER FROM A SODIUM SMECTITE CLAY

10.2.1. Link with the equilibrium desorption isotherm

From the semi-analytical model of Eq. (6.104), we would expect the rate of release of water from the sodium smectite to be dependent on the water vapour pressure at the surface of the smectite sample. This surface pressure being given by the equilibrium desorption isotherm of water on the smectite, we expect therefore the equilibrium desorption isotherm to be reflected in the curve of the rate of release. Indeed a comparison between the equilibrium desorption isotherm of water on the smectite at 25 °C (Fig. 10.103a) and the rate of release of 5 µl of water from a clay granule at 25 °C (Fig. 10.103b) shows that the different curvatures appearing in the equilibrium desorption isotherm are also present in the release curve. This figure shows also that the initial rate of evaporation of a 5 µl water droplet (Fig. 10.103c) is close to that of 5 µl of water from the clay granule (Fig. 10.103b). This can be understood from Eq. (6.104). As can be seen from the equilibrium sorption isotherm, at high water content in the smectite, the vapour pressure over the smectite sample is close to the saturated vapour pressure of bulk water, therefore producing a rate of evaporation close to that of bulk water for similar samples height.

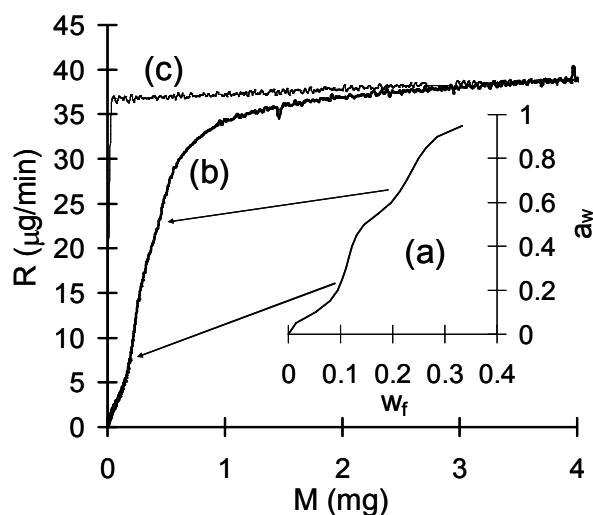


Fig. 10.103. (a) Equilibrium sorption isotherm of water on the smectite at 25 °C, (b) rate of release R of 5 μl of water from a clay granule at 25 °C under a dry nitrogen carrier gas flow rate of 5 ml/min as a function of the remaining amount of water M in the smectite sample, an (c) rate of release R of a 5 μl droplet under a nitrogen carrier gas flow rate of 5 ml/min as a function of the remaining amount of water M in the crucible (same as in Fig. 6.55). a_w stands for the relative vapour pressure and w_f stands for the amount of water relative to the dry smectite

10.2.2. Effect of the internal diffusion coefficient

The rates of release of water from spherical clay granules equilibrated at different relative humidities are presented hereafter. No precise data on diffusion coefficients could be used for the finite element calculations. Literature data of the effective diffusion coefficients of water in the sodium smectite smectite as a function of the water content were found for much higher water contents than those considered in the present experiments, or with large variabilities (see section 2.7). A strong decrease in the T_2 spin relaxation time meant NMR measurements did not allow us to probe the diffusion of water in the smectite at the water contents for the measured equilibrium desorption isotherm. In order to have an idea of the order of magnitude of the expected effective diffusion coefficients of water in the sodium smectite smectite, for a compact aggregation of the smectite platelets, we used literature data on the measured molecular diffusion coefficient of water in smectites for water contents equivalent to one and two “hydration layers” (see section 2.7.3) and the restricted diffusion models of Bharadwaj and Fricke (see section 2.7.4), for random macroscopic average orientation of the platelets. The diameters of the platelets are chosen from the mode and peak of the distribution of platelets average diameters obtained in section 7.3. The results, shown in Table 10.64, indicate a magnitude of the order of 10^{-12} m^2/s . We note also that the two models are consistent in terms of tortuosity factors, and thus, effective diffusion coefficients.

Table 10.64: Calculated effective diffusion coefficients of water in a smectite clay for 1 and 2 “hydration layers” and different average platelet diameters, assuming a compact aggregation of the platelets and a random orientation of the platelets at the macroscopic level. ‡ Tortuosity model from Baradwaj [100] (section 2.7.4.4) and † Tortuosity model from Fricke [106] (section 2.7.4.2).

platelet diameter (nm)	number of "hydration layers"	Tortuosity factor	molecular diffusion coefficient (m ² /s)	effective diffusion coefficient (m ² /s)
120	1	15 ‡	(1–3) x 10 ⁻¹⁰	(4–6) x 10 ⁻¹²
	2	17 ‡	(5–10) x 10 ⁻¹⁰	(5–9) x 10 ⁻¹²
566	1	67 ‡	(1–3) x 10 ⁻¹⁰	(0.4–1) x 10 ⁻¹²
	2	78 ‡	(5–10) x 10 ⁻¹⁰	(1–2) x 10 ⁻¹²
120	1	19 †	(1–3) x 10 ⁻¹⁰	(2–5) x 10 ⁻¹²
	2	22 †	(5–10) x 10 ⁻¹⁰	(4–8) x 10 ⁻¹²
566	1	86 †	(1–3) x 10 ⁻¹⁰	(0.3–1) x 10 ⁻¹²
	2	99 †	(5–10) x 10 ⁻¹⁰	(0.8–2) x 10 ⁻¹²

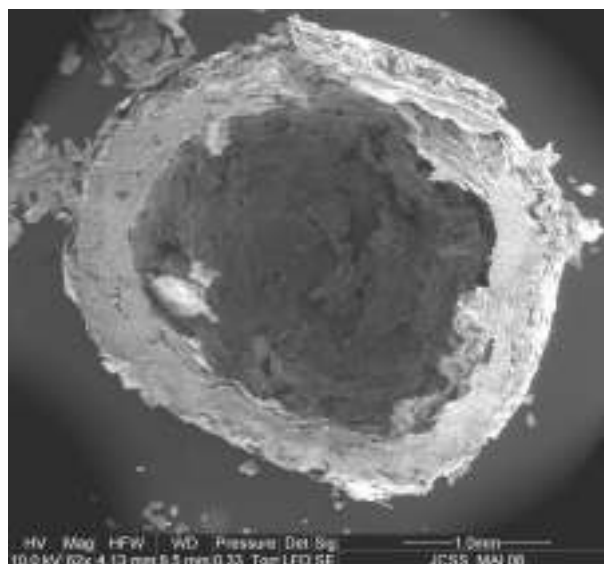


Fig. 10.104. SEM micrograph of a half smectite granule

Because of imprecise data on the real effective diffusion coefficients of water in the smectite as a function of water contents of interests for this study, we decided to calculate the effect of diffusion by performing calculations at various constant diffusion coefficients. Fig. 10.104 shows a SEM micrograph of a half smectite granule used for the experiments, with an external average diameter of 1.65 mm, an average wall thickness of 0.43 mm, and a weight of 16.23 mg. Fig. 10.105a shows the measured release of water from this equilibrated granule and Fig. 10.105b to f show the corresponding finite element calculations of the rate of release of water from a granule with the same dimensions as the one shown in Fig. 10.104 for different constant values of the effective diffusion of water in the smectite. The arrow in Fig.

10.105(ii) indicates the direction of decreasing diffusion coefficient and is placed at the level of the inflection points of the respective curves. We note that, for a fixed rate of release, a decrease in the diffusion coefficient corresponds to a higher amount of water in the smectite sample. A decrease in the diffusion coefficients reduces the local amount of water at the surface of the sample by building a concentration gradient inside the sample. As a result, the surface vapour pressure, and therefore the rate of release by the semi-analytical model of Eq. (6.104) are reduced. In an analogous manner, the inflection points of the different curves are the signature of a specific concentration of water at the surface of the smectite sample, which defines a specific rate of release. Therefore those inflection points appear at the same rate of release for all the curves.

Comparison between experimental results and numerical calculations shows that calculations performed with low diffusion coefficients do not reflect the observed experimental behaviour. Indeed, the average density of the dry granule (1.45 g/cm^3) is significantly smaller than the measured and calculated densities of the smectite crystal calculated in section 7.2, indicating that the aggregation of the smectite platelets may not form a fully compact structure, such that the effective diffusion coefficient of water in this sample, for the initial part of the release curve, is likely to be significantly higher than the approximate values given in Table 10.64.

The prolonged release observed in the experimental data as compared with calculations at fixed diffusion coefficients (Fig. 10.105(i)) indicates that the effective diffusion coefficient is likely to decrease as water is released from the smectite, as can be expected from the decrease in the molecular diffusion coefficient when going from a water content corresponding to a “two layer hydrate” to a water content corresponding to a “one layer hydrate”, and from the increase in tortuosity with a decrease in water content (see sections 2.7.3 and 2.7.4).

It was found that the release curves of water from the same granule equilibrated at different water contents overlapped within the experimental error. Moreover for different granules equilibrated at different water contents, the measured heat of vaporization plotted as a function of the water fraction overlapped within experimental error. These are further indications that the surface water content may be close to the average water content in the granule and that, for the present experimental conditions, the rate of release is not strongly limited by internal diffusion effects, in accordance with the results from the finite element calculations. However, for thicker granules, the effect due to inner diffusion would be enhanced, as shown in Fig. 10.106.

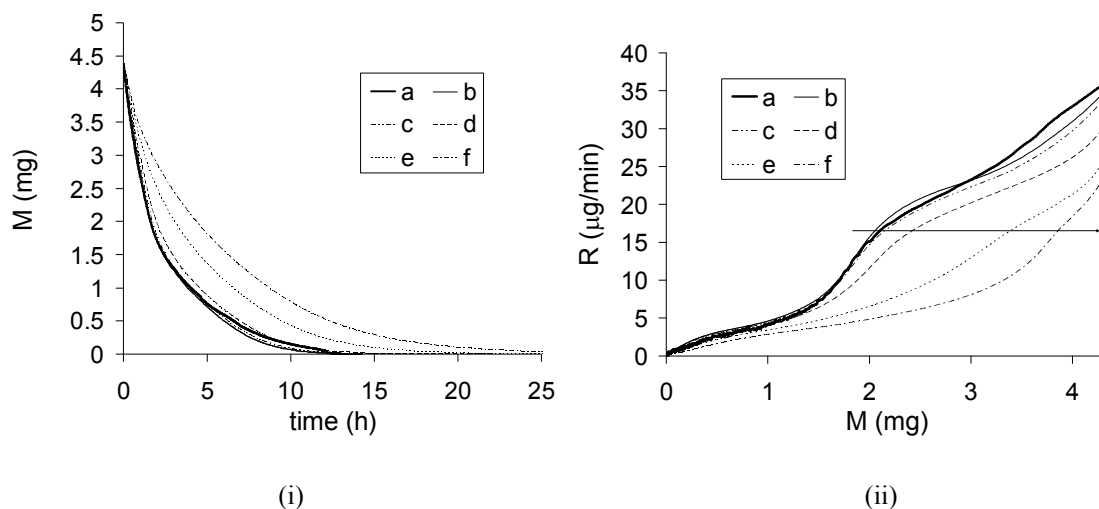


Fig. 10.105. (i) Amount of water M in the clay as a function of time. (ii) Rate of release R as a function of the remaining amount of water M in the smectite., a) Experimental data. b) to f): Finite element calculations for effective constant inner diffusion coefficients of b) $1 \cdot 10^{-9} \text{ m}^2/\text{s}$; c) $5 \cdot 10^{-10} \text{ m}^2/\text{s}$; d) $5 \cdot 10^{-11} \text{ m}^2/\text{s}$; e) $1 \cdot 10^{-11} \text{ m}^2/\text{s}$; f) $5 \cdot 10^{-12} \text{ m}^2/\text{s}$. The granule had an average external diameter of 1.65 mm, an average wall thickness of 0.43 mm, and a weight of 16.23 mg. The carrier gas flow rate was 5 ml/min and the temperature was 25 °C. The arrow indicates decreasing diffusion coefficients and it is placed at the level of the inflection point.

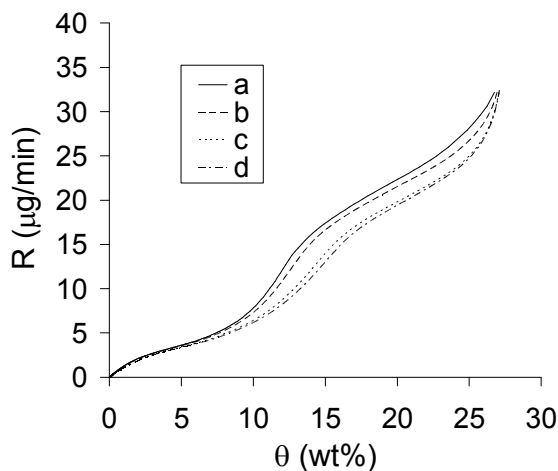


Fig. 10.106. Finite element calculations of the rate of release R at 25 °C and a carrier gas flow rate of 5 ml/min of water from a smectite granule with an external average diameter of 1.65 mm, a weight of 16.23 mg, an effective constant diffusion coefficient of water in the granule of $5 \cdot 10^{-11} \text{ m}^2/\text{s}$, and an average wall thickness of a) 0.25 mm; b) 0.43 mm; c) 1 mm; d) 1.65 mm (plain granule), as a function of the amount of water M in the smectite

10.2.3. Heat of vaporization and temperature effect

The relationship between the equilibrium desorption isotherm and the kinetics of release can be further observed in the measured heat of vaporization. The equilibrium desorption isotherm

of a spherical smectite granule shows a series of steps (Fig. 10.103a and Fig. 10.107), as previously observed for smectites. When the first pseudo plateau ends the water content corresponds to about 6 water molecules per unit cell chemical formula, or, equivalently, per counter ion. This corresponds to the coordination of a sodium cation in bulk water [169]. When the second pseudo plateau ends the water corresponds to about 12 water molecules per unit cell. The average heat of vaporization of water released from smectite granules equilibrated at various water contents shows the same kind of behaviour (Fig. 10.107), i.e. three distinct transition steps at about 44 kJ/mol, 46 kJ/mol, and probably 49 kJ/mol. As can be seen in Table 10.65, the water contents at the inflection points of the heat of vaporization curve are very close to the water content at the shoulders of the equilibrium desorption isotherm curve, such that the steps observed in the heat of vaporization correlate with the steps observed in the equilibrium desorption isotherm. The part of the equilibrium desorption isotherm at high water contents can be attributed to capillary adsorption of the water in the microstructure of the clay, corresponding to a liquid state of water with a heat of vaporization of 44 kJ/mol. This value is also consistent with the observation that the vapour pressure above the clay should be close to the saturated vapour pressure and thus, that the initial rate of release of water from the clay is close to the rate of evaporation of bulk water.

Using the temperature dependence of the rate of release (Eq. (6.109)), obtained in section 6.3 for the semi-analytical model, and the average heat of vaporization curve shown in Fig. 10.103, the rate of release of water from a smectite granule was calculated at 25 °C and 30 °C from the experimental data curve at 35 °C. As for bulk water, the results, shown in Fig. 10.108, indicate the calculations to be in good agreement with the data, with a decrease of the rate of release of around 25 % for a decrease in the temperature of 5 °C.

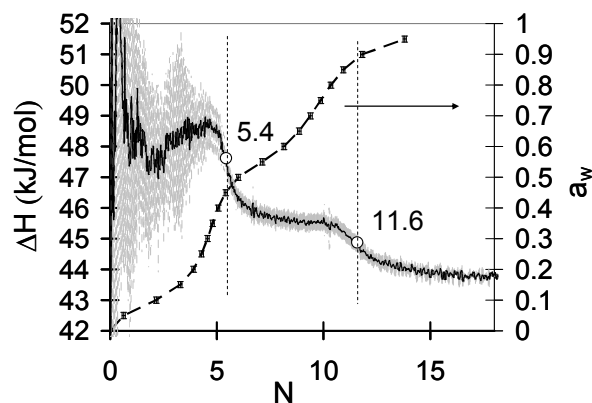


Fig. 10.107. Measured equilibrium sorption isotherm of water on the smectite at 25 °C (a_w stands for the relative vapour pressure), and average and standard deviation of the measured heat of vaporization ΔH of water released from smectite granules as a function of the number of water molecule N per clay crystal unit cell at 25 °C under a dry nitrogen flow rate of 5 ml/min

Table 10.65: Number of water molecules per unit cell at the calculated inflection points of the heat of vaporization and at the calculated shoulder of the equilibrium desorption isotherm curves

	at 1 st inflection point / shoulder	at 2 nd inflection point / shoulder
for the heat of vaporization	5.4	11.6
for the equilibrium sorption isotherm	5.4	11.5

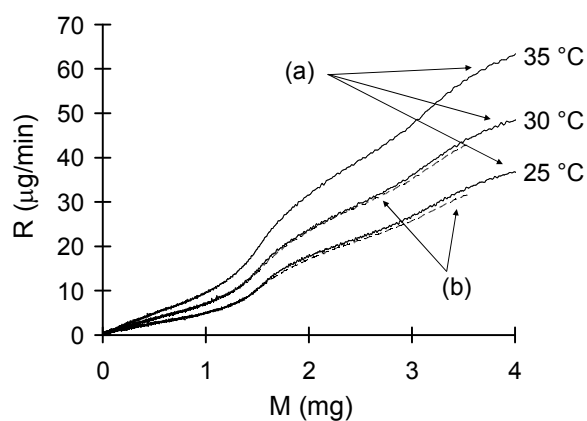


Fig. 10.108. (a) Measured rate of release R of water from smectite granules at 25 °C, 30°C, and 35°C under a dry nitrogen flow rate of 5 ml/min as a function of the amount of water M in the sample. (b) Numerical calculations of the rate of release of water from a smectite granule at 25 °C and 30 °C, using the experimental data at 35 °C

10.3. RELEASE KINETICS OF WATER FROM THE MODIFIED SMECTITES

10.3.1. Rate of release

Experimental data are shown in Fig. 10.109i for the rate of release of water from cylindrical samples of the Ca-, Na-, PHTMA-, and HTMA-smectites equilibrated at water activities higher than 95 %RH. Fig. 10.109ii shows the rate of release of water from the clays calculated using the semi-analytical model of Eq. (6.104) and the equilibrium sorption isotherms in Fig. 9.102, assuming a uniform water concentration inside the smectite sample. Finite element calculations were also performed assuming constant internal effective diffusion coefficients of $2.3 \times 10^{-9} \text{ m}^2/\text{s}$ (Fig. 10.109iii) and $5 \times 10^{-10} \text{ m}^2/\text{s}$ (Fig. 10.109iv). Both the experimental curves and the calculations reflect the characteristic features of the equilibrium desorption isotherms. A decrease in the value of the internal diffusion coefficient reduces the concentration of water at the surface of the smectite sample, owing to an increased concentration gradient within the sample, and from Eq. (6.104), this leads to a decrease in the release rate. Comparison of the calculations and the experimental data suggests that the measured release rates are nevertheless relatively insensitive to diffusion effects at intermediate and high values of θ , although the behavior at low θ for the sodium smectite sample does suggest diffusion to play a more important role.

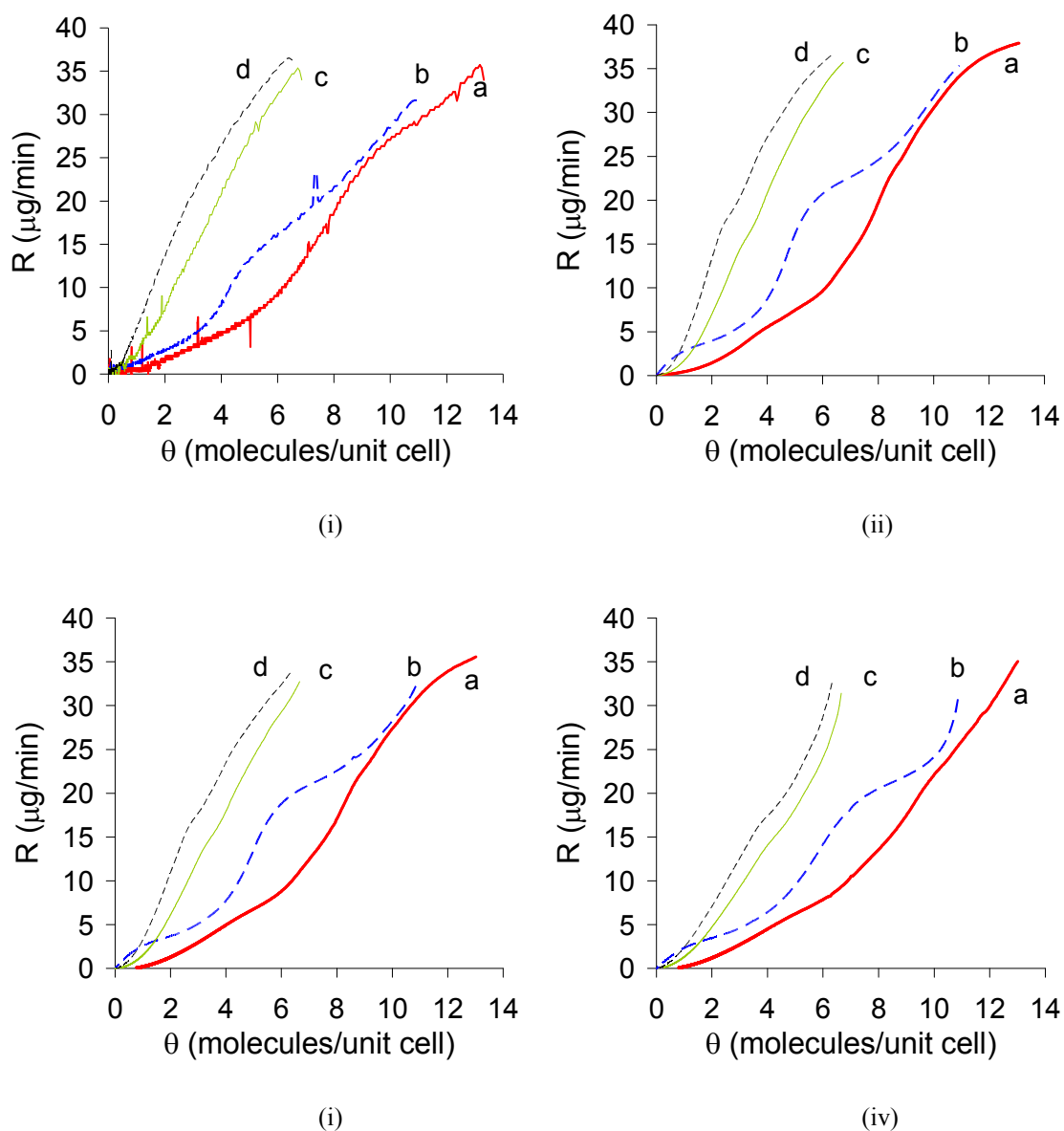


Fig. 10.109. R as a function of θ . (i) Measured values. (ii) Semi-analytical calculations (iii) Finite element calculations using a constant effective internal diffusion coefficient of $2.3 \times 10^{-9} \text{ m}^2/\text{s}$ (iv) Finite element calculations using a constant effective internal diffusion coefficient of $5 \times 10^{-10} \text{ m}^2/\text{s}$ (a) Ca; (b) Na; (c) PHTMA; (d) HTMA.

10.3.2. Heat of vaporization

In the present case, despite the lower statistics in the data, steps in the enthalpy of vaporization were again observed for the release of water from the sodium smectite cylindrical sample at 35°C . The value of $44 \text{ kJ}/\text{mol}$ obtained at high θ is equal to that of bulk water. This is consistent with the observation that the initial rate of release of water from the smectite sample was the same as that of bulk water. Fig. 10.110 shows that all the smectite

samples had an initial enthalpy of vaporization that tended to that of bulk water at high θ , implying the same initial release rate. However, whereas both the Na-, and Ca-smectites showed steps in the enthalpy of vaporizations, the PHTMA-, and HTMA-smectites showed a smooth increase from 44 kJ/mol. Moreover, the second step in the enthalpy of vaporization for the Ca-smectite was higher by about 2 kJ/mol than that for the Na-smectite and a higher enthalpy of vaporization at low θ for the Ca-smectite would be expected given the stronger affinity of calcium with water. Globally, therefore, the results confirm the rate of release of water from the modified smectites to follow the equilibrium desorption isotherms, with a transition from an initial state close to that of bulk water to a final state where the water interacts directly with the smectite surface, and principally with the counter ion.

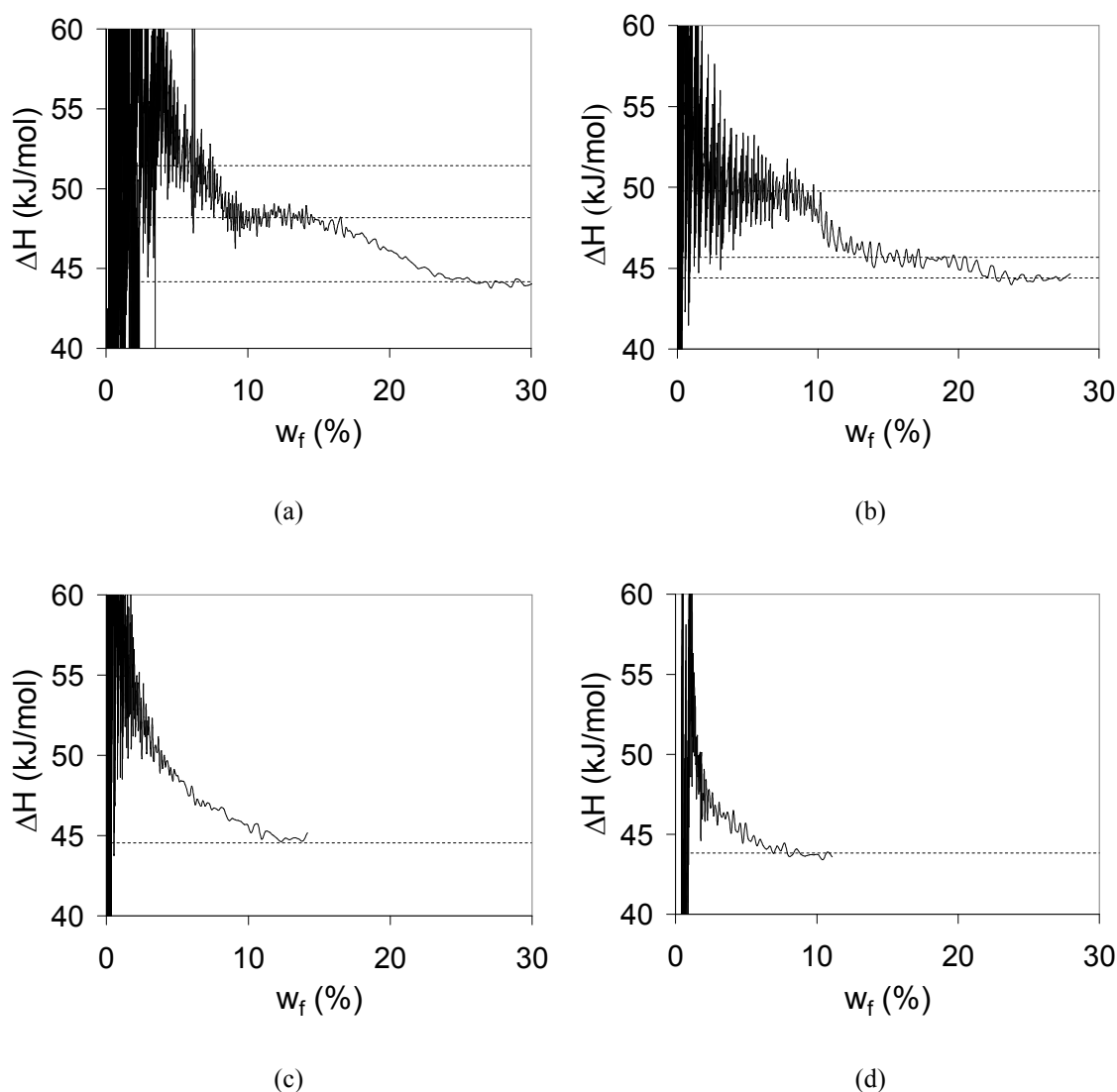


Fig. 10.110. Measured heat of vaporization ΔH of water from the clays modified with different cations. (a) Ca; (b) Na; (c) PHTMA; (d) HTMA.

10.4. RETENTION OF VOLATILES FROM THE SMECTITE ION EXCHANGED WITH LITHIUM CATIONS

If the smectite clay mainly interacts with water, ethanol, ethyl acetate and toluene, via its counter ion, at low θ , as suggested in our *ab initio* calculations (section 8.5), the Li-smectite should show a stronger retention of these volatiles than the Na-smectite, because of its greater ionic strength. This was observed previously for water equilibrated at various relative humidities [246,25].

In the present experiments, 5 μl droplets of the volatile liquids were deposited on cylindrical samples of the Li-, and Na-smectites and the release was studied by temperature ramp

measurements from 23 °C to 200 °C. The measurements were slightly dependent on the exact amount of liquid deposited on the clay surface, and duplicate measurements were therefore performed for each experiment. In these measurements, stronger retention was reflected by evaporation at higher temperatures. Thus, the temperature ramp measurements performed on the Li-, and the Na-smectites, shown in Fig. 10.111, suggested stronger retention of all four volatiles by the Li-smectite. This effect was particularly marked for ethanol and ethyl acetate (Fig. 10.111ii and iii), but less pronounced for toluene and water (Fig. 10.111i and iv). The toluene molecules are mainly sorbed at the external surface (see sections 2.8 and 9.2), so that fewer toluene molecules interact with the counter ions, and the observed signal is weaker. In the case of water, which has a relatively low molar mass, the number of molecules deposited on the surface is higher than for the other volatiles. The relative amount of water molecules bound to the cation is therefore reduced and may be partially masked by the high number of water molecules not-bound to the cation. Another difference with the other volatiles, is the macroscopic swelling of the smectite sample as a result of water adsorption, that may be involved in the observed behavior.

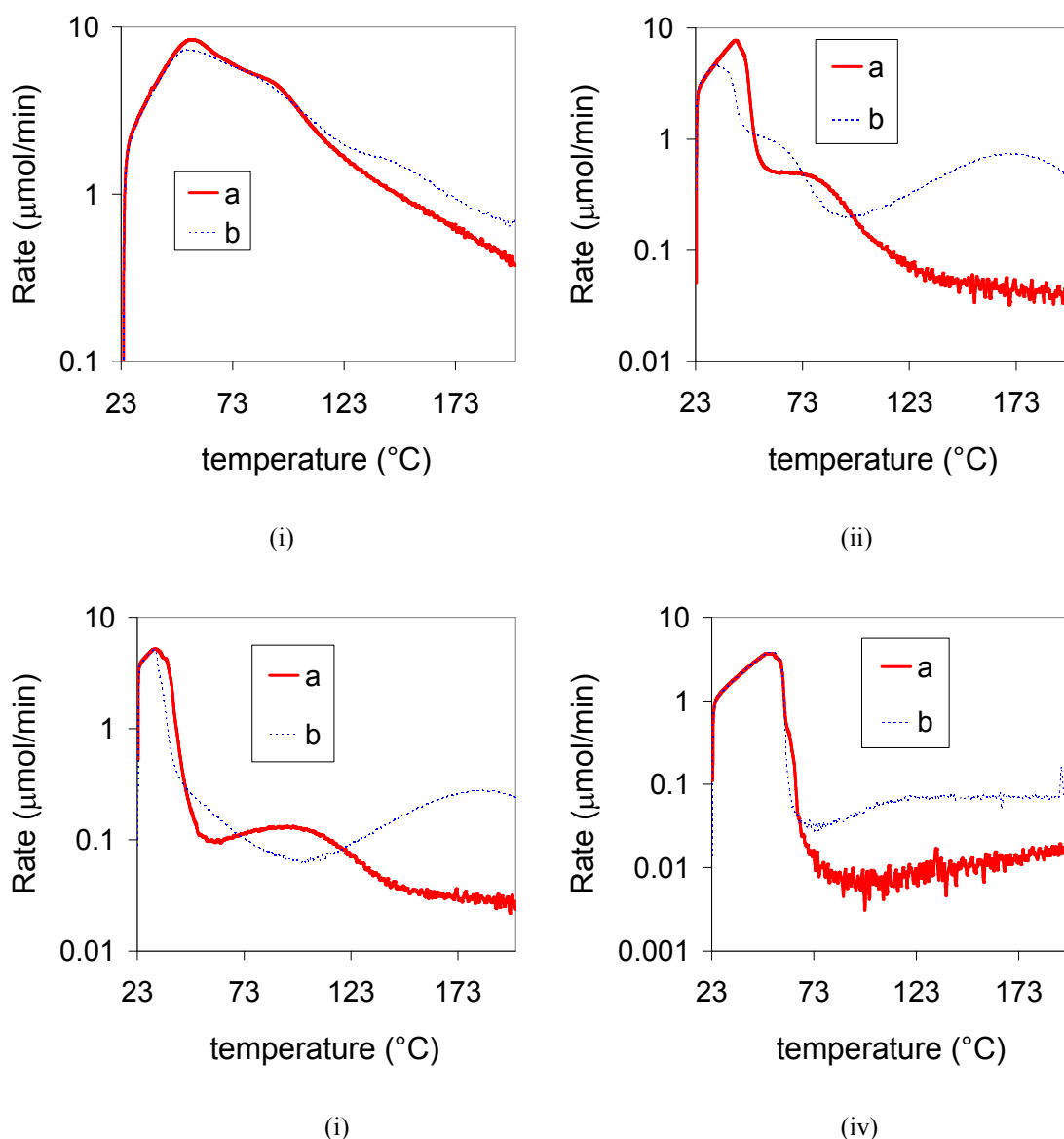


Fig. 10.111. Temperature ramp measurements of the release of 5 μl droplets of (i) water, (ii) ethanol, (iii) ethyl acetate and (iv) toluene deposited on cylindrical samples of Na-, and Li-smectites. (a) Na-smectites and (b) Li-smectites. The curves shown are averages over the duplicate measurements.

10.5. RELEASE OF VOLATILES FROM THE SODIUM SMECTITE

Experimental data for the release of water and ethanol at 35 $^{\circ}\text{C}$ from cylindrical samples of Na-smectites equilibrated at activities higher than 0.95 are shown in Fig. 10.112. Despite the lower initial coverage of ethanol, as compared with water, the release of ethanol from the clay was more prolonged than for water (Fig. 10.112i). The initial rate of release of ethanol was higher than that of water, as expected given the behavior of the bulk liquids (section 6.5). However, at lower coverage, the inverse was observed. The higher affinity of ethanol for the

the sodium counter ion on the smectite influences the equilibrium desorption isotherm (section 9.2.4) and hence, according to the semi-analytical model given by Eq. (6.104) in section 6.2, the rate of release (Fig. 10.113). However, comparison of the predictions using the semi-analytical model (Fig. 10.113) and the experimental data (Fig. 10.112ii) shows that the cross-over between the two experimental curves appears at a significantly higher θ . Given that the semi-analytical calculation is based on the assumption of a uniform concentration of volatiles in the smectite sample, this difference may be due to the presence of concentration gradients in the samples, implying that the slower release of ethanol is also related to its rate of diffusion. Ethanol has a higher molar mass than water and interacts more strongly with the counter ion, and so is expected to have a lower diffusion coefficient than water.

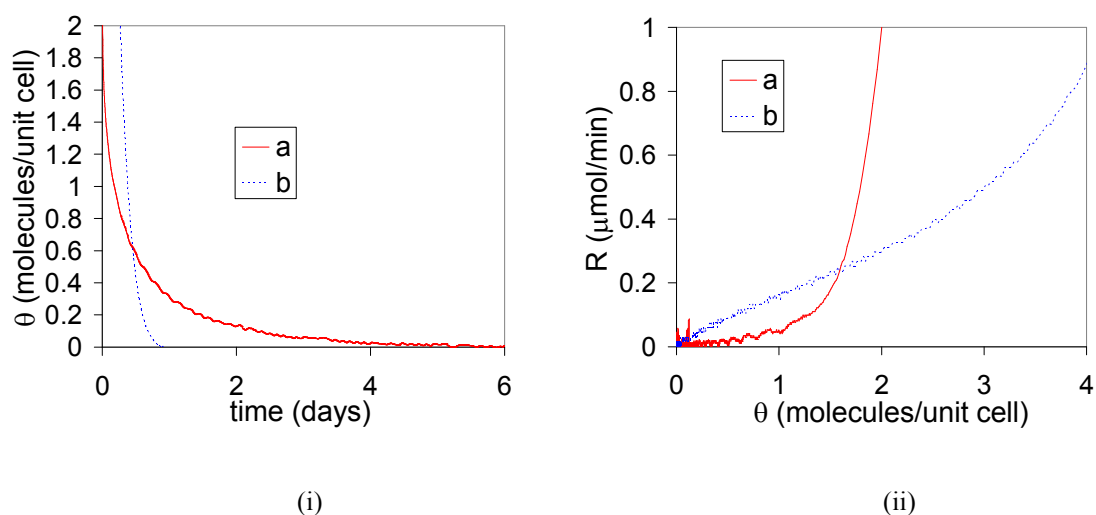


Fig. 10.112. Measured release of (a) ethanol and (b) water from cylindrical samples of Na-smectites at 35 °C. (i) θ as a function of time. (ii) R as a function of θ .

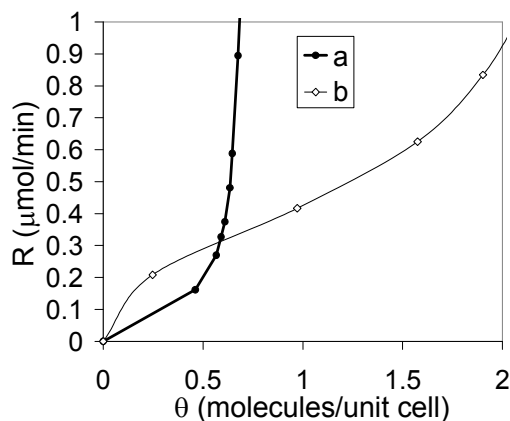


Fig. 10.113. Values of R for (a) ethanol and (b) water from cylindrical samples of Na-smectites at 35 °C calculated from the semi-analytical model.

Experimental data for the release of ethanol and ethyl acetate at 35 °C from cylindrical samples of Na-smectites are shown in Fig. 10.114. The rate of release was initially higher for the ethyl acetate, consistent with the behavior of the bulk liquids (section 6.5). However, at sufficiently low θ , the trend was again reversed, so that the release of ethyl acetate was prolonged with respect to that of ethanol. The higher affinity of ethyl acetate for the sodium counter ion (section 8.5.2) may account for this behavior, but the available data for the equilibrium desorption isotherm of ethyl acetate on sodium smectite were not precise enough to allow assessment of the role of diffusion in this case (section 9.2.4).

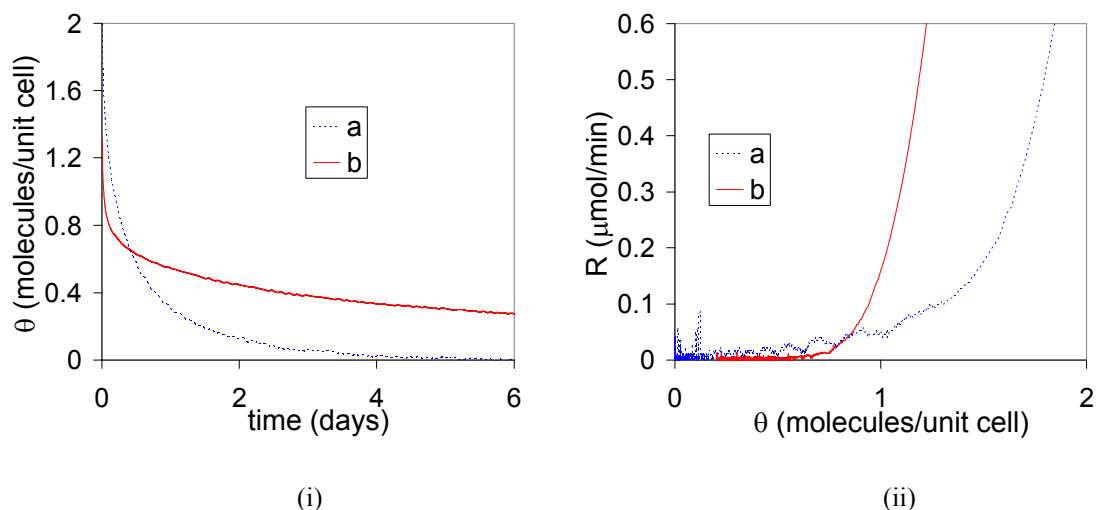


Fig. 10.114. Measured release of (a) ethanol and (b) ethyl acetate from cylindrical samples of Na-smectites at 35 °C. (i) θ as a function time. (ii) R as a function of θ .

Toluene is mainly adsorbed at the external surface of the smectite and its equilibrium desorption isotherm showed a higher c than water for a given θ . The rate of release calculated from the semi-analytical model given by Eq. (6.104) in section 6.2, assuming a uniform concentration within the sample (Fig. 10.116), predicts faster release of toluene than water. However the experimental data (Fig. 10.115) show the release of toluene to be slower, suggesting the diffusion coefficient of toluene in the clay to be a dominant factor in this case.

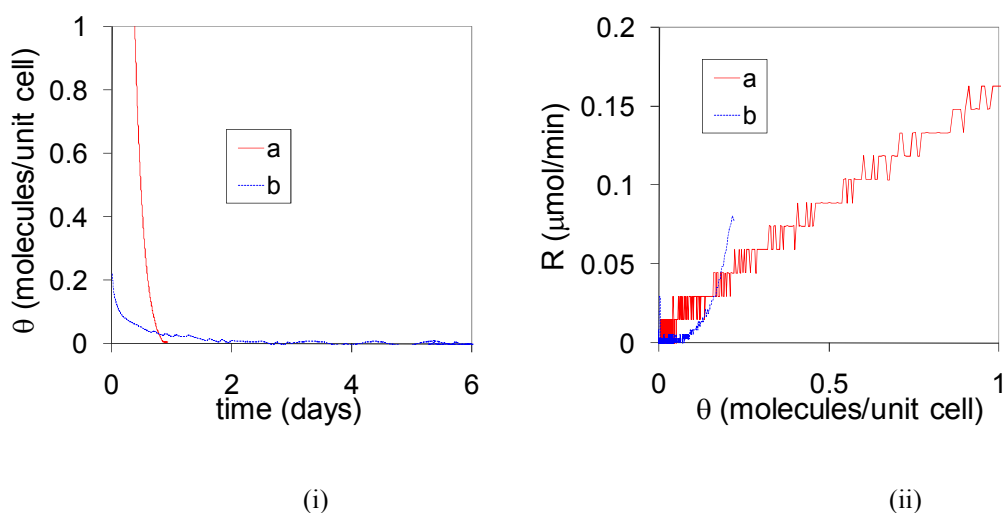


Fig. 10.115. Measured release of (a) water and (b) toluene from cylindrical samples of Na-smectites at 35 °C. (i) θ as a function time. (ii) R , as a function of θ .

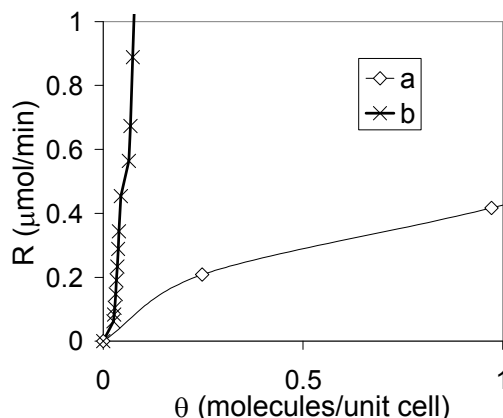


Fig. 10.116. Calculated rate of release of (a) water and (b) toluene from cylindrical samples of Na-smectite at 35 °C using the semi-analytical model.

10.6. CONCLUSION

Results for the release kinetics of water, ethanol, ethyl acetate, and toluene from Na-, Li-, Ca-, PHTMA-, HTMA-smectite clays and of water, ethanol, ethyl acetate, and toluene on Na-, and Li-smectite clays have been presented. Analysis of the experimental and theoretical results showed the rate of release to be strongly influenced by the equilibrium desorption isotherms. The initial state was similar to that of the bulk liquid, so that the type of counter ion had no effect on the initial rate of release and the initial heat of vaporizations of water from the clay samples was close to that of bulk water at 44 kJ/mol. For lower coverage, the rate of release followed the equilibrium desorption isotherms, the final state being determined by the strength of interaction between the volatile and the smectite counter ion, although internal diffusion also played a role. In particular, the slow release of toluene, previously reported in the literature (2.9.3), could be attributed to diffusion effects. An increase in the ionic strength of the counter ion from sodium to lithium led to a stronger retention of the water, ethanol, ethyl acetate, and toluene molecules, showing the counter ion to be the main binding site at low coverage, in agreement with our *ab initio* calculations (8.5). As a confirmation of the observed relationship between the equilibrium desorption isotherm and the kinetics of release, the steps observed in the heat of vaporization curve of water from the clay, i.e. 44 kJ/mol, 46 kJ/mol, and about 49 kJ/mol, could be related to the steps observed in the equilibrium desorption isotherm. Moreover, pseudo-plateaus were observed in the heat of vaporization of water from sodium and calcium smectites, whereas a continuous transition from the enthalpy of vaporization of bulk water to values greater than 49 kJ/mol was observed for the organic

smectites, as observed in the behavior of the equilibrium desorption isotherm. The dependence of the rate of evaporation of the volatiles on temperature could be predicted with very good accuracy by the Arrhenius-type equation developed in CHAPTER 6 for the evaporation of the bulk volatile liquids. In particular, a decrease of 5 °C in the temperature resulted in a decrease of about 25 % in the rate of release.

CHAPTER 11 APPLICATION

11.1. INTRODUCTION

In the previous chapters we improved our understanding on the release of single volatiles from smectite clays. A knowledge of the malodorous compounds present in cat urine is necessary to propose a clay modification for a better odour control of cat urine from the clay. Therefore in a first step malodor in cat urine are characterized. In a second step ion exchange of the clay with lithium for improved control on the release of urine from the clay is tested.

11.2. CHARACTERIZATION OF ODOROUS COMPOUNDS IN CAT URINE

Odorous compounds in urine were investigated by SPME GC/MS methods and sniffing experiments. Table 11.66 shows the list of possible malodorous compounds that were smelt in vapours of castrated male urine extracted in dichloromethane. Despite their strong smell, the peaks are generally small and noisy, and coelution can arise (see Fig. 11.117, Fig. 11.118, and Fig. 11.119). Ion extraction of specific masses, together with sensorial characteristics and retention indexes, helped to determine the compounds. Eighteen odorants have been found. However uncertainties remained for some of them. Possible malodours compounds in the extracted urine include compounds with different functional groups and smells. The acids (acetic acid, butanoic acid, 3-methyl butanoic acid, pentanoic acid, and octanoic acid) have a characteristic sweaty, cheese, rancid and acid smell. The nitro-compounds (pyrazines) have a characteristic roasty and nutty smell. Phenolic compounds have pigsty and fecal smell (p-cresol), medicinal smell (guaiacol) or aromatic and bouillon smell (4-ethenyl-2-methoxy phenol). Sulphur compounds have cat urine and blackcurrant smell (3-mercapto 3-methylbutyl formate), cabbage smell (dimethyl trisulfide), meaty smell (2,5-dimethyl 3-furanthiol and 1-butanethiol, 2-methyl). Other odorants were found having a terpenic smell (sabinene), mushroom smell (2-

heptanol), floral smell (1-hexanol), and caramel and strawberry smell (furanol). The odour intensities of the various odorants, calculated from the area of the sniffing experiments, are given in Fig. 11.120. p-cresol was felt by far the most smelly compound. It is followed by 3-mercapto 3-methylbutyl formate, which is a degradation product of felinine, a putative pheromone precursor of cats [247].

Compared with urine extracted in dichloromethane, vapours of non-treated urine samples are expected to be more representative of the different smell intensities. However despite the significant smell intensities, corresponding peaks of the mass spectra were small or absent in addition to the occurrence of coelution for some of them. Therefore large uncertainties remain in the assignment of specific odours. The female and castrated urine samples showed very similar spectra (Fig. 11.121) and , except for indole, that was found only in castrated male urine, the odorants shown in Table 11.66 were smelt in both female and castrated male urine. Some compounds that were detected in male urine extracted in dichloromethane are found in non-treated urine as well (2-heptanol, pyrazine 2,n-dimethyl, 1-hexanol, 3-mercapto-3-methylbutyl formate, butanoic acid 3-methyl, phenol 2-methoxy, p-cresol, phenol 4-ethenyl-2-methoxy), though with different relative intensities (Fig. 11.122); in particular the intensities of p-cresol and 3-mercapto-3-methylbutyl formate are strongly reduced relative to the other compound. Compared to extracted urine, new sensorial descriptors are given for some compounds in the non-treated urine like dusty smell (oxazole 2,4-dimethyl), chocolate smell (butanoic acid, 3-methyl pentyl ester and thiazole, 2,4,5-trimethyl), and honey smell (2-butanone 3-hydroxy-4-phenyl and 1H-imidazole). We note that the spectra of female and castrated male urines contain a number of additional peaks with absent or very low smell intensities that may compete with the odorants for the sorption sites. The complete list of organic compounds found in the non-treated cat urine is given in Table 11.68.

Table 11.66 : Main odorous compounds in male cat urine extracted in dichloromethane. The question marks indicate uncertainty in the assignation of the smelly compounds. The retention indexes are given for a polar (CW) poly(ethylene glycol) column.

retention time	possible compound	retention index		sensorial	
		this work	database	this work	database
4.50	1-butanethiol, 2-methyl? piperidine?	1007	1001 1011	food, bouillon, roasty, sulphury, meaty	meaty, sulphury
5.75	sabinene	1104	1120	terpenic, spicy, food, earth, urine, sulphury, meaty, goat	burnt, fishy, gasoline, narcotic camphoreous, pine, spicy, terpenic, woody
10.02	2-heptanol?	1300	1312	mushroom	earthy, fatty, fresh, green, mushroom, rancid coconut
11.06	pyrazine, 2,5-dimethyl pyrazine, 2,6-dimethyl pyrazine, 2,3-dimethyl	1337	1316 1324 1338	pyrazine, roasty, food, cook, nut, caramel, bread's crust	nutty, raw potato, roasty cocoa, nutty
11.34	3-furanthiol, 2,5-dimethyl?	1347	1391	dirty socks, food, meaty, burnt	burnt, chicken, fatty, lamb, meaty, pork, roat meat, sulphury
11.75	1-hexanol? trisulfide, dimethyl?	1363	1344 1392	acid, piquely, green, plant, pfeffery, garlic, fruity, aldehyde, wood, cabbage	caprylic, fermented, fresh, fruity, green, resinous, oily, sweet floral aliaceous, cabbage, cauliflower, garlic, metallic, onion, sulphury
14.03	acetic acid	1447	1426	piquely, vinegar	acid, pungent, sour, vinegar
14.53	pyrazine, 2,3-diethyl-5-methyl?	1460	1486	roasty, nutty, pyrazine, meaty	earthy, fragrant, fruity, roasty, nutty, meaty, potato, sweet

CHAPTER 11 Application

16.02	3-mercapto 3-methylbutyl formate	1516	1494	blackcurrant, cat urine, sulphury	blackcurrant, buccchu, catty, durian, fruity
19.13	butanoic acid	1627	1599	vomit, feet, sweaty, cheese	penetrating, rancid, rancid butter, sweaty
20.30	butanoic acid, 3-methyl	1669	1671	acid, sweaty, cheese	acid, cheese, sweaty
21.61	?	1714		mushroom, earth, cucumber	
22.19	pentanoic acid	1738	1714	vomit, seaty, cheese, urine	acid, caprylic, cheese, sweaty
25.23	phenol, 2-methoxy (guaiacol)	1856	1838	pharmacy, medical, guaiacol, camphor	aromatic, burnt, phenolic, spicy
29.65	furaneol	2031	2029	caramel, strawberry, sweet, fruity, honey	caramel, cotton candy, fired meat, fruity, hot sugar, pineapple, roasted almonds, strawberry, sweet
30.25	octanoic acid	2056	2042	sweaty, urine, blackcurrant, flower, fermented, fruity, aldehyde, plant	caprylic, fatty, oily, sweaty
31.00	p-cresol	2079	2066	horse, urine, cresylic	cresylic, drain, fecal, medicinal, pigsty, stale
33.52	phenol, 4-ethenyl-2-methoxy	2198	2184	aromatic, maggi, bouillon, coffee	aromatic, clove, phenolic, spicy, tarry

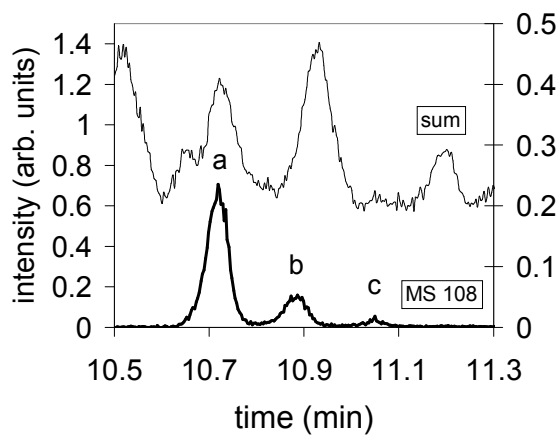


Fig. 11.117 : Sum of mass spectra and spectra of mass 108 of pyrazine malodorous compounds in male urine extracted in dichloromethane. a) pyrazine, 2,5-dimethyl. a) pyrazine, 2,6-dimethyl. a) pyrazine, 2,3-dimethyl.

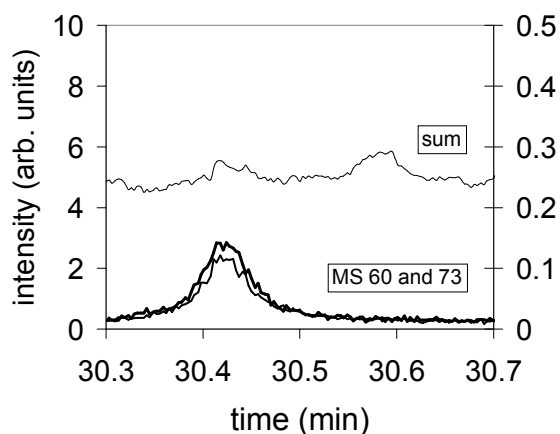


Fig. 11.118 : Sum of mass spectra and spectra of mass 60 and 73 of octanoic acid in male urine extracted in dichloromethane.

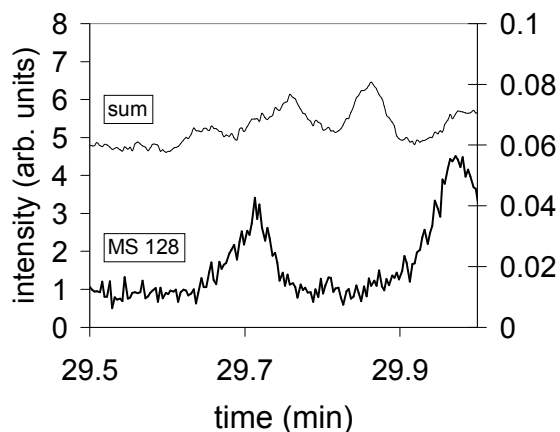


Fig. 11.119 : Sum of mass spectra and spectra of mass 128 of 3(2H)-furanone, 4-hydroxy 2,5-dimethyl (furaneol) in male urine extracted in dichloromethane.

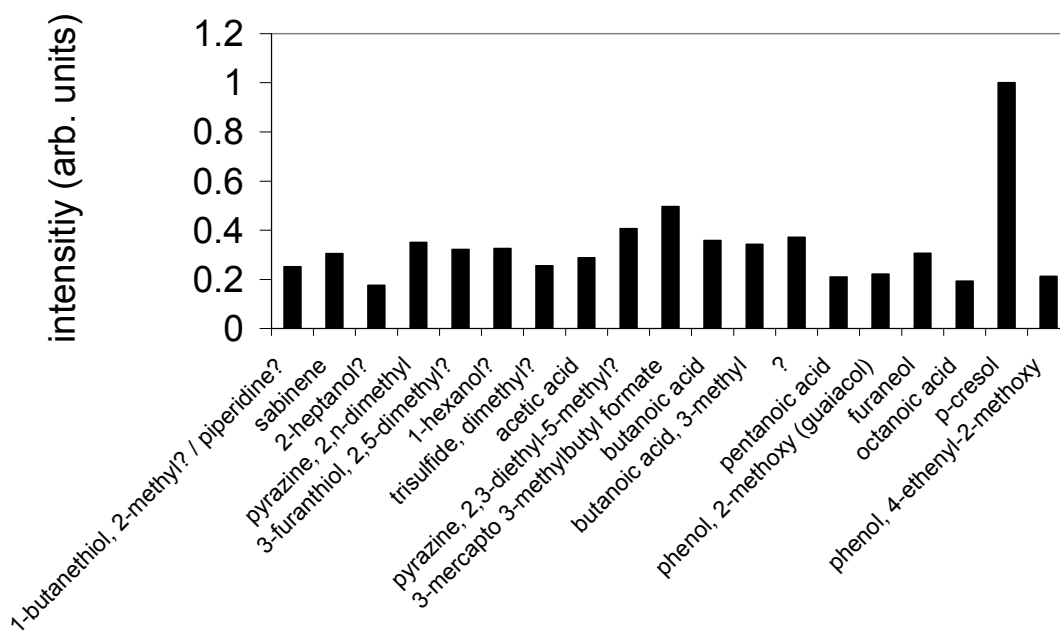


Fig. 11.120 : Intensities of the various odorants found in male cat urine extracted in dichloromethane.

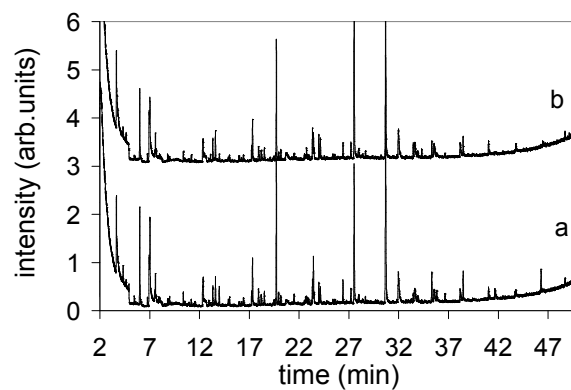


Fig. 11.121 : Chromatograph of non-treated urine samples measured by SPME GC/MS. a) female. b) castrated male.

Table 11.67 : Main odorous compounds in non-treated male and female cat urine. The question marks indicate uncertainty in the assignment of the smelly compounds. The retention indexes are given for a polar (CW) poly(ethylene glycol) column.

retention time	possible compound	retention index		sensorial	
		this work	database	this work	database
9.54	oxazole, 2,4-dimethyl?	1094	1088	dusty, sulphury, bread, earth, chemical	dusty, narcotic, pungent, roasted
16.32	2-heptanol?	1295	1312	mushroom	earthy, fatty, fresh, green, mushroom, rancid coconut
16.69	butanoic acid, 3-methyl pentyl ester?	1307	1316	chocolate, wood	chocolate, fatty, fruity
17.52	pyrazine, 2,5-dimethyl	1333	1316	chemical, urine,	nutty, raw potato, roasty
	pyrazine, 2,6-dimethyl		1324	pyrazine, roasty,	cocoa, nutty
	pyrazine, 2,3-dimethyl		1338	popcorn	acetone, caramel, cocoa, coffee, green, hydrolized
18.38	1-hexanol?	1359	1344	green, sulphury, stinky flower, nutty, chocolate, cocoa	caprylic, fermented, fresh, fruity, green, resinous, oily, sweet floral
	thiazole, 2,4,5-trimethyl?		1366		chocolate, cocoa, coffee, earthy, nutty,
23.21	3-mercaptop 3-methylbutyl formate	1512	1494	sulphury, blackcurrant, cat urine	blackcurrant, buccu, catty, durian, fruity
27.74	butanoic acid, 3-methyl	1667		feet, dirty socks	acid, cheese, sweaty
31.73	pentanoic acid, 3-methyl?	1773	1787	leek, fermented cabbage, flower, sulphury, cheese	cheese, pungent

CHAPTER 11 Application

32.84	phenol, 2-methoxy (guaiacol)	1855	1838	pharmacy, guaiacol, vanilla, honey	aromatic, phenolic, spicy
38.50	p-cresol	2083	2066	cresol, stale, horse, camphor	cresylic, drain, fecal, medicinal, pigsty, stale
41.56	phenol, 4-ethenyl-2-methoxy? 2(5H)-furanone, 3-hydroxy 4,5-dimethyl? 2-butanone, 3-hydroxy-4-phenyl? 1H-imidazole?	2214	2184 2203 2271 ?	food, maggi, honey, phenolic, sweet wood	aromatic, clove, phenolic, spicy, tarry cotton candy, fenugreek, lovage, maggi, seasoning dirty, honey, hyacinth, vert de lilas, phenyl acetic, perspiration phenolic, sweet, strong, honey
46.26	indole (<i>only male urine</i>)	2442	2450	phenolic, cabbage	animal, cheese, faeces, mothballs, musk

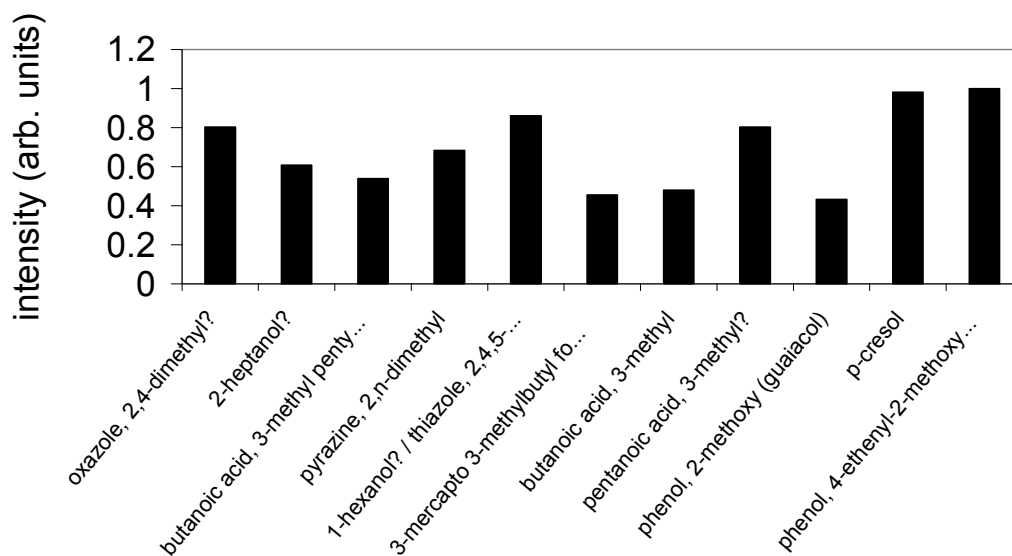


Fig. 11.122 : Intensities of the various odorants found in non-treated male and female cat urine.

Table 11.68 : List of possible compounds in non-treated cat urine. The question marks indicate uncertainty in the assignment of the compounds. Bold format indicates smelly compounds. The retention indexes are given for a polar (CW) poly(ethylene glycol) column.

possible compound	retention index	
	peak	database
trimethyl amine	<700	622
carbon disulfide	714	745
acetone	810	815
furan, 3-methyl	861	870
furan, 2-methyl	891	882
2-butanone	897	905
butanal, 2-methyl	908	923
butanal, 3-methyl	913	917
2-butanone, 3-methyl	925	939
furan, 2-ethyl	948	951
2-pentanone	972	977
2-pentanone, 4-methyl	1005	1024
1-butanethiol, 2-methyl?	1007	1001
piperidine?		1011
2-pentanone, 3-methyl	1013	1018
furan, 2-ethyl-5-methyl	1029	1016

CHAPTER 11 Application

toluene	1034	1039
1-propanol	1043	1020
3-hexanone, 4-methyl?	1071	?
3-hexanone, 5-methyl	1072	1079
hexanal	1078	1083
oxazole, 2,4-dimethyl?	1094	1088
sabinene	1104	1120
4-heptanone	1122	1126
furan, 2,3-dihydro 3-methyl?	1125	?
cyclohexene, 1,1,5-trimethyl-1-methylene?	1136	?
cyclohexene, 1,3,3-trimethyl-4-methylene?		?
4-heptanone, 2-methyl	1147	1152
1-butanol	1150	1129
2-heptanone	1180	1177
2-butenal, 3-methyl	1195	1207
cyclopentanone, 3-methyl?	1208	?
furan, 2-pentyl	1229	1232
3-buten-1-ol, 3-methyl	1252	1255
1-pentanol	1256	1233
methyl pyrazine	1265	1255
2-butanone, 3-hydroxy	1285	1272
2-heptanol?	1295	1312
1H-pyrrole, 1-pentyl?	1299	?
butanoic acid, 3-methyl pentyl ester?	1307	1316
pyrazine, 2,5-dimethyl	1322	1316
3-ethyl, cyclopentanone?	1326	?
pyrazine, 2,6-dimethyl	1329	1324
pyrazine, 2,3-dimethyl	1337	1338
furan, 2-methyl 3-methylthio	1345	1361
3-furanthiol, 2,5-dimethyl?	1347	1391
1-hexanol?	1359	1343
thiazole, 2,4,5-trimethyl?		1366
cyclohexanone, 3-methyl	1363	1340
?	1397	?
?	1400	?
trimethyl pyrazine?	1406	1396
dimethyl trisulfide?	1407	1392
?	1414	?
?	1432	?
acetic acid	1447	1426
1-octen-3-ol (good spectra)	1456	1443

pyrazine, 2,3-diethyl-5-methyl?	1460	1486
pyrazine, 2-ethenyl-5-methyl	1489	1489
pyrazine, 2-ethenyl-6-methyl		1483
1,3-benzodioxole, 5-propyl?	1493	?
1-hexanol, 2-ethyl	1496	1480
decanal	1498	1498
3-mercapto 3-methylbutyl formate	1512	1494
p-menth-1-en-3-one, semicarbazone?	1516	?
benzaldehyde	1519	1513
pyrrole, 1-acetyl?	1542	?
benzonitrile	1600	1587
1-butanol, 3-mercapro 3-methyl	1620	1631
butanoic acid	1627	1599
acetophenone	1648	1639
butanoic acid, 3-methyl	1674	1670
pentanoic acid	1738	1714
pentanoic acid, 3-methyl?	1773	1787
benzenemethanol, alpha-methyl	1816	1790
phenol, 2-methoxy	1860	1838
benzyl alcohol	1878	1866
dimethyl sulfone	1897	1889
1-dodecanol	1974	1956
phenol	2006	1981
furaneol	2031	2029
octanoic acid	2056	2042
p-cresol	2083	2066
phenol, 4-ethenyl-2-methoxy?	2214	2184
2(5H)-furanone, 3-hydroxy 4,5-dimethyl?		2203
2-butanone, 3-hydroxy-4-phenyl?		2271
1H-imidazole?		?
phenol, 2,4-bis(1,1-dimethylethyl)?	2317	?
1H-inden-1-one, 2,3-dihydro, 5,6-dimethoxy, 3-methyl?		?
indol (only for male urine)	2442	2450

11.3. ION-EXCHANGE WITH LITHIUM COUNTER IONS FOR IMPROVED CONTROLLED RELEASE OF CAT URINE

The possible malodours determined in the cat urine have an electronegative atom (oxygen, nitrogen or sulfur), and for some of them an aromatic ring. Fig. 11.123a to d show the

structures of some of those malodours with a characteristic odour. The phenol 4-methyl (p-cresol) with characteristic fecal and stale smell has one oxygen atom from the hydroxyl group and an aromatic ring. The 3-mercapto-3-methylbutyl-formate with characteristic catty smell has two oxygen atoms and a sulfur atom from the thiol group. The pyridine 2,3-dimethyl has two nitrogen atoms and an aromatic ring. The 3-methyl butanoic acid with characteristic sweaty smell has an oxygen with resonant double bond and an hydrogen from the hydroxyl group. It is worth noting that those molecules and the ethanol, ethyl acetate, pyridine, and toluene molecules used for the *ab initio* calculations (CHAPTER 8) have common structural features in terms of electronegative atoms and aromatic ring. A reasonable expectation is therefore that the malodours can potentially bind with the clay counter ion through their electronegative atom or aromatic ring. We saw that the retention of the volatile is strongly dependent on the strength of interaction between the volatile and the sodium counter ion, which is in turn controlled by the ionic strength of the counter ion (section 10.4). We expect therefore that an ion exchange of the sodium counter ion for a cation with stronger ionic strength will result in stronger retention of the malodours. The hydration energy of a cation gives an indication of its ionic strength. Table 11.69 shows a list of possible candidates. We showed that the limitation effects due to internal diffusion are enhanced for an increase in the aggregate⁷ size (section 10.2.2). For this reason, it is of interest to have a clay that swells beyond a water content equivalent to three layer hydrates, thus showing clumping properties. Ca^{2+} has the strongest ionic strength. However, ion exchange with the calcium cation would make the clay to loose in its clumping property, because the expansion of the platelets for a Ca-smectite does not extend beyond a double layer of water (see section 2.5.4.2). The next candidate is the hydrogen cation. Because of its small size, the hydrogen cation was shown to penetrate into the clay layer and attack the clay structure, decreasing the charge of the clay (section 2.3). Our best candidate is therefore the lithium cation.

The sodium clay was therefore modified by column ion exchange with lithium cations and the two clays were compared in terms of their controlled release properties of cat urine. Because of the low signal intensity of the malodours, the release of urine could not be monitored under isothermal conditions. Figure 11.124 shows mass spectra of the ramp temperature measurements of a 5 μl droplet of urine alone (a), of a 5 μl droplet of urine

deposited on a sodium-smectite cylinder (b), and a 5 μl droplet of urine deposited on a lithium-smectite cylinder (c). The results show that, even by temperature ramp, the signals of characteristic masses of fragments of p-cresol (mass = 107) and 3-mercapto-3-methylbutyl-formate (mass = 69) are not seen because of the small content of malodours in the cat urine samples. However, the masses 43 and 45 are frequent fragments of organic compounds. Monitoring the signals from those masses gives therefore a general indication of the retention of volatile organic compounds in cat urine. A comparison between Figure 11.124a and Figure 11.124b and c shows that the release of urine from the Na-, and Li-clays is shifted to higher temperature, compared to urine alone, showing the retention effect of the clays. The figure shows also that the release of urine from the Li-clay is shifted to higher temperature, compared to the Na-clay. This shift is seen at both low temperatures (50 °C), and high temperatures (~200 °C). The results show therefore that the Li-clay, compared to the Na-clay, provides a better retention control on the organic compounds present in cat urine. The control of the release of cat urine malodorous compounds, that are part of those organic compounds, is therefore improved by ion exchange with lithium cations.

Bloomfield (calcium) clay granules used by Nestlé Purina have been ion exchanged by lithium cations using column exchange, preserving the size of the granules. Figure 11.125 shows that the deposition of a 1 ml water droplet on the non-modified Bloomfield (calcium) clay granules did not clump, whereas the same 1 ml water droplet did form a clump for the modified Bloomfield, as expected for the monovalent lithium counter ions. Ion exchange of the Bloomfield clay for lithium counter ions by the column exchange method can therefore provide a modified Bloomfield with potential improved controlled release properties of malodorous compounds. Replacement by lithium counter ions takes advantage of both the sodium and the calcium counter ions of having a significant binding strength plus the ability to clump. Compared to sodium, the greater ionic strength of the lithium counter ion decreases the rate of release through the equilibrium desorption isotherm, as well as through a reduction in the diffusion coefficient. Compared to calcium, both the clumping ability of the lithium clay and the larger number of lithium counter ions in the interlayer, restricting the diffusion of volatiles, contribute enhancing the effect

of internal diffusion on the equilibrium desorption isotherm, and reducing therefore the rate of release.

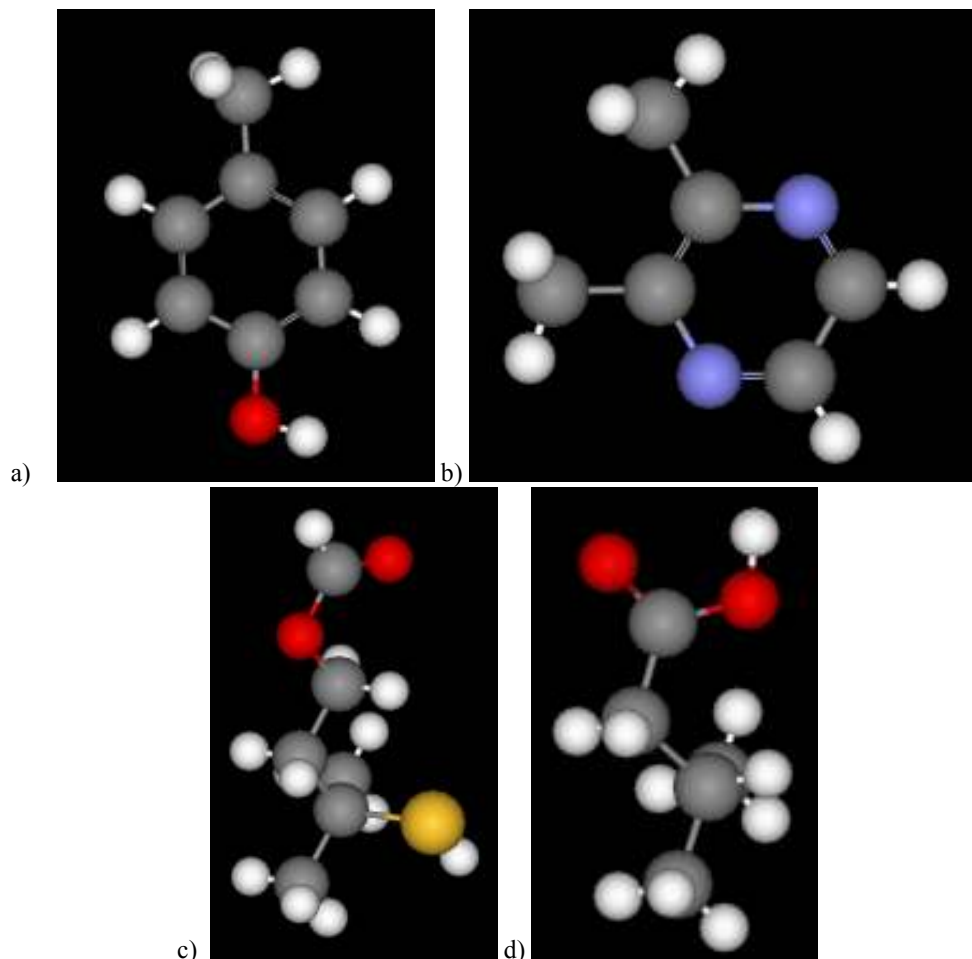


Fig. 11.123 : a) 4-methyl phenol (p-cresol). b) Pyridine, 2,3-dimethyl. c) 3-mercapto-3-methylbutyl-formate. d) Butanoic acid 3-methyl. Oxygens atom are in red, the hydrogen atoms are in white, carbon atoms are in grey, nitrogen atoms are in blue, and sulfur atoms are in yellow.

Table 11.69: Hydration energies of selected cations.

cation	hydration energy (kJ/mol)
Ca ²⁺	-1577
H ⁺	-1130
Li ⁺	-520
Na ⁺	-406

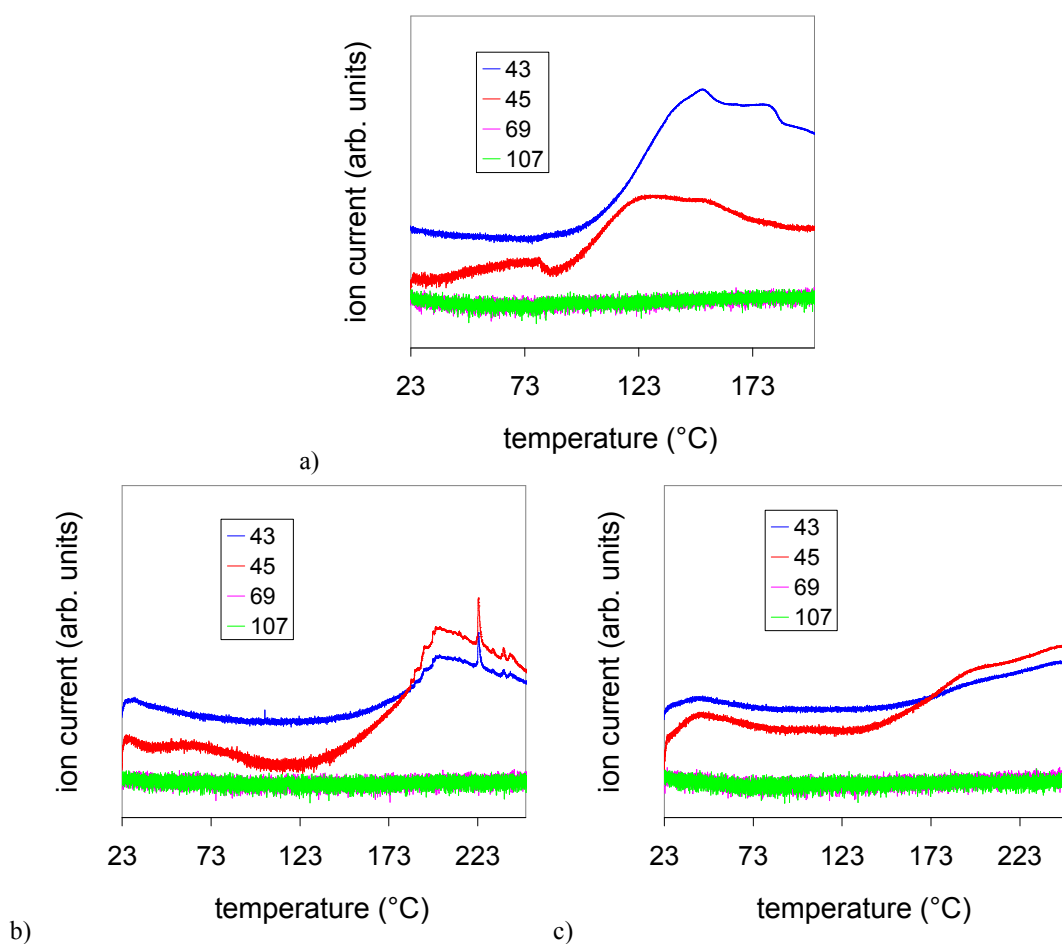


Figure 11.124 : Temperature ramp measurements of the release of a) liquid urine, b) urine from a Na-smectite cylindrical sample, and c) urine from a Li-smectite cylindrical sample. The signals of masses 43, 45, 69 and 107 are shown.



Figure 11.125 : a) Bloomfield clay modified with lithium cations and forming a clump after deposition of a 1 ml water droplet.

11.4. CONCLUSION

Smelly compounds in cat urine have been determined by sniffing experiments and mass spectrometry. Some compounds had strong odors, though their signals were small, often close to the noise level. In particular, we found acids, with were sweaty, cheese, rancid and acid smell, nitro-compounds with roasty and nutty smell, phenolic compounds, with pigsty and fecal smell, medicinal smell or aromatic and bouillon smell, sulphur compounds with cat urine and blackcurrant smell, cabbage smell, or meaty smell. Other odorants were found to have a terpenic smell, mushroom smell, floral smell, or caramel and strawberry smell.

Similarities in the chemical structures between the malodorous compounds in cat urine and the model volatiles used for the *ab initio* calculations suggested the use of lithium as optimal counter ion to reduce the release of urine from the clay used by Purina. Experimental results were successful in showing the lithium clay to combine both advantages of a sodium and a calcium clay in controlling the release of volatiles: significant binding strength and good clumping ability.

CHAPTER 12 CONCLUSION

We presented results on the evaporation kinetics of bulk volatile liquids and the release kinetics of volatiles from smectite clays. The rates of release were measured by thermogravimetry, differential calorimetry and mass spectrometry and modeled using finite element methods. We also investigated the interactions between the volatiles and the clay using *ab initio* calculations based on density-functional theory in the pseudopotential-plane-wave scheme.

Results on the rates of evaporation of water, ethanol, ethyl acetate, toluene, pyridine, toluene and n-octane liquids showed the experimental data to be in good agreement with the finite element calculations with an average relative error of 7.4 %. Results of the finite element calculations in terms of volatile concentrations and gas convection allowed us to develop a semi-analytical model for the calculation of the rates of evaporation. The model was found to be in good agreement with the experimental data and allowed us to rationalize the effect of the carrier gas flow rate, the geometry of the instrumentation, the temperature, the total pressure, and the type of chemical. The rate of evaporation was driven by the difference between the volatile concentration at the surface of the liquid, given by the surface equilibrium pressure (saturated vapour pressure in the case of liquid compounds) and the volatile concentration at the top of the crucible, the carrier gas flow rate acting as a dilution gas for the concentration at the top of the crucible. The equilibrium conditions at the surface of the liquid assumed in the calculations was confirmed by the measured value of the heat of vaporization during the evaporation of the liquid water sample that was found to be the same as the enthalpy of vaporization of bulk water (44 kJ/mol). The temperature was found to obey an Arrhenius-type equation derived from the semi-analytical model. In particular, a decrease of 5 °C of the temperature led to a decrease of about 25 % of the rate of evaporation. For this simple case, the semi-analytical model is specific to the geometry of the thermogravimetric instrument, which raises questions as the use of general analytical equations to model

complex release systems. The results validated the approach used to measure and model the rates of evaporation. To the best of the authors' knowledge those results represent the first comparison between experimental and numerical calculations of the evaporation of volatile liquids under convective conditions.

In the case of the release of volatiles from smectite clays, the equilibrium surface pressure is given by the equilibrium desorption isotherm of the volatiles on the clays, that was used as input parameter for the finite element calculations and the calculations using the semi-analytical model, assuming, for the later, an homogenous concentration of the volatiles in the clay sample. In particular, predictions of the temperature dependence of the rate of release of water from the sodium smectite using an Arrhenius-type of equation were found to be in very good agreement with experimental measurements with a decrease of about 25 % of the rate of release for a decrease in temperature of 5 °C. The semi-analytical model could explain the similarities observed in the features of the curves of the rates of release of the volatiles from the smectites and those observed in the equilibrium desorption isotherms. Also, at the initial stage of release, the rate of release and the heat of vaporization of water from the sodium smectite clay sample were found to be the same as those for a water droplet of similar height. This was explained from the semi-analytical model by the high activity of the volatiles in the clay sample given in the initial stage of the equilibrium desorption isotherm. When an adsorbent is saturated with an aqueous solution, its initial activity is high, so that modifications of the clay will not affect the initial stage of release. Equilibrium conditions at the surface of the clay samples were confirmed by the connection made between the experimental curve of the heat of vaporization and the equilibrium isotherm.

For the conditions investigated in those experiments, the release of water from the clay was found not to be strongly influenced by internal diffusion effects. An estimation of the order of magnitude of the diffusion coefficient of water in a sodium smectite showed also that the aggregation of the smectite platelets do not form a fully compact structure, so that the clay sample contained micropores that enhance the average value of the apparent diffusion coefficient of water. However, finite element calculations showed that with a decrease of the value of the internal diffusion coefficient and/or an increase in the clay sample internal diffusion effects are enhanced, by a reduction of the surface pressure

through the equilibrium desorption isotherm. This means that a clumping clay, that can form a large aggregate after adsorption of an aqueous solution, is preferable over a non-clumping clay for controlled release of cat urine from cat litters.

The differences observed in the equilibrium desorption isotherms of water, ethanol, ethyl acetate and toluene could be rationalized by the results of *ab initio* calculations. The *ab initio* calculations showed the sodium counter ion to be the main binding site at low coverage (estimation barrier of diffusion of about 10 kJ/mol). This was confirmed by the increased retention of water, ethanol, ethyl acetate and toluene on the lithium smectite as compared to the sodium smectite, due to its greater ionic strength. *Ab initio* calculations showed also that the sodium sites were essentially independent. This justified the use of the Langmuir lattice model suggesting that, at low coverage, a greater binding energy corresponds to a lower thermodynamic activity. Indeed, at low coverage, the ranking of activities (toluene > water > ethanol > ethyl acetate) was found to be the inverse of that found for the calculated binding energies of the single-molecule configurations of the volatiles on the sodium smectite surface (n-octane (9 kJ/mol) < toluene (25 kJ/mol) < water (45 kJ/mol) < ethanol (48 kJ/mol) < ethyl acetate (52 kJ/mol) < pyridine (63 kJ/mol)). The differences in binding energies between water, ethanol, ethyl acetate, and pyridine, could be explained by the electron-donor ability of the electronegative atom (oxygen or nitrogen), characterized by the ionization potential of the single volatiles. For these particular volatiles, the ranking of thermodynamic activities corresponded to the same ranking in the gas phase surface concentrations. At high coverage, the ranking of concentrations corresponded to those of the bulk liquids, since the activities approach the value of one. The equilibrium desorption isotherms of water on the smectites modified by ion exchange with small organic cations were found to be very similar and with activities greater than that for the sodium smectite, whereas the activities of the water molecules adsorbed on the calcium smectite were to be lower than that sodium smectite. This was attributed, at low coverage, to their difference in ionic strength and, at high coverage, to the inability of the organic cations to be fully hydrated by the water molecules and thus the lack of expansion of the clay platelets.

The equilibrium desorption isotherms of the volatiles on the smectites were used to rationalize the differences observed in the rates of release of the same volatiles from the

smectites. The rates of release of water from the modified smectites was found to be not strongly affected by internal diffusion effects at middle and high coverage, whereas, at low coverage, internal diffusion played a more important role for the present experimental conditions. The differences in the rates of release of water, ethanol, and ethyl acetate from the sodium smectite could be directly related to their differences in the equilibrium desorption isotherms, though diffusion effects played a minor role. The difference between the rates of release of water and toluene could only be explained by a low internal diffusion of toluene as compared to water.

The conclusions derived on the mechanisms involved in the rate of release of volatile from the smectite clays were used to test a clay modification on the controlled release of urine. The chemical structures of the smelly compounds determined in castrated cat urine samples showed the molecules to have potential ability to bind with the clay counter ion. Indeed mass spectrometry ramp temperature measurements showed the retention of volatile organic compounds on the lithium smectite to be generally increased as compared to the sodium smectite. It was shown also that the clay used by Purina can be modified in high quantities using ion column exchange. Ion exchange by lithium cations allowed to combine both advantages of the calcium and the sodium cations:

- Reduced water activity at low coverage and reduced average molecular diffusion coefficient of the volatiles through the stronger binding between the clay counter ions and the volatiles due to the higher ionic strength of the lithium cation, as compared to the sodium cation;
- Reduced average molecular diffusion coefficient of the volatiles in the clay through the stronger binding between the clay counter ions and the volatiles due to the higher ionic strength of the lithium cation, as compared to the sodium cation, and through the enhanced number of obstacles due to the higher concentration of lithium counter ions, as compared to calcium counter ions;
- Enhanced diffusion effects through the ability of the lithium clay to form a clump due to its greater swelling capacity, as compared to the calcium clay.

The approach undertaken in this thesis showed that modification of the clay by ion exchange with lithium cations enhance the controlled release properties of the clay. Our approach based on a basic understanding of the mechanisms of release showed that, for the range of modifications by ion-exchange, replacement of the counter ions by lithium cations is optimal as regard to the ionic strength of the cation, the clumping properties of the modified clay, and the extend of our present knowledge. However, we note that the toxicity of the lithium clay is unknown and the magnesium cation would be of interest because of its hydration properties, though the effect of its divalent charge on the swelling of the clay is not clear to the author.

Further results from the *ab initio* calculations for the binding of one to six molecules on the surface of the sodium smectite clay showed the binding energy of the water molecules on the smectite surface to depend significantly on the specific location of the counterion, the net charge on the underlying sheet, and the possibility of forming hydrogen bonds with basal oxygen atoms, which play an important role in stabilizing the adsorbate, especially for a basal oxygen atom linked to an aluminum substitution. From one to five water molecules on the clay surface, the counter ions located above rings with aluminum substitution in the tetrahedral layer are more attractive centers than the counter ions located on rings with magnesium substitutions in the octahedral layer. With increasing number of water molecules, the intermolecular interaction becomes gradually more effective than the sodium-water interaction thus limiting the number of sodium-bound molecules to five. In particular, we observed the progressive formation of water dimers, trimers, and pentamers. At the level of six molecules, the onset of a structural transition is observed for the adsorbate (water 3D-hexamer) showing that water-water interaction starts to dominate over the clay (counterions and basal oxygens) in determining its configuration. This order-disorder transition can be interpreted as a possible origin of the hysteresis observed in the equilibrium sorption isotherm. Also, an increase of the number of molecules bound to the counterion corresponds to its progressive detachment from the clay surface, which could be related to energy losses in the clay structure (including counterions).

A 11.77 ps Car-Parrinello dynamic calculations of water molecules in the interlayer gallery of the clay at a water content of twelve water molecules for one cation showed the

average diffusion of the water molecules to be reduced of a factor two as compared to that of bulk water, due to restrictions imposed by the clay surface and the counterions. Each counterion was hydrated with almost six water molecules. The water molecules tend to form hydrogen bonds between each others, and, at a lower extend, weaker bonds with the basal oxygens. Also, the water molecules were found to be preferentially oriented with their hydroxyl perpendicular to the clay surface, in agreement with interpretations from previous NMR experiments. However, no double layer of water was observed, as opposed to usual interpretations from the literature, and the density profile of the water molecules was suggested to result from the arrangement of the water molecules around the counterions, so that the notion of “double-water” layer may be strongly dependent on the distribution of the counterions inside the interlayer gallery. Further dynamic calculations at a water content of six water molecules per counterion for variable interlayer distances showed the counterions to be quite mobile, so that the counterions, initially positioned close to the clay surface, in a first set of calculations, and positioned in the midplane, for a second set of calculations, did not remain at their position during the simulation time (about 10 ps). We note that it would be of interest to validate the results by repeating the calculations with other functionals.

References

1. Virta R., Clay and Shale, *American Geological Institute*, 2002
2. Low P. F., *Adv. Agron.*, 13 (1961) 269
3. Raymond M., Identification and amelioration of cat and dog odors, *Nestlé Purina*, 2004
4. Raymond M., Application of a liquid fragrance to a clay surface and subsequent release of aroma after moisture activation, *Nestlé Purina*, 2002
5. Bergaya F., *Appl. Clay Sci.*, 19 (2001) 1
6. Haderlein S. B. and Schwarzenbach R. P., *Environ. sci. technol.*, 27 (1993) 316
7. Groisman L. et al., *J. Environ. Qual.*, 33 (2004) 1930
8. Kijima T., *J. Inclus. Phenom. Mol.*, 4 (1986) 333
9. Goltsov Y. G. et al., *Mendeleev Commun.*, 6 (1999) 241
10. Dau J. and Lagaly G., *Croat. Chem. Acta*, 71 (1998) 983
11. Gougeon W. D. et al., *Eur. J. Inorg. Chem.*, 7 (2003) 1366
12. Muminov S. Z. and Gulyamova D. B., *Colloid Journal*, 66 (2004) 619
13. Applebaum R. S. and Marth E. H., *Z. Lebensm. Unters. Forsch.*, 174 (1982) 303
14. Diaz D. E., *Mycopathologia*, 157 (2004) 233
15. Venaruzzo J. L., *Micropor. Mesopor. Mater.*, 56 (2002) 73
16. Rodrigues N. G. F., *Ceramica*, 49 (2003) 149
17. Tavani E. L. and Volzone C., *Ceramica*, 45 (1999)
18. Komadel P., *Clay Miner.*, 38 (2003) 127
19. Mikhail S. et al., *Appl. Catal. A-Gen.*, 227 (2002) 265
20. Madejová J., *Vib. Spectrosc.*, 31 (2003) 1
21. Murray H. H., *Appl. Clay Sci.*, 17 (2000) 207
22. Murray H. H., *Clay Miner.*, 34 (1999) 39

23. Sposito G. and Prost R., *Chem. Rev.*, 82 (1982) 553
24. Woessner D. E. and Snowden B. S., *J. Colloid Interface Sci.*, 30 (1969) 54
25. Zabat M. and Van Damme H., *Clay Miner.*, 35 (2000) 357
26. Al-Mukhtar M. et al., *Clay Miner.*, 35 (2000) 537
27. Hendricks S. B. et al., *J. Am. Chem. Soc.*, 62 (1940) 1457
28. Bishop J. L. et al., *Clays Clay Miner.*, 42 (1994) 702
29. Xu W. et al., *Clays Clay Miner.*, 48 (2000) 120
30. Sposito G. et al., *Clays Clay Miner.*, 31 (1983) 9
31. Ohkubo T. et al., *Sci. Technol. Adv. Mater.*, 5 (2004) 693
32. Carrado K. A. and Xu L. Q., *Chem. Mater.*, 10 (1998) 1440
33. Wada N. et al., *Phys. Rev. B*, 41 (1990) 12895
34. Zhang F. et al., *J. Colloid Interface Sci.*, 173 (1995) 34
35. Fowler R. H., *Proc. Cambridge Phil. Soc.*, 31 (1935) 260
36. Brunauer S. et al., *J. Am. Chem. Soc.*, 60 (1938) 309
37. Hill T. L., *J. Chem. Phys.*, 14 (1946) 263
38. Timmermann E. O., *J. Chem. Soc., Faraday Trans. 1*, 85 (1989) 1631
39. Khalfaoui M. et al., *J. Coll. Interf. Sci.*, 263 (2003) 350
40. Mooney R. W. et al., *J. Am. Chem. Soc.*, 74 (1952) 1367
41. Norrish K., *Discuss. Faraday Soc.*, 18 (1954) 120
42. Mooney R. W. et al., *J. Am. Chem. Soc.*, 74 (1952) 1371
43. Brooks C. S., *Soil Sci.*, 99 (1965) 182
44. Tamura K. et al., *Clays Clay Miner.*, 48 (2000) 400
45. Fu M. H. et al., *Clays Clay Miner.*, 38 (1990) 485
46. Bérend I. et al., *Clays Clay Miner.*, 43 (1995) 324
47. Rinnert E. et al., *J. Phys. Chem. B*, 109 (2005) 23745
48. Cases J.-M. et al., *Clays Clay Miner.*, 45 (1997) 8
49. Gillery F. H., *Am. Mineral.*, 44 (1959) 806

50. Kittrick J. A., *Soil Sci. Soc. Am. J.*, 33 (1969) 193
51. Michot L. J. et al., *Am. Mineral.*, 90 (2005) 166
52. Sato T. et al., *Clays Clay Miner.*, 40 (1992) 103
53. Mourchid A. et al., *Langmuir*, 11 (1995) 1942
54. Mourchid A. et al., *Langmuir*, 14 (1998) 4718
55. Fossum J. O., *Phys. Chem. Miner.*, A 270 (1999) 270
56. Fossum J. O. et al., *Energy*, 30 (2005) 873
57. Van Der Beek D., *Europhys. Lett.*, 61 (2003) 702
58. Michot L. J. et al., *Langmuir*, 20 (2004) 10829
59. Dudley W. et al., *J. Colloid Interface Sci.*, 151 (1992) 236
60. Balnois E. et al., *Langmuir*, 19 (2003) 6633
61. McBride M. B. and Baveye P., *Soil Sci. Soc. Am. J.*, 66 (2002) 1207
62. Slade P. G. et al., *Clays Clay Miner.*, 39 (1991) 234
63. Laffer B. G. et al., *Clay Miner.*, 6 (1966) 311
64. Slade P. G. and Quirk J. P., *J. Colloid Interface Sci.*, 144 (1991) 18
65. Laird D. A. et al., *J. Colloid Interface Sci.*, 171 (1995) 240
66. Luckham P. F. and Rossi S., *Adv. Colloid. Interface Sci.*, 82 (1999) 43
67. Zhang Z. Z. and Low P. F., *J. Colloid Interface Sci.*, 133 (1989) 461
68. Kittrick J. A., *Soil Sci. Soc. Amer. Proc.*, 33 (1969) 222
69. Norrish K., *Discuss Faraday Soc.*, 18 (1954) 120
70. Keren R. and Shainberg I., *Clays Clay Miner.*, 23 (1975) 193
71. Sanger R. et al., *Helv. Phys. Acta*, 5 (1932) 200
72. Robinson R. A. and Stokes R. H., *Electrolyte Solutions*, *Butterworths*, 1959
73. Cross P. C. et al., *J. Am. Chem. Soc.*, 59 (1937) 1134
74. Radoslovich E. W. and Norrish K., *Amer. Mineral.*, 47 (1962) 599
75. Ravina I. and Low P. F., *Clays Clay Miner.*, 25 (1977) 201
76. Porion P. et al., *J. Phys. Chem. B*, 108 (2004) 10825

77. Trizac E. et al., *J. Phys. Condens. Matter*, 14 (2002) 9339
78. Michot L. J. et al., *CR Geoscience*, 334 (2002) 611
79. Murad M. A. and Cushman J. H., *Int. J. Eng. Sci.*, 38 (2000) 517
80. Tuck J. J. et al., *J. Chem. Soc. Faraday Trans*, 81 (1985) 833
81. Swenson J. et al., *J. Chem. Phys.*, 113 (2000) 2873
82. Anderson M. A. et al., *Clays Clay Miner.*, 47 (1999) 28
83. Cebula D. J. et al., *Clays Clay Miner.*, 29 (1981) 241
84. Malikova N. et al., *J. Phys. Chem. B*, 110 (2006) 3206
85. Chang F.-R. C. et al., *Langmuir*, 11 (1995) 2734
86. Skipper N. T. et al., *Chem. Geol.*, 230 (2006) 182
87. Tuck J. J. et al., *Chem. Soc. Faraday Trans.*, 80 (1984) 309
88. Poinسیون J. et al., *Physica B*, 156-157 (1989) 140
89. Tuck J. J. et al., *Chem. Soc. Faraday Trans.*, 80 (1984) 309
90. Bourg I. C. et al., *Clays Clay Miner.*, 54 (2006) 363
91. Limbach K. W. and Wei J., *AIChE J.*, 36 (1990) 242
92. Nielsen L. E., *J. Macromol. Sci. Chem.*, 1967) 929
93. Shen L. and Chen Z., *Chem. Eng. Sci.*, 62 (2007) 3748
94. Duval F. P. et al., *J. Colloid Interface Sci.*, 242 (2001) 319
95. Nakashima Y., *Am. Mineral.*, 85 (2000) 132
96. Nakashima Y., *Clays Clay Miner.*, 48 (2000) 603
97. Nakashima Y., *Clays Clay Miner.*, 50 (2002) 1
98. Nakashima Y., *Clays Clay Miner.*, 51 (2003) 9
99. Nakashima Y., *Clay minerals*, 41 (2006) 659
100. Bharadwaj R. K., *Macromolecules*, 34 (2001) 9189
101. Lusti H. R. et al., *Modelling Simul. Mater. Sci. Eng.*, 12 (2004) 1201
102. Fujii N. et al., *Mater. Sci. Res. Int.*, 9 (2003) 117
103. Sato H. and Suzuki S., *Appl. Clay Sci.*, 23 (2003) 51

104. Suzuki A. et al., *J. Contam. Hydrol.*, 68 (2004) 23
105. Porion P. et al., *J. Phys. Chem. B*, 107 (2003) 4012
106. Duval F. P. et al., *J. Phys. Chem.*, 103 (1999) 5730
107. Bailey G. W. et al., *Soil Sci. Soc. Amer. Proc.*, 32 (1968) 222-&
108. Zhu D. et al., *J. Environ. Qual.*, 33 (2004) 1322
109. Suzuki S. et al., *Science*, 257 (1992) 942
110. Kumpf R. A. and Dougherty D. A., *Science*, 261 (1993) 1708
111. Xiong J. C. and Maciel G. E., *J. Phys. Chem. B*, 103 (1999) 5543
112. Cosultchi A. et al., *Colloids Surf. , A*, 243 (2004) 53
113. Ovadyahu D. et al., *J. Therm. Anal.*, 51 (1998) 415
114. Bissada K. K. and Johns W. D. C. F. S., *Clay Miner.*, 7 (1967) 155
115. Bissada K. K. and Johns W. D., *Clays Clay Miner.*, 17 (1969) 197
116. Stul M. S. and Uytterhoeven J. B., *J. Chem. Soc. , Faraday Trans. 1*, 1975) 1396
117. Hiltabrand R. R., *Mod. Geol.*, 2 (1971) 49
118. Rappe A. K. et al., *J. Am. Chem. Soc*, 114 (1992) 10024
119. Siantar D. P. et al., *Clays Clay Miner.*, 42 (1994) 187
120. Chou C. T. and Rutherford D. W., *Clays Clay Miner.*, 45 (1997) 867
121. Jaynes W. F. and Vance G. F., *Soil Sci. Soc. Am. J.*, 60 (1966) 1742
122. Boyd S. A. et al., *Soil Sci. Am. J.*, 52 (1988) 652
123. Roberts M. G. et al., *Clays Clay Miner.*, 54 (2006) 426
124. Tian S. et al., *Environ. Sci. Technol.*, 38 (2004) 489
125. Girard F. et al., *Langmuir*, 22 (2006) 11085
126. Hu H. and Larson R. G., *J. Phys. Chem. B*, 106 (2002) 1334
127. Crafton E. F. and Black W. Z., *Int. J. Heat Mass Transfer*, 47 (2004) 1187
128. Widjaja E. et al., *Comput. Chem. Eng.*, 31 (2007) 219
129. Rahimi P. and Ward C. A., *Int. J. Thermodyn.*, 8 (2005) 1
130. Ward C. A. and Fang G., *Phys. Rev. E*, 59 (1999) 429

131. Elliot J. A. W. and Ward C. A., *J. Chem. Phys.*, 106 (1997) 5667
132. Elliot J. A. W. and Ward C. A., *J. Chem. Phys.*, 106 (1997) 5677
133. Frezzotti A. et al., *Phy. Fluids*, 17 (2005) 012102
134. Bray H. J. and Redfern S. A. T., *Phys. Chem. Miner.*, 26 (1999) 591
135. Morrissey F. A. and Grismer M. E., *J. Contam. Hydrol.*, 36 (1999) 291
136. Keyes B. R. and Silcox G. D., *Environ. Sci. Technol.*, 28 (1994) 840
137. Li Q. and Gupta G., *J. Soil Contam.*, 3 (1994) 127
138. Montes-H G. and Geraud Y., *Colloids Surf. , A*, 235 (2004) 17
139. Grismer M. E., *Soil Sci.*, 144 (1987) 1
140. Grismer M. E., *Soil Sci.*, 143 (1987) 367
141. Yin Y. et al., *Ibid.*, 31 (1997) 496
142. Li H. et al., *Environ. Sci. Technol.*, 38 (2004) 5433
143. Chang M.-L. et al., *Environ. Toxicol. Chem.*, 22 (2003) 1956
144. Shih Y.-H. and Wu S.-C., *Environ. Toxicol. Chem.*, 23 (2004) 2061
145. Steinberg S. et al., *J. Soil Contam.*, 3 (1994) 249
146. Mortland M. M. and Boyd S. A., *Environ. Sci. Technol.*, 23 (1989) 223
147. Arocha M. et al., *Environ. Sci. Technol.*, 30 (1996) 1500
148. Yanful E. K. et al., *Adv. Environ. Res.*, 7 (2003) 783
149. Yanful E. K. and Mousavi A. M., *Sc. Tot. Environ.*, 313 (2003) 141
150. Wilson G. W. et al., *Can. Geotech. J.*, 31 (1994) 151
151. Skipper N. T. et al., *Clays Clay Miner.*, 43 (1995) 285
152. Skipper N. T. et al., *Clays Clay Miner.*, 43 (1995) 294
153. Teppen B. J. et al., *J. Phys. Chem. B*, 101 (1997) 1579
154. Cygan R. T., *J. Phys. Chem.*, 108 (2003) 1255
155. Suter J. L. et al., *J. Phys. Chem. C*, 111 (2007) 8248
156. Sinsawat A. et al., *J. Polym. Sci. Part B: Polym. Phys.*, 41 (2003) 3272
157. Larentzos J. P. et al., *J. Phys. Chem. C*, 111 (2007) 12752

158. Spangberg D. and Hermansson K., *J. Chem. Phys.*, 120 (2004) 4829
159. Delville A., *Langmuir*, 7 (1991) 547
160. Chatterjee A. et al., *J. Chem. Phys.*, 118 (2003) 10212
161. Chatterjee A. et al., *J. Phys. Chem. A*, 106 (2002) 641
162. Chatterjee A. et al., *J. Phys. Chem. A*, 105 (2001) 10694
163. Boulet P. et al., *J. Mol. Struct.*, 762 (2006) 33
164. Boek E. S. et al., *J. Am. Chem. Soc.*, 117 (1995) 12608
165. Tambach T. J. et al., *J. Phys. Chem.*, 108 (2004) 7586
166. Smith D. E. et al., *Fluid Phase Equilibr.*, 222-223 (2004) 189
167. Whitley H. D. and Smith D. E., *J. Chem. Phys.*, 120 (2004) 5387
168. Hensen E. J. M. and Smit B., *J. Phys. Chem. B*, 106 (2002) 12664
169. Ohtaki H. and Radnai T., *Chem. Rev.*, 93 (1993) 1157
170. Tambach T. J. et al., *Langmuir*, 22 (2006) 1223
171. Berend I. et al., *Clay. Clay Miner.*, 43 (1995) 324
172. Tamura K. et al., *Clays Clay Miner.*, 48 (2000) 400
173. Tambach T. J. et al., *Langmuir*, 22 (2006) 1223
174. Chatterjee A. et al., *J. Chem. Phys.*, 120 (2004) 3414
175. Chatterjee A., *J. Chem. Sci.*, 117 (2005) 533
176. Boek E. S. and Sprik M., *J. Phys. Chem. B*, 107 (2003) 3251
177. Suter J. L. et al., *J. Phys. Chem. C*, 112 (2008) 18832
178. Tunega D. et al., *J. Soil Sci.*, 58 (2007) 680
179. Teppen B. J. et al., *J. Phys. Chem. A*, 106 (2002) 5498
180. Dittrich, *Nestlé Purina*, 2002
181. Monell, *Nestlé Research Center*, 2002
182. Pazos C., Volatile compounds in cat's urine, *Nestlé Research Center*, 2002
183. Mattina M. J. I. et al., *J. Chem. Ecol.*, 17 (1991) 451
184. Schiraldi A. and Fessas D., *J. Therm. Anal. Cal.*, 71 (2003) 221

185. Odom J. W. and Low P. F., *Soil Sci. Soc. Am. J.*, 47 (1983) 1039
186. Girard F. et al., *Langmuir*, 22 (2006) 11085
187. Hu H. and Larson R. G., *J. Phys. Chem. B*, 106 (2002) 1334
188. Crider W. L., *J. Am. Chem. Soc.*, 78 (1956) 924
189. Altshuller A. P. and Cohen I. R., *Anal. Chem.*, 32 (1960) 802
190. Mato F. and Cimavilla J. M., *An. Quim.*, 79 (1983) 445
191. Nagata I. and Hasegawa T., *J. Chem. Eng. Jpn.*, 3 (1970) 143
192. Schwertz F. A. and Brow J. E., *J. Chem. Phys.*, 19 (1951) 640
193. Arnikar H. J. and Ghule H. M., *Int. J. Electron.*, 26 (1969) 159
194. Clarke J. K. and Ubbelohde A. R., *J. Chem. Soc.*, 393 (1957) 2050
195. Cummings G. A. M. and Ubbelohde A. R., *J. Chem. Soc.*, 767 (1953) 3751
196. Gilliland E. R., *Ind. Eng. Chem.*, 26 (1934) 681
197. Hippenmeyer B., *Angew. Phys.*, 1 (1949) 549
198. Hudson G. H. et al., *Trans. Faraday Soc.*, 56 (1960) 1144
199. Ibrahim S. H. and Kuloor N. R., *Brit. Chem. Eng.*, 6 (1961) 862
200. Lugg G. A., *Anal. Chem.*, 40 (1968) 1072
201. Nelson E. T., *J. Appl. Chem.*, 6 (1956) 286
202. O'Connell J. P. et al., *J. Phys. Chem.*, 73 (1969) 2000
203. Bridgeman O. C. and Aldrich E. W., *J. Heat Transfer*, 86 (1964) 279
204. Besley L. M. and Bottomley G. A., *J. Chem. Thermodyn.*, 6 (1974) 577
205. Gaw W. J. and Swinton F. L., *Trans. Faraday Soc.*, 64 (1968) 637
206. McCullough J. P. et al., *J. Am. Chem. Soc.*, 79 (1957) 4289
207. Polak J. and Mertl I., *Collect. Czech. Chem. Commun.*, 30 (1965) 3526
208. Kretschmer C. B. and Wiebe R., *J. Am. Chem. Soc.*, 71 (1949) 1793
209. Ambrose D. and Sprake C. H. S., *J. Chem. Thermodyn.*, 2 (1970) 631
210. Carruth G. F. and Kobayashi R., *J. Chem. Eng. Data*, 18 (1973) 115
211. Williamham C. B. et al., *J. Res. Natl. Bur. Stand. (U. S.)*, 35 (1945) 219

212. Kohn W. and Sham L. J., *Phys. Rev.*, 137 (1965) A1697
213. CPMD Copyright IBM Corp 1990-2008; Copyright MPI für Festkörperforschung Stuttgart 1997-2001, (see www.cpmd.org)
214. Perdew J. P. et al., *Phys. Rev. Lett.*, 77 (1996) 3865
215. Trouiller N. and Martins J. L., *Phys. Rev. B*, 43 (1991) 1993
216. Kleinman L. and Bylander D. M., *Phys. Rev. Lett.*, 48 (1982) 1425
217. Goedecker S. et al., *Phys. Rev. B*, 54 (1996) 1703
218. Louie S. G. et al., *Phys. Rev. B*, 26 (1982) 1738
219. Perdikatsis B. and Burzlaff H., *Z. Kristallogr.*, 156 (1981) 177
220. Lee J. H. and Guggenheim S., *Am. Mineral.*, 66 (1981) 350
221. Wardle R. and Brindley G. W., *Am. Mineral.*, 57 (1972) 732
222. Car M. and Parrinello M., *Phys. Rev. Lett.*, 55 (1985) 2471
223. Refson K. et al., *J. Phys. Chem. B*, 107 (2003) 13383
224. Sainz-Diaz I. et al., *Am. Mineral.*, 87 (2002) 965
225. Lide D. R., *Handbook of Chemistry and Physics*, CrC Press, 1994
226. Sugino M. et al., *J. Mol. Struct.*, 245 (1991) 357
227. Mathisen H. et al., *Acta Chem. Scand.*, 21 (1967) 127
228. Huang J. et al., *J. Mass Spectrom. Soc. Jpn.*, 50 (2002) 296
229. Dzidic I. and Kebarle P., *J. Phys. Chem.*, 74 (1970) 1466
230. *Handbook of Chemistry and Physics*, Lewis Pub, 1994
231. Jung-Hoo L. and Stephen G., *Am. Mineral.*, 66 (1981) 350
232. Rinnert E. et al., *J. Phys. Chem. B*, 109 (2005) 23745
233. Michot L. J. et al., *Am. Mineral.*, 90 (2005) 166
234. Chiou C. T. and Rutherford D. W., *Clays Clay Miner.*, 45 (1997) 867
235. Wada N. et al., *Phys. Rev. B*, 41 (1990) 12895
236. Skipper N. T. et al., *Clays Clay Miner.*, 43 (1995) 294
237. Van Olphen H., *J. Colloid Sci.*, 20 (1965) 822
238. Nakashima Y., *Am. Mineral.*, 85 (2000) 132

239. Ochs M. et al., *Phys. Chem. Earth*, 29 (2004) 129
240. Franks F., *Water: A matrix of life*, Royal Society of Chemistry, 2000
241. Provencher S. W., *Comput. Phys. Commun.*, 27 (1982) 213
242. Hansen S., *J. Chem. Phys.*, 21 (2004) 9111
243. Kile D. E. and Eberl D. D., *Am. Mineral.*, 88 (2003) 1514
244. Sun H., *J. Phys. Chem. B*, 102 (1998) 7338
245. Schwegler E. et al., *J. Chem. Phys.*, 121 (2004) 5400
246. Hendricks S. B. et al., *J. Am. Chem. Soc.*, 62 (1940) 1457
247. Miyazaki K. et al., *Condens. Matter Phys.*, 4 (2001) 315

Pascal CLAUSEN, *Physicist*, PhD

Rte de Berne 1, CH-1010 Lausanne
phone: +41 (0)78 8258005 / +41 (0) 21 6527518 email: pascal.clausen@epfl.ch

Research Interests: Physically-based simulations, Physical-Chemistry, Photonics.

EDUCATION

Ph.D., *Material Science*, Ecole Polytechnique Fédérale de Lausanne (EPFL), 2005 – 2009

Description: Characterization of the release mechanisms of volatiles from smectite clay minerals adsorbents by finite element methods, DFT-based *ab initio* calculations in the plane-wave pseudopotential scheme, thermogravimetry, differential calorimetry, and mass spectrometry.

M.S., *Physics*, Eidgenössische Technische Hochschule Zürich (ETHZ), 2003

- Master thesis: *Optimization of V-groove quantum wire light emitting diodes*
- Robotic competition: *Image recognition of bottles and cans*
- Semester work: *Fabrication and characterization of a ring fiber laser*

PROFESSIONAL EXPERIENCE

- 2004 Development of electronic sensors for the control of alimentary oils, *Alpsens Technologies*
- 2004 Fabrication of clay/polymer nanocomposites for packaging materials with improved gas barrier properties, *Ecole Polytechnique Fédérale de Lausanne*
- 2003 Fabrication of nanoscaled interdigitated electrodes arrays for the detection of genetically modified food, *Ecole Polytechnique Fédérale de Lausanne*

COMPUTING SKILLS

- Programming languages: *Matlab, Fortran, Labview, visual basic, visual C++*,
- Simulation softwares: *CPMD, COMSOL*
- Operating systems: *Unix, Windows*

SCIENTIFIC PUBLICATIONS

- Clausen P., Watzke B., Hughes E., Plummer J. G. C., Månson E. J.-A., “Evaporation kinetics of volatile liquids and release kinetics of water from a smectite clay: comparison between experiments and finite element calculations”, submitted in *International Journal of Engineering Science*
- Clausen P., Andreoni W., Curioni A., Plummer J. G. C. “Adsorption of low-molecular-weight molecules on the surface of a sodium smectite clay: an ab initio study”, submitted in *The Journal of Physical Chemistry*
- Clausen P., Signorelli M., Fessas D., Hughes E., Schiraldi A., Plummer J. G. C., Månson E. J.-A., “Equilibrium desorption isotherms of water, ethanol, ethyl acetate and toluene on a sodium smectite clay”, submitted in *Journal of Thermal Analysis and Calorimetry*
- Clausen P., Meier L., Plummer J. G. C., Månson E. J.-A., “Release kinetics of water, ethanol, ethyl acetate and toluene from smectite clays modified by ion exchange”, submitted in *Clays and Clay Minerals*
- Clausen P., Andreoni W., Curioni A., Plummer J. G. C., “Water adsorption on a sodium smectite clay surface: an ab initio study”, submitted in *The Journal of Physical Chemistry*

LANGUAGES

French (*mother tongue*), English (*fluent*), German (*good*)